Charge Transport in Protic Ionic Liquids

Unraveling the Charge Carrier Dynamics in 1-Methylimidazolium Acetate/Trifluoroacetate Mixtures

Dissertation zur Erlangung des Grades

Doktor rerum naturalium (Dr.rer.nat.)

im Promotionsfach Chemie

am Fachbereich 09
Chemie, Pharmazie, Geographie und Geowissenschaften
der Johannes Gutenberg-Universität Mainz

Johannes Wolfgang Sutter

Mainz, 2024

1. Gutachter:

Prof. Dr. [redacted]

2. Gutachter:

Prof. Dr. [redacted]

Tag der mündlichen Prüfung: 29.11.2024

Declaration of Authorship

I hereby declare that I wrote this dissertation submitted without any unauthorized external assistance and used only sources acknowledged in the work. All textual passages which are appropriated verbatim or paraphrased from published and unpublished texts as well as all information obtained from oral sources are duly indicated and listed in accordance with bibliographical rules. In carrying out this research, I complied with the rules of standard scientific practice as formulated in the statutes of Johannes Gutenberg-University Mainz to insure standard scientific practice.
In chapters 4 to 7, I will write in the first person plural instead of singular (we instead of I) to make the text more readable and to account for the specified contributions of others to those chapters.

Johannes Wolfgang Sutter
Mainz, September 2024

"*Every great and deep difficulty bears in itself it's own solution. It forces us to change our thinking in order to find it.*"

- Niels Bohr

Abstract

The transition to renewable energy sources represents one of the biggest challenges facing modern society. As this endeavour is driven forward globally, the importance of efficient and cost-effective energy storage technologies becomes increasingly apparent. Batteries are at the forefront of this effort, serving as the primary storage solution for the intermittent output of renewable energy sources. Beyond this, batteries are present in various facets of daily life, including mobility, medical & healthcare, and personal electronics. However, the success of this transition depends heavily on overcoming critical challenges, notably the reliance on materials such as lithium, rare earth elements and other critical raw materials that are essential to current battery compositions. Uncertainty about the sustainable and secure supply and potentially escalating cost of these materials, coupled with safety concerns such as flammability, underline the urgent need for alternative solutions.

In the pursuit of efficient battery electrolytes, ionic liquids have emerged as promising candidates. However, the widespread use of conventional aprotic ionic liquids has been hampered by limited conductivities due to high viscosities. Protic ionic liquids (PILs), formed by reversible proton transfer, offer a solution, in principle allowing to decouple charge from mass transport and enabling high conductivities. In particular, 1-methylimidazolium acetate has shown unexpectedly high conductivity, suggesting a significant proton transport contribution. Despite extensive studies, the complex dynamics of charge carriers in protic ionic liquids remain somewhat elusive.

This thesis aims to unravel the charge carrier dynamics in protic ionic liquids at the molecular level and to contribute to a deeper understanding of the latter on the way to a task-specific design of PILs using state-of-the-art experimental spectroscopic and computational methods, including nuclear magnetic resonance spectroscopy, dielectric relaxation spectroscopy, ultrafast visible pump-infrared probe spectroscopy, density functional theory calculations, and polarizable molecular dynamics simulations.

In Chapter 4, the role of proton conduction for the enhanced charge transport in protic ionic liquids based on 1-methylimidazolium is investigated. Dielectric relaxation (DR) and nuclear magnetic resonance (NMR) spectroscopy provide the dipolar response and conductivity, as well as the average proton distribution and mobility. The effect of the acidity of the Brønsted acid is elucidated by the gradual variation of the anion and thus the composition of the PIL from 1-methylimidazolium acetate [MimH][AcO] to 1-methylimidazolium trifluoroacetate [MimH][TFA]. The results show the dominance of electro-neutral species in [MimH][AcO] forming extended H-bonded networks. Addition of [MimH][TFA] increases the degree of protonation and reduces

the dipolar response. Diffusion-ordered spectroscopy reveals enhanced proton mobility, indicating that Grotthuss-like proton transport is observed with increasing TFA content. Variations in ion-pair formation and proton exchange dynamics are observed in different solvent environments (protic and aprotic), highlighting the sensitivity of protonation equilibria and transport to the surrounding environment.

Chapter 5 investigates the dynamic behaviour and intermolecular interactions of 1-methylimidazolium acetate [MimH][AcO] upon substitution with [MimH][TFA]. A combined approach using experimental dielectric relaxation spectroscopy and polarizable molecular dynamics simulations is used to decompose and interpret the dielectric spectra at the molecular level. The accuracy of the simulation model is assessed by comparison between experimental and computational results. The addition of [MimH][TFA] increases the ionicity of the system while decreasing the dielectric constant, mainly due to reduced translational contributions. Strong correlations in molecular orientations are observed upon addition of [MimH][TFA]. The remarkable increase in conductivity found at high trifluoroacetate concentrations is attributed to enhanced proton transport and a reduction of hindered translation in favour of free ionic motion.

In Chapter 6, the temperature-dependent dynamics of 1-methylimidazolium-based PIL systems are investigated. By studying the thermal activation of the dielectric response, it is possible to experimentally disentangle the translational and rotational contributions to the dielectric response. The temperature-dependent dielectric spectra show an acceleration of the dynamics with increasing temperature, indicated by a shift of its dominant contribution to higher frequencies. The effective dipole moments of the high frequency modes are insensitive to PIL composition, suggesting a rotational origin, supported by similar activation energies. In contrast, the effective dipole moment of the low-frequency mode varies significantly with composition, supporting marked contributions due to hindered translations to the dielectric response. The similarity of the activation energies for the hindered translations and the overall conductivity confirms this assignment, which is further supported by molecular dynamics simulations. In contrast to the acidity of the anion, the thermal energy within the studied temperature range appears insufficient to disrupt these cage structures, that lead to hindered translational motion. Yet, increased temperatures result in enhanced fluctuations of ions in their cages.

In Chapter 7, proton transport is experimentally distinguished from ion transport using visible pump-infrared probe spectroscopy. The experiments allow for tracking of the transport of an excess proton released by a photoacid in 1-methylimidazolium acetate in MeOH. In addition to the induced absorption associated with the protonation of the acetate, transient spectra also showed a slightly red-shifted bleach. Pump-probe experiments with acetic acid revealed that the bleach can be related to the protonation of acetic acid. Further experiments with AcOH/AcO^- mixtures indicate that not only the $AcO^- \rightleftharpoons$AcOH equilibrium, but also the AcOH$\rightleftharpoons AcOH_2^+$ equilibrium plays an essential role in the proton transfer dynamics in [MimH][AcO]. Protonation of acetic

acid occurs predominantly when it is in excess relative to its conjugate base, acetate. Concentration dependent measurements allowed to estimate average proton diffusion coefficients.

In general, the proton contribution can drastically increase the conductivity in protic ionic liquids. However, ionic species must be mobile for vehicular transport. Conductivity depends on a complex interplay between the intrinsic properties and the chemical environment of PIL systems. This work shows that in such systems, depending on the environment, ions can be bound in ion pairs or cages, resulting in hindered translational motion. A suitable choice of chemical environment or acidity of the anion reduces the restrictions on charge carrier mobility in PILs. The deepened understanding of molecular dynamics and its tunability, gained by the results presented in this thesis, will allow PILs with high conductivities to be specifically tailored for the above-mentioned applications.

Zusammenfassung

Der Wandel hin zu erneuerbaren Energiequellen stellt eine der größten Herausforderungen für die moderne Gesellschaft dar. Da die Energiewende weltweit vorangetrieben wird, wird die Bedeutung effizienter und kostengünstiger Technologien zur Energiespeicherung immer wichtiger. Dabei stehen Batterien unter anderem im Fokus, da sie als primäre Speicherlösung für die schwankende Leistung erneuerbarer Energiequellen dienen. Darüber hinaus sind Batterien in verschiedenen Bereichen des täglichen Lebens zu finden, beispielsweise in der Mobilität, der Medizintechnik und im Gesundheitswesen sowie in persönlichen Geräten des alltäglichen Gebrauchs. Der Erfolg der Energiewende hängt jedoch in hohem Maße von der Bewältigung kritischer Herausforderungen ab, wie etwa der Abhängigkeit von begrenzt verfügbaren Materialien wie Lithium, seltenen Erden und anderen Rohstoffen, die für derzeitige Batteriezusammensetzungen unerlässlich sind. Die Ungewissheit bezüglich der nachhaltigen und sicheren Versorgung mit diesen Materialien und die potenziell steigenden Kosten sowie Sicherheitsbedenken wie Entflammbarkeit unterstreichen den dringenden Bedarf an alternativen Lösungen.

Auf der Suche nach effizienten Batterieelektrolyten haben sich ionische Flüssigkeiten als vielversprechende Kandidaten erwiesen. Die breite Anwendung herkömmlicher aprotischer ionischer Flüssigkeiten wird jedoch durch begrenzte Leitfähigkeiten aufgrund hoher Viskositäten begrenzt. Protische ionische Flüssigkeiten, die durch reversiblen Protonentransfer entstehen, könnten das Problem lösen, da sie im Prinzip eine Entkopplung von Ladungs- und Massentransport und somit hohe Leitfähigkeiten ermöglichen. Insbesondere 1-Methylimidazoliumacetat zeigt eine unerwartet hohe Leitfähigkeit, was auf einen erheblichen Beitrag der Protonen zum Ladungstransport schließen lässt. Trotz umfangreicher Studien sind die komplexen Ladungsträgerdynamiken in protischen ionischen Flüssigkeiten nach wie vor nicht gänzlich aufgeklärt.

Ziel dieser Arbeit ist es, die Ladungsträgerdynamik in protischen ionischen Flüssigkeiten auf molekularer Ebene zu entschlüsseln und zu einem tieferen Verständnis jener auf dem Weg zu einem aufgabenspezifischen Design von PILs beizutragen. Dazu werden modernste experimentelle spektroskopische Methoden in Kombination mit Computersimulationen eingesetzt, wie Kernspinresonanzspektroskopie, dielektrische Relaxationsspektroskopie, *Pump-Probe*-Spektroskopie im Femtosekundenbereich, *Density Functional Theory*-Rechnungen und *Molecular Dynamics*-Simulationen.

In Kapitel 4 wird die Rolle des Protonentransports für die verbesserte Leitfähigkeit in 1-Methylimidazolium-basierten protischen ionischen Flüssigkeiten untersucht. Die dielektrische Relaxations- (DR) und die Kernspinresonanzspektroskopie (NMR) geben Aufschluss über die Dynamik dipolarer Moleküle und die Leitfähigkeit, sowie die

durchschnittliche Protonenverteilung und deren Beweglichkeit. Die Auswirkung der Säurestärke der Brønsted-Säure wird durch die schrittweise Substitution des Anions und damit der Zusammensetzung der PIL von 1-Methylimidazoliumacetat [MimH][AcO] zu 1-Methylimidazoliumtrifluoroacetat [MimH][TFA] untersucht. Die Ergebnisse zeigen die Dominanz elektoneutraler Spezies in [MimH][AcO], die ausgedehnte H-Brückennetzwerke bilden. Die Zugabe von [MimH][TFA] erhöht den Protonierungsgrad und verringert die dipolaren Beiträge. Diffusionsaufgelöste NMR-Experimente zeigen eine erhöhte Protonenmobilität, was darauf hindeutet, dass mit zunehmendem TFA-Gehalt ein Grotthuss-ähnlicher Protonentransport stattfindet. Variationen in der Ionenpaarbildung und der Protonenaustauschdynamik werden in verschiedenen Lösungsmittelumgebungen (protisch und aprotisch) beobachtet, was die Empfindlichkeit der Protonierungsgleichgewichte und des Transports gegenüber der chemischen Umgebung hervorhebt.

In Kapitel 5 werden das dynamische Verhalten und die intermolekularen Wechselwirkungen von 1-Methylimidazoliumacetat [MimH][AcO] nach Substitution mit [MimH][TFA] untersucht. Eine Kombination aus experimenteller dielektrischer Relaxationsspektroskopie und polarisierbaren MD-Simulationen wird angewandt, um die Beiträge zu den dielektrischen Spektren auf molekularer Ebene aufzugliedern und zu interpretieren. Die Genauigkeit des Simulationsmodells wird durch den Vergleich zwischen experimentellen und simulierten Ergebnissen überprüft. Die Zugabe von [MimH][TFA] erhöht die Ionizität des Systems bei gleichzeitiger Verringerung der Dielektrizitätskonstante, was hauptsächlich auf reduzierte Translationsbeiträge zurückzuführen ist. Bei Zugabe von [MimH][TFA] werden starke Korrelationen in der Orientierung der Moleküle beobachtet. Der bemerkenswerte Anstieg der Leitfähigkeit bei hohen Konzentrationen an Trifluoroacetat wird auf einen verbesserten Protonentransport und eine Verringerung der eingeschränkten Translation zugunsten der freien Ionenbewegung zurückgeführt.

In Kapitel 6 wird die temperaturabhängige Dynamik von 1-Methylimidazolium-basierten PIL-Systemen untersucht. Durch Untersuchung der thermischen Aktivierung der dielektrischen Dynamiken ist es möglich, die Translations- und Rotationsbeiträge zur Gesamtdynamik experimentell zu entwirren. Die temperaturabhängigen dielektrischen Spektren zeigen eine Beschleunigung der Dynamik mit zunehmender Temperatur, was durch eine Verschiebung des dominanten Beitrags zu höheren Frequenzen indiziert wird. Die effektiven Dipolmomente der Moden bei hohen Feldfrequenzen sind unempfindlich gegenüber der Zusammensetzung der PIL, was auf signifikante Rotationsbeiträge hindeutet, was durch ähnliche Aktivierungsenergien unterstützt wird. Im Gegensatz dazu variiert das effektive Dipolmoment der niederfrequenten Mode signifikant mit der Zusammensetzung, was auf deutliche Beiträge durch eingeschränkte Translationen zur dielektrischen Antwort hindeutet. Die Ähnlichkeit der Aktivierungsenergien für die eingeschränkte Translationen und die Gesamtleitfähigkeit bestätigt diese Zuordnung, die durch MD-Simulationen weiter untermauert wird. Im Gegensatz zur Azidität des Anions, scheint die thermische Energie im untersuchten

Temperaturbereich nicht auszureichen, um die Käfigstrukturen aufzubrechen, die zur eingeschränkten Translationsbewegung führen. Höhere Temperaturen führen jedoch zu verstärkten Fluktuationen der Ionen in ihren Käfigen.

In Kapitel 7 wird der Protonentransport mit Hilfe von *Visible Pump-IR Probe*-Spektroskopie experimentell vom Ionentransport getrennt adressiert. Die Experimente ermöglichen es, den Transport eines Überschussprotons, welches durch eine Photosäure in der 1-Methylimidazoliumacetat-MeOH Lösung freigesetzt wird, zu verfolgen. Das transiente Spektrum zeigt neben einer induzierten Absorption, die der Protonierung des Acetats zugeordnet werden kann, einen leicht rotverschobenen Bleach. *Pump-Probe*-Experimente in Essigsäure-MeOH Lösungen ergaben, dass dieser Bleach mit der Protonierung der Essigsäure zusammenhängt. Weitere Experimente mit AcOH/AcO^--Mischungen deuten darauf hin, dass nicht nur das AcO^- $\rightleftharpoons$AcOH-Gleichgewicht, sondern auch das AcOH$\rightleftharpoons$$AcOH_2^+$-Gleichgewicht eine wesentliche Rolle für die Protonentransferdynamik in [MimH][AcO] spielt. Die Protonierung von Essigsäure tritt vor allem dann auf, wenn sie im Vergleich zu ihrer konjugierten Base, Acetat, im Überschuss vorhanden ist. Durch konzentrationsabhängige Messungen konnten die durchschnittlichen Protonendiffusionskoeffizienten abgeschätzt werden.

Im Allgemeinen kann der Beitrag der Protonen die Leitfähigkeit in protischen ionischen Flüssigkeiten drastisch erhöhen. Allerdings müssen die ionischen Spezies für einen vehikelähnlichen Transport mobil sein. Die Leitfähigkeit hängt von einem komplexen Zusammenspiel zwischen den intrinsischen Eigenschaften und der chemischen Umgebung der PIL-Systeme ab. Diese Arbeit zeigt, dass Ionen in solchen Systemen, je nach Umgebung, in Ionenpaaren oder Käfigen gebunden sein können, was zu einer eingeschränkten Translationsbewegung führt. Eine geeignete Wahl der chemischen Umgebung oder der Säurestärke des Anions verringert die Einschränkungen der Ladungsträgerbeweglichkeit in PILs. Das tiefgehende Verständnis der Ladungsträgerdynamik auf molekularer Ebene, sowie die Möglichkeiten zu deren Konfiguration, das durch die in dieser Arbeit vorgestellten Ergebnisse gewonnen wurde, ermöglicht es, PILs mit hohen Leitfähigkeiten speziell für die oben genannten Anwendungen zu entwickeln.

Publications Covered in this Thesis

Chapter 4:

Sutter, J. [redacted] Charge transport in protic ionic liquids: Effect of protonation state in 1-methylimidazolium – acetate/trifluoroacetate mixtures. *J. Mol. Liq.* **2023**, 390.
https://doi.org/10.1016/j.molliq.2023.122975.

Chapter 5:

[redacted] **Sutter, J.*** [redacted]
Comparative Analysis of Dielectric Spectra in Protic Ionic Liquids: Experimental Findings and Computational Molecular Decomposition. *J. Mol. Liq.* **2024**, 396.
*Authors contributed equally
https://doi.org/10.1016/j.molliq.2023.123834.

Chapter 6:

Sutter, J. [redacted] On the effect of temperature on the ion dynamics in 1-methylimidazolium-based protic ionic liquids.
in preparation

Chapter 7:

Sutter, J. [redacted] Insights into proton transfer intermediates and dynamics in solution of the protic ionic liquid 1-methylimidazolium acetate from transient spectroscopy.
in preparation

Other publications:

[redacted] **Sutter, J.** [redacted]
Stable Molybdenum(0) Carbonyl Complex for Upconversion and Photoredox Catalysis. *J. Am. Chem. Soc.* **2023**,145, 16597-16609.
https://doi.org/10.1021/jacs.3c03832.

Outline and Contribution

This thesis focuses on the investigation of charge transport in protic ionic liquids, in particular 1-methylimidazolium acetate and 1-methylimidazolium trifluoroacetate, as well as their mixtures, by combining different experimental spectroscopic methods, such as dielectric relaxation spectroscopy, nuclear magnetic spectroscopy and ultrafast pump-probe spectroscopy, with computational simulations, namely density functional theory and polarizable molecular dynamics simulations.

Chapter 4 investigates the average proton distribution and the charge carrier dynamics in 1-methylimidazolium acetate using dielectric relaxation and nuclear magnetic resonance spectroscopy. In addition, the influence of the immediate chemical environment (e.g. solvent) and the acidity of the Brønsted acid is elucidated by substituting acetate with trifluoroacetate.
J.S. and J.H. designed the research project and interpreted the experimental results. J.S. synthesized the PILs and prepared all samples, performed the dielectric relaxation experiments and analysed the data. J.S. characterised the PILs by ^{1}H- and ^{13}C-NMR spectroscopy. J.S. performed the DFT and dipole moment calculations. C.H. performed the NMR measurements (except for characterisation). C.H. and R.G. analysed and interpreted the NMR experiments. The results were discussed by all authors. All authors contributed to the drafting of the manuscript.

Chapter 5 investigates the dielectric spectra of 1-methylimidazolium acetate/trifluoroacetate mixtures using dielectric relaxation spectroscopy and molecular dynamics simulations. Computational results allow the spectra to be decomposed at the molecular level and the proton contribution to be identified.
J.S., F.J., J.H. and C.S. designed the research project and interpreted the results. J.S. synthesised the PILs, performed the dielectric relaxation experiments and analysed the data. J.S. performed the DFT calculations. F.J. carried out the molecular dynamics simulations and analysed the results. All authors discussed the results and participated in the drafting of the manuscript.

Chapter 6 examines the temperature-dependent dynamics of 1-methylimidazolium acetate/trifluoroacetate mixtures using dielectric relaxation spectroscopy and molecular dynamics simulations. Experimental and computational results provide insight into the decomposition of the translational and rotational contributions to the dielectric response.

J.S., F.J., J.H. and C.S. designed the research project and interpreted the results. J.S. synthesised all PILs, performed the dielectric relaxation experiments and analysed the data. F.J. carried out the molecular dynamics simulations and analysed the results. All authors discussed the results.

Chapter 7 specifically isolates the proton contribution to the charge transport in 1-methylimidazolium acetate/methanol mixtures using visible pump - infrared probe spectroscopy. Concentration-dependent measurements allow to extract the transport time of the proton as a function of average distance.
J.S. and J.H. designed the research project and interpreted the experimental results. J.S. synthesized all PILs. J.S. and C.W. prepared the samples and performed the pump-probe experiments, J.S. analysed the data. All authors discussed the results.

Contents

Chapter 1

Introduction

Ionic liquids (ILs) have attracted considerable research interest, ranging from green chemistry to advanced materials for energy storage, over the last few decades.[1] Typically, ILs are composed entirely of ionic species and, with melting points below 100 °C, they are also known as molten salts.[2]
In 1888, Gabriel reported what is believed to be the first salt considered to be an ionic liquid, ethanolammonium nitrate, with a melting point of ~52-55 °C.[3, 4] Walden made a landmark achievement in 1914 by introducing the first room-temperature ionic liquid (RTIL), a subclass of ILs that is liquid at ambient temperatures.[5] Although now considered a milestone in IL research, the compound ethylammonium nitrate, with a melting point of 14 °C, did not attract much attention at the time.[5]
It was not until the end of the 20th century that ILs returned to the focus of scientific research with the emergence of a new class of RTILs, dialkylimidazolium chloroaluminates.[6] However, the severe sensitivity of these chloroaluminate systems to water made them very difficult to handle and drastically limited their application possibilities.[7] Ten years later, air- and water-stable ILs based on the 1-methyl-3-methylimidazolium cation and weakly coordinating anions (e.g. hexafluorophosphate PF_6^-, tetrafluoroborate BF_4^-, etc.) were reported, apparently allowing a wider range of potential applications.[8] However, the claimed thermal and hydrolytic stability was later found to be somewhat exaggerated.[9, 10] Since then, research interest has continued to grow, fuelled in particular by Freemantle, who coined the term 'designer solvents' to highlight the properties and possibilities of ILs.[11, 12] More than 10^6 possible combinations of different cations and anions yielding ionic liquids have been predicted.[12] This sheer number allows almost unlimited task-specific tunability of IL properties compared to conventional organic solvents and indeed justifies the term 'designer solvent'.[7]
The tunability and unique physicochemical properties such as negligible vapour pressure[13], large electrochemical window[14], high thermal stability[15] and solvation potential[16–18] are key features of ILs and enable a broad variety of possible applications. To date, ionic liquids have been used not only as solvents in chemical synthesis[19–21], but also in reaction catalysis[22, 23]. In particular, the supported ionic liquid phase (SILP) concept of Wasserscheid and co-workers[24] has received major attention.[25] Their low volatility is an important advantage over conventional synthetic oils when used as lubricants.[26, 27] Jork and co-workers found that ILs

could act as entrainers (separation agents) for azeotropic mixtures.[28] In addition to their use for separations in analytical chemistry, ILs can be used to extract bioactive compounds[29] and nuclear materials[30]. Pharmaceutical applications[31–34] attracted much interest and were first introduced in 1998 by Davis et al[35]. ILs have been reported as solvents or active components in the synthesis of drug carrier nanoparticles with high anti-tumor potential.[36–39]

In 2003, BASF introduced the first commercial industrial process using ILs.[40] In the Biphasic Acid Scavenging Utilising Ionic Liquids (BASIL) process, methylimidazole is used to replace triethylamine as a proton scavenger in the synthesis of alkoxyphenylphosphanes, resulting in the formation of 1-methylimidazolium chloride.[40]

Perhaps one of the most exciting applications of ILs, however, is in energy technologies.[41, 42] The potential use of ILs as electrolytes for future battery generations was considered shortly after the discovery of the chloroaluminate systems in the 1980s.[43] Since then, ILs have been used in dye-sensitised solar cells[44, 45], supercapacitors[46, 47] and fuel cells[48, 49].

In recent years, ionic liquids have been successfully applied in many areas of science and technology. However, some aspects should be viewed critically. For example, initial claims of thermal and chemical stability need to be revised for some compounds.[50, 51] In addition, it has been shown that ILs do not have zero vapour pressure.[52] The supposed low toxicity of ILs is also a matter of dispute. Studies on toxicity and biodegradability have concluded that this perception is not generally valid.[53, 54] Obstacles such as low conductivity due to the high viscosity of conventional aprotic ionic liquids (AILs) still need to be overcome, particularly in energy storage applications.[55] Protic ionic liquids (PILs), a subclass of ILs formed by reversible proton transfer between Brønsted acids and Brønsted bases, are capable of overcoming these limitations.[56, 57] An essential feature of PILs is their ability to form extended hydrogen-bonded networks.[2, 58–60] Via these proton transfer equilibria, it may be possible to decouple charge transport from (diffusion-limited) mass transport and drastically enhance conductivities.[1] Many studies have attempted to investigate the molecular-scale charge transport dynamics and proton distribution in PILs, but so far this has remained somewhat elusive.[61–64]

In particular, 1-methylimidazolium acetate [MimH][AcO], an intensively studied example of PILs, has received a great deal of attention due to its relatively high ionic conductivity.[57, 61] However, previous Raman and potentiometric studies suggested that 1-methylimidazolium acetate may be dominated by neutral species, consistent with the low acidity of acetic acid ($pK_a \approx 4.76$).[61, 65] Density functional theory (DFT) calculations support these experimental results by showing that the neutral complex (e.g. acetic acid and 1-methylimidazole) is more stable than an ionic complex (e.g. 1-methylimidazolium acetate).[61] A recently published molecular dynamics simulation study further confirms this conclusion.[66] Simulations with only 30 % ionic species could best reproduce the experimental results.[66] In contrast, NMR experiments on this PIL system revealed a degree of protonation of the 1-methylimidazole

molecules higher than 90 %.[67, 68] Furthermore, a strong decrease in ionicity was observed with the addition of polar solvents.[68] However, some studies suggest a more continuous transition between the extremes of purely neutral hydrogen-bonded molecules and ion-paired species.[69, 70] Although these preliminary studies are quite complementary, they indicate that the protonation equilibrium in [MimH][AcO] is sensitive to several influences. As a consequence, thermal fluctuations could lead to variations of this equilibrium, and thus the proton transfer could play a crucial role in the dynamics of the overall charge carrier dynamics. While molecular dynamics simulations explicitly declared that proton transfer occurs[71], experimental results provided only indirect evidence. For example, Grotthusss-like proton transport in 1-methylimidazolium acetate was suggested by comparing the activation energies of translational and rotational motions.[72] Other studies have shown that the proton equilibrium can be effectively altered by variation in the acidity of the anion. The substitution of acetate by trifluoroacetate leads to a quantitative protonation of [Mim] and, respectively, to a change in the proton transport mechanism from proton hopping to vehicular transport.[73] Even though molecular dynamics simulations have indicated a number of possible proton transport channels in 1-methylimidazolium acetate, only acetic acid chain-like structures allow for a Grotthusss-like transport mechanism.[71] In conclusion, the conductivity of PILs is highly dependent on the delicate balance between neutral and ionic species. Therefore, by varying the acidity of the Brønsted acid and hence the degree of protonation, the overall charge carrier dynamics can be tuned.

The aim of this work is to unravel the charge carrier dynamics and, in particular, the proton contribution to the latter in [MimH][AcO] at the molecular level. In addition, the gradual increase of the ionicity by the substitution of acetate by trifluoroacetate should provide a deeper understanding of the influence of the acidity of the Brønsted acid on the way to an application-specific design of PILs.
Therefore, dielectric relaxation spectroscopy (DRS) is used to study the dynamics of dipolar species.[74, 75] DRS is particularly sensitive to ion pairs, but also provides information on ion mobility via conductivity.[76, 77] In addition, nuclear magnetic resonance spectroscopy is used to obtain information about the molecular structure of the investigated PIL system. In particular, the protonation state of [Mim] can be accessed by measuring the ^{15}N chemical shifts. The mobility of individual molecular species can be measured by diffusion-ordered spectroscopy (DOSY). Both the average proton distribution and the dynamics in the studied PIL systems can be accessed by these two powerful experimental methods. To understand the influence of the chemical environment, binary mixtures of the PILs and a solvent will be studied. Therefore, a protic and an aprotic solvent, methanol and dimethylformamide, respectively, will be considered.
Polarizable molecular dynamics (MD) simulations will provide valuable insights into the dynamics and intermolecular interactions at the molecular scale in the investigated

PIL systems.[66, 78] The comparison of computational results with experimental data will ensure the accuracy of the applied simulation model. In particular, MD simulations allow the decomposition of the dielectric response into molecular translational and rotational contributions.[66, 78] Furthermore, these simulations provide insights into orientational correlations and the role of proton transfer in the overall conductivity.[66, 78]

Temperature-dependent dielectric relaxation measurements of the PIL systems will provide information about the contributions of rotational and translational motions to the overall dynamics. These dynamics, in turn, determine the dielectric response. Increasing temperature enhances translational motion of the ionic species resulting in an increase in the experimental dielectric amplitude.[79] Dipolar rotation also increases with increasing temperature, however, the maximal rotational amplitude is countered by enhanced thermal fluctuations.[79] This results in a decrease of the total experimental dielectric amplitude with increasing thermal energy.[79]

Finally, to specifically isolate the proton contribution, femtosecond pump-probe spectroscopy is used.[80–82] Therefore, a photoacid releasing a proton upon electronic excitation via a short laser pulse will be added to [MimH][AcO]. This excess proton will be transported within the PIL until it protonates an acetate ion. The protonation and the transport time, respectively, is monitored via the infrared (IR) probe pulse. The time-dependent proton dynamics will be studied by spectral changes of the carbonyl stretching vibration.[80, 81]

Chapter 2

Theoretical Background

2.1 Interaction of Matter with External Electromagnetic Fields

The interaction of electromagnetic radiation with a molecular system leads to energy-dependent, quantized transitions between electronic, vibrational and rotational states, which can be monitored by various spectroscopic methods.[83] In principle, the external electromagnetic field applied to a medium can be considered a force that causes the displacement of electrons and nuclei of atoms or molecules, which is referred to as polarization. Several mechanisms contribute to the overall macroscopic polarization, including electronic, atomic/ionic, interfacial, and orientational polarization.[84] Depending on the frequency of the electromagnetic radiation, different types of transitions can be induced. Rotational transitions can be effectively studied by broadband Dielectric Relaxation spectroscopy (DRS) using radiation in the microwave range (~MHz-GHz range).[84] The external field leads to the rotation and alignment of permanent dipoles according to the field. Vibrational transitions can be studied by Infrared spectroscopy (IR spectroscopy) using electromagnetic radiation in the infrared range (above ~1 THz). Intramolecular motion, e.g., vibration, results from the resonant absorption of electromagnetic radiation. Electronic transitions require ultraviolet-visible radiation (above several hundred THz) and can be studied by UV-Vis spectroscopy. Resonant absorption of electromagnetic radiation causes electrons to transition into higher energetic states.

A schematic representation of a complex permittivity spectrum is shown in Figure 2.1. At lower frequencies, interfacial polarization can contribute to the spectrum, including potential trapping at interfaces, impurities, etc.[84] In addition, the long-range translation of mobile ions contributes to the imaginary part of the spectrum. However, the main contribution in the microwave region comes from the rotational motion of molecules with permanent dipole moments, leading to dispersion in the real part and absorption in the imaginary part. Typically, up to several THz librations, intermolecular vibrations and hindered rotations (e.g., cage rattling motions) can contribute to the complex permittivity spectrum in addition to the rotational motions.[85] At higher frequencies (above several THz), intramolecular transitions occur. These include vibrations in the IR and electronic excitations in the UV-Vis range. Typically, compared

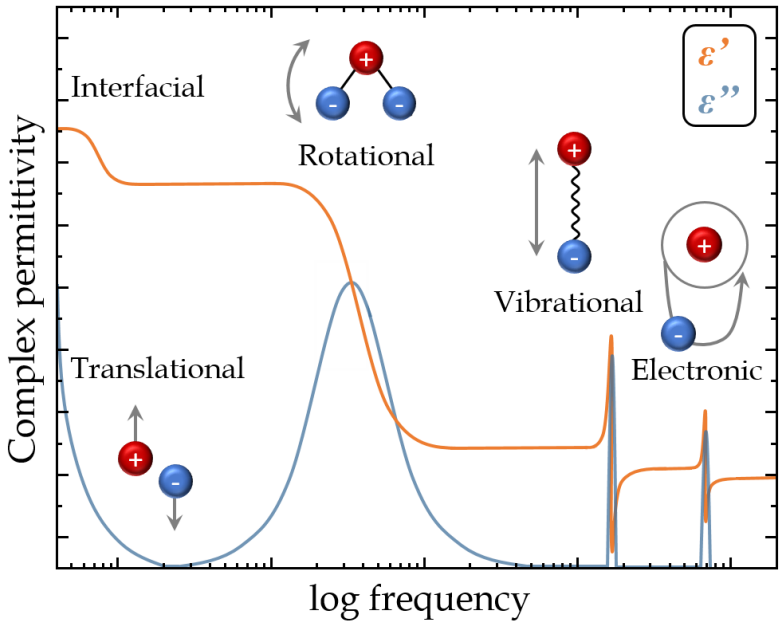

FIGURE 2.1: Schematic representation of a complex permittivity spectrum, including different types of intermolecular motions and intramolecular transitions. ε' is the real part and ε'' is the imaginary part of the complex permittivity.

to the rotational transitions in the spectrum, these resonant dispersion steps and absorption peaks are sharper.[86] The basic principles of light-matter interaction are discussed in more detail in the following section. In particular, dielectric relaxation and infrared spectroscopy are covered. A brief introduction to nuclear magnetic resonance spectroscopy concludes the chapter.

2.1.1 Maxwell's and Constitutive Equations

Maxwell's equations are four coupled partial differential equations that mathematically describe how electromagnetic fields interact with matter.[87–89] They form the basis of electromagnetism.[87–89]

$$\vec{\nabla} \cdot \vec{D} = \rho_{\text{el}} \tag{2.1}$$

$$\vec{\nabla} \cdot \vec{B} = 0 \tag{2.2}$$

$$\vec{\nabla} \times \vec{E} = -\frac{\partial \vec{B}}{\partial t} \tag{2.3}$$

$$\vec{\nabla} \times \vec{H} = \vec{j} + \frac{\partial \vec{D}}{\partial t} \tag{2.4}$$

where $\vec{D}$ is the electric flux density (e.g., dielectric displacement), ρ_{el} the charge density, $\vec{B}$ the magnetic flux density, $\vec{E}$ the electric field strength, $\vec{H}$ the magnetic field strength, and $\vec{j}$ the electric current density.

Gauss's law (Equation 2.1) defines that an electric charge is the source of an electric field.[83, 87, 90] There are no magnetic monopoles as sources of magnetic fields, according to the Equation 2.2.[83, 87, 90] Faraday's law (Equation 2.3) relates the change in an electric field to the change in the magnetic flux density with time.[83, 87, 90] Electric currents, including displacement currents, generate magnetic fields, according to Ampere's law (Equation 2.4).[83, 87, 90]

In combination with Newton's equation of motion[83] Maxwell's equations (equations 2.1–2.4) allow the calculation of most electromagnetic phenomena:

$$m\frac{\partial^2}{\partial t^2}\vec{r} = q(\vec{E} + \vec{v} \times \vec{B}) \tag{2.5}$$

where q is a moving charge with its velocity, $\vec{v}$.

For homogeneous, isotropic and non-dispersive materials, the constitutive equations (equations 2.6–2.8) apply, describing the response of bound charges and currents to the applied electromagnetic field.[83, 89]

$$\vec{D} = \varepsilon\varepsilon_0\vec{E} \tag{2.6}$$

$$\vec{j} = \sigma\vec{E} \tag{2.7}$$

$$\vec{B} = \mu\mu_0\vec{H} \tag{2.8}$$

with the vacuum permittivity ε_0, and the vacuum permeability μ_0. The constitutive equations relate the field quantities $\vec{E}$ and $\vec{B}$ to $\vec{D}$ and $\vec{H}$, respectively, including material-dependent properties.[83] In particular, these properties are the relative permittivity ε, the specific conductivity σ, and the relative permeability μ.[83]

2.1.2 Matter in Time-Dependent Electric Fields

In the context of a harmonically oscillating electric field $\vec{E}$, defined by its amplitude $\vec{E}_0$ and angular frequency $\omega = 2\pi\nu$,

$$\vec{E}(t) = \vec{E}_0 \cos(\omega t) \tag{2.9}$$

the dielectric displacement $\vec{D}$ (as described in Equation 2.10) responds to fluctuations in the external field $\vec{E}$.[83, 89] However, the response of $\vec{D}$ to changes in $\vec{E}$ may not be instantaneous, especially at frequencies of $\vec{E}$ above a certain threshold, resulting in a phase shift $\delta(\omega)$ (e.g., time delay between the external electric field and the dielectric displacement).[85] Various factors, such as temperature or molecular structure of the material, affect the magnitude of the delay. The dielectric displacement $\vec{D}(t)$ is given by

$$\begin{aligned}\vec{D}(t) &= \vec{D}_0 \cos(\omega t - \delta(\omega)) \\ &= \vec{D}_0 \cos(\delta(\omega)) \cos(\omega t) + \vec{D}_0 \sin(\delta(\omega)) \sin(\omega t) \\ &= \varepsilon'(\omega)\varepsilon_0 \vec{E}_0 \cos(\omega t) + \varepsilon''(\omega)\varepsilon_0 \vec{E}_0 \sin(\omega t)\end{aligned} \tag{2.10}$$

using trigonometric identities and introducing

$$\vec{D}_0 \cos(\delta(\omega)) = \varepsilon'(\omega)\varepsilon_0 \vec{E}_0 \tag{2.11}$$

$$\vec{D}_0 \sin(\delta(\omega)) = \varepsilon''(\omega)\varepsilon_0 \vec{E}_0 \tag{2.12}$$

According to Equation 2.10, the dielectric displacement separates into a dispersive part (in phase with $\vec{E}(t)$; real part) and a dissipative part (out of phase by $\pi/2$ to $\vec{E}(t)$; imaginary part).[85, 89] The real part ε' of the complex permittivity (Eq. 2.13) describes the frequency-dependent permittivity (e.g., dielectric constant), the imaginary part ε'' the loss of electric field energy (e.g., dielectric loss or absorption).[74, 89]

$$\hat{\varepsilon}(\omega) = \varepsilon'(\omega) - \mathrm{i}\varepsilon''(\omega) \tag{2.13}$$

Correspondingly, the constitutive equations 2.6–2.8 have to be adapted for the dynamic case of a time-dependent electric field:[85]

$$\hat{\vec{D}}(t) = \hat{\varepsilon}(\omega)\varepsilon_0 \hat{\vec{E}} \tag{2.14}$$

$$\hat{\vec{j}}(t) = \hat{\sigma}(\omega)\hat{\vec{E}}(t) \tag{2.15}$$

$$\hat{\vec{B}}(t) = \hat{\mu}(\omega)\mu_0 \hat{\vec{H}}(t) \tag{2.16}$$

with the complex conductivity $\hat{\sigma}(\omega)$ and the complex relative permeability $\hat{\mu}(\omega)$.

2.2 Dielectric Relaxation Spectroscopy

2.2.1 Wave Equations and Conductivity

Separating the electric and magnetic components leads to the following expressions for a harmonically oscillating electromagnetic field.

$$\hat{\vec{E}}(t) = \vec{E}_0 \cos(\mathrm{i}\omega t) \tag{2.17}$$

$$\hat{\vec{H}}(t) = \vec{H}_0 \cos(\mathrm{i}\omega t) \tag{2.18}$$

By means of the separation approach for the field components, Maxwell's equations 2.3 and 2.4 can be rewritten under consideration of the constitutive equations (eqs. 2.15–2.16) as follows.

$$\vec{\nabla} \times \vec{E}_0 = (-\mathrm{i}\omega\hat{\mu}(\omega)\mu_0)\hat{H}_0 \tag{2.19}$$

$$\vec{\nabla} \times \vec{H}_0 = (\hat{\sigma}(\omega) + \mathrm{i}\omega\hat{\varepsilon}(\omega)\varepsilon_0)\hat{E}_0 \tag{2.20}$$

Application of the rotation operator to Equation 2.20 and combination with Equation 2.19 and the Legendre vectorial identity,

$$\vec{\nabla} \times \left(\vec{\nabla} \times \vec{H}_0\right) = \vec{\nabla}\left(\vec{\nabla} \cdot \vec{H}_0\right) - \Delta\vec{H}_0 = \vec{\nabla}(0) - \Delta\vec{H}_0 = -\Delta\vec{H}_0 \tag{2.21}$$

results in the reduced wave equation of the magnetic field:[91]

$$\Delta\vec{H}_0 + \hat{k}^2\vec{H}_0 = 0 \tag{2.22}$$

The parameter $\hat{k}$, representing the propagation constant, is defined as follows.[91–93]

$$\hat{k}^2 = k_0^2\left(\hat{\mu}(\omega)\hat{\varepsilon}(\omega) + \frac{\hat{\mu}(\omega)\hat{\sigma}(\omega)}{\mathrm{i}\omega\varepsilon_0}\right) \tag{2.23}$$

with $k_0 = \omega\sqrt{\varepsilon_0\mu_0} = \frac{2\pi}{\lambda_0}$ representing the propagation constant in free space, where λ_0 is the wavelength of a monochromatic wave in vacuum.

Analogously for $\vec{E}$ (for $\operatorname{div}\vec{E} = 0$) the reduced wave equation is:[93]

$$\Delta\vec{E}_0 + \hat{k}^2\vec{E}_0 = 0 \tag{2.24}$$

And the propagation constant for non-polarizable systems (e.g., $\hat{\mu} = 1$) is given by:[93]

$$\hat{k}^2 = k_0^2 \left(\hat{\varepsilon}(\omega) + \frac{\hat{\sigma}(\omega)}{\mathrm{i}\omega\varepsilon_0} \right) \equiv k_0^2 \hat{\eta}(\omega) \tag{2.25}$$

with $\hat{\eta}(\omega)$ representing the generalized complex permittivity.[92]

$$\hat{\eta}(\omega) = \eta'(\omega) - \mathrm{i}\eta''(\omega) \tag{2.26}$$

Real and imaginary part of the generalized complex permittivity, $\eta'(\omega)$ and $\eta''(\omega)$ respectively, are related to the complex permittivity $\hat{\varepsilon}(\omega)$ by:[74]

$$\eta'(\omega) = \varepsilon'(\omega) - \frac{\sigma''(\omega)}{\omega\varepsilon_0} \tag{2.27}$$

$$\eta''(\omega) = \varepsilon''(\omega) + \frac{\sigma'(\omega)}{\omega\varepsilon_0} \tag{2.28}$$

The sole quantity that can be measured experimentally is $\hat{\eta}(\omega)$.[74, 92] Evidently, equations 2.27 and 2.28 show, that a separation of contributions from dipolar polarization mechanisms $\left(\text{e.g., } \hat{\varepsilon}(\omega)\right)$ and contributions from electrical conductivity $\left(\text{e.g., } \hat{\sigma}(\omega)\right)$ is impossible. In addition, a dispersion of the complex conductivity $\hat{\sigma}$ is predicted by the Debye-Falkenhagen theory.[94, 95] However, as an approximation for conductive samples ($\lim_{\omega\to 0}\sigma' = \sigma(0)$ and $\lim_{\omega\to 0}\sigma'' = 0$), $\hat{\varepsilon}(\omega)$ can be calculated from $\hat{\eta}(\omega)$ by subtraction of the ohmic loss contribution $\sigma(0)$ (e.g., dc conductivity).[93] Thus, the real and imaginary parts of $\hat{\varepsilon}(\omega)$, which still contain the frequency-dependent conductivity $\sigma(\omega)$ (e.g., cage vibrations), are given by:[74, 78, 93]

$$\varepsilon'(\omega) = \eta'(\omega) \tag{2.29}$$

$$\varepsilon''(\omega) = \eta''(\omega) - \frac{\sigma(0)}{\omega\varepsilon_0} \tag{2.30}$$

2.2.2 Polarization

The response of a material to an applied electric field is called polarization $\hat{\vec{P}}$.[85, 90] It is proportional to the applied electric field $\hat{\vec{E}}$ (for small field strengths).[85, 96] The macroscopic polarization is defined as the sum of the microscopic dipole moments per volume unit.[85]

$$\hat{\vec{P}} = (\hat{\varepsilon} - 1)\varepsilon_0 \hat{\vec{E}} = \hat{\chi}\varepsilon_0 \hat{\vec{E}} \tag{2.31}$$

where $\hat{\chi}$ is the susceptibility.

Despite being a macroscopic effect, the polarization can be split into microscopic contributions, namely orientational polarization $\hat{\vec{P}}_\mu$ and induced polarization $\hat{\vec{P}}_\alpha$:[85]

$$\hat{\vec{P}} = \hat{\vec{P}}_\mu + \hat{\vec{P}}_\alpha \tag{2.32}$$

The orientational polarization $\hat{\vec{P}}_\mu$ (Eq. 2.33) describes the alignment of permanent dipoles according to the external field.[85, 97] Typically, orientational polarization in liquids occurs on picosecond to nanosecond timescales (e.g., approximately in the frequency range of 1 MHz - 10 THz).[96] Coupling of rotating dipoles with their chemical environment (e.g., solvent, other dipolar species, etc.) results in the observation of rather broad bands in the dielectric spectra.[98] Yet, the thermally induced motion of the molecular dipoles counteracts orientational polarization.[99]

$$\hat{\vec{P}}_\mu = \sum_k \rho_k \left\langle \vec{\mu}_k \right\rangle \tag{2.33}$$

with the species of the molecular dipoles k, the number density ρ_k, and the dipole moment $\vec{\mu}_k$.[85]

The induced polarization $\hat{\vec{P}}_\alpha$ (Eq. 2.34) arises from the displacement of electrons or atoms due to the external field, resulting in the induction of electrical dipoles.[83, 85] In the microwave range relevant to this work, the value of the induced polarization $\hat{\vec{P}}_\alpha$ is rather constant.[99] Contributions from atomic and electronic polarization occur at infrared and ultra-violet/visible frequencies, respectively.[83, 90] These absorption bands are typically narrower than those associated with orientational polarization.[96]

$$\hat{\vec{P}}_\alpha = \sum_k \rho_k \, \alpha_k \left(\hat{\vec{E}}_i \right)_k \tag{2.34}$$

with the polarizability α_k and the inner electric field $\left(\hat{\vec{E}}_i \right)_k$.[85]
Since $\hat{\vec{P}}_\mu$ and $\hat{\vec{P}}_\alpha$ occur on significantly different time scales, they can be treated as linearly independent and thus be described separately (with the infinite frequency permittivity ε_∞):[100, 101]

$$\hat{\vec{P}}_\mu = (\hat{\varepsilon} - \varepsilon_\infty)\, \varepsilon_0 \hat{\vec{E}} \tag{2.35}$$

$$\hat{\vec{P}}_\alpha = (\varepsilon_\infty - 1)\, \varepsilon_0 \hat{\vec{E}} \tag{2.36}$$

In addition, ionic species can have significant effects on the dielectric spectrum. As discussed in the previous section, long-range diffusive ion transport contributes to the imaginary part (dielectric loss) of the permittivity (see Equation 2.30). For visual

clarity, this absorption contribution is usually subtracted from the imaginary part of the permittivity spectrum.[102–104]
However, since ions are particularly sensitive to their environment through coulombic interactions with their immediate neighbors, the confined translational motion of a central ion in its cage (e.g., first solvation shell) contributes to the dielectric spectra.[105] Confined conduction is a cooperative motion, although the ion cage may be quite heterogeneous.[105] Similar to rotational motions, such confined translational motions can lead to characteristic dispersion and loss in experimental dielectric spectra.[105] Yet, since rotational and confined translational contributions are intrinsically entangled in the experiment, their separation can only be addressed using molecular dynamics simulations.[105]
At high frequencies, typically in the THz and far IR range, librations, etc., can additionally contribute to the dielectric spectra.[106]

2.2.3 Linear Response Function

The alignment or response of dipolar species to an externally applied field does not occur instantaneously at higher frequencies due to the effects of friction and inertia.[85, 89] The latter results in a phase difference between the external field and the dielectric displacement field and, thus, a decrease in the orientational polarization.[85, 89] In the context of a linear dielectric medium, the principle of superposition applies, where the accumulation of individual electric fields $\sum \vec{E}_i$ results in a corresponding sum of induced polarizations $\sum \vec{P}_i$. In the given scenario, an externally applied electric field $\vec{E}$ induces an equilibrium polarization at $t = 0$ and is subsequently switched off, assuming that the displacement polarization $\vec{P}_\alpha$ dissipates immediately following the cessation of $\vec{E}$, the persisting polarization is described accordingly.[85, 89, 96]

$$\vec{P}_\mu(t) = \vec{P}_\mu(0) \cdot \phi(t) \quad \text{with} \quad \phi(0) = 1\,,\ \phi(\infty) = 0 \tag{2.37}$$

where the step response function of the orientational polarization $\phi(t)$ is defined by the following autocorrelation function.[89, 97]

$$\phi(t) = \frac{\left\langle \vec{P}_\mu(t) \cdot \vec{P}_\mu(0) \right\rangle}{\left\langle \left(\vec{P}_\mu(0)\right)^2 \right\rangle} \tag{2.38}$$

2.2.4 Empirical Relaxation Models

A variety of empirical and semi-empirical mathematical models are available in literature for the description of experimental dielectric spectra.[86, 107] Some of the most common models will be presented below.

The Debye Equation

Neglecting inertia effects and assuming a single relaxation time, the Debye equation is a simple model to describe dielectric behaviour.[89, 108] The reduction in (orientational) polarization in the absence of an external electric field is supposed to follow a first-order time law.[108]

$$\frac{\partial}{\partial t}\,\vec{P}_{\mu}(t) \;=\; -\,\frac{1}{\tau}\,\vec{P}_{\mu}(t) \tag{2.39}$$

with a characteristic relaxation time τ.

The orientation polarization step response function can be obtained by solving the differential equation, resulting in the following expression:[89]

$$\phi(t) = \exp\left(-\frac{t}{\tau}\right) \tag{2.40}$$

The complex dielectric function $\hat{\varepsilon}(\omega)$ of the Debye equation is obtained by application of the Laplace transformation (conversion from the time domain to the frequency domain).[93, 108]

$$\hat{\varepsilon}(\omega) = \varepsilon_{\infty} + \frac{\varepsilon_{\mathrm{s}} - \varepsilon_{\infty}}{1 + \mathrm{i}\omega\tau} \tag{2.41}$$

Nonetheless, numerous liquids show behaviours divergent from the singular relaxation process assumed within the Debye model.[89] In such scenarios, the assumption of a continuous relaxation time distribution is suggested to accurately describe the spectra.[85]

The Cole-Cole Equation

The Cole-Cole equation is derived from the Debye equation by incorporating of an empirical parameter $\alpha \in [0\,..\,1]$.[109, 110] It supposes a symmetric distribution of relaxation times centered around a principal relaxation time τ_0 on a logarithmic scale.[109, 110]. This assumption results in a flatter dispersion and a broader absorption curve when compared to the Debye model. In the scenario where $\alpha \to 0$, the Debye equation is obtained.

$$\hat{\varepsilon}(\omega) = \varepsilon_{\infty} + \frac{\varepsilon_{\mathrm{s}} - \varepsilon_{\infty}}{1 + (\mathrm{i}\omega\tau_0)^{1-\alpha}} \tag{2.42}$$

The Cole-Davidson Equation

The derivation of the Cole-Davidson equation is achieved by incorporation of an empirical parameter $\beta \in [0\,..\,1]$ to the Debye equation.[111, 112] This modification implies an asymmetric distribution of relaxation times centered around a principal relaxation time τ_0.[111, 112]. Consequently, this leads to asymmetric dispersion and absorption curves, compared to the Debye equation. The limiting case $\beta \to 0$ yields the Debye equation.

$$\hat{\varepsilon}(\omega) = \varepsilon_\infty + \frac{\varepsilon_\mathrm{s} - \varepsilon_\infty}{(1 + \mathrm{i}\omega\tau_0)^\beta} \tag{2.43}$$

The Havriliak-Negami Equation

Incorporating two parameters, $\alpha \in [0\,..\,1]$ and $\beta \in [0\,..\,1]$, into the Debye equation gives the Havriliak-Negami equation.[113] This modification assumes a broad, asymmetric distribution of relaxation times, corresponding to asymmetric dispersion and absorption curves.[113] Notably, in the limit where $\alpha \to 0$ and $\beta \to 1$, the Debye equation is recovered.

$$\hat{\varepsilon}(\omega) = \varepsilon_\infty + \frac{\varepsilon_\mathrm{s} - \varepsilon_\infty}{(1 + (\mathrm{i}\omega\tau_0)^{1-\alpha})^\beta} \tag{2.44}$$

Combining Several Models

In reality, several relaxation processes can contribute to broadband dielectric spectra. In an ideal case, these spectra can be modelled as a superposition of n individual relaxation processes. Each relaxation process with its own response function, relaxation time τ_j and amplitude S_j is considered linearly independent.[85]

$$\hat{\varepsilon}(\omega) = \varepsilon_\infty + \sum_{j=1}^{n} S_j\, F_j(\omega) = \varepsilon_\infty + \sum_{j=1}^{n} (\varepsilon_j - \varepsilon_{j+1})\; F_j(\omega) \tag{2.45}$$

2.2.5 Microscopic Models of Dielectric Relaxation

Up to now, dielectric relaxation has been considered independently of the molecular structure of the system under investigation. In the following, the microscopic properties of the system will be combined with the properties that are observed at the macroscopic level. For this reason, the Cavell equation and the Debye model will be discussed below.

The Cavell Equation

Cavell's equation can be applied to describe systems with multiple dispersion steps.[114] Cavell's equation defines a relationship between the amplitude S_j of the species j, its concentration c_j and its effective dipole moment $\mu_{\mathrm{eff},j}$.[114]

$$\frac{\varepsilon + A_j(1-\varepsilon)}{\varepsilon} S_j = \frac{N_\mathrm{A}\, c_j}{3 k_\mathrm{B}\, T\, \varepsilon_0} \mu_{\mathrm{eff},j}^2 \tag{2.46}$$

where A_j is the form factor of the respective molecule of species j, N_A is the Avogadro constant, k_B is the Boltzmann constant and T is the temperature.

The effective dipole moment $\mu_{\mathrm{eff},j}$ is related to the gas phase dipole moment μ_j of the isolated molecular species as follows:[103]

$$\mu_{\mathrm{eff},j} = \frac{\mu_j}{1-\alpha_j f_j}\sqrt{g_j} \tag{2.47}$$

where α_j is the polarizability and f_j the reaction field factor of the respective molecular species j. Both α_j and f_j correct for cavity and local field effects.[103] The empirical parameter g_j accounts for dipole-dipole correlations, and thus gives an estimation for orientational (parallel or antiparallel) correlations.[103]

For a spherical cavity with radius a_j and a dipolar species positioned at its center, the reaction field factor f_j can be described as (with $A_j = 1/3$):[114]

$$f_j = \frac{2\varepsilon - 2}{4\pi\varepsilon_0(2\varepsilon+1)a_j^3} \tag{2.48}$$

In the case of an ellipsoidal species with its semi-axes $a_j > b_j > c_j$ the reaction field factor f_j is given by:[115]

$$f_j = \frac{3}{4\pi\varepsilon_0 a_j b_j c_j} \frac{A_j(1-A_j)(\varepsilon-1)}{\varepsilon + (1-\varepsilon)A_j} \tag{2.49}$$

The form factor A_j can be calculated using the following general expression:[85]

$$A_j = \frac{a_j b_j c_j}{2} \int_0^\infty \frac{\mathrm{d}s}{(s+a_j^2)^{3/2}\,(s+b_j^2)^{1/2}\,(s+c_j^2)^{1/2}} \tag{2.50}$$

Given the case of a prolate elipsoid ($a_j > b_j = c_j$) the improper integral (Eq. 2.50) can be solved via:[115, 116]

$$A_j = -\frac{1}{p_j^2-1} + \frac{p_j}{(p_j^2-1)^{3/2}} \ln\left(p_j + \sqrt{p_j^2-1}\right) \qquad \text{with} \qquad p_j = \frac{a_j}{b_j} \tag{2.51}$$

For oblate elipsoids ($a_j < b_j = c_j$) Equation 2.50 can be solved via:[116]

$$A_j = \frac{1}{1-p_j^2} - \frac{p_j}{(1-p_j^2)^{3/2}} \cos^{-1} p_j \qquad \text{with} \qquad p_j = \frac{a_j}{b_j} \tag{2.52}$$

The Debye Model of Rotational Diffusion

The Debye model of rotational diffusion can be used to relate the relaxation time to the microscopic properties of the system under consideration.[108] The following assumptions are made within the model. The system consists of a number of dipoles that do not interact with each other.[108] The dipoles are assumed to be rigid spheres, freely rotating in all spatial directions.[89] Collisions between neighbouring molecules, also called diffusion of dipolar orientation, lead to a reorientation of the dipoles.[108] Neglecting inertia effects as well as dipole-dipole interactions and assuming a Lorentz field for the description of the inner field, the step response function of the orientational polarization can be expressed as:[89, 108]

$$\Phi(t) = \exp\left(-\frac{t}{\tau_{\mathrm{rot}}}\right) \tag{2.53}$$

The microscopic relaxation time τ_{rot} can be described using the friction factor ζ.[117]

$$\tau_{\mathrm{rot}} = \frac{\zeta}{2k_{\mathrm{B}}T}. \tag{2.54}$$

Utilizing the principles of hydrodynamics to examine the rotational motion of a spherical entity within a viscous environment yields the Stokes-Einstein-Debye equation.[117]

$$\tau_{\mathrm{rot}} = \frac{3V_{\mathrm{m}}\ \eta'}{k_{\mathrm{B}}\,T} \tag{2.55}$$

In this context, V_{m} represents the molecular volume of the spherical entity, while η' denotes the dynamic (microscopic) viscosity within the sphere's direct surroundings.[117] Nevertheless, the applicability of this theory is constrained due to the insufficient comprehension of the correlation between microscopic and macroscopic viscosity.[117] This limitation is compensated for by an extension developed by Dote *et al.*[117]

$$\tau_{\mathrm{rot}} = \frac{3V_{\mathrm{eff}}\ \eta}{k_{\mathrm{B}}T} + \tau_{\mathrm{rot}}^{0} \tag{2.56}$$

The effective rotational volume of a molecule V_{eff} relates the microscopic η' to the macroscopic viscosity η. The parameter τ_{rot}^{0} is understood as the correlation time of the unrestrictedly rotating molecule.[117]

Relationship between the Macroscopic and the Microscopic Relaxation Time

The relaxation time τ is the experimentally measurable quantity.[91] The underlying step response function (Equation 2.38) depends on the polarization of a sample. Consequently, the corresponding relaxation time τ is, per definition, a macroscopic and hence collective observable.[85, 99] For dipole reorientation, the microscopic relaxation time τ_{rot} is defined by the dipole correlation function.[91, 99]

$$\Phi(t) = \frac{\left\langle \vec{\mu}(t) \cdot \vec{\mu}(0) \right\rangle}{\left\langle \left(\vec{\mu}(0)\right)^2 \right\rangle} \tag{2.57}$$

Since there is no satisfactory general theory to relate the macroscopic relaxation time, τ, to the microscopic relaxation time, τ_{rot}, some approaches found in literature are presented below.[99] Debye proposed the following expression, assuming a Lorentz Field.[108]

$$\tau = \frac{\varepsilon + 2}{\varepsilon_\infty + 2}\, \tau_{\mathrm{rot}} \tag{2.58}$$

In the case of polar dielectrics, this approach proved to be imprecise. Assuming rotational diffusion, Powles and Glarum derived the following relationship.[118, 119]

$$\tau = \frac{3\varepsilon}{2\varepsilon + \varepsilon_\infty}\, \tau_{\mathrm{rot}} \tag{2.59}$$

Including dipole-dipole correlations by introducing the Kirkwood correlation factor g_{K} and the dynamic correlation factor $\dot{g}$, Madden and Kivelson proposed the following relationship.[120]

$$\tau = \frac{3\varepsilon}{2\varepsilon + \varepsilon_\infty}\, \frac{g_{\mathrm{K}}}{\dot{g}}\, \tau_{\mathrm{rot}} \tag{2.60}$$

2.2.6 Temperature Dependence of Relaxation Times

Relaxation times generally depend on temperature. As the temperature increases, the kinetic energy and, therefore, the mobility of the molecules increases, usually resulting in shorter relaxation times.

The Arrhenius Equation

The Arrhenius equation is an easy model to describe the temperature dependence of rate constants and hence relaxation times.[83]

$$\ln(\tau) = \ln(\tau_0) + \frac{E_{\mathrm{A}}}{RT} \tag{2.61}$$

where E_A is the activation energy (energy barrier separating two stable energetic states) and τ_0 is the shortest possible relaxation time.

The Vogel-Fulcher-Tammann Equation

Liquids in proximity to the glass transition temperature typically show a pronounced increase in viscosity, which can be described by the Vogel-Fulcher-Tammann (VFT) equation.[121, 122] Such cases are characterized by the cooperative motion of the dipolar species and usually do not follow the Arrhenius behaviour.

$$\ln(\tau) = \ln(\tau_0) + \frac{B_{VFT}}{T - T_0^{VFT}} \tag{2.62}$$

where τ_0 and B_{VFT} are material-specific temperature-independent parameters and T_0^{VFT} is the Vogel temperature (usually below the glass transition temperature).[123]

2.3 Linear Vibrational Spectroscopy

The interaction of light and matter leads to polarization phenomena as explained in Chapter 2.1. The following section describes the resonant absorption of electromagnetic waves by matter leading to intramolecular vibrational transitions. Vibrational or IR spectroscopy probes these vibrations in molecules and provides information about the structure, functional groups, and interactions between molecules.[90] Typically, in linear spectroscopy, the incident field is considered to be weak. Therefore, the response of the system to the interaction with light is treated as linear with respect to the incident field strength.[85, 96] The proportionality factor between the incident field and the polarization (or dielectric displacement) is the first order or linear susceptibility (as described in Equation 2.31).

2.3.1 Harmonic Oscillator and Transition Dipole Moment

The vibration in the simple case of a diatomic molecule can be described in terms of a harmonic oscillation. In the classical picture, the displacement from equilibrium of two atoms connected by a spring is described by Hooke's law:[83, 90]

$$F = -Dx = -\frac{\mathrm{d}V}{\mathrm{d}x} \quad \text{with} \quad V = \frac{1}{2}\,Dx^2 \tag{2.63}$$

where D is the force constant, x is the displacement and V is the potential energy. The force F is proportional to the displacement x according to Equation 2.63. Assuming that the diatomic molecule consists of two atoms with masses m_1 and m_2, by introducing Newton's law[83] with the reduced mass m^* of the system[90],

$$F = m^*\,\frac{\mathrm{d}^2x}{\mathrm{d}t^2} \quad \text{with} \quad m^* = \frac{m_1\,m_2}{m_1 + m_2} \tag{2.64}$$

and by solving the differential equation[83] (obtained by combining eqs. 2.63 and 2.64),

$$\frac{\mathrm{d}^2x}{\mathrm{d}t^2} + \frac{D}{m^*}\,x = 0 \tag{2.65}$$

the vibrational frequency ν_0 of the harmonic oscillation can be derived as follows:[83]

$$\nu_0 = \frac{1}{2\pi}\sqrt{\frac{D}{m^*}} \tag{2.66}$$

The harmonic oscillator has a parabolic potential as shown by Equation 2.63 (see Figure 2.2 a)). Considering the harmonic oscillation in a quantum mechanical way, the substitution of the potential energy V into the Schrödinger equation (with wave function ψ) yields:[83]

$$\frac{\mathrm{d}^2\psi}{\mathrm{d}x^2} + \frac{2m^*}{\hbar^2}\left(E - \frac{1}{2}\,Dx^2\right)\psi = 0 \tag{2.67}$$

where $\hbar$ is the reduced Planck constant.
Since the atom cannot be moved arbitrarily far from its equilibrium position, the asymptotic limit, $x \to \pm\infty$, of ψ has to be considered:[83]

$$\frac{\mathrm{d}^2\psi_\infty}{\mathrm{d}x^2} - \frac{m^*}{\hbar^2}\,Dx^2\,\psi_\infty = 0 \quad \text{with} \quad \psi_\infty = e^{-\frac{1}{2}\,\beta x^2} = A\,e^{-\frac{1}{2\hbar}\sqrt{m^* D}\,x^2} \tag{2.68}$$

Inserting ψ_∞ (Eq. 2.68) and its second derivative into Equation 2.67 yields:[83]

$$E = \frac{1}{2}\,h\nu_0 \tag{2.69}$$

where h is the Planck constant.

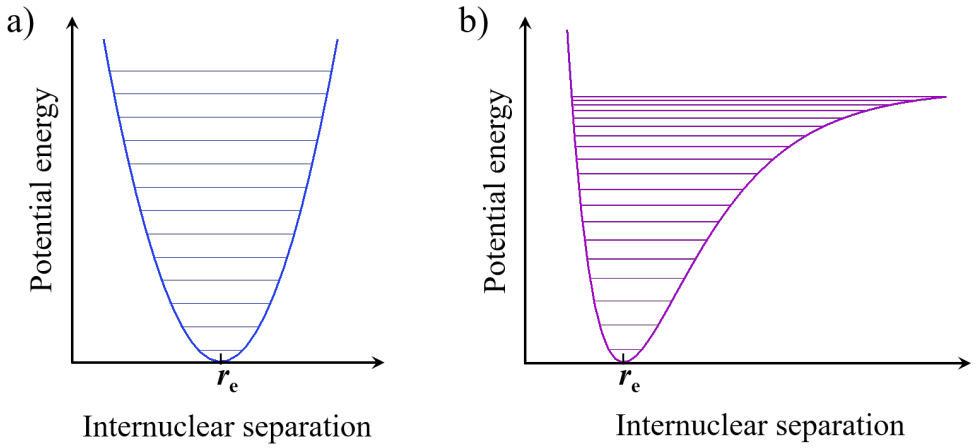

FIGURE 2.2: Schematic representation of the potential energy as a function of the internuclear distance for a) the harmonic oscillator and b) the anharmonic oscillator. The internuclear equilibrium distance is denoted by r_e.

According to Equation 2.69 the vibrational states are quantised.[83, 90] The general solution to Equation 2.67,

$$\psi_\upsilon = N_\upsilon\,H_\upsilon(x)\,e^{-\frac{1}{2}\,\beta x^2} \tag{2.70}$$

with the quantum number υ (with $\upsilon = 0, 1, 2, ...$), the Hermite polynomial $H_\upsilon(x)$, and the normalization factor N_υ, gives the energy Eigenstates of the harmonic oscillator in dependence of υ:[83]

$$E_\upsilon = h\nu_0\left(\upsilon + \frac{1}{2}\right) \tag{2.71}$$

In contrast to classical mechanics, quantum mechanical systems fluctuate even at the lowest energy level. At $\upsilon = 0$, molecules maintain a vibrational motion equal to $E_0 = \frac{1}{2}\,h\nu_0$, the so-called zero point energy.[83]
However, molecules must satisfy certain selection rules in order to show IR activity. The general selection rule that must be fulfilled to show measurable absorption of resonant incident IR light is that the transition dipole moment $\boldsymbol{\mu_{if}}$ between the initial and final vibrational states (with their wave functions ψ_i and ψ_f, respectively) is non-zero.[90]

$$\boldsymbol{\mu}_{if} = \langle\psi_f|\hat{\boldsymbol{\mu}}|\psi_i\rangle \neq 0 \tag{2.72}$$

In addition to the general selection rule, a specific selection rule is derived from the harmonic oscillator. Therefore, only transitions from two neighbouring energetic states are allowed:[90]

$$\Delta\upsilon = \pm 1 \tag{2.73}$$

2.3.2 Anharmonic Oscillator

Although the harmonic oscillator is a good approximation, the parabolic potential does not account for molecular dissociation.[83, 90] For a given large displacement of the atoms in a diatomic molecule, one would expect a drastic decrease in bond strength, leading to the breakage of the bond. Especially at highly excited states, the repulsive force is no longer proportional to the displacement of the atoms from their equilibrium position, resulting in an anharmonic molecular motion.[83] Furthermore, in the harmonic approximation, energy levels are equidistant, which would result in indistinguishable absorption bands in a spectrum. Moreover, in a perfectly harmonically oscillating molecule, transitions with $\left|\Delta\upsilon\right| > 1$ are strictly forbidden (see Equation 2.73). However, such higher harmonics (e.g., overtones) can be observed in vibrational spectra, but their intensities are typically very weak compared to bands with $\Delta\upsilon = \pm 1$.[90]
The empirical model by Morse accounts for the anharmonicity in the potential $V(r)$ (see Figure 2.2 b)).

$$V(r) = D_\mathrm{e}\Big[1 - \mathrm{e}^{-\beta(r-r_\mathrm{e})}\Big]^2 \quad \text{with} \quad \beta = \tilde{\nu}_0\sqrt{\frac{2\pi^2 c\, m^*}{hD_\mathrm{e}}} \tag{2.74}$$

with the dissociation energy D_e, the bond displacement r, and the equilibrium position r_e of the oscillator (minimum of the potential). The constant β describes the steepness

of the potential and includes the wave number corresponding to the harmonic oscillator $\tilde{\nu}_0$, and the speed of light c. Solving the Schrödinger equation for the Morse potential leads to the energy levels of the vibrational terms $G(\upsilon)$ depending on the anharmonicity constant x_e.[83]

$$G(\upsilon) = \tilde{\nu}_0\left(\upsilon + \frac{1}{2}\right) - \tilde{\nu}_0 x_\mathrm{e}\left(\upsilon + \frac{1}{2}\right)^2 \quad \text{with} \quad x_\mathrm{e} = \frac{\beta^2\hbar}{2m^*\omega} \tag{2.75}$$

The dissociation energy D_e can be approximated by:[83]

$$D_\mathrm{e} \approx \frac{\tilde{\nu}_0}{4x_\mathrm{e}} \tag{2.76}$$

The selection rule (Equation 2.73) must be adapted as follows as a result of introducing anharmonicity.[83]

$$\Delta\upsilon = \pm1, \pm2, \pm3, ... \tag{2.77}$$

Yet the number of vibrational states within the Morse approximation is finite (with $\upsilon = 0, 1, 2, 3, ..., \upsilon_\mathrm{max}$). The transition with $\Delta\upsilon = \pm1$ is called the fundamental transition, while the transitions with $\Delta\upsilon = \pm2, \pm3, ...$ are called overtones.[83] As $\Delta\upsilon$ increases, however, the overtone intensities decrease.[83] Although the Morse potential compensates for some of the shortcomings of the harmonic approach, in practice, a universal expression is required that includes not only the quadratic term but also terms of higher power.[90]

$$G(\upsilon) = \tilde{\nu}_0\left(\upsilon + \frac{1}{2}\right) - \tilde{\nu}_0 x_\mathrm{e}\left(\upsilon + \frac{1}{2}\right)^2 + \tilde{\nu}_0 y_\mathrm{e}\left(\upsilon + \frac{1}{2}\right)^3 + ... \tag{2.78}$$

where x_e and y_e are empirical constants, molecule specific and dimensionless.

2.3.3 Linewidth

For an isolated molecule with an infinitesimally precise vibrational frequency ω (e.g., without any broadening), the resulting spectral line of the corresponding transition would be sharp and discrete. However, in molecular ensembles, various mechanisms contribute to spectral broadening, specifically homogeneous and inhomogeneous broadening.[124] Homogeneous broadening occurs when an external perturbation equally affects all molecules.[125] Following impulsive excitation by a laser pulse, the amplitude of the macroscopic polarization decays over time (see Figure 2.3a)). The Fourier Transform (FT) of this polarization decay yields a spectral peak at a specific vibrational frequency ω, determining the homogeneously broadened spectral linewidth Γ (see Figure 2.3b)).[125] Additionally, loss of phase coherence (e.g., due to collisions with

the environment) also contributes to homogeneous broadening.[125] In the context of inhomogeneous broadening, the local environment surrounding each individual molecule can vary, leading to slight variations in their vibrational frequencies.[124] Moreover, large molecules can have different structures, also leading to variations in the vibrational frequencies.[124] The macroscopic polarization is therefore given by the interference of the polarizations of the individual molecules.[124] At a given time after impulsive excitation with a laser pulse, these different molecular polarizations will be phase-shifted relative to one another, leading to destructive interference and an inhomogeneously broadened linewidth.[124]

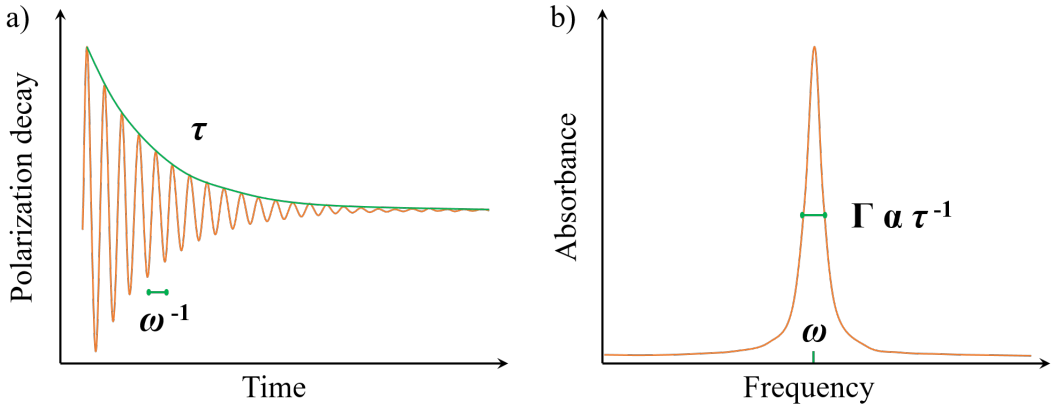

FIGURE 2.3: Schematic representation of a) the Free Induction Decay (FID) of the polarization induced by the interaction of a laser pulse with matter and b) the Fourier transform of the polarization decay resulting in a spectral peak with a certain linewidth.

2.4 Visible Pump–Infrared Probe Spectroscopy

Visible pump-infrared probe spectroscopy is a spectroscopic technique for studying ultrafast dynamical processes in molecules, materials, and biological systems.[126–129] Two distinct laser pulses are used in this method: a visible light pulse (pump pulse) that initiates a photochemical or photophysical process by exciting the system, and a delayed infrared pulse (probe pulse) that interrogates the subsequent dynamics by probing the changes in the infrared absorption spectrum. The essential strength of this technique lies in its ability to capture transient molecular states and dynamics occurring on femtosecond to picosecond timescales.[80, 82, 126, 129, 130] By systematically varying the time delay between the pump and probe pulses (by changing the path length of the pump pulse, typically via a mechanical delay stage), time-resolved dynamics of post-excitation processes such as electronic relaxation, chemical reactions and proton transfer reactions can be studied.[80, 82, 128, 131, 132] The choice of visible light for the pump pulse allows for selective excitation of specific electronic states, while the infrared probe pulse is sensitive to changes in molecular vibrations and therefore provides information about structural changes, bond formation or breaking, and energy

transfer mechanisms.[81, 131, 133] The signal is usually displayed as the transient absorption $\Delta\alpha$, which is the difference between the pumped and the unpumped spectrum.[134–136]

$$\Delta\alpha = -\ln\left(\frac{T(\omega)}{T_0(\omega)}\right) \tag{2.79}$$

Both positive ($\Delta\alpha > 0$) and negative ($\Delta\alpha < 0$) contributions can typically be observed in a transient spectrum. A positive change in the transient absorption $\Delta\alpha$ is referred to as induced absorption. It appears when probe light is absorbed by absorption bands of certain molecular species that emerge following excitation by the pump pulse. Conversely, as the system is excited by the pump pulse, a bleach or negative change in $\Delta\alpha$ means a reduction in the probe pulse absorption intensity of a particular molecular vibration.

Visible pump–infrared probe spectroscopy is a well-established method for the investigation of proton transfer reactions.[80–82, 137, 138] In this technique, a photo-acid is excited by a visible pump pulse, initiating the release of a proton. The subsequent proton transport is monitored in real-time by detecting the protonation of an anion via the probe pulse. Within the scope of this thesis, visible pump–infrared probe spectroscopy is employed to investigate proton transfer dynamics in protic ionic liquids, specifically from the photo-acid to the acetate anion in 1-methylimidazolium acetate.

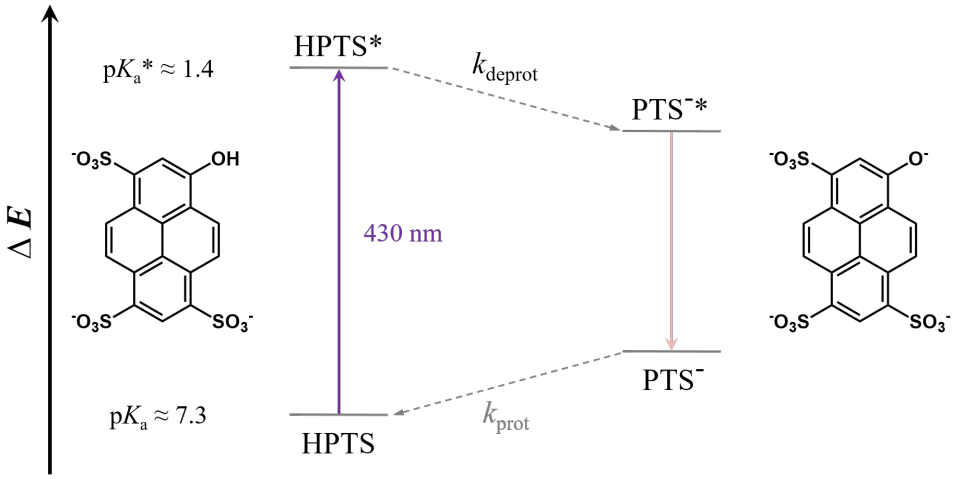

FIGURE 2.4: Schematic representation of the relevant states of the photoprotolytic cycle of HPTS.[139] Electronic excitation at 430 nm from the ground state (HPTS) to the excited state (HPTS*) triggers reversible deprotonation of the hydroxyl group with k_{deprot} to PTS^{-*}. PTS^{-*} relaxes to PTS^{-}, which can be protonated to HPTS with k_{prot}.

Controllable proton release is achieved using the photo-acid 8-hydroxypyrene-1,3,6-trisulphonic acid (HPTS, pyranine).[80, 82] Electronic excitation of HPTS at 430 nm

leads to a significant decrease in pK_a of about 6 units from pK_a(HPTS) ≈ 7.3 to pK_a(HPTS*) ≈ 1.4 (Figure 2.4).[139] The excitation triggers the release of an excess proton from the HPTS* excited state, which is then transported within the PIL sample. At some point, these protons reach an anion, leading to its protonation. Since the vibrational modes of acetic acid $\nu_{C=O}$ and acetate ν_s & ν_{as} are spectrally well separated, it is possible to monitor the vibrational dynamics during protonation (Figure 2.5).[82] Therefore, the IR probe pulse is centred at $\nu_{C=O}$ ≈1700 cm^{-1} and protonation leads to an induced absorption peak (positive contribution) in the transient signal $\Delta\alpha$.

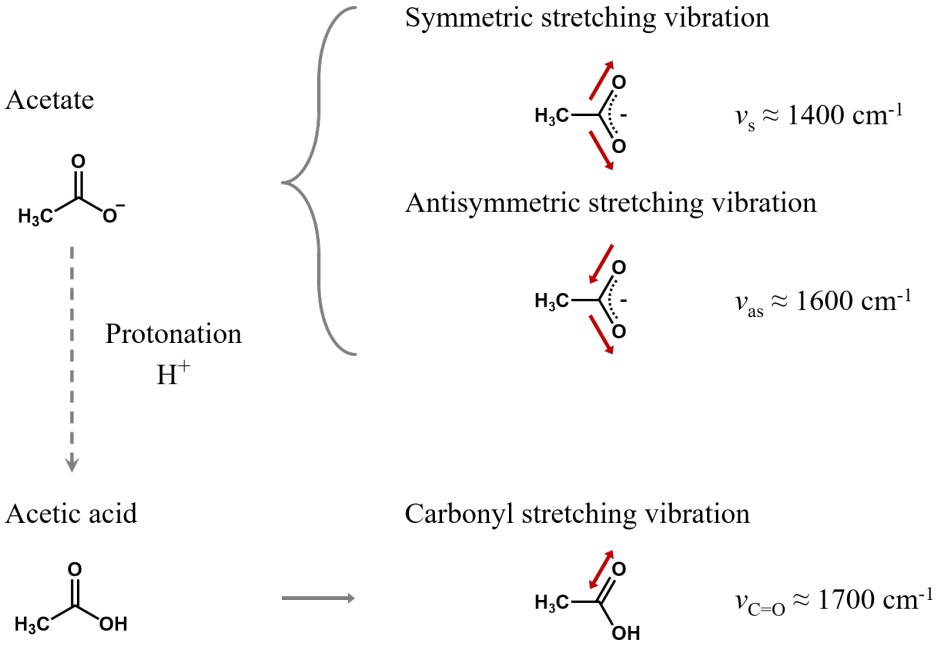

FIGURE 2.5: Schematic representation of the different vibrational modes of the COO group in both acetate and acetic acid. Acetate shows the symmetric and asymmetric stretching vibrations ν_s and ν_{as}, respectively. Acetic acid shows the carbonyl stretching vibration $\nu_{C=O}$.

2.5 Nuclear Magnetic Resonance Spectroscopy

Nuclear magnetic resonance (NMR) spectroscopy is an analytical technique that allows the transition between distinct quantized spin states of specific nuclei, as well as their electronic environment, to be probed in response to an external magnetic field. NMR spectroscopy cannot only be applied to determine the chemical structure of molecules, but also to monitor reactions, study metabolism and many other applications.[90, 140–143] In the following sections the basic principles of NMR spectroscopy will be explained.

2.5.1 Angular Momentum and Magnetic Moment

Most nuclei have an angular momentum $|\vec{P}|$, which is quantized:[83]

$$|\vec{P}| = \sqrt{I(I+1)}\ \hbar \tag{2.80}$$

where $\hbar$ is the reduced Planck constant and I the spin (with I=0, 1/2, 1, 3/2 ...). The angular momentum $|\vec{P}|$ is associated with a magnetic moment $\vec{\mu}$:[143]

$$\vec{\mu} = \gamma\vec{P} \tag{2.81}$$

where γ is the gyromagnetic ratio, a nucleus-specific property that determines the sensitivity of a particular nucleus in the NMR experiment. The combination of equations 2.80 and 2.81 results in the following expression for the magnetic moment:[143]

$$\vec{\mu} = \gamma\sqrt{I(I+1)}\ \hbar \tag{2.82}$$

According to Equation 2.82, nuclei with a spin $I = 0$ lack a magnetic moment and are therefore undetectable in NMR experiments. For most nuclei $\vec{P}$ and $\vec{\mu}$ are in parallel alignment, however, there are a few exceptions, for example ^{15}N and ^{29}Si (and the electron), where they are in antiparallel alignment.[143]

2.5.2 Nuclei in Static Magnetic Fields

When a static magnetic field $\vec{B}_0$ is applied to an NMR active nucleus (spin quantum number $I > 0$) with a magnetic moment $\vec{\mu}$, its angular momentum $\vec{P}$ is spatially oriented at certain angles to the magnetic field.[144] The energetic degeneracy of the spin states is split due to the external magnetic field (Zeemann splitting, see Figure 2.6 a)).[90] The angular momentum in the z-direction of the field will assume (half-)integer values of $\hbar$.[143]

$$\vec{P}_z = m\,\hbar \tag{2.83}$$

where m is the magnetic quantum number (with $m = I, I-1, \ldots -I$).
Combining the equations 2.82 and 2.83 gives the magnetic moment in the field direction z:[143]

$$\vec{\mu}_z = m\,\gamma\,\hbar \tag{2.84}$$

A nucleus in a magnetic field $\vec{B}_0$ has $(2I+1)$ possible energetic states (and orientations) with the potential energy:[90]

$$E = -\vec{\mu}_z\,\vec{B}_0 = -m\,\gamma\,\hbar\,\vec{B}_0 \tag{2.85}$$

The energy difference ΔE as a function of the magnetic field strength between two adjacent states is given by (Figure 2.6 a)):[143]

$$\Delta E = \gamma\,\hbar\,\vec{B}_0 \tag{2.86}$$

The population of different energetic states at thermal equilibrium depends on the energy difference ΔE and is given by the Boltzmann distribution:[143]

$$\frac{N_\beta}{N_\alpha} = \mathrm{e}^{-\Delta E/k_B T} \tag{2.87}$$

where N_β and N_α are the number of nuclei in the higher and lower energy states, respectively, k_B is the Boltzmann constant, and T is the temperature. Compared to $k_\mathrm{B}T$, however, this energy difference is rather small for nuclei, resulting in almost equally populated states.[90]

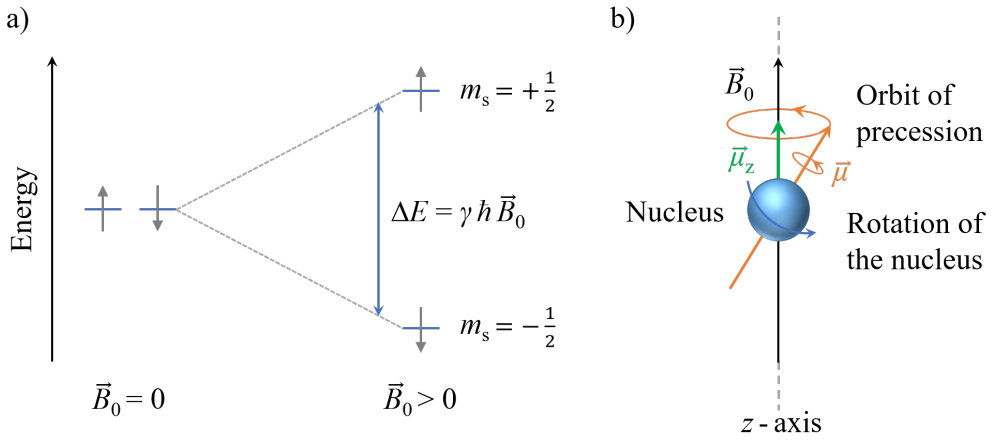

FIGURE 2.6: Schematic representation of a) the Zeeman splitting in the presence of a static magnetic field (with spin magnetic quantum number m_s) and b) the Larmor precession of the magnetic moment $\vec{\mu}$ of a nucleus in the presence of an external magnetic field. $\vec{\mu}$ precesses with the Larmor frequency ν_L.

2.5.3 Resonance Condition

The basic principle of an NMR experiment is the induction of transitions between different energy levels of the nuclei. To stimulate such transitions, an additional magnetic field is applied. The nuclear dipoles interact with the electromagnetic wave at a certain frequency ν_1. Transitions from one spin state to another (e.g., absorption of electromagnetic radiation) are possible if equation 2.88 is fulfilled.[143]

$$\Delta E = h\,\nu_1 \tag{2.88}$$

The intensity of the absorption (e.g., signal) is proportional to the population difference $(N_\alpha - N_\beta)$.[90] The following resonance condition applies for transitions between different spin states:[143]

$$\nu_1 = \nu_\mathrm{L} = \left|\frac{\gamma}{2\pi}\right| \vec{B}_0 \tag{2.89}$$

where ν_L is the Larmor frequency, which is proportional to the magnetic flux density.[143] The Larmor frequency is the characteristic frequency of spins precessing around the axis corresponding to the direction of the magnetic field $\vec{B}_0$ (Figure 2.6 b)).[143]

2.5.4 Magnetization and Bloch Equations

In a typical Fourier transform NMR experiment, all nuclei of a given species are excited simultaneously by short magnetic pulses of a few μs applied to the sample. The excitation leads to a deflection of the macroscopic magnetisation vector M_0 away from the direction of the static field $\vec{B}_0$.[143] The relaxation to the equilibrium state after the pulse can be described by the Bloch equations:[143]

$$\frac{\mathrm{d}M_\mathrm{z}}{\mathrm{d}t} = -\frac{M_\mathrm{z} - M_0}{T_1} \tag{2.90}$$

$$\frac{\mathrm{d}M_{\mathrm{x}'}}{\mathrm{d}t} = -\frac{M_{\mathrm{x}'}}{T_1} \qquad \text{and} \qquad \frac{\mathrm{d}M_{\mathrm{y}'}}{\mathrm{d}t} = -\frac{M_{\mathrm{y}'}}{T_2} \tag{2.91}$$

where M_z is the magnetisation component in the z direction, $M_{\mathrm{x}'}$ and $M_{\mathrm{y}'}$ are the magnetisation components in the x' and y' directions of a rotating coordinate system. T_1 and T_2 are the longitudinal (spin-lattice) and transverse (spin-spin) relaxation times, respectively.[143]

The observable signal is the free induction decay, FID (see Figure 2.3a) in the previous section). However, the intensity of a single FID is usually very small.[143] This is especially true for nuclei with low sensitivity or low natural abundance, such as ^{13}C.[143] For this reason, a large number of FIDs – up to hundreds of thousands – are collected in an experiment and averaged to improve the signal-to-noise ratio.[143]

To obtain the typical frequency domain spectra, the time domain signal is Fourier transformed.

2.5.5 Shielding Effect and Chemical Shift

In a molecule, the nucleus under investigation is not isolated, but is surrounded by a large number of other nuclei and electrons. Consequently, the nucleus experiences a magnetic field smaller than the external field B_0, depending on the chemical environment. This effective magnetic field B_{eff} due to the shielding can be expressed as:[143]

$$\vec{B}_{\text{eff}} = \vec{B}_0 - \sigma\vec{B}_0 = (1-\sigma)\vec{B}_0 \tag{2.92}$$

where σ is the shielding constant, which increases with the number of electrons.
For Equation 2.89 results:[143]

$$\nu_1 = \left|\frac{\gamma}{2\pi}\right|(1-\sigma)\,\vec{B}_0 \tag{2.93}$$

The resonance frequency ν_1 is proportional to $(1-\sigma)$; therefore, nuclei that are not chemically equivalent will give rise to spectrally separated signals.[143]
As apparent from Equation 2.93, the resonance frequency is related to the magnetic flux density, and therefore NMR experiments only probe relative Larmor frequencies. As a standardized scale, the chemical shift δ is introduced using tetramethylsilane (TMS) as a reference.[143] The chemical shift δ is expressed in parts per million (ppm) with the TMS signal set to $\delta_{\text{TMS}} = 0\,\text{ppm}$.[143]

$$\delta = \frac{\nu_{\text{sample}} - \nu_{\text{TMS}}}{\nu_{\text{TMS}}}\,10^6 \tag{2.94}$$

2.5.6 Two-Dimensional NMR Experiments

By introducing a second frequency dimension, NMR experiments allow the investigation of homo- and heteronuclear coupling between nuclei. 2D-NMR experiments consist of a complex sequence of pulses and delay times, which vary depending on the experiment.[143] However, there are four main stages that most 2D-NMR experiments have in common:[145, 146]

- **The Preparation Period**, where a magnetization coherence (desired non-equilibrium spin state) is created by a series of pulses and delays.[145, 146]
- **The Evolution Period**, where no additional pulses are applied and the spins are allowed to precess freely. During this phase, NMR quantities such as chemical shift and J-coupling evolve with time.[145, 146]

- **The Mixing Period**, where the coherence is altered by a second series of pulses and delays. In this stage the information evolved in the previous period is transferred from one nucleus to the signal and/or phase of another nucleus.[145, 146]
- **The Detection Period**, where the observable FID signal is collected as a function of time (similar to FT-NMR experiments).[145, 146]

Proton-proton coupling is studied using homonuclear through-bond correlation methods (e.g., COSY, TOCSY).[146] Magnetization transfer occurs by J-coupling to neighboring nuclei.[146] Coupling between nuclei of two different types (mostly ^{1}H and a hetero-nucleus) is studied by heteronuclear through-bond correlation methods (e.g., HSQC, HMBC). HMBC is able to detect heteronuclear correlations over long ranges of up to several bonds.[147, 148] Through-space correlation methods (e.g., NOESY) study correlations between nuclei that are spatially close to each other, regardless of whether they are bonded or not.[146] They make use of the nuclear Overhauser effect (NOE), where atoms within about 5 Å undergo cross-relaxation (a mechanism related to spin-lattice relaxation).[146]

Diffusion-ordered spectroscopy (DOSY) distinguishes molecular species by their different translational diffusion. The second dimension is therefore not another frequency axis, but the diffusion coefficients, which depend on molecular mass, hydrodynamic properties (e.g., shape, size, charge) and environmental properties (e.g., temperature, solvent viscosity) as described by the Stokes-Einstein equation:[149, 150]

$$D = \frac{k_\mathrm{B} T}{6\pi\eta r_\mathrm{H}} \tag{2.95}$$

where η is the viscosity and r_H the hydrodynamic radius.

Typically, a DOSY experiment consists of several pulsed field gradient spin echo (PFG-SE) experiments in which a linearly varying field gradient is applied to the sample.[150, 151] The spin echo (refocusing of the spin magnetization) is induced by a resonant electromagnetic pulse, resulting in an inversion of the magnetization vectors to remove inhomogeneous dephasing effects.[152]

Chapter 3

Materials and Methods

3.1 Materials

Reproduced from [104] *with minor changes.*

3.1.1 Chemicals

N,N-dimethylacetamide (DMA, 99 %) was purchased from VWR and used to calibrate the dielectric reflectometer without further purification. *N,N*-dimethylformamide (DMF, 99.8 %) was purchased from ACROS and used to calibrate the dielectric reflectometer and to prepare the PIL solutions without further purification. Methanol (MeOH, VWR, HPLC gradient quality), used for sample preparation, was dried over a molecular sieve (3 Å) prior to use. Deuterated *N,N*-dimethylformamide-d_7 (DMF-d_7, $>$ 99.5 %) was purchased from Sigma Aldrich and deuterated methanol-d_4 and dimethylsulfoxide-d_6 (DMSO-d_6, 99.95 %) from Deutero GmbH. Deuterated solvents used for NMR sample preparation of the PILs were individually dried over a molecular sieve (4 Å) before use. 8-Hydroxypyrene-1,3,6-trisulphonic acid (HPTS, ACROS, 98 %) was stored in an Ar-filled glove box and used as purchased.

3.1.2 PIL Synthesis

The physicochemical properties of ionic liquids can be significantly affected by various types of impurities and, as numerous ILs tend to be hygroscopic, they are extremely sensitive to moisture.[153–155] Therefore, synthesis was performed under inert gas conditions to avoid water absorption. The starting materials 1–methylimidazole (Mim, 99 %, ACROS), acetic acid, (AcOH, $>$ 99 %, Alfa Aesar) and trifluoroacetic acid (99.5 %, VWR) were purified by distillation prior to use. All starting materials were stored and handled in an Ar filled glovebox. 1-Methylimidazolium acetate [MimH][AcO] and 1-methylimidazolium trifluoroacetate [MimH][TFA] were synthesised by gradually adding small amounts of acetic acid and trifluoroacetic acid, respectively, stepwise to Mim to obtain each PIL in an equimolar ratio of the respective reactants. To avoid evaporation, the reaction solution was cooled in an ice bath. After completion of the addition of the respective acid, the reaction mixture was stirred under reflux (at 65 °C)

for 6 h. The obtained PILs [MimH][AcO] and [MimH][TFA] were stored in an Ar-filled glove box. Both PILs were characterized by ^{1}H- & ^{1}3C-NMR-spectroscopy (spectra are shown in Figures 4.7,4.9,4.10,4.11 in Chapter 4). [MimH][TFA] was found to be solid at room temperature, consistent with a reported melting point of ~338 K.[65] However, other studies based on synthesis involving the addition of water to the reaction mixture have suggested that [MimH][TFA] is liquid at room temperature.[156, 157]

3.1.3 Preparation of PIL Mixtures

To investigate the effect of the acidity of the Brønsted acid, mixtures of the PILs [MimH][AcO] and [MimH][TFA] with molar fractions of [MimH][AcO] $\chi(\mathrm{Ac}) = 0$-1 in 0.1 increments were prepared by weight using an analytical balance. As [Mim][TFA] is solid at room temperature, mixtures were also partially solid, resulting in a limited composition range for the PIL mixtures to molar fractions of acetate, $\chi(\mathrm{Ac}) \leq 0.6$.

3.2 Methods

3.2.1 Dielectric Relaxation Spectroscopy

In this work, a vector network analyzer (VNA) is used to measure the dielectric response of the medium under investigation. VNAs simultaneously acquire amplitude and phase information, typically expressed as the complex permittivity.[89] Commercially available devices are capable of operating over a broad range of frequencies, from a few MHz to several hundred GHz.[158] Two-port devices determine the reflected and transmitted electrical signal, expressed in terms of the scattering matrix $\hat{S}$:[158]

$$\begin{pmatrix} \hat{b}_1 \\ \hat{b}_2 \end{pmatrix} = \begin{pmatrix} \hat{S}_{11} & \hat{S}_{12} \\ \hat{S}_{21} & \hat{S}_{22} \end{pmatrix} \begin{pmatrix} \hat{a}_1 \\ \hat{a}_2 \end{pmatrix} \tag{3.1}$$

with $\hat{a}_j$ and $\hat{b}_j$ representing the incident and reflected waves at port j, respectively.

In the course of this study, reflection measurements (one-port measurement, where $j = 1$) were performed. In this instance, the complex scattering parameter $\hat{S}_{11}$ is delineated by an impedance step from $\hat{Z}_1$ to $\hat{Z}_2$.[159] Consequently, $\hat{S}_{11}$ is related to the normalized aperture impedance $\hat{Y} = \hat{Z}_2/\hat{Z}_1$ (with respect to the impedance of the coaxial cable; nominally 50 Ω) via the following expression.[159]

$$\hat{S}_{11} = \frac{1 - \hat{Y}}{1 + \hat{Y}} \tag{3.2}$$

Calibration of the VNA setup is decisive for the accuracy of reflection or one-port measurements. In particular, it is essential to correct for systematic errors in directivity ($\hat{e}_\mathrm{d}$), frequency response ($\hat{e}_\mathrm{r}$) and source matching ($\hat{e}_\mathrm{s}$).[158, 159] In this work a three-point calibration (open, short, and load) is used. The following expression relates the actual scattering parameter $\hat{S}_{11}^\mathrm{act}$ (at the interface of interest, e.g. the sample-probe interface) to the measured scattering parameter $\hat{S}_{11}^\mathrm{meas}$, including the above-mentioned errors.[159, 160]

$$\hat{S}_{11}^\mathrm{meas} = \hat{e}_\mathrm{d} + \frac{\hat{e}_\mathrm{r}\,\hat{S}_{11}^\mathrm{act}}{1 - \hat{e}_\mathrm{s}\,\hat{S}_{11}^\mathrm{act}} \tag{3.3}$$

The following simplified numerical model can be used to calculate the normalized aperture impedance $\hat{Y}(\omega)$ for probes with open-ended geometry, as used in the present work.[159, 160]

$$\hat{Y}(\omega) = \frac{\hat{k}_{\mathrm{m}}^2(\omega)}{\pi\,\hat{k}_{\mathrm{c}}(\omega)\ln\left(D/d\right)}\left[\mathrm{i}\left(I_1 - \frac{\hat{k}_{\mathrm{m}}^2(\omega)I_3}{2!} + \frac{\hat{k}_{\mathrm{m}}^4(\omega)I_5}{4!} - \ldots\right) + \right. \\ \left. + \left(I_2\hat{k}_{\mathrm{m}}(\omega) - \frac{\hat{k}_{\mathrm{m}}^3(\omega)I_4}{3!} + \frac{\hat{k}_{\mathrm{m}}^5(\omega)I_6}{5!} - \ldots\right)\right] \tag{3.4}$$

with the propagation constant within the sample, $\hat{k}_{\mathrm{m}}(\omega) = \omega\sqrt{\hat{\varepsilon}(\omega)\varepsilon_0\mu_0}$, and the propagation constant in the probe head at frequency ω, $\hat{k}_{\mathrm{c}}(\omega) = \omega\sqrt{\hat{\varepsilon}_{\mathrm{c}}\varepsilon_0\mu_0}$. The radii of the inner and outer conductor of the coaxial line are D and d, respectively, μ_0 is the vacuum permeability. The coefficients I_{n} result from a Taylor expansion of the normalised impedance $\hat{Y}(\omega)$ and were obtained for the given probe head geometry (r, θ) by integration of the following equation.[160]

$$I'_{\mathrm{n}} = \int_d^D \int_d^D \int_0^\pi \left(\sqrt{r^2 + r'^2 - 2rr'\cos\left(\theta\right)}\right)^{\mathrm{n}-2} \cos\left(\theta\right) d\theta\, dr\, dr' \tag{3.5}$$

Experimental setup

Reproduced from [104] *with minor changes.*

The experimental dielectric spectra were acquired using a VNA (Anritsu MS4647A). Therefore, the signal reflected from coaxial probes as a function of field frequency was measured. The frequency ranges $0.13 \leq \nu\,/\,\mathrm{GHz} \leq 9.5$ and $9.5 \leq \nu\,/\,\mathrm{GHz} \leq 54$ were covered using open-ended coaxial probes based on SMA and 1.85 mm connectors.[159, 160] An open-ended probe connected to an external frequency converter (Anritsu 3744A mmW) by 1 mm connectors covered the frequency range $54 \leq \nu\,/\,\mathrm{GHz} \leq 125$.[161] A thermostat (Julabo F12-ED) was used to maintain a constant temperature. The sample was therefore placed in a silicone oil bath connected to the thermostat. The dielectric reflectometer was calibrated for systematic errors as described in the previous paragraph. Therefore, a conductive silver paint (short), air (open) and a varying third calibration standard (load; DMA for neat PILs, DMF and MeOH for PILs in solution) was used.[162, 163]

3.2.2 Nuclear Magnetic Resonance Spectroscopy

Reproduced from [104] *with minor changes.*

The characterization of the synthesised PILs was verified by measuring ^{1}H- & ^{13}C-NMR spectra using a Bruker 300 MHz Avance III spectrometer. For this purpose the PILs were dissolved in $CDCl_3$. The resulting proton spectra were referenced to the residual $CHCl_3$ signal at 7.26 ppm.[164] 16 scans were measured for ^{1}H experiments with a recycle delay of 1 s. For ^{13}C experiments, 1024 scans were acquired with a recycle delay of 2 s. In the carbon spectra obtained, the signal at 77.1 ppm was assigned to $CDCl_3$.[164]
A Bruker 700 MHz Avance III spectrometer equipped with a four-channel inverse detection probe head (QXI:^{1}H, ^{19}F, ^{13}C, ^{15}N) was used to measure the temperature-dependent ^{1}H-NMR spectra as well as the diffusion-ordered spectra. A bipolar gradient stimulated echo pulse sequence was used for the DOSY experiments. In addition, simultaneous ^{19}F depolarization was applied to reduce transient heteronuclear nuclear Overhauser phenomena in samples containing fluorinated components. The DOSY measurements consist of 32 individual pulsed field-gradient spin-echo (PFG-SE) experiments, each with 16 scans and a recycle delay of 8 s. The gradient strength was varied linearly. The single pulse ^{1}H NMR spectra consist of 8 scans with a recycle delay of 8 s. The spectra were referenced to the DMSO-d_5h_1 signal at 2.54 ppm.[164]. Therefore, to allow accurate shimming and field locking of the NMR spectrometer, a sealed DMSO-d_6 capillary was added to the NMR tube.
The ^{1}H-^{15}N-HMBC NMR spectra were measured by a Bruker 850 MHz spectrometer with a four-channel inverse detection probe head (QXI: ^{1}H, ^{31}P, ^{13}C, ^{15}N) with pulsed z-gradients of 0.5 T/m. The ^{1}H-^{15}N-HMBC spectra consist of 16 scans with a recycle delay of 1.5 s and 256 increments in the indirect dimension. The spectra have been referenced to nitromethane. The ^{15}N chemical shifts were determined from the obtained ^{1}H-^{15}N-HMBC NMR spectra.

3.2.3 Visible Pump–IR Probe Spectroscopy

A Ti:sapphire regenerative amplifier (Spitfire Ace, Spectra Physics) was used to generate 800 nm pulses (~35 fs, 1 kHz repetition rate; see Figure 3.1 for a schematic representation of the setup). In an optical parametric amplification (OPA) process, the signal and idler beams were generated from a fraction of the 800 nm beam using a TOPAS Prime system (Spectra-Physics). The signal and idler beams were combined in a silver gallium selenide ($AgGaSe_2$) crystal-based non-collinear difference frequency generation (NDFG) stage to generate ~100 fs tunable IR pulses. A wedged CaF_2 window was used to split the IR light. Using both reflections, the reference and probe beams were obtained. The 400 nm pump beam was generated from a fraction of the 800 nm beam by frequency doubling using a β-BaB_2O_4 (BBO) crystal. The pump pulse energy was tuned to ~12 μJ. To effectively control the timing between the pump pulse and the probe pulse, the pump beam was sent through a computer-controlled mechanical delay stage.

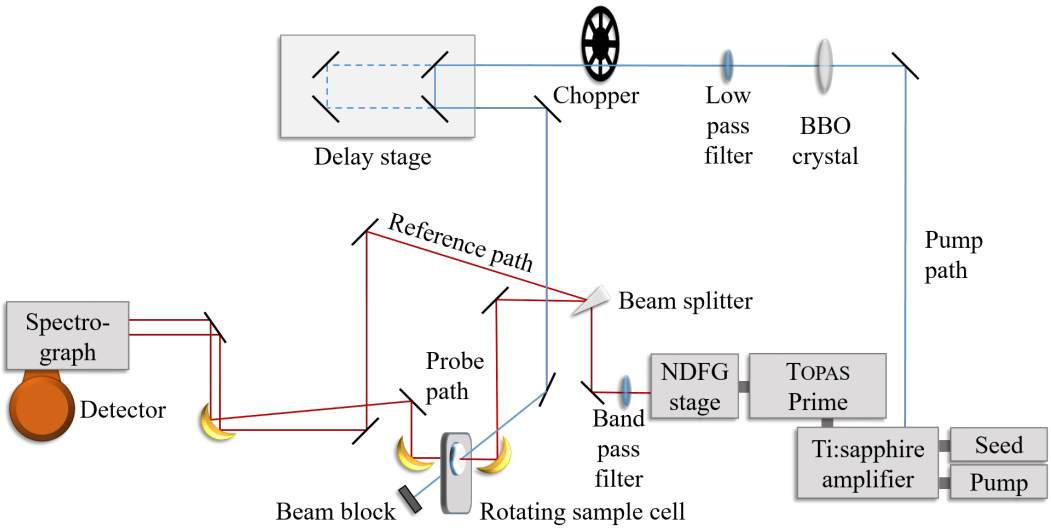

FIGURE 3.1: Schematic representation of the pump-probe setup. 800 nm radiation is generated and amplified in the Ti:sapphire amplifier. 400 nm pump light is generated via a BBO crystal. A mechanical chopper is used to modulate the pump pulse. Timing of the pump pulse is controlled via the delay stage. Tunable IR pulses were generated by a TOPAS Prime system with a NDFG stage. Pump and probe beam were focused and overlapped (in space and time) on the sample. After the sample the pump pulse is blocked. Intensities of both probe and reference beam are detected using a spectrograph and a MCT line detector.

Both the pump and probe beams were focused on the sample and spatially overlapped. The probe beam was focused by an off-axis parabolic mirror. To avoid photo degradation of HPTS and local heating of the sample, the latter was placed in a rotating sample cell. The pump beam was blocked after the sample and the probe beam was re-collimated using another parabolic mirror. Together with the reference beam, the

probe beam was then focused onto the entrance slit of a monochromator (Triax 180, Horiba Scientific). Both beams were spectrally dispersed by a grating with 300 grooves per mm and finally detected by a mercury cadmium telluride (MCT) line detector (2x32 pixels, $5\,\mathrm{cm}^{-1}$ resolution, InfraRed Associates). Fluctuations in laser intensity were corrected from shot to shot using the reference beam intensity. A mechanical chopper (at 500 Hz) blocked every second pump pulse to obtain the pump-induced changes in the frequency-dependent IR transmission. The setup was flushed with N_2 to prevent absorption of the probe pulse by water vapour. The sample cell consisted of a pair of CaF_2 windows with the sample in between the windows. A PTFE spacer was used to keep the layer thickness constant at $25\,\mu$m. The transient signal $\Delta\alpha$ was calculated as a function of the waiting time t_w as follows:

$$\Delta\alpha(\nu, t_\mathrm{w}) = -\ln \frac{T^\mathrm{probe}(\nu, t_\mathrm{w}) T_0^\mathrm{ref}(\nu, t_\mathrm{w})}{T_0^\mathrm{probe}(\nu, t_\mathrm{w}) T^\mathrm{ref}(\nu, t_\mathrm{w})} \tag{3.6}$$

3.2.4 Fourier Transform Infrared Spectroscopy

Fourier transform infrared (FTIR) spectra were obtained using a Bruker Vertex 70. Measurements were conducted in transmission geometry with a spectral resolution of $4\,\mathrm{cm}^{-1}$. The measurement chamber was purged with dry air. The sample cell consisted of two CaF_2 windows with a $25\,\mu$m PTFE spacer in between to keep the layer thickness of the sample constant.

3.2.5 Auxilary Measurements

Reproduced from [104] *with minor changes.*

Viscosity

Viscosities of the samples (at 25 °C) were determined using a ball viscometer (Anton Paar, Lovis 2000 M) with a measurement distance of 99.88 mm in a capillary with a diameter of 1.59 mm.

Density

Densities of the samples (at 25 °C) were determined using a DM40 density meter (Mettler Toledo).

3.3 Quantum Mechanical Calculations

3.3.1 Calculations Discussed in Chapter 4

Reproduced from [104] *with minor changes.*

The ORCA software package (version 4.0.1.2)[165] was used to calculate the electric dipole moments based on density functional theory (DFT). Geometry optimisation was performed using the B3LYP[166, 167]/def2-TZVP[168] level of theory with closed-shell self-consistent field calculations set to tight convergence (the optimised geometries are shown in detail in Figure 4.12). A conductor-like polarizable continuum model was applied to mimic the solvent environment. The exemplary solvent chosen was dichloromethane ($\varepsilon = 8.8$).
Typically for gas phase calculations, the center of mass is used as the reference point for molecular rotations. For the liquid phase, however, friction plays a significant role in molecular motion. As a consequence, the center of hydrodynamic stress must be adapted as the pivot.[115, 169] The center of hydrodynamic stress was approximated by the centroid ($\sum_{i=1...k} x_i/k$, where x_i are the coordinates of all k atoms of an ion) in order to be able to compare the experimental dielectric relaxation strengths with the calculated dipole moments.
The electric dipole moments were calculated based on the optimised atomic coordinates and the CHELPG atomic charges[170, 171]. A detailed comparison between the dipole moments based on the two different pivots (center of mass and center of hydrodynamic stress) and those based on the full electron density is given in Chapter 4.5 (DFT calculations).

3.3.2 Calculations Discussed in Chapter 5

Reproduced from [78] *with minor changes.*

Quantum-mechanical calculations were performed using as well as the ORCA software package (version 4.0.1.2).[165] To this end, geometry optimizations employing the PWPB95[172] functional were performed, which has been shown to provide electrical dipole moments with high accuracy.[172] The def2-TZVPP[168, 173] basis set together with Grimme's dispersion correction with Becke-Johnson damping was used.[174] A conductor-like polarizable continuum model with the dielectric properties of dichloromethane ($\varepsilon = 8.8$) was applied to emulate a liquid solvent environment. Dipole moments were calculated using optimized atomic coordinates and CHELPG[170, 171] charges of the atoms, $q_{i\beta}$. Several functionals and basis sets (see Chapter 5 Table 5.6 for details) were tested and no significant effect of the computational details on the dipole moments were found. Also, adding dispersion corrections seemed to be of minor importance. This is probably due to the use of the polarizable continuum model,

which screens the Coulomb interactions and consequently also their differences by a significant amount.
The ion pair binding energies were computed via the difference in energy of the ion pair and the separate energies of the cation and anion, represented as:

$$E_{\text{binding}} = E_{\text{ionpair}} - E_{\text{cation}} - E_{\text{anion}} \tag{3.7}$$

For charged species, the center of mass, $\vec{r}_{\text{i,COM}}$ was used in previous studies,[175] as the reference point for the molecular dipole moments $\vec{\mu}_{\text{i}}$

$$\vec{\mu}_{\text{i,COM}} = \sum_{\beta} q_{\text{i}\beta} \left(\vec{r}_{\text{i}\beta} - \vec{r}_{\text{i,COM}} \right) \tag{3.8}$$

The atomic partial charges, $q_{\text{i}\beta}$, were taken from the polarizable force field. In the case of molecular ions, this dipole moment represents a vector from the center of mass to the center of charge times the molecular charge $q_{\text{i}} = \sum_{\beta} q_{\text{i}\beta}$ of the ion i:

$$\begin{aligned}
\vec{\mu}_{\text{i,COM}} &= q_{\text{i}} \left(\vec{r}_{\text{i,COQ}} - \vec{r}_{\text{i,COM}} \right) && (3.9)\\
&= q_{\text{i}} \frac{\sum_{\beta} q_{\text{i}\beta}\, \vec{r}_{i\beta}}{q_i} - q_i\, \vec{r}_{\text{i,COM}} && (3.10)\\
&= \sum_{\beta} q_{\text{i}\beta}\, \vec{r}_{\text{i}\beta} - \sum_{\beta} q_{\text{i}\beta}\, \vec{r}_{\text{i,COM}} && (3.11)\\
&= \sum_{\beta} q_{\text{i}\beta} \left(\vec{r}_{\text{i}\beta} - \vec{r}_{\text{i,COM}} \right) && (3.12)
\end{aligned}$$

Alternatively, the center of hydrodynamic stress is often used as a reference point for rotation.[169] As the center of hydrodynamic stress is not well-defined, we approximate it by the centroid (geometric center), $\vec{r}_{\text{i,COG}}$:

$$\vec{r}_{\text{i,COG}} = \frac{1}{N} \sum_{\beta}^{N} \vec{r}_{\text{i}\beta} \tag{3.13}$$

The molecular dipole moment $\vec{\mu}_{\text{i,COG}}$ with respect to the center of geometry can be represented as:

$$\vec{\mu}_{\text{i,COG}} = \sum_{\beta} q_{\text{i}\beta} \left(\vec{r}_{\text{i}\beta} - \vec{r}_{\text{i,COG}} \right) \tag{3.14}$$

Molecular dipole moments $\vec{\mu}_{\text{i,COM}}$ equal $\vec{\mu}_{\text{i,COG}}$ for neutral molecules, yet can markedly differ for molecular ions Im_1H^+, OAc^-, and TFA^-.
The sum of the molecular dipole moments yields the collective rotational dipole moment:

$$\vec{M}_{\text{D}} = \sum_{\text{i}} \vec{\mu}_{\text{i}} \tag{3.15}$$

Its autocorrelation function is the basis of the computation of the dielectric permittivity $\hat{\varepsilon}(\nu)$.[175]

3.4 MD Simulations

Reproduced from [78] *with minor changes.*

In contrast to classical molecular dynamics (MD) force fields, polarizable force fields aim at providing a more accurate description of the electronic structure's response to local environmental changes, surpassing the fixed charge approximation on each atom. This approach offers several advantages, such as improved dynamics,[176, 177] enabling a better representation of properties like diffusivity and conductivity.[177]
The Drude oscillator model was employed to incorporate polarizability explicitly. Details on the development and optimization of the underlying force fields can be found in the referenced previous work.[66] Parameters for the additional molecules, namely TFA^- and HTFA, were obtained from the ParaChem website,[178], which uses the Charmm General Force Field[179] (CGenFF) as a reference and employs an analogy-based approach to determine the best-matching parameters. Subsequently, FFParam[180] was utilized to convert the force field description into a polarizable form that can be used in conjunction with the Drude General Force Field[181] (DGenFF). Drude particles with a mass of 0.4 u were tethered to all non-hydrogen atoms with a force constant k=1000 kcal/mol/Å^2. The maximum displacement for the mobile Drude oscillators was restricted to 0.25 Å.
The Lennard-Jones ϵ_β for each atom β was scaled

$$\epsilon_\beta^{\mathrm{LJ}} = \epsilon_\beta^{\mathrm{LJ,unscaled}} \frac{\Big(\max(\alpha_\beta) - \alpha_\beta\Big) + s \cdot \max(\alpha_\beta)}{\max(\alpha_\beta) + s \cdot \Big(\max(\alpha_\beta) - \alpha_\beta\Big)} \tag{3.16}$$

using the approach introduced by Vlugt and co-workers[182] to counteract double counting of dispersive forces.[177] α_β is the atomic polarizability of the atom β and $\max(\alpha_\beta)$ is the maximum polarizability of all atoms. Three replicas consisting of 1000 molecules were created for each system (see Table 5.1), and a s-value of 0.25 was employed.
The initial configurations were generated using the software Packmol[183]. Subsequently, Charmm[184] was employed for a short energy minimization, topology generation, and coordinate file creation. Due to better performance, production runs were performed in OpenMM[185]. The equilibration phase was carried out in the NPT ensemble using a Monte Carlo barostat set at 1 atm pressure. To ensure stable simulations, an initial equilibration period of 20 ps was performed, using a timestep of 0.1 fs at a temperature of 300 K. Subsequently, a time step of 0.5 fs was used. To facilitate proper mixing and equilibration of the system, an additional 2 ns simulation at 500 K was conducted before equilibrating for 3 ns at 300 K. The final box length used for the production simulations was obtained from the last nanosecond of the equilibration trajectories. Subsequently, 50 ns of trajectories were generated in the NVT ensemble for further analysis. The polarizable MD simulations employed the velocity Verlet

algorithm for particle propagation, following the methodology described in references [186] and [187]. A temperature-grouped Dual-Nosé-Hoover thermostat was utilized to regulate the system temperature. The non-Drude particles were kept at a temperature of 300 K, while the Drude particles were kept at 1 K. For the temperature-dependent simulations discussed in Chapter 6, non-Drude particles where additionally maintained at $T/\mathrm{K}=\{288, 298, 308, 318, 328, 338\}$. The corresponding results were averaged over three replicas for a given mole fraction and temperature. Collision frequencies of $10\,\mathrm{ps}^{-1}$ and $200\,\mathrm{ps}^{-1}$ were set for the atoms and Drude particles, respectively. Periodic boundary conditions were applied in all simulations, and the Particle Mesh Ewald algorithm was employed with a cutoff distance of 11 Å and a switch distance of 10 Å. Bonds involving hydrogen atoms were kept fixed throughout the simulations. The error tolerance δ was set to 0.0001. The simulations were performed on the CUDA platform, utilizing the default mixed precision setting. This implies that forces were calculated in single precision, while the integration was performed in double precision. Trajectory analysis was conducted using the MDANALYSIS package.[188, 189]

Chapter 4

Charge Transport in Protic Ionic Liquids: Effect of Protonation State in 1-Methylimidazolium Acetate/Trifluoroacetate Mixtures

Reproduced from [104] *with minor changes.*

4.1 Abstract

Despite the potential to overcome slow charge transport in ionic liquids by decoupling charge transport from mass transport in protic ionic liquids (PILs), the average proton distribution and the contribution of proton conduction to the overall charge transport in PILs has not been fully established. To elucidate the predominant underlying molecular species in the PILs and the molecular dynamics of the PILs, we study the dipolar response and conductivity using dielectric relaxation (DR) spectroscopy and the nucleis chemical environment and molecular mobility using nuclear magnetic resonance (NMR) spectroscopy of prototypical PILs based on 1-methylimidazolium as Brønsted base. To elucidate the effect of the acidity of the Brønsted acid we gradually vary the composition of the PILs from 1-methylimidazolium acetate [MimH][AcO] to 1-methylimidazolium trifluoroacetate [MimH][TFA]. In the neat ionic liquids, both ^{15}N-NMR chemical shifts and the sample conductivities suggest that in [MimH][AcO] electro-neutral molecular species dominate, consistent with earlier findings. The dipolar response of these molecular species as detected via the DR spectra is stronger than what one would expect based on the molecular dipole moments estimated from density functional theory calculations, which points to the formation of an extended H-bonded network. Upon addition of [MimH][TFA], this dipolar response is reduced as the degree of protonation of 1-methylimidazolium gradually increases, which is apparent from the conductance and ^{15}N chemical shifts. Interestingly, diffusion ordered NMR spectroscopy indicate protons to become more mobile than the constituting acid and base molecules, consistent with Grotthuss-like proton transport. To vary the immediate environment of the PILs, we study solutions of the PIL mixtures in aprotic dimethylformamide (DMF) and protic methanol (MeOH) as two limiting cases. We find that [MimH][AcO] exclusively forms electroneutral species in DMF, as evident from the negligible conductivity, while with increasing TFA content the fraction of charged molecular species increases. Although these ionic species give rise to a finite conductivity, demonstrating the presence of mobile ions, a large fraction of these ions are bound in [MimH][TFA] ion-pairs, as detected in the DR spectra. Yet, temperature dependent H-NMR linewidths of the acidic proton signals suggest proton exchange to occur on the NMR timescale, presumably between $[MimH]^+$ and [Mim]. Conversely, in MeOH we find no evidence for the presence of ion-pairs, while the high conductivity of these solutions shows that MeOH can efficiently solvate ions and may participate in proton transfer. Together, our results highlight the sensitivity of protonation equilibria to the immediate environment and of proton dynamics to these protonation equilibria. Our results show that tuning these equilibria using PIL mixtures can provide routes to tailor the contribution of proton transport to charge transport in PILs.

4.2 Introduction

Over the last decades ionic liquids (ILs) have attracted substantial interest due to their unique properties, such as their high thermal stability, low vapor pressure, and large electrochemical window.[15, 19, 52, 190–192] Consisting solely of ionic species with a melting point below 100 °C, ILs are also known as molten salts. The almost unlimited number of possible combinations of cations and anions that form ILs leads to vast structural variations and widely tunable properties.[1, 7, 12] Therefore ILs are a promising material class for diverse applications, such as green solvents in synthesis,[191, 193] pharmaceutical ingredients,[194–196] or electrolytes for fuel cells and batteries.[192, 197–201]

However, low ionic conductivities due to high viscosities of aprotic ionic liquids (AILs) limit possible applications in e.g. energy-storage technologies.[55] In principle, protic ionic liquids (PILs) could overcome these limitations,[56] as PILs form via reversible proton transfer between Brønsted acids and Brønsted bases.[57] Due to such proton transfer equilibria, PILs can form extended hydrogen-bonded networks,[202–205] and it is possible to decouple charge transport from the (slow) diffusive mass transport to enable high ionic conductivities.[1] Although several studies have attempted to elucidate the underlying molecular level dynamics and proton distributions, charge transport in PILs is not yet fully understood.[61–64, 206]

One prominent example for a PIL is 1-methylimidazolium acetate [MimH][AcO]. Previous studies have suggested that [MimH][AcO] consists predominantly of neutral species as the acidity of acetic acid is moderately low: Raman and potentiometric measurements have suggested that neutral species of AcOH and Mim dominate in [MimH][AcO].[61, 65] Consistent with this notion, molecular dynamics simulations with a 30 % degree of protonation could reproduce experimental dynamics.[66] The low degree of protonation has been further supported by density functional theory calculations, which have shown that a complex of the neutral species is more stable than a pair of charged molecules.[61] These studies have further suggested that the environment, such as the continuum solvent used for the computations, can facilitate proton transfer and shift protonation equilibria towards ion-pairs.[61] Yet, for other acid base mixtures NMR experiments have revealed a continuous transition between these extreme scenarios, hydrogen-bonded neutral species and ion-paired charged molecules.[69, 70] This may explain why the ^{1}H NMR experiments on [MimH][AcO] have suggested that more than 90 % of the [Mim] is protonated[67, 68] with a marked decrease in ionicity upon addition of polar solvents, such as dimethylsulfoxide.[68] Altogether, these previous studies point towards the protonation states of [MimH][AcO] being very sensitive to various factors. As such, thermal fluctuations could give rise to fluctuations in the protonation states and consequently to a marked contribution of proton transfer to the overall conductivity. In fact, the relatively high ionic conductivities of [MimH][AcO] seem to support this notion[57, 61, 71] and comparison of the activation energies for translational and rotational diffusion has indicated that a Grotthuss-like charge

transport takes place in [MimH][AcO].[72] It has been further suggested that increasing the acidity of the anion by replacing acetic acid by trifluoroacetic acid, results in a shift of the protonation equilibria to the fully protonated species, which goes along with a change in the proton conduction mechanism from proton hopping to vehicle transport.[73]

Yet, experimentally information on proton transport in this PIL has been only indirectly inferred. Molecular dynamics simulations can directly visualize proton transport and it has been shown that a multitude of proton transfer channels exist in [MimH][AcO].[71] Yet, to allow for proton mobilities that markedly exceed the mobilities of the ionic species, cf. Grotthuss-type conduction, chain like structures of neutral acetic acids are required.[71] Therefore, the conductivity of the PIL relies on the subtle balance between charged and neutral species, which can act as proton donors and acceptors. The sensitivity of conductivity to this balance implies that the transport properties can be tuned by altering the ratio of charged and electro-neutral species, which can be readily tuned via variation of the acidity of the Brønsted acid.

Here, we explore the effect of this balance on the transport properties, by studying mixtures of partly ionized [MimH][AcO], and 1-methylimidazolium trifluoroacetate ([MimH][TFA]) with a high ionicity.[73] We explore the dynamics in these mixtures using dielectric relaxation (DR) spectroscopy, which can detect the dynamics of dipolar species, in particular ion pairs.[74, 75] Additionally, DR spectroscopy provides information on the mobility of ions via the conductivity.[76, 77] We complement this information using nuclear magnetic resonance spectroscopy (NMR), which can reveal information about structure and dynamics of the investigated ionic liquids. In particular, the ^{15}N chemical shifts provide information on the degree of protonation of the Brønsted base and diffusion ordered spectroscopy (DOSY) allows for assessing molecular mobilities. The combination of both experimental techniques provides the average proton distribution in equilibrium and their dynamics and allows for gaining insight into the charge transfer in these PILs. We study the neat PIL mixtures and explore the influence of the chemical environment on the PIL mixtures using protic and aprotic solvents. Our results demonstrate that increasing acidity of the Brønsted acid increases the iconicity and may result in decoupling of the proton transport from ionic diffusion. Our results further indicate that in aprotic dimethylformamide, aggregation of the PIL is enhanced resulting in a reduction of the conductivity. In turn, addition of the protic solvent methanol suppresses the formation of electroneutral aggregates resulting in a marked enhancement of the conductivity.

4.3 Results and Discussion

In this work we study the effect of the protonation state of the PIL and of the addition of solvents on the dynamics and transport properties of methylimidazolium based PILs. To systematically vary the protonation state of 1-methylimidazole ([Mim]), that is the ratio [Mim]/[MimH]$^+$, we vary the acidity of the Brønsted acid by studying binary mixtures of [MimH][AcO] and [MimH][TFA].[2] To elucidate the effect of added solvent, we investigate the dynamics of [MimH][AcO]/[MimH][TFA] mixtures in the aprotic solvent DMF, which barely dilutes the acid/base molecules, and in MeOH, which can act as proton acceptor and donor and can therefore contribute to a Grotthuss-type proton conduction.[207]
The following chapter is structured as follows: we first study the dynamics using dielectric relaxation spectroscopy to obtain insights into ions' translational and dipolar rotational dynamics.[98, 102, 208] Secondly, we use NMR chemical shift experiments to deduce the protonation state,[209] diffusion ordered NMR spectroscopy to detect correlations between the mobility of the individual molecular species,[210] and the NMR linewidths to evidence chemical (proton-) exchange. We conclude with the joint discussion of the findings.

4.3.1 Dynamics of Neat PIL Mixtures

To investigate the impact of TFA on the dipolar response and the conductivity of the ionic liquid mixtures we use DRS, which probes the macroscopic polarization dynamics of a sample as a response to an externally applied oscillating electric field. The measured polarization is usually expressed as complex permittivity $\hat{\varepsilon}(\nu)$:[98]

$$\hat{\varepsilon}(\nu) = \varepsilon'(\nu) - \mathrm{i}\varepsilon''(\nu) + \frac{\kappa}{2\pi \mathrm{i}\nu\varepsilon_0} \tag{4.1}$$

with the real part $\varepsilon'(\nu)$ representing the dielectric permittivity and the imaginary part $\varepsilon''(\nu)$ representing the dielectric loss. The last term of Equation 4.1 accounts for the contribution of translational dynamics of charged molecules, typically expressed in terms of the conductivity. Here, we assume the conductivity, κ, to be real and independent of frequency (i.e. the d.c. conductivity). ε_0 is the permittivity of free space. Typically, polarization dynamics due to rotation of dipolar species (e.g. dipolar molecules or ion-pairs) give rise to a dispersion in $\varepsilon'(\nu)$ and peaks in $\varepsilon''(\nu)$. We note that by assuming κ to be constant and real, $\varepsilon'(\nu) - \mathrm{i}\varepsilon''(\nu)$ contains all frequency dependent polarization dynamics, irrespective of being due to ion translations or dipolar rotations. As such, also a frequency dependent conductivity (e.g. due to spatially confined translation of ions) will contribute to $\varepsilon'(\nu) - \mathrm{i}\varepsilon''(\nu)$. In fact, molecular dynamics simulations have suggested that ions' translations contribute to the polarization response of ionic liquids. Yet, for ionic liquids with small, rather spherical ions these translational dynamics are minor at MHz - GHz frequencies and this spectral window is dominated by dipolar rotations.[208, 211] For less spherical ions – such as

acetate containing ionic liquids – MD simulations have suggested that translational and rotational contributions can be similar in magnitude.[66] Yet, the separation of translational and rotational contributions depends on the choice of the center of charge and the center of mass is typically assumed as pivot (see also Methods section) in MD analysis. For diffusive rotation with the center of hydrodynamic stress as pivot, the balance between translational and rotational contributions differs and our calculated dipole moments suggest that rotational contributions are underestimated (translational contributions are overestimated) in particular for the acetate anion, where center of mass and center of hydrodynamic stress markedly differ (see Table 4.1, SI). Neglecting translational contributions, the magnitude of the dielectric amplitudes of the $\varepsilon'(\nu) - i\varepsilon''(\nu)$ spectra is a measure for the density and magnitude of dipoles in the samples, while the conductivity κ reports on the number density and mobility of mobile charges (i.e. ions).

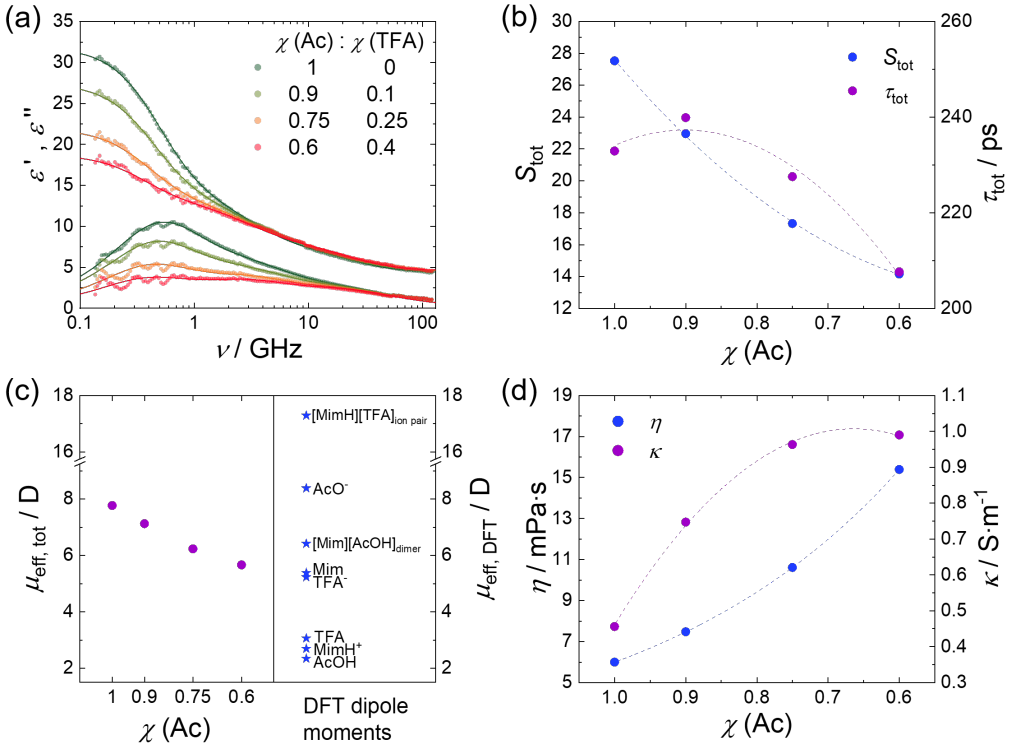

FIGURE 4.1: (a) Complex permittivity spectra of neat PIL mixtures at 298 K. Symbols show experimental data, solid lines represent the fits of Equation 4.2 to the data. Note the last terms of equations 4.1 and 4.2 have been subtracted for visual clarity. (b) Total relaxation amplitude, S_{tot}, and amplitude-weighted relaxation time τ_{tot} as a function of χ(Ac). Symbols represent parameters from the fit, dotted lines are a guide to the eye. (c) Left: total effective dipole moment $\mu_{\mathrm{eff,tot}}$, obtained from experimental total amplitudes S_{tot} as a function of χ(Ac). Right: Molecular dipole moments based on DFT calculations. For ionic species the centroid is taken as the center of charge. (d) Viscosity η and dc conductivity κ as a function of χ(Ac). Symbols represent experimental data, dotted lines are a guide to the eye. *Reproduced from* [104].

In Figure 4.1(a) we show the dielectric spectra for the [MimH][AcO]/[MimH][TFA]

mixtures at 298 K. As commonly observed for ionic liquids,[77, 212] the spectra appear rather broad and featureless. Consistent, with earlier studies,[72, 73] the spectrum of [MimH][AcO] is dominated by a loss peak centered at ~0.5 GHz, which is asymmetrically broadened towards higher frequencies. With increasing TFA content, the magnitude of this relaxation at ~0.5 GHz decreases, whereas the spectral range at > 10 GHz is rather insensitive to an increased fraction of TFA. Additionally, the frequency of the peak maximum of the imaginary part somewhat shifts to lower frequencies. We note that we observe similar trends at an elevated temperature of 333 K, at which the samples are liquid over a wider composition range (except $\chi(\mathrm{Ac}) < 0.2$, see SI, Figure 4.13).
To quantify these changes to the spectra, we use a relaxation model consisting of three relaxation modes:

$$\hat{\varepsilon}(\nu) = \frac{S_1}{1 + (2\pi \mathrm{i} \nu \tau_1)} + \frac{S_2}{1 + (2\pi \mathrm{i} \nu \tau_2)} + \frac{S_3}{1 + (2\pi \mathrm{i} \nu \tau_3)} + \frac{\kappa}{2\pi \mathrm{i} \nu \varepsilon_0} \tag{4.2}$$

With S_j and τ_j representing the relaxation amplitudes and relaxation times, respectively. The high frequency limit of the permittivity, ε_0, contains all polarization dynamics, which are not accessible in the frequency range covered in this work. From these fits we find the three relaxations to be centered at ~0.5 GHz, at ~4 GHz, and ~25 GHz (fit parameters are listed in Table 4.2, SI). Previous work on ionic liquids indicated that the lower frequency relaxations can be predominantly ascribed to cation reorientation, while the intermediate relaxations predominantly originate from the rotation of dipolar anions,[77, 103, 107] which is also in broad agreement with what has been found for different ionic liquids based on molecular dynamics simulations.[208]
Yet, given the complexity of the present samples with anticipated contributions from different anions, electroneutral acids, protonated cations ($[\mathrm{MimH}]^+$) and electro-neutral [Mim], such assignment is challenging for the present mixtures. Therefore, we consider the relaxation model merely as a formal description of the experimental spectra and only discuss the overall trends in relaxation parameters: We calculate the total relaxation amplitude $S_{\mathrm{tot}} = \sum_{i=1}^{3} S_j$, that represents the strength of all relaxation dynamics in the PILs, and the amplitude-weighted average relaxation time $\tau_{\mathrm{tot}} = \sum_{i=1}^{3} S_j \, \tau_j / \sum_{i=1}^{3} S_j$, which are shown in Figure 4.1(b). The relaxation times τ_{tot} are somewhat insensitive to the addition of TFA with a minor decrease with increasing mole fraction of TFA, which is indicative of an acceleration of the overall dynamics. For diffusive rotational relaxation of uncorrelated molecules, this relaxation is expected to scale with the molar volume of the rotating species and the samples' microscopic viscosity.[213] Given the comparable molecular volume of all molecular species ([Mim], $[\mathrm{MimH}]^+$, $[\mathrm{AcO}]^-$, [AcOH], and $[\mathrm{TFA}]^-$) and the increasing viscosity (Figure 4.1(d)) with increasing molar fraction of TFA, the insensitivity of τ_{tot} to $\chi(\mathrm{Ac})$ may be surprising.
However, the data in Figure 4.1(b) point at correlated dynamics within the PILs (see below): for correlated dynamics, dipole-dipole correlations can markedly alter the observed relaxation time.[214] The presence of such correlations is consistent with the H-bonded structure of the PILs and upon addition of [MimH][TFA] breaking of the

H-bonded structure results in altered (reduced) dynamic correlations of the molecular dynamics.

As already apparent from the raw spectra in Figure 4.1(a), the total relaxation strength, S_{tot}, decreases with increasing TFA content (Figure 4.1(b)). Assuming only a single dipolar species giving rise to the observed relaxation dynamics, the dielectric amplitude S_j can be related to the effective dipole moment $\mu_{\mathrm{eff},j}$ of this species and its concentration c via:[114]

$$\frac{2\varepsilon_{\mathrm{s}}+1}{\varepsilon_{\mathrm{s}}} S_j = \frac{N_{\mathrm{A}} c_j}{k_{\mathrm{B}} T \varepsilon_0} \mu_{\mathrm{eff},j}^2 \tag{4.3}$$

where is $\varepsilon_{\mathrm{s}} = S_{\mathrm{tot}} + \varepsilon_\infty$, N_{A} the Avogadro constant, k_{B} the Boltzmann constant, and T the thermodynamic temperature. To relate the dipolar response to the dipole moment of molecular species, without discriminating between the individual molecular species, we calculate the total electrical dipole moment $\mu_{\mathrm{eff,tot}}$, from S_{tot} by assuming $c_{\mathrm{tot}} = c_{\mathrm{Mim}} + c_{\mathrm{Ac}} + c_{\mathrm{TFA}}$, as determined from the sample compositions and the measured density. We note that this approach exclusively assumes dipolar contributions to the spectra and neglects translational polarization dynamics.

We find $\mu_{\mathrm{eff,tot}}$ to decrease from ~8 D for $\chi(\mathrm{Ac}) = 1$ to ~5.5 D for $\chi(\mathrm{Ac}) = 0.6$ as $\chi(\mathrm{Ac})$ decreases (Figure 4.1(c)). Similar trends are observed, when restricting the analysis to the lowest frequency relaxation (see Figure 4.14, SI). The DFT-calculated dipole moments $\mu_{\mathrm{eff,DFT}}$ of the individual electro-neutral or ionic molecules range from 2.34 D for [AcOH] to 8.39 D for $[\mathrm{AcO}]^-$ (Figure 4.1(c)). The calculated dipole moments are listed in Table 4.1 (see SI) and the optimized molecular geometries are displayed in Figure 4.12 (see SI). The comparison of the calculated values to $\mu_{\mathrm{eff,tot}}$ indicates that the $\mu_{\mathrm{eff,DFT}}$ values of the individual molecular species are closer to the experimental values than those of the dimers, hence, rotational contribution of acid-base dimers to the spectra are rendered unlikely.

It is worth noting, that the DFT calculations suggest that for two limiting cases that substitution of AcOH by TFA does (i) not alter the overall ionicity or (ii) TFA is fully ionized an moderately decreasing or constant $\mu_{\mathrm{eff,tot}}$ would be expected if the observed relaxations are due to uncorrelated ionic/molecular rotations: For scenario (i) a moderate decrease of $\mu_{\mathrm{eff,tot}}$ with decreasing $\chi(\mathrm{Ac})$ would be expected, as $\mu_{\mathrm{eff,DFT}}$ ($[\mathrm{TFA}]^-$) < $\mu_{\mathrm{eff,DFT}}$ ($[\mathrm{AcO}]^-$) and $\mu_{\mathrm{eff,DFT}}$ ([TFA]) > $\mu_{\mathrm{eff,DFT}}$ ([AcOH]). This decrease would be consistent with the experimentally observed decrease of $\mu_{\mathrm{eff,tot}}$, however, given the significant difference in acidities of AcOH (pK_a of 4.75) and TFA (pK_a of 0.5), constant iconicity seems rather unlikely. In scenario (ii) $\mu_{\mathrm{eff,tot}}$ should be rather independent of TFA content, as $\mu_{\mathrm{eff,DFT}}$ ($[\mathrm{MimH}]^+$) ≈ $\mu_{\mathrm{eff,DFT}}$ ([AcOH]) and $\mu_{\mathrm{eff,DFT}}$ ([Mim]) ≈ $\mu_{\mathrm{eff,DFT}}$ ($[\mathrm{TFA}]^-$).

As such, this simplified consideration of only isolated dipoles with their dipole moments estimated from DFT calculations giving rise to the experimental dielectric response cannot explain the observed decrease of $\mu_{\mathrm{eff,tot}}$ with decreasing $\chi(\mathrm{Ac})$. In turn, the

higher values of $\mu_{\text{eff,tot}}$ relative to $\mu_{\text{eff,DFT}}$ of the individual molecular species may point to the presence of dynamic correlations to $\mu_{\text{eff,tot}}$. In this case, the decreasing $\mu_{\text{eff,tot}}$ with decreasing χ(Ac) can be rationalized by a TFA induced reduction of the dipolar correlations, e.g. TFA weakens the correlations imposed by the hydrogen-bonded structure of [MimH][AcO]. Yet, also translational contributions to the observed dynamics may explain these differences and molecular dynamics simulations would be required to fully disentangle these different contributions.
Remarkably, the determined conductivities indicate that, despite the increase of the viscosity with increasing TFA content (Figure 4.1(d)), κ markedly increases. In light of previous studies,[57, 61, 71] which indicate that in neat [MimH][AcO] neutral species ([Mim] and [AcOH]) dominate and form an extended hydrogen-bonded network, the observed increase of conductivity can be explained by an increasing fraction of ionic species upon substitution of AcOH by TFA: Based on the higher acidity of TFA with a pKa of 0.5 as compared to the weaker acid acetic acid with a pKa of 4.75 the fraction of ions in the PIL mixtures is expected to increase with addition of TFA.[65] Apparently, the increasing ion density can outnumber the viscosity induced decrease in the ions' mobility. Yet, also a contribution of more mobile charge carriers (e.g. Grotthuss-type transport of protons) may contribute to the observed increase in conductance.

4.3.2 Dynamics of PILs in Solution

We proceed with discussion of the dielectric response of 1 M [MimH][AcO]/[MimH][TFA] in DMF, for which effects of altered viscosities are reduced. [MimH][AcO]/[MimH][TFA] mixtures dissolved in DMF and MeOH with an ionic liquid concentration of $c_{\text{PIL mixture}} = 1\,\frac{\text{mol}}{\text{L}}$ were liquid over the full composition range (χ(Ac) = 0-1). The latter were prepared by weight in volumetric flasks and addition of the respective solvent.
The dielectric spectra for [MimH][AcO]/[MimH][TFA] mixtures in DMF in Figure 4.2(a) are dominated by a relaxation centered at ~15 GHz, which can be assigned to the orientational relaxation of DMF.[162] For χ(Ac) = 1 the experimental spectra of the PIL solution are shifted to lower frequencies, as compared to neat DMF, and also appear asymmetrically broadened (see Figure 4.2(a)).[162] With decreasing χ(Ac) a contribution at low frequencies (~1.5 GHz) emerges, indicative of the formation of dipolar species. To quantify these spectral contributions, we use a combination of two Debye-type relaxations, to model the dominant DMF relaxation and the lower-frequency dynamics associated with the PIL:

$$\hat{\varepsilon}(\nu) = \frac{S_{\text{PIL}}}{1 + (2\pi \mathrm{i}\nu\tau_{\text{PIL}})} + \frac{S_{\text{DMF}}}{1 + (2\pi \mathrm{i}\nu\tau_{\text{DMF}})} + \frac{\kappa}{2\pi \mathrm{i}\nu\varepsilon_0} \tag{4.4}$$

with S_{PIL} and τ_{PIL} the relaxation strength and time of the lower frequency relaxation, respectively. S_{DMF} and τ_{DMF} are the strength and time of the higher frequency relaxation. Given the similarity of the relaxation parameters of the higher frequency

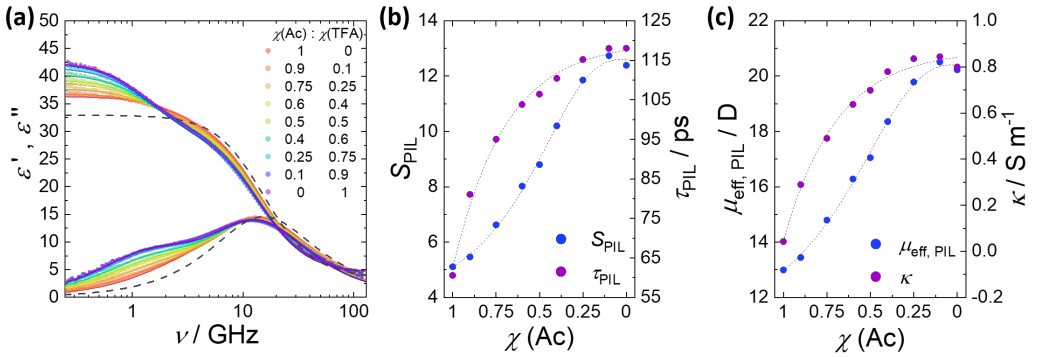

FIGURE 4.2: (a) Complex permittivity spectra of PIL mixtures (1 M) in DMF at 298 K. Symbols represent experimental data, solid lines represent the fit (Eq. 4.4). The grey dotted line represents the literature spectrum of DMF,[162] scaled by a factor of 0.88. For visual clarity the Ohmic loss (last term of Equation 4.2 & 4.4) has been subtracted. (b) Dielectric amplitude S_{PIL} and relaxation times τ_{PIL} of the PIL relaxation (low frequency mode) as a function of the composition of the PIL mixture. Dotted lines are a guide to the eye. (c) Effective PIL dipole moment $\mu_{\mathrm{eff,PIL}}$ calculated from S_{PIL} and dc conductivity κ of PILs in DMF as a function of χ(Ac). Dotted line is a guide to the eye. *Reproduced from* [104].

relaxation to those of neat DMF we assign this relaxation to be dominated by the orientational dynamics of DMF (fit parameters are listed in Table 4.3, SI). Conversely, the lower frequency relaxation is attributed to stem from the PIL. We note that these fits somewhat deviate from the experimental data at higher frequencies (Figure 4.2(a)), which is presumably due to an additional fast relaxation process, which is also present in neat DMF,[162] yet not fully covered by the present frequency range.

In all mixtures we find τ_{DMF} to be longer than in neat DMF[162] (Figure 4.2(a)) and, τ_{DMF} slightly increases with decreasing χ(Ac). This minor slow-down in orientational dynamics of the DMF molecules can most likely be attributed to an increase in viscosity due to the addition of PIL and decreasing χ(Ac), respectively. In accordance with Equation 4.3, the decrease in amplitude S_{DMF} compared to S_{DMF} in neat DMF[162] is due to the lower concentration of DMF molecules and kinetic depolarization[215, 216] in the solutions of the PILs.

The parameters of the lower frequency relaxation allow for obtaining information on the state of the PIL in the solvent. The relaxation time τ_{PIL}, which is associated with the dynamics of the PIL solute, increases with decreasing χ(Ac), which points towards an increase of the samples' viscosities or to an increase in the molecular volume of the underlying dipolar species with increasing TFA content (Figure 4.2(b)). To elucidate the underlying molecular species, we calculate from the relaxation strengths S_{PIL}, which also gradually increase with decreasing χ(Ac) (Figure 4.2(b)), the corresponding effective dipole moment $\mu_{\mathrm{eff,PIL}}$ (eq 3, $c_{\mathrm{PIL}} = c_{\mathrm{Mim}} + c_{\mathrm{Ac}} + c_{\mathrm{TFA}}$, which also exhibits a marked and gradual increase with decreasing χ(Ac). For $\chi(\mathrm{Ac}) = 0$ the thus obtained value of $\mu_{\mathrm{eff,PIL}} \approx 20$ D is close the dipole moment for an isolated [MimH][TFA] ion-pair

of ~17 D as obtained from the DFT calculations (see Figure 4.1(c)). As such, our results suggest that at high TFA concentrations, ion-pairs are the dominant underlying molecular level species. Conversely, at $\chi(\mathrm{Ac}) = 1$ $\mu_{\mathrm{eff,PIL}}$ is twice as high as the calculated value for a hydrogen-bonded [Mim][AcOH] dimer (see Figure 4.1(c)). The observation that the experimental dipole moment exceeds the value expected for a hydrogen-bonded [Mim][AcOH] dimer suggests that also for $\chi(\mathrm{Ac}) = 1$ ion-pairs (with markedly higher dipole moments) partially exist, in line with the partially ionized character of neat [Mim][AcOH].
Yet, also other molecular aggregates such as acetic acid selfdimers[217–219] (with distorted symmetry) or larger aggregates consisting of multiple acetic acid molecules and a [Mim] base,[220] which allow for a larger charge separation and thus result in higher dipole moments, may be formed. In this context it is important to note that the samples conductivity at $\chi(\mathrm{Ac}) = 1$ is negligibly small, which demonstrates that aggregates in solution are predominantly electro-neutral (see Figure 4.2(c)). With decreasing $\chi(\mathrm{Ac})$ the conductance increases (see Figure 4.2(c)), demonstrating that in the presence of TFA mobile ions are partially present.

Conversely, the trends of the dielectric spectra of the PIL mixtures in hydrogen-bonding MeOH (Figure 4.3(a)), differ from the trends of the PILs in DMF: Irrespective of PIL composition, the experimental spectra are dominated by a relaxation centered at ~3 GHz, similar to the spectrum of neat MeOH.[221] While the overall spectral amplitude decreases with decreasing $\chi(\mathrm{Ac})$, the shape of the spectra is rather insensitive to the PIL composition. To quantify the spectral contributions, we model the spectra using a combination of three Debye-type relaxation modes (Eq. 6.3), analogously to the neat PIL mixtures and to the spectra for neat MeOH.[221]
A relaxation mode at low frequencies associated to PIL species can be fitted to the experimental spectra (Table 4.4, see SI). As this PIL relaxation overlaps with the MeOH relaxation (~3 GHz) resolving[222] the PIL contribution is challenging and correlations of the fit parameters of the two overlapping modes does not allow for a meaningful interpretation.[222] Therefore, we determine the total relaxation amplitude S_{tot}, representing contributions of both MeOH and PIL species to the dielectric spectra, and the amplitude weighted average relaxation time τ_{tot} from the obtained parameters (see Figure 4.3(b), parameters are listed in Table 4.4, SI). The value of τ_{tot} represents the amplitude weighted average of both, PIL relaxations and methanol relaxations and is therefore lower than τ_{PIL} found for mixtures with DMF, which is associated with PIL dynamics. As already apparent from the insensitivity of the spectral shape of the raw spectra to $\chi(\mathrm{Ac})$, the overall dynamics as determined from τ_{tot} hardly vary with PIL composition and only moderately increase at high TFA concentrations. This is further supported by the normalized dielectric loss spectra (see SI, Figure 4.15), which confirm that the spectral shape does not vary with composition. As such, the data show that the characteristic timescales of the PILs' (and methanol) contributions to the spectra do not drastically change with PIL composition.

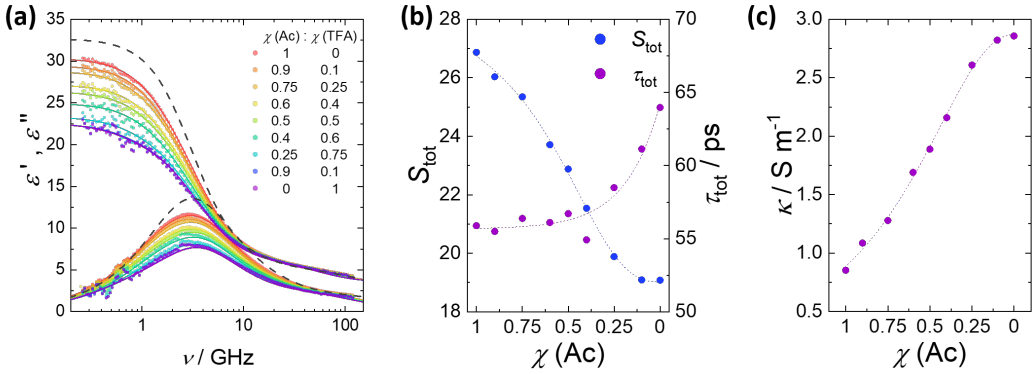

FIGURE 4.3: (a) Complex permittivity spectra of PIL mixtures (1 M) in MeOH at 298 K. Symbols represent experimental data, solid lines represent the fit. The grey dashed line represents the spectrum of MeOH, taken from ref.[221], scaled by a factor of 0.95. (b) Total dielectric amplitude S_{tot} and relaxation times τ_{tot} as a function of the composition of PIL mixture. Symbols represent parameters from the fit, dotted lines are a guide to the eye. (c) dc conductivity κ of PILs in MeOH as a function of the composition. Symbols represent parameters from the fit, dotted lines are a guide to the eye. *Reproduced from* [104].

The total dielectric amplitude S_{tot} markedly decreases with decreasing χ(Ac). Such decrease, commonly referred to as depolarization, can have different origins, including dilution of dipoles, solvation, and kinetic depolarization.[215, 216] For the present samples, kinetic depolarization — the coupling between (ionic) translational currents and (dipolar) rotational currents — can quantitatively describe the reduction of S_{tot} as a function of χ(Ac) (see SI, Figure 4.16). The fact that the experimental decrement agrees with the reduction due to the expected kinetic dielectric decrement for MeOH implies that the dynamic correlations of MeOH[223] are little affected by the PIL. This may be somewhat surprising as such correlations can be readily reduced by ions.[224] Most importantly, the experimental amplitude S_{tot} differs by a constant offset from the amplitude estimated for the contribution of methanol, corrected for kinetic depolarization (see SI, Figure 4.16). This constant offset — irrespective of χ(Ac) — demonstrates that contributions of the PIL to the total amplitude do not vary with PIL composition. As such the underlying dipolar species (e.g. ions, electroneutral species, ion-pairs, etc.) giving rise to the PILs' contributions do not vary with χ(Ac). Hence, and in contrast to our findings for solutions in DMF, we find no evidence for a transition from the presence of isolated molecules/ions to the formation of highly dipolar ion-pairs in MeOH.

Despite the negligible effect of the PIL mixtures on the dipolar dynamics of MeOH, the conductance of the PILs in MeOH (Figure 4.3(c)) exceeds the conductivity of the neat PIL mixtures (Figure 4.1(d)) and of the PIL solutions in DMF (Figure 4.2(c)). This elevated conductivity demonstrates the presence of mobile charge carriers in the solutions and the increase of κ with decreasing χ(Ac) (Figure 4.3(c)) suggests that the number density of these charge carriers increases upon substitution of AcOH by

TFA. This trend may be explained by an increasing formation of ionic species, e.g. increasing protonation of [Mim] upon addition of TFA but could also stem from MeOH forming together with [Mim] and TFA an extended hydrogen-bonded network allowing for a Grotthuss-type charge transport in solution. Conversely, in the mixtures with DMF such Grotthuss-type transport is not possible and the macroscopic conductivity is reduced (as compared to the neat PILs, Figure 4.1(d)) and vanishes for solutions of [MimH][AcO] (Figure 4.2(c)). Irrespective of the exact molecular-level conduction mechanism, comparison of the neat PIL mixtures and the PILs dissolved in DMF and MeOH demonstrates that the immediate environment of the PIL, like the nature of the solvent, can profoundly affect protonation equilibria and – possibly – proton transport within the PIL.

4.3.3 ^{15}N NMR Chemical Shifts

To further elucidate the contribution of ions and protons to charge transport in the PILs and their mixtures we further investigate the protonation state of the [Mim] base in these samples. As the protonatable site of [Mim] is located at the non-methylated nitrogen atom (referred to as N1; while N2 represents the methylated nitrogen atom), we determine the chemical environment of these nuclei as reflected by their ^{15}N chemical shift.

The corresponding ^{15}N chemical shifts of the neat PILs and their solutions in MeOD and DMF are shown in Figure 4.4. For all samples we find the chemical shift of N1 decreases with increasing TFA concentration. Conversely, N2 only slightly shifts down-field with decreasing χ(Ac). Given that these chemical shifts are the motionally averaged signals of all Mim molecular species ([Mim] and [MimH]$^+$), these results imply that the fraction of protonated [MimH]$^+$ increases[225] in all samples with decreasing χ(Ac), irrespective to the (solvent) environment. Yet, the absolute chemical shift values for N1 depend on the environment for $\chi(\mathrm{Ac}) = 1$, whereas the chemical environment of N2 is rather insensitive to the solvent. Upon decreasing χ(Ac), the chemical shifts of N1 for solutions in DMF and MeOD become more similar. The different values for the two solvents can be attributed to the hydrogen-bond donor/acceptor properties of both solvents:[226] While the aprotic solvent DMF is a H-bond acceptor and can stabilize [MimH]$^+$, but cannot donate a H-bond to [Mim], the protic solvent MeOD can accept and donate a H-bond from [MimH]$^+$ and to [Mim], respectively, which helps rationalizing the higher sensitivity of N1 to the solvent as compared to N2.

It is interesting to note, that for the neat ionic liquid the N1 signal for $\chi(\mathrm{Ac}) = 1$ cannot be resolved. Taking our dielectric results into account, which suggest that at $\chi(\mathrm{Ac}) = 1$ neutral species dominate in solution, the absence of the N1 signal in the spectra may point towards a very short dephasing times, which lead to peak broadening, such that the signals cannot be resolved. We speculate that hydrogen-bond formation of acetic acid to the N1 atom together with the high viscosities in the neat PILs restrict the rotational degrees of freedom of the [Mim]/[MimH]$^+$ molecules. Such reduced mobility can cause a reduction of the dephasing time.[227] Apparently, upon increasing TFA

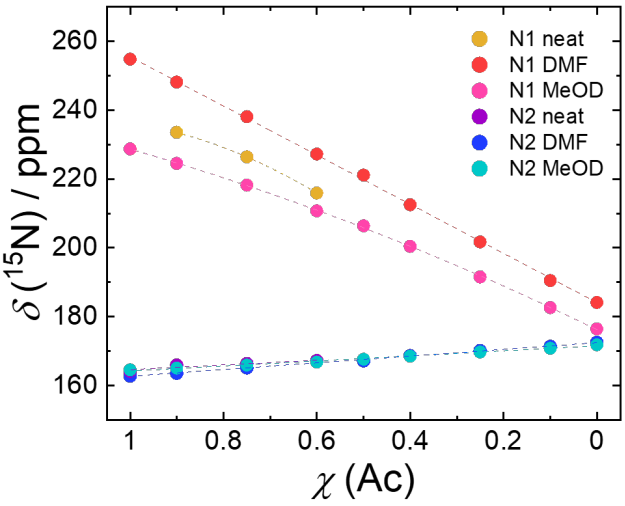

FIGURE 4.4: ^{1}5N chemical shifts as a function of χ(Ac) for the methylated nitrogen atom N2 and non-methylated nitrogen atom N1 for neat PILs and for PILs in solution. Symbols represent experimental data, dotted lines serve as a guide to the eye. *Reproduced from* [104].

content, the hydrogen-bonds between [Mim] and acetic acid break, and the dephasing time becomes longer, making the N1 signals to be readily detectable.
The ^{15}N chemical shift experiments demonstrate that, despite the vastly different polarization dynamics detected for the neat PILs and their solutions, the effect of the Brønsted acidity on the protonation state of the Mim base is rather similar in the neat PILs and the solutions in DMF and methanol. Therefore, the different charge transport dynamics cannot stem from vastly different degrees of protonation but must have different molecular origins.

4.3.4 Diffusion Ordered (NMR) Spectroscopy

To study the transport dynamics of the different molecular species in the PILs and their solutions we use pulse-field gradient spin echo (PFGSE) NMR experiments, often referred to as diffusion ordered spectroscopy (DOSY).[210, 228] In a DOSY experiment a series of spin echo spectra is recorded applying different pulsed field gradient strengths. The use of inhomogeneous magnetic fields can provide spatially resolved information. Based on the decay of the signals, the mobility (diffusivity) of the different molecular species with spectrally resolved NMR signals can be obtained. For samples containing TFA, ^{19}F depolarization was applied to reduce transient heteronuclear nuclear Overhauser contributions. The irradiation frequency, especially for the acidic proton, was adjusted to reduce off-resonant biases. For the present samples we discriminate the following four different species: [Mim]/[MimH]$^{+}$ via their aromatic proton signals, [AcOH]/[AcO]$^{-}$ via the motionally averaged CH_3 signal, [TFA]/[TFA]$^{-}$ via the CF_3 signals, and the acidic proton H^{+}, which can be separately detected via its proton NMR signal in the range between 13−17 ppm, depending on

the concentration of the acids. The PFGSE-determined diffusion coefficients, D, for these different species are shown in Figure 4.5(a) for the neat PILs and in Figure 4.5(b) for solutions of the PILs in DMF. Note, that we did not determine the diffusivities for solutions of the PILs in MeOD as the exchange of deuterons will interfere with the other ^{1}H exchange processes in the PILs and cause oscillatory results depending on the different exchange rates and the duration of the spatial encoding pulses as discussed elsewhere.[229]

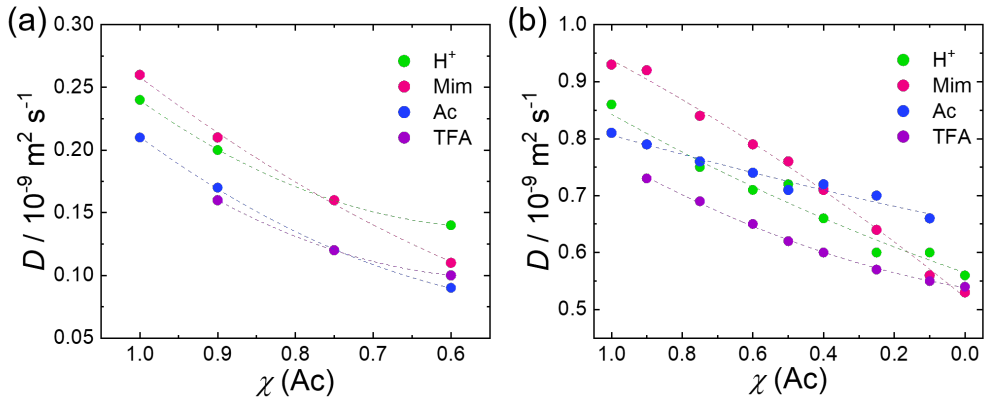

FIGURE 4.5: (a) Diffusion coefficients as a function of χ(Ac) of neat PILs measured at room temperature. Symbols represent experimental data, dotted lines serve as a guide to the eye. (b) Diffusion coefficients as a function of χ(Ac) of PILs in DMF measured at room temperature. Symbols represent experimental data, dotted lines serve as a guide to the eye. *Reproduced from* [104].

Overall, for both the neat PIL mixtures and the solutions in DMF, the diffusion coefficients decrease with decreasing χ(Ac), which can be explained by the increasing viscosity. For the neat PIL mixtures, the mobility of the acidic species ([AcO]$^-$/[AcOH] or [TFA]$^-$/[TFA]) is consistently lower than the mobility of [Mim]/[MimH]$^+$, which may be explained by the different molecular volumes or stronger interaction with the immediate environment. Additionally, self-aggregation[230] of the acids could result in a fraction of larger aggregates with a higher molecular volume (slower diffusivity). At $\chi(\mathrm{Ac}) = 1$, the mobility of the acidic proton lies between the mobility of [AcO]$^-$/[AcOH] and [Mim]/[MimH]$^+$, which one may expect for vehicular transport[231] of the proton with either [AcO]$^-$ or [Mim] as 'vehicle'. The fact that the proton mobility neither coincides with the mobility of the acid nor the base suggests that the proton is partially transferred between both molecular entities. Remarkably, with decreasing χ(Ac) the retardation of the proton diffusivity is less pronounced than the slow-down of the other molecular entities. In fact, at $\chi(\mathrm{Ac}) = 0.6$ the acidic proton shows the highest diffusivity amongst all species. Apparently, the acidic protons diffuse faster than the potentially available molecular vehicles, which points at a Grotthuss-type transport for this composition.

For solutions of the PILs in DMF (Figure 4.5(b)), the diffusion coefficients are generally higher than in the neat PILs due to the reduced viscosities.[232,

233] At $\chi(\mathrm{Ac}) = 1$ the trend in mobilities is comparable to the neat PIL: $D([\mathrm{AcO}]^-/[\mathrm{AcOH}]) < D(\mathrm{H}^+) < D([\mathrm{Mim}]/[\mathrm{MimH}]^+)$. This observation implies that exclusive formation of [MimH][AcO] aggregates can be ruled out at $\chi(\mathrm{Ac}) = 1$, as in that case the diffusivities of all species would coincide. Conversely, upon decreasing $\chi(\mathrm{Ac})$ the diffusivities of $[\mathrm{Mim}]/[\mathrm{MimH}]^+$, H^+, and TFA converge to virtually the same value at $\chi(\mathrm{Ac}) = 0$, consistent with [MimH][TFA] aggregates (cf. ion-pair formation discussed above) dominating at this composition. The significantly higher diffusivity of $[\mathrm{AcO}]^-/[\mathrm{AcOH}]$ at low $\chi(\mathrm{Ac})$ implies that acetic acid is not entirely bound in PIL aggregates.

Together, the diffusivities suggest that with increasing TFA content, the mobilities of molecular species become more correlated in the neat PILs, while the proton motion somewhat decouples. For solutions in DMF, only the motion of $[\mathrm{TFA}]/[\mathrm{TFA}]^-$, H^+, and $[\mathrm{Mim}]/[\mathrm{MimH}]^+$ become highly correlated (in line with ion-pair formation), while the mobility of $[\mathrm{AcO}]^-/[\mathrm{AcOH}]$ seems to decouple from these transport dynamics.

4.3.5 Temperature Dependent Proton Linewidths

Analysis of the DOSY spectra revealed indications for a Grotthuss–type of proton conduction in the PILs. To further support this observation, we analyze thermal effects on the chemical shift and the linewidth of the NMR signal of the acidic proton at 13−17 ppm in more detail. Here, we focus on PILs in DMF as for neat PILs with $\chi(\mathrm{Ac}) < 0.6$, the viscosity increases in the accessible temperature range to such an extent that the chemical shift resolution in the NMR measurements is lost. For the temperature dependent studies, we focus on the two neat PILs ([MimH][AcO] ($\chi(\mathrm{Ac}) = 1$) and [MimH][TFA] ($\chi(\mathrm{Ac}) = 0$)) and an equimolar PIL mixture.

Figure 4.6(a) shows the ^{1}H chemical shift values of the acidic proton as a function of the inverse temperature for the three investigated PIL mixtures. For $\chi(\mathrm{Ac}) = 0$ the chemical shift is rather insensitive to temperature variations, indicating that the average electronic environment of H^+ is not altered. For $\chi(\mathrm{Ac}) = 0.5$ and $\chi(\mathrm{Ac}) = 1$, the chemical shift values decrease with increasing temperature. This decrease is most pronounced for $\chi(\mathrm{Ac}) = 1$, where the chemical shift values vary by about 2 ppm between $T = 263$ K and $T = 400$ K. This change in chemical shift is indicative of a change in the electronic surrounding of the acidic proton and, as such, of altered chemical equilibria in the samples.

Considering that for $\chi(\mathrm{Ac}) = 1$, and to a lesser extent for $\chi(\mathrm{Ac}) = 0.5$, mostly electroneutral species are present in solution (as evidenced by the negligible conductivity, Figure 4.2(c)) the variation of the chemical environment suggests temperature induced variations of the hydrogen-bonded structure: hydrogen-bonds of [AcOH] to [Mim], DMF, or other [AcOH] molecules (AcOH selfdimers-dimers) can be broken and result in a redistribution of the H-bonded species. These altered equilibria in turn result in a marked variation of the detected chemical environment.

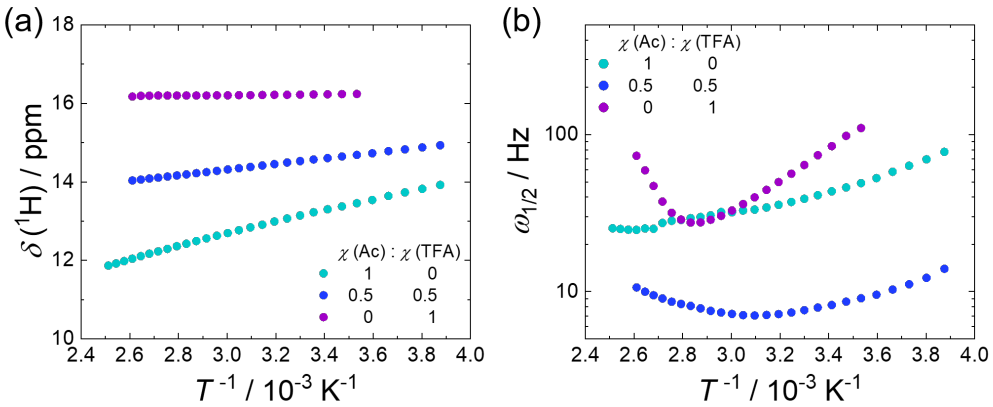

FIGURE 4.6: (a) Temperature dependence of the ^{1}H chemical shift and (b) linewidth of the acidic proton for the two limiting cases χ(Ac)=1 and χ(Ac)=0 and the equimolar PIL mixture in DMF. *Reproduced from* [104].

The temperature dependent linewidths of these signals (Figure 4.6(b)) provide evidence for chemical exchange dynamics on a millisecond timescale in the presence of TFA: At $\chi(\mathrm{Ac}) = 1$ the linewidth of the acidic proton becomes continuously narrower with increasing temperature. This behaviour is common to systems with a temperature-independent chemical environment, for which enhanced thermal fluctuations lead to enhanced averaging of local heterogeneities and, as such, longer dephasing times.[227] In turn, for $\chi(\mathrm{Ac}) = 0.5$ and $\chi(\mathrm{Ac}) = 0$ the thermally induced narrowing is only observed at reduced temperatures. At elevated temperatures the signals become broader with increasing temperature resulting in a marked minimum of the linewidth at $T \approx 350\,\mathrm{K}$ for $\chi(\mathrm{Ac}) = 0$ and at $T \approx 320\,\mathrm{K}$ for $\chi(\mathrm{Ac}) = 0.5$. Such thermally induced broadening can be explained by thermal shifts of chemical equilibria resulting in dynamic exchange processes. While the chemical shift values indicate variations of the chemical environment of the acidic proton with temperature for $\chi(\mathrm{Ac}) = 1$ and, to a lesser extent, for $\chi(\mathrm{Ac}) = 0.5$, the chemical shift of the acidic proton is constant for $\chi(\mathrm{Ac}) = 0$.

Yet, we observe an increasing linewidth at high temperatures for $\chi(\mathrm{Ac}) = 0$. This clearly points to the onset of a dynamic process, which leaves the chemical environment unchanged. This suggests, together with the high degree of protonation of the Mim molecules for $\chi(\mathrm{Ac}) = 0$ deduced from the ^{15}N chemical shift data, that the dynamic process at high temperature is most likely related to proton hopping between $[\mathrm{MimH}]^{+}$ and [Mim] species. For $\chi(\mathrm{Ac}) = 0.5$ an increase in linewidth can also be observed at elevated temperatures but to a lesser extent, as compared to $\chi(\mathrm{Ac}) = 0$. This observation indicates that such proton dynamics might also occur at lower TFA concentrations. Complete analysis of the thermal activation of this dynamic process, however, is beyond the scope of this study and the examples given here only serve to support the results presented above.

4.4 Conclusion

In the present study we investigate molecular-level dynamics in Mim-based PILs using DR and NMR spectroscopy. For [MimH][AcO] we find the total dielectric amplitude, S_{tot}, to exceed the amplitude that would be expected for uncorrelated reorientation of molecular-level dipoles, with the molecular dipole moments estimated using DFT calculations. This enhanced dipolar relaxation amplitude indicates the presence of dynamic dipolar correlations, typical for the dipolar response of hydrogen-bonded liquids. The finite conductivity, κ, evidences the existence of mobile ions, although the ^{15}N-NMR chemical shifts demonstrate a moderate degree of protonation of the [Mim] base. Diffusion ordered H-NMR spectra show that the diffusion coefficients of the acidic proton at 13 - 17 ppm is somewhat higher than the diffusion coefficient of the acetic acid species, yet, lower than the mobilities of the species associated with the [Mim] base. These mobilities are consistent with a partial proton transfer from AcOH to [Mim], and suggest charge transport to be dominated by vehicular dynamics. Yet, also self-aggregation of AcOH and the formation of acetic acid chains – pertinent to Grotthuss transport – could result in a reduced mobility of the acid. Upon substitution of AcOH by TFA, we find an increasing fraction of $[\mathrm{MimH}]^+$, as apparent from the marked decrease of the ^{15}N chemical shift of the N1 nitrogen atom and an increase of the sample conductivity – despite the increase in the viscosity of the PIL. Simultaneously, the dipolar amplitude S_{tot} decreases, which implies that the increasing presence of ionic species partly reduces dynamic dipolar correlations. Diffusion ordered H-NMR spectra indicate that with decreasing $\chi(\mathrm{Ac})$ the diffusivities of the acidic protons decrease less, as compared to the other molecular species, and at $\chi(\mathrm{Ac}) = 0.6$ the diffusion coefficient of the acidic proton exceeds those of the molecular species ($D(\mathrm{H}^+) > D([\mathrm{Mim}]/[\mathrm{MimH}]^+) > D([\mathrm{TFA}]/[\mathrm{TFA}]^-) > D([\mathrm{AcOH}]/[\mathrm{AcO}]^-)$). This enhanced proton mobility suggests a Grotthuss-type mechanism contributing to charge transport in the PIL.

Our findings further show that the nature of the solvent in PIL solutions critically affects chemical equilibria: [MimH][AcO] forms in DMF nearly exclusively electroneutral molecular species/aggregates, which virtually supresses the macroscopic conductivity, consistent with a low degree of protonated [Mim] base as deduced from the ^{15}N chemical shifts. Nevertheless, the H-NMR determined mobility of the acidic proton is somewhat higher than the mobility of $[\mathrm{AcOH}]/[\mathrm{AcO}]^-$ species, yet lower than the mobility of $[\mathrm{Mim}]/[\mathrm{MimH}]^+$, which again points at partial deprotonation of AcOH or self-aggregation of AcOH. Upon increasing TFA content, the conductivity increases, evidencing the formation of mobile ($[\mathrm{MimH}]^+$, $[\mathrm{TFA}]^-$) ions. Yet, the emergence of the PIL associated lower-frequency dielectric relaxation suggests that a large fraction of the ions is bound in [MimH][TFA] ion-pairs. Temperature dependent linewidths of the ^{1}H-NMR signal of the acidic proton demonstrate that these protons can chemically exchange on the NMR timescale. The presence of ion-pairs and free ions is consistent with the enhanced degree of protonation of [Mim], as detected via the ^{15}N-chemical

shifts. In fact, these chemical shifts exhibit similar trends for the neat PILs, solutions in DMF, and solutions in MeOH, which suggests similar trends in protonation upon substituting AcOH by TFA. Yet, in MeOH the PIL solutes do not form highly dipolar aggregates and the conductivity of all PIL solutions in MeOH exceeds those of the neat PILs and PIL solutions in DMF. This high charge mobility in MeOH demonstrates efficient solvation of the free ions and is consistent with MeOH and the PIL forming an extended hydrogen-bonded network, which may also allow for a Grotthuss-type transport of protons.

In general, our results show that protonation equilibria and dynamics in these PILs are highly sensitive to the immediate environment. In particular, altering proton acceptors and proton donors, e.g. by substitution of AcOH by TFA, offers opportunities to engineer these equilibria and dynamics such that charge transport and the electrochemical performance can be optimized.

4.5 Supplementary Information

Figures in this section have been reproduced from the SI of [104].

NMR Spectroscopy

To monitor the synthesis of 1-methylimidazolium acetate [MimH][AcO] and 1-methylimidazolium trifluoroacetate [MimH][TFA], ^{1}H- and ^{13}C NMR spectra were recorded. The ^{1}H-NMR signals for [MimH][AcO] in Figure 4.7 can be assigned as follows: δ/ppm: 15.31 (s, 1H, -COOH), 7.52 (s, 1H, C2-H), 6.92 (s, 1H, C4-H), 6.77 (s, 1H, C5-H), 3.56 (s, 3H, N-CH3), 1.90 (s, 3H, CH3COOH), with the corresponding labels of the nuclei in Figure 4.8. The 1:1 ratio of the integrated methyl signals at 1.90 ppm and 3.55 ppm confirm the equimolar concentration of acid and base in the PIL. The ^{13}C-NMR chemical shifts (Figure 4.9) were assigned to: δ/ppm: 175.20 (-COOH), 137.44 (C2), 127.67 (C4), 120.23 (C5), 33.67 (N-C), 21.53 (CH3COOH).

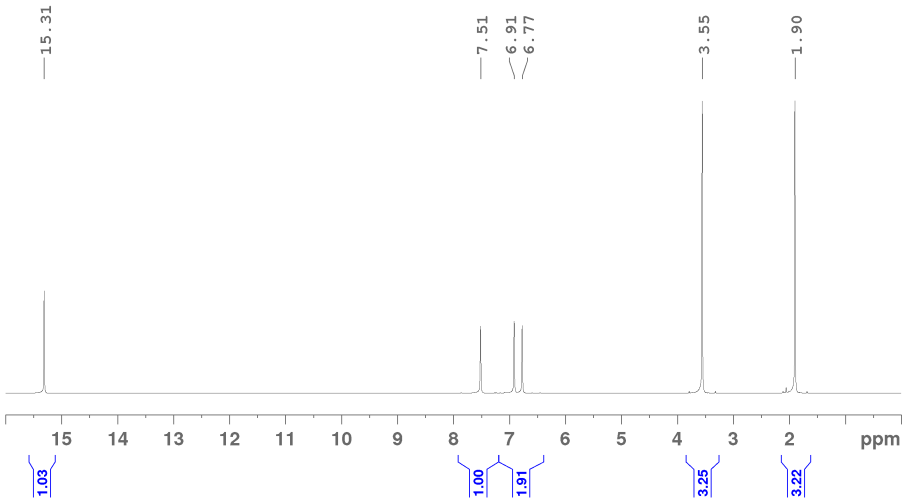

FIGURE 4.7: ^{1}H-NMR spectrum of [MimH][AcO] in $CDCl_3$.

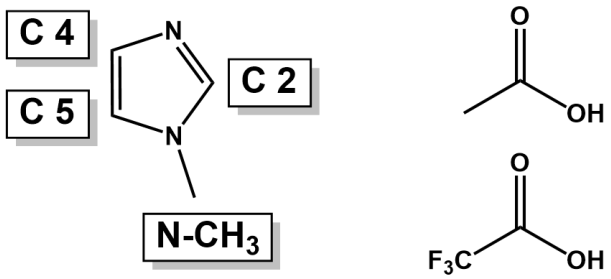

FIGURE 4.8: Chemical structure of the individual components 1-methylimidazole, acetic acid, and trifluoroacetic acid with corresponding labels of the carbon nuclei of interest.

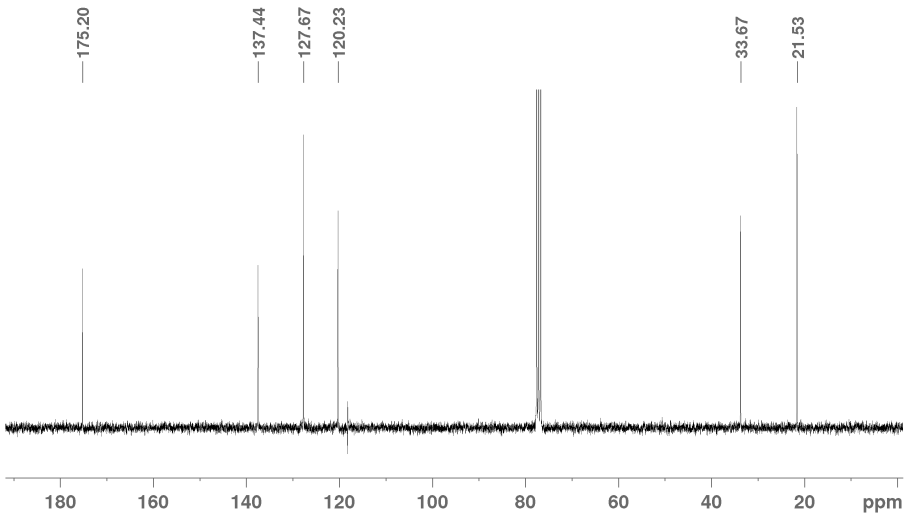

FIGURE 4.9: ^{13}C-NMR spectrum of [MimH][AcO] in $CDCl_3$.

The ^{1}H-NMR signals of [MimH][TFA] (Figure 4.10) were assigned to: δ/ppm: 8.89 (s, 1H, C2-H), 7.30 (s, 1H, C4-H), 7.12 (s, 1H, C5-H), 3.88 (s, 3H, N-CH3). The signal of the acidic proton was not detected, presumably due to fast exchange beyond the timescale of the experiment and/or marked line broadening. The ^{13}C-NMR chemical shifts (Figure 4.11) were assigned to: δ/ppm: 162.16 (-COO-), 135.92 (C2), 121.90 (C4), 120.92 (C5), 116.73 (-CF3), 35.58 (N-C). As fluorine ($I = 1/2$) is a NMR active nucleus, the carboxyl-C (162.16 ppm) and the $-CF_3$ (116.73 ppm) carbon signal of trifluoroacetate split into quartets.

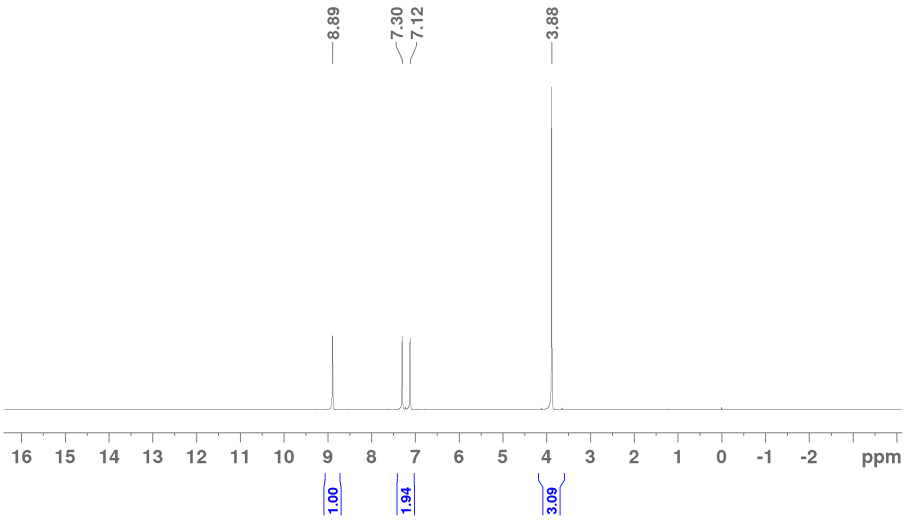

FIGURE 4.10: ^{1}H-NMR spectrum of [MimH][TFA] in $CDCl_3$

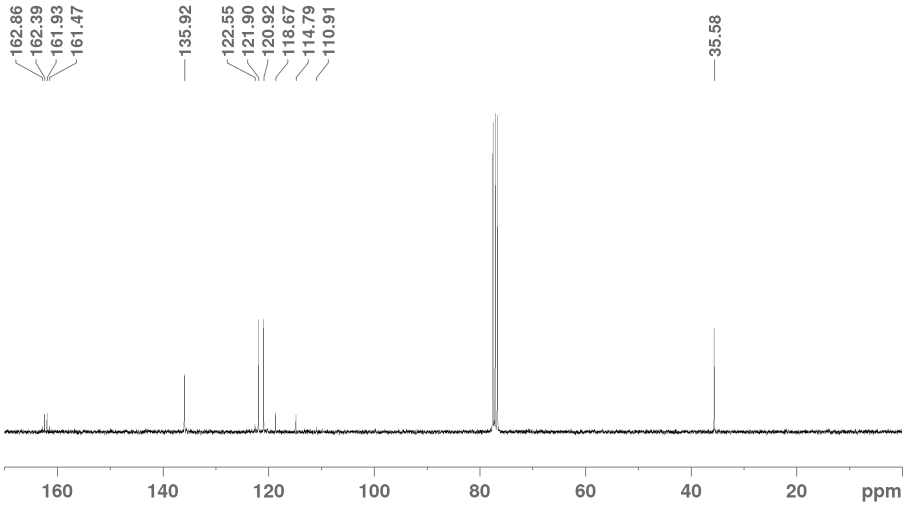

FIGURE 4.11: ^{13}H-NMR spectrum of [MimH][TFA] in $CDCl_3$

DFT Calculations

To illustrate the effect of the center of charge on the calculated dipole moment, we compare the dipole moments based on the full electron density with the center of mass as the center of charge, $\mu_{\mathrm{eff,DFT}}^{\mathrm{full,COM}}$, the dipole moment based on the CHELPG partial charges with the center of mass as the center of charge, $\mu_{\mathrm{eff,DFT}}^{\mathrm{part,COM}}$, and the dipole moment based on the CHELPG partial charges with the centroid as the center of charge, $\mu_{\mathrm{eff,DFT}}^{\mathrm{part,CHS}}$, in Table 4.1. In Figure 4.1 of the main text the values $\mu_{\mathrm{eff,DFT}}^{\mathrm{part,CHS}}$ are displayed.

TABLE 4.1: Calculated dipole moments relative to the center of hydrodynamic stress (CHS), the center of mass (COM) and based on partial charged (part) and full electron density (full) based on DFT calculations for neutral and ionic molecular species, H-bonded [Mim][AcOH] dimer, and [MimH][TFA] ion pair.

	$\mu_{\mathrm{eff,DFT}}^{\mathrm{part,CHS}}$	$\mu_{\mathrm{eff,DFT}}^{\mathrm{part,COM}}$	$\mu_{\mathrm{eff,DFT}}^{\mathrm{full,COM}}$
AcOH	2.34	2.34	2.33
AcO^-	8.39	4.66	4.69
Mim	5.38	5.38	5.50
$MimH^+$	2.69	1.90	1.92
TFA	3.06	3.06	3.02
TFA^-	5.23	5.72	5.81
[Mim][AcOH]	6.42	6.42	6.38
[MimH][TFA]	17.29	17.29	17.14

To illustrate the effect of the continuum solvent on the calculated dipole moments of acetic acid, we compare DFT calculations with different dielectric constants (dichloromethane ($\varepsilon = 8.8$), methanol ($\varepsilon = 32.7$) and ethanol ($\varepsilon = 24.5$)). The impact of the continuum medium on the calculated dipole moments is minor, indicating that the exact choice of the dielectric constant of the medium has minimal influence on the obtained dipole moment: $\mu_{\mathrm{eff,DFT}}^{\mathrm{part,COM}}$ (AcOH, $\varepsilon = 8.8$) = 2.34 D; $\mu_{\mathrm{eff,DFT}}^{\mathrm{part,COM}}$ (AcOH, $\varepsilon = 24.5$) = 2.39 D; $\mu_{\mathrm{eff,DFT}}^{\mathrm{part,COM}}$ (AcOH, $\varepsilon = 32.7$) = 2.40 D.

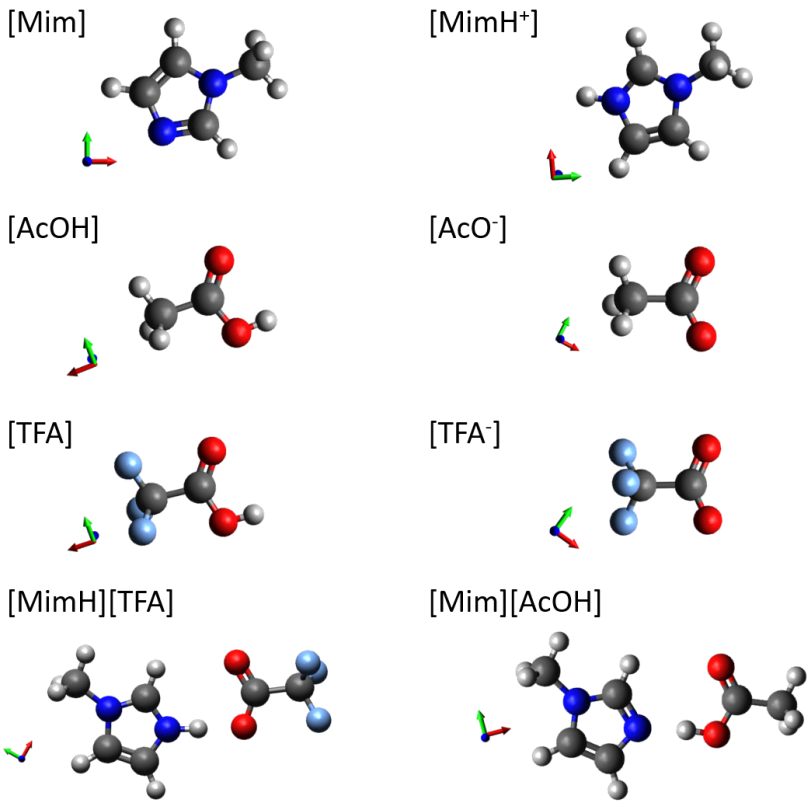

FIGURE 4.12: Optimized molecular geometries based on DFT calculations.

Dielectric Relaxation Spectroscopy

Neat PIL Mixtures

To confirm the observed trends in the dielectric spectra of the neat PILs at ambient temperature (Figure 4.1, main text) also hold over a wider composition range, we measured the spectra of the neat [MimH][AcO]/[MimH][TFA] mixtures at 333 K (Figure 4.13). As discussed in the main text, the spectra appear broad and featureless. The spectrum of [MimH][AcO] is dominated by a relaxation centered at ~1 GHz. Upon increasing χ(TFA) the amplitude of this relaxation decreases. Conversely, the spectral range > 10 GHz is rather insensitive to increasing χ(TFA). The maximum of the loss peak shifts to lower frequencies with increasing χ(TFA). These trends parallel the trends at 298 K in Figure 4.1.

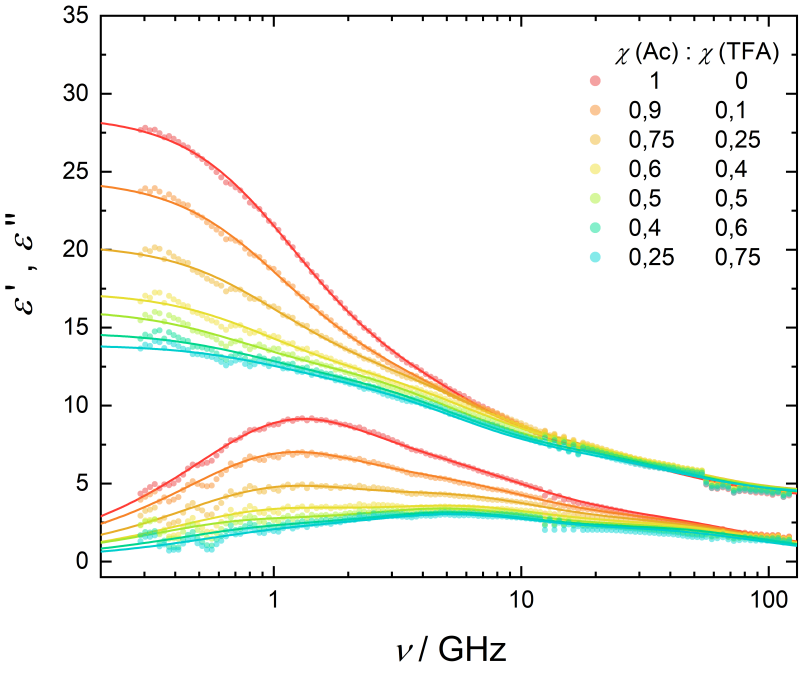

FIGURE 4.13: Complex permittivity spectra of neat PIL mixtures at 333 K. Symbols show experimental data, solid lines represent fits of Equation 4.2 to the data. Note the last term of Equation 4.2 has been subtracted for visual clarity.

The spectra shown in Figure 4.1 of the main text were modelled using Equation 4.2. The thus obtained parameters, ε_∞ (limiting permittivity at high frequencies), relaxation amplitudes S_i, relaxation times τ_i, and conductivity κ are listed in Table 4.2.

TABLE 4.2: Fit parameters according to Equation 4.2 for the dielectric spectra of [MimH][AcO]/[MimH][TFA] mixtures at 298 K.

χ(Ac)	ε_∞	S_1	S_2	S_3	τ_1 / ps	τ_2 / ps	τ_3 / ps	κ / S m^{-1}
1	4.3	19.5	5.3	2.7	317	43	6.4	0.46
0.9	4.5	14.9	5.0	3.0	352	45	6.6	0.75
0.75	4.6	9.4	4.8	3.0	391	46	6.5	0.96
0.6	4.6	6.3	4.7	3.2	428	50	6.7	0.99

In the main text we derive dipole moments based on the total relaxation strength, S_{tot}, assuming only (dipolar) rotational contributions to the spectra (Figure 4.1c). As translational contributions to the dielectric spectra often contribute at higher frequencies[66, 208, 211], we show in Figure 4.14 the according analysis using only the relaxation strength of the lowest frequency relaxations (S_1). Despite reduced dipole moments $\mu_{\text{eff,tot}}$, the trend of decreasing $\mu_{\text{eff,tot}}$ with decreasing χ(Ac) as also observed for this analysis.

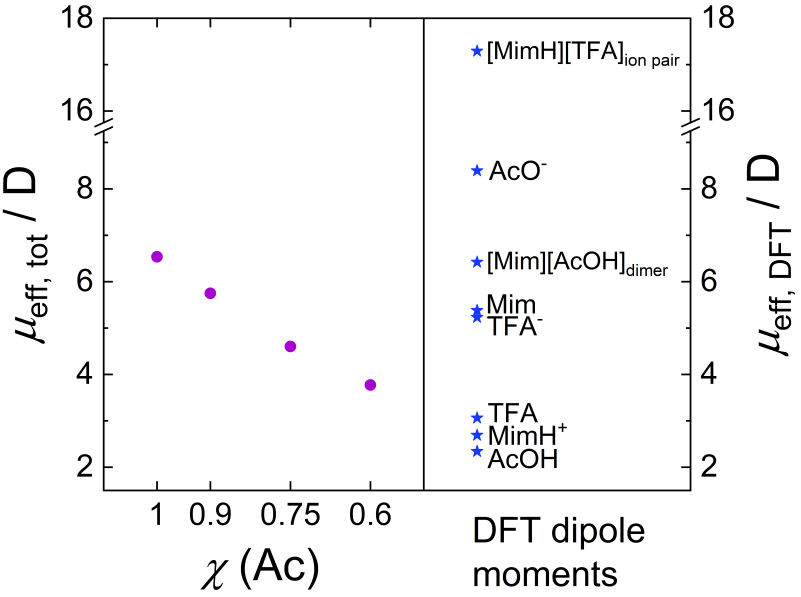

FIGURE 4.14: Left: total effective dipole moment $\mu_{\mathrm{eff,tot}}$, obtained from experimental amplitude S_1 of the low frequency relaxation as a function of χ(Ac). Right: Molecular dipole moments based on DFT calculations.

PILs in DMF

The spectra in Figure 4.2 of the main text were modelled using Equation 4.4 (main text). The obtained parameters, ε_∞, relaxation amplitudes S_{PIL} and S_{DMF}, relaxation times τ_{PIL} and τ_{DMF}, and conductivity κ are listed in Table 4.3.

TABLE 4.3: Fit parameters according to Equation 4.4 for the dielectric spectra of [MimH][AcO]/[MimH][TFA] mixtures in DMF at 298 K.

χ(Ac)	ε_∞	S_{PIL}	S_{DMF}	τ_{PIL} / ps	τ_{DMF} / ps	κ / S m^{-1}
1	4.5	4.7	27.2	65	11	0.04
0.9	4.6	5.2	27.1	85	11	0.29
0.75	4.7	6.4	26.8	99	11	0.49
0.6	4.7	7.9	26.4	108	12	0.63
0.5	4.7	8.6	26.1	110	12	0.69
0.4	4.8	10.1	25.7	114	12	0.77
0.25	4.8	11.7	25.2	118	12	0.83
0.1	4.8	12.6	25.0	121	12	0.84
0	4.8	12.3	25.6	121	12	0.79

PILs in MeOH

To visualize the insensitivity of the peak shape of the dielectric spectra to the composition of the [MimH][AcO]/[MimH][TFA] mixtures in methanol, we show the loss spectra displayed in Figure 4.3a normalized to the peak maxima in Figure 4.15. With decreasing χ(Ac) the spectral shape is virtually insensitive to the PIL composition, the peak only slightly shifts to higher frequencies. From the similar spectral shape, we conclude, that the change in PIL composition hardly affects the distribution of relaxation times, which implies that also the underlying molecular level dipoles (e.g. methanol, ions, ion-pairs) remain very similar over the entire composition range.

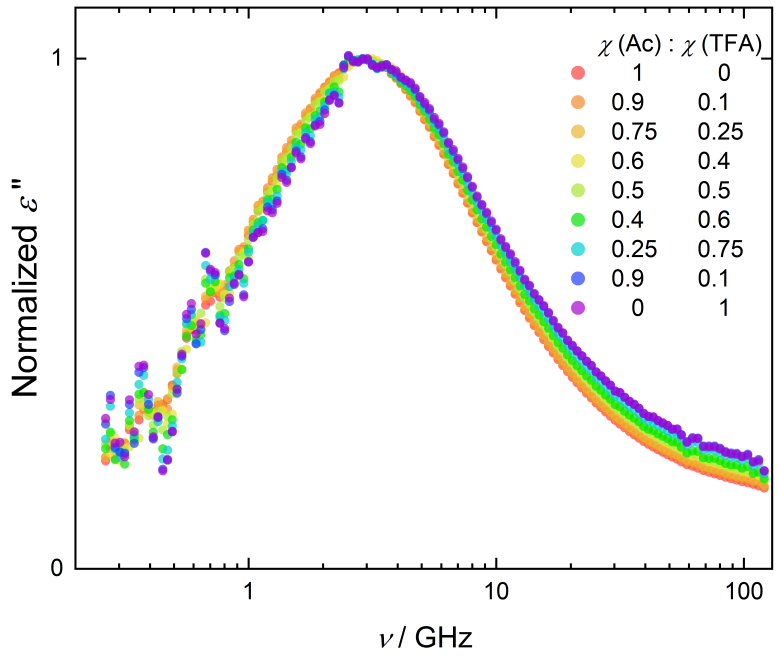

FIGURE 4.15: Normalized dielectric loss spectra of [MimH][AcO]/[MimH][TFA] mixtures in MeOH at 298 K.

The spectra in Figure 4.3 were modelled using Equation 4.2. The obtained parameters, ε_∞, relaxation amplitudes S_i, relaxation times τ_i, and conductivity κ are listed in Table 4.4.

TABLE 4.4: Fit parameters according to Equation 4.2 for the dielectric spectra of [MimH][AcO]/[MimH][TFA] mixtures in MeOH at 298 K.

χ(Ac)	ε_∞	S_1	S_2	S_3	τ_1 / ps	τ_2 / ps	τ_3 / ps	κ / S m^{-1}
1	3.5	7.5	17.0	2.4	101	43.3	2.4	0.9
0.9	3.4	9.7	14.0	2.4	91	40.3	2.3	1.1
0.75	3.4	6.7	16.2	2.4	108	43.3	2.5	1.3
0.6	3.5	6.1	15.1	2.4	110	42.7	2.5	1.7
0.5	3.5	4.9	15.5	2.5	125	43.7	2.6	1.9
0.4	3.4	4.7	14.4	2.5	120	42.9	2.7	2.2
0.25	3.4	3.0	14.4	2.5	172	44.6	2.9	2.6
0.1	3.5	2.6	14.0	2.5	207	44.5	2.9	2.8
0	3.5	2.6	14.0	2.5	227	44.4	2.9	2.9

As discussed previously, the total relaxation strength for the PIL mixtures in MeOH markedly varies with PIL composition. Given the increasing conductivity of the samples with increasing χ(TFA), kinetic depolarization is a plausible explanation for the observed dielectric decrement. To test this hypothesis, we compare the observed relaxation strengths to what would be expected for the contribution of methanol, reduced by kinetic depolarization. Therefore, we estimate the relaxation strength of methanol based on the concentration of methanol in the samples, $S_{\text{Cavell}}^{\text{MeOH}}$:[114]

$$S_{\text{Cavell}}^{\text{MeOH}} = \frac{\varepsilon_\text{s}}{\varepsilon_\text{s} + (1-\varepsilon_\text{s})/3} \frac{N_\text{A} c_{\text{MeOH}}}{3 k_\text{B} T \varepsilon_0} \mu_{\text{eff,MeOH}}^2 \tag{4.5}$$

With the static permittivity $\varepsilon_\text{s} = \varepsilon_\infty + \sum_{j=1}^{3} S_j$, the Avogadro constant N_A, the Boltzmann constant k_B, and the thermodynamic temperature T. c_{MeOH} is the concentration of MeOH, as determined from the mass of MeOH added to the volumetric flasks. We measured a dielectric spectrum of neat MeOH to calculate the effective dipole moment of MeOH $\mu_{\text{eff,MeOH}}$ via Equation 4.5 (with $S_{\text{MeOH}} = 29.87$, $\varepsilon_\text{s} = 32.7$ and $c_{\text{MeOH}} = 24.66$ M). The effective dipole moment $\mu_{\text{eff,MeOH}}$ is assumed to be independent of PIL addition/composition. Kinetic depolarization $S_{\text{KD}}^{\text{MeOH}}$ can be estimated according to the Hubbard-Onsager model.[234]

$$S_{\text{KD}}^{\text{MeOH}} = f \frac{S_{\text{Cavell}}^{\text{MeOH}}}{\varepsilon_\text{s}} \frac{\tau_2}{\varepsilon_0} \kappa \tag{4.6}$$

Here, we assume slip boundary conditions for the friction coefficient $f = 2/3$. Accordingly, we calculate the relaxation strength that would be expected based on the contribution of kinetically depolarized methanol, S_{calc}:

$$S_{\text{calc}} = S_{\text{Cavell}}^{\text{MeOH}} - S_{\text{KD}}^{\text{MeOH}} \tag{4.7}$$

The thus determined values of S_{calc} parallel the experimental relaxation amplitudes

S_{tot} (Figure 4.16). The offset by ~2.5 can be explained by dipolar PIL components contributing to the experimental spectra. The constant offset over the entire composition range again indicates that the underlying molecular level dipoles (e.g. dipolar ions, rather than ion-pairs) are similar at all PIL compositions.

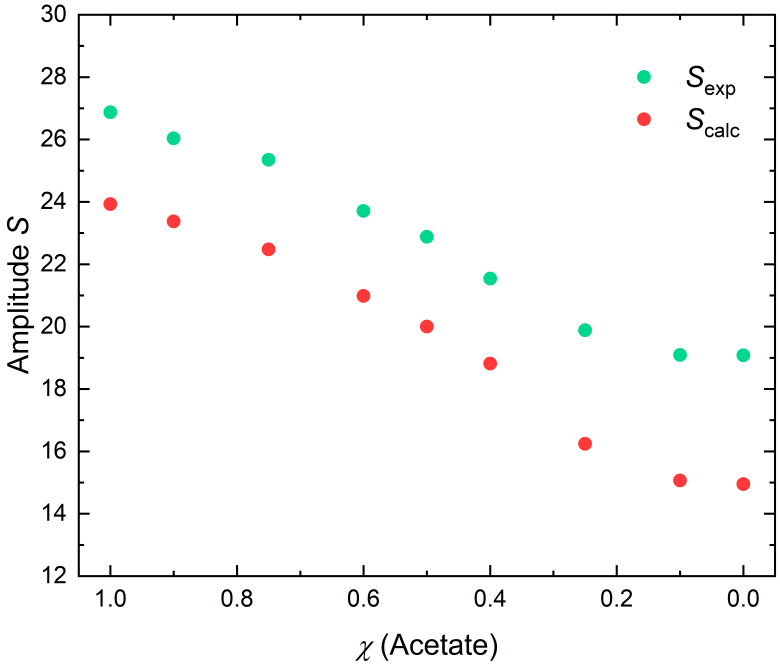

FIGURE 4.16: Experimental relaxation amplitude S_{tot} and calculated relaxation amplitude of the kinetically depolarized methanol relaxation S_{calc} according to Equation 4.7.

Chapter 5

Comparative Analysis of Dielectric Spectra in Protic Ionic Liquids: Experimental Findings and Computational Molecular Decomposition

Reproduced from [78] *with minor changes.*

5.1 Abstract

Using a combination of experimental measurements and polarizable molecular dynamics simulations, we investigate the dielectric spectra of the protic ionic liquid 1-methylimidazolium acetate, shedding light on their dynamic behavior and intermolecular interactions when adding 1-methylimidazolium trifluoroacetate to increase the fraction of a strong Brønsted acid in the system. The comparison between experimental and computational results provides valuable insights into the accuracy of the simulation models (with and without explicit proton transfer) and the ability to capture the intricate dynamical features of the protic ionic liquid. The investigation revealed complete deprotonation of trifluoroacetate, inducing a shift in the ionic liquid towards a more pronounced ionic state. The computational decomposition of the dielectric spectra into molecular translational and rotational contributions unveiled a reduction in the dielectric constant. This reduction was primarily ascribed to a decrease of translational contributions. Additionally, a strong correlation of the mutual orientation of molecules was found. The observed rise in conductivity upon the addition of 1-methylimidazolium trifluoroacetate to the system was attributed to an increase in proton transport.

5.2 Introduction

Ionic liquids (ILs) have garnered significant attention in recent decades due to their unique properties and diverse range of applications.[9] These liquid salts typically consist of ionic species with melting points below 100 °C and offer a wide range of properties, including a broad liquid range, excellent solvation properties,[29] and high electrical conductivity.[41] Due to the manifold of potential cation/anion combinations to tailor these properties, multifaceted approaches are desirable that integrate existing experimental[29, 41, 98, 212, 235] and computational investigations[177, 236] to elucidate the intermolecular interactions, structure, and dynamics of ILs.
ILs can be categorized into aprotic ILs and protic ILs (PILs). The latter are formed by a reversible proton exchange reaction between a Brønsted acid and base. The presence of proton donors and acceptors in PILs results in the formation of extended hydrogen-bonded networks in PILs[57, 58], which facilitates reversible proton transfer and enhances conductivity and often reduces their viscosity. Protonation equilibria and hydrogen-bond strengths in PILs are intimately connected to the Brønsted acidity of the constituting acids and bases. As such, variation of the acidity of the ionic liquids' ions offers additional degrees of freedom to tune the properties of PILs. Yet, altered acidity also affects ionicity and Coulombic interactions, which in turn changes the dynamics and transport properties of PILs. As such, the factors governing the macroscopic properties of PILs[63], including polarity[237], ionicity[67], thermal stability and viscosity[238], or transport properties[239] depend on the interplay between these factors, yet the exact details have remained elusive.

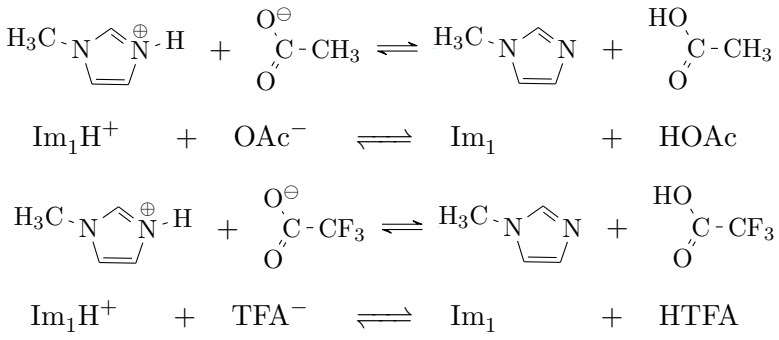

FIGURE 5.1: Equilibrium between the IL 1-methylimidazolium acetate [Im_1H]OAc and its neutral analogues 1-methylimidazole Im_1 and acetic acid HOAc and the fluorinated species. *Reproduced from* [78].

Amongst the plethora of protic ionic liquids, for which physico-chemical and transport properties have been elucidated[63, 240, 241], most comprehensive experimental and computational information is available for PILs based on 1-methylimidazole.[65, 68, 71–73, 104, 242] Here, we systematically study the effect of the acidity of the Brønsted acid on 1-methylimidazolium-based ionic liquids. Starting from 1-methylimidazolium acetate [Im_1H]OAc we gradually add 1-methylimidazolium trifluoroacetate [Im_1H]TFA,

with the acidity of trifluoroacetic acid (HTFA) being ~4 pK_a units lower than that of acetic acid (HOAc). The two main protonation equilibria for the two PILs are shown in Fig. 5.1. The impact of the fluorinated acid will be explored, in particular as reflected in the polarization dynamics and ion conductivity as measured with dielectric relaxation spectroscopy. For neat [Im_1H]OAc, Raman, and potentiometric studies have indicated that the PIL is predominantly composed of neutral species (e.g. HOAc, Im_1) due to the relatively low acidity of acetic acid.[61, 65] This notion is supported by DFT calculations with which complexes of neutral species were energetically favorable over ion pairs.[61] In contrast, ^{1}H-NMR experiments have indicated more than 90 % protonation of 1-methylimidazole [Im_1].[67, 68] However, with the addition of polar solvents, the ionicity was suggested to decrease significantly.[68] As such, these earlier studies indicate that the protonation equilibrium in [Im_1H]OAc is highly sensitive to various factors. In fact, fluctuations in protonation states may be related to the relatively high conductivity of [Im_1H]OAc[57, 61, 71, 243] and comparison of activation energies for translational and rotational diffusion has suggested a Grotthuss-like charge transport contributing to the conductivity of [Im_1H]OAc.[72] Indeed, ab initio molecular dynamics simulations have evidenced a variety of proton transfer channels in [Im_1H]OAc.[71, 244] In contrast to the findings for [Im_1H]OAc, the protonation equilibrium in [Im_1H]TFA appears to be shifted to fully protonated species resulting in a purely vehicular charge transport for neat [Im_1 H]TFA[73], while in mixtures a Grotthuss-like transport is suggested to be enhanced, relative to neat [Im_1H]OAc.[104] Here, we aim to understand the influence of substitution of HOAc by HTFA on the dynamics and transport in [Im_1] based PILs, pertinent to their application in batteries and fuel cells. We focus on the dynamics as encoded in the dielectric relaxation spectra, as these are sensitive to both translational and rotational dynamics.[98] By employing a combination of broadband dielectric spectroscopy experiments and polarizable molecular dynamics simulations,[66, 243] we explore the effect of substitution of HOAc by HTFA in 1-methylimidazolium-based PILs. Thus, we contribute to a generic understanding of the role of acidity in PILs for intermolecular interactions, structure, and dynamics, ultimately leading to enhanced understanding of its electrical behavior. Such insights have broader implications for the development of novel PILs with adapted properties for various applications.

5.3 Computationally Investigated Systems

Fig. 5.1 illustrates the two primary reactions occurring in the PILs 1-methylimidazolium acetate and 1-methylimidazolium trifluoroacetate. 1-methylimidazolium (Im_1H^+) either reacts with acetate (OAc^-) or Trifluoroacetate (TFA^-) to form 1-methylimidazole (Im_1) and acetic acid (HOAc) or trifluoroacetic acid (HTFA), respectively. In our previous study, we determined the equilibrium composition of [Im_1H]OAc to consist of approximately 30 % charged species (Im_1H^+, OAc^-) and 70 % neutral species (Im_1, HOAc).[66] Consequently, this mixture served as the starting point for our subsequent investigations. We replaced OAc^-/HOAc with the corresponding fluorinated species, TFA^-/HTFA, up to a concentration of 40 %. Beyond this concentration, the IL is no longer liquid at room temperature.

We pursued two strategies for these substitutions: Firstly, we merely exchanged the equivalent number of OAc^- and HOAc molecules with TFA^- and HTFA molecules, respectively, without altering the equilibrium between charged and neutral species. The resulting molecular quantities for each species are presented in Table 5.1 as System No. I. Secondly, we considered that HTFA is a significantly stronger acid than HOAc ($pK_a = 4.756$ for HOAc versus $pK_a = 0.52$ for HTFA), implying a higher degree of dissociation. Thus, we assumed that all HTFA molecules in the system completely dissociate into TFA^-. Consequently, the number of Im_1H^+ molecules increases to account for the additional negatively charged TFA^- ions. As a result, the protonation equilibrium is shifted towards the ionic side. This configuration can be found as System No. II in Table 5.1. Importantly, both systems maintained an overall neutral charge.

TABLE 5.1: Number of the respective molecules Im_1H^+, OAc^-, Im_1, HOAc, TFA^-, HTFA in the various simulated mixtures. c denotes the percentage of charged and n of neutral species.

No.	χ_{TFA}	Im_1H^+	OAc^-	TFA^-	Im_1	HOAc	HTFA	c	n
		[# molecules]						%	
	0.00	150	150	0	350	350	0	30	70
I	0.10	150	135	15	350	315	35	30	70
I	0.25	150	112	38	350	263	87	30	70
I	0.40	150	90	60	350	210	140	30	70
II	0.10	185	135	50	315	315	0	37	63
II	0.25	241	111	130	259	259	0	48	52
II	0.40	290	90	200	210	210	0	58	42

5.4 Results and Discussion

Throughout the text, uncertainties correspond to the standard deviation within eight independent experiments. We note that these uncertainties thus represent the precision of the experiments (i.e. reproducibility) and do not contain systematic errors. Systematic errors of the experiments have been estimated to ~1-3 % in $\varepsilon'(\nu)$.[98]

To explore which of the two limiting cases, constant ionicity upon increasing TFA content as in the simulation system No. I or full dissociation of HTFA as in simulation system No. II better describes the experimental data, we first consider the densities of the systems (data shown in SI Table 5.4). Although the density in both simulation systems and the experimentally determined densities increase linearly as a function of χ_{TFA^-}, the slope of system No. I is flatter due to the constant ionicity. Conversely, enhanced Coulombic interactions with increasing χ_{TFA^-} result in a much steeper decrease of the density of system No. II with increasing χ_{TFA^-}, closer to the experimental values. As such, already the densities of the systems provide first hints to HTFA being fully dissociated in the PIL mixtures. However, as one single property does not allow for a precise determination of the degree of dissociation and thereby the discrimination between system No. I or No. II, we consider the frequency-dependent dielectric spectra of all systems in the following.

5.4.1 Dielectric Spectrum as a Function of the TFA Concentration

In the case of charged molecules, the translational motion of the (molecular) ions measured by the frequency-dependent conductivity $\sigma(\nu)$ additionally contributes to the generalized dielectric spectrum $\Sigma(\nu)$. Usually, the hyperbola of the static conductivity $\sigma(0)$ is removed from the generalized dielectric spectrum $\Sigma(\nu)$ both in simulations and experiments

$$\Sigma_0(\nu) = \hat{\varepsilon}(\nu) + 2i\,\frac{\sigma(\nu)-\sigma(0)}{\nu} + \varepsilon_\infty \tag{5.1}$$

$$= \hat{\varepsilon}(\nu) + \vartheta_0(\nu) + \varepsilon_\infty \tag{5.2}$$

Even after removing the $\sigma(0)$-contribution from the dielectric spectrum, higher frequency translational motions like cage vibrations still contribute to the dielectric spectrum.[175, 245] This "dielectric conductivity" $\vartheta_0(\nu) = 2i(\sigma(\nu)-\sigma(0))/\nu$ cannot be measured separately and the experiment consequently monitors $\hat{\varepsilon}(\nu) + \vartheta_0(\nu)$.

We first consider the static polarization of the ionic liquids, i.e. the static dielectric constant, which is relevant to the solvation of charged entities in the PILs. In the simulations, the static values of the generalized dielectric constant $\Sigma_0'(0)$ can be derived from the sum of the individual contributions of the species k in the simulations

$$\Sigma_0'(0) = \sum_k \varepsilon_k'(0) + \vartheta_0'(0) + \epsilon_\infty \tag{5.3}$$

where the high-frequency limit ϵ_∞ can be determined from the polarizabilities via the Lorentz-Lorenz equation. Experimentally, the static dielectric constant, $\Sigma_0'(0)$ and the limiting permittivity at high frequencies, ϵ_∞, is obtained by extrapolating Σ_0' to $\nu = 0$ and $\nu = \infty$ using a relaxation model (see SI, section 5.6). Fig. 5.2 delineates the total dielectric strength $\Sigma_0'(0) - \epsilon_\infty$, as obtained from both experiments (represented by black circles) and simulation data (denoted by x), as a function of χ_{TFA^-}. The data depicted in Fig. 5.2 show a noticeable linear decrease in the dielectric strength $\Sigma_0(0) - \epsilon_\infty$ of the experimental results and system No. II. Contrarily, system No. I demonstrates an upward trend as a function of χ_{TFA^-}. This observation substantiates the hypothesis that fully dissociated TFA^- molecules in system No. II provide a more accurate representation of the experimental findings as already concluded from the densities. This also goes in line with the difference in $\mathrm{p}K_\mathrm{a}$ for OAc^- and TFA^- and thus the stronger dissociation of TFA^-.

To proceed with the comparison of the dynamics, we compare in Fig. 5.3 the real part of the dielectric spectra from both experimental data and simulation No. II at 298 K for $[\mathrm{Im_1H}]\mathrm{OAc}$ and mixtures with gradual substitution of OAc^- by TFA^-. The experimental spectra are dominated by a marked dispersion in $\Sigma_0'(\nu)$ at ~1 GHz, whereas at higher frequencies (ν >5 GHz) the decrease of $\Sigma_0'(\nu)$ is less pronounced. As the TFA^- content increases, the magnitude of the dispersion at lower frequencies decreases. On the other hand, the higher frequency polarization dynamics contributing

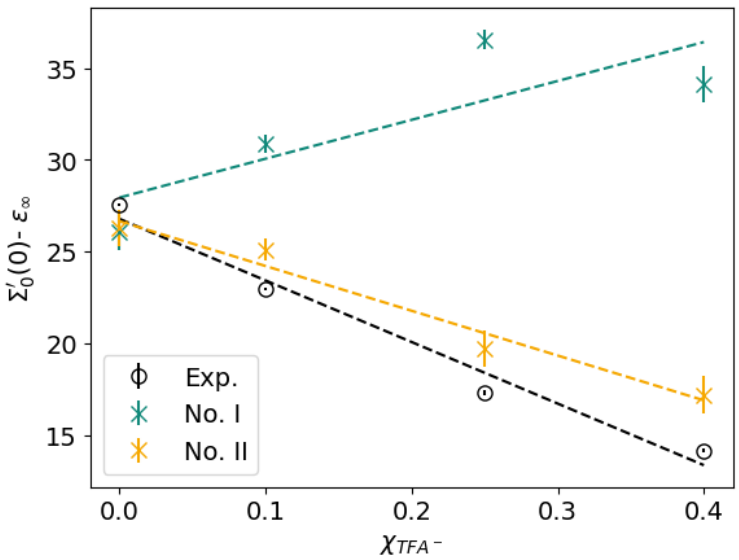

FIGURE 5.2: Static values of the generalized dielectric constant measured by the experiment (circles) and from polarizable MD simulations of system No. I (turquoise x) and system No. II (yellow x). The error bars are smaller than the size of the symbols. *Reproduced from* [78].

to the spectra at $\nu > 5\,\mathrm{GHz}$ remain largely unaffected by changes in the composition of the ionic liquid. The reasonable agreement between system No. II and experiment is also visible for the frequency-dependent dielectric spectrum in Fig. 5.3.

As such, also the dynamical aspects confirm that the 1-methylimidazolium acetate/trifluoroacetate mixture becomes increasingly ionic in response to an increased TFA^- concentration. Specifically, at a mole fraction χ_{TFA} of 0.25, the concentration of charged species is almost identical to that of the neutral counterparts. When χ_{TFA} reaches 0.40, the majority of the molecules, approximately 60 %, assumes a charged state, thereby underscoring the appropriateness of the term "protic ionic liquid" in this context.

To elucidate the contributions of individual molecular species to the dielectric spectra, we calculated effective dipole moments for each species $k \in \{\mathrm{HOAc}, \mathrm{OAc}^-, \mathrm{Im_1}, \mathrm{Im_1H^+}, \mathrm{TFA}^-\}$ from the simulations using the self-correlation function of the total dipole moments at $t = 0$.

The effective dipole moment is given by:[246]

$$\mu_{\mathrm{eff}}^{k-k} = \sqrt{\frac{< M_{\mathrm{D}}^k(0) M_{\mathrm{D}}^k(0) >}{N_k}}, \tag{5.4}$$

with N_k being the number of molecules of species k. Please note that cross-correlations between different species, e.g. ion pairs, are not considered by Eq. 5.4. However, they should be short-lived in neat ILs.[247] Dimers of acetic acid are taken into account by

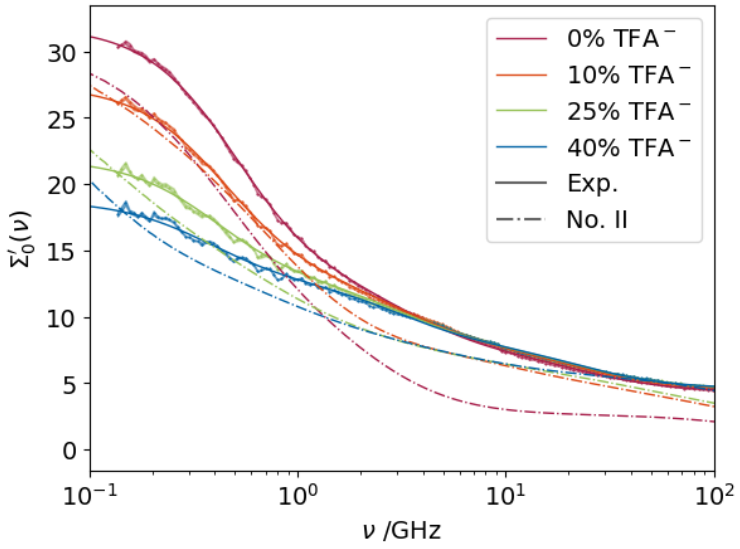

FIGURE 5.3: Real part of the generalized permittivity spectra, $\Sigma_0'(\nu)$. Symbols show the real part of the experimental data with the deviations within eight experiments indicated as shaded areas. The solid line shows the fit of the relaxation model (see SI, Eq. 5.12) to the experimental data. The dash-dotted lines represent the computationally calculated spectra for system No. II. Different TFA^- concentrations are displayed in red (0 % TFA^-), orange (10 % TFA^-), green (25 % TFA^-), and blue (40 % TFA^-). *Reproduced from* [78].

TABLE 5.2: Comparison of dipole moments μ^{PCM} derived from quantum-mechanical calculations of a single molecule in a polarizable continuum model (PCM, $\varepsilon = 8.8$) and effective dipole moments μ_{eff} from the polarizable MD simulation. COM and COG denote the reference site, i.e. the center of mass or the geometric center.

	$\mu^{\mathrm{PCM}}_{\mathrm{COM}}$	$\mu^{k-k}_{\mathrm{eff,COM}}$	$\mu^{\mathrm{PCM}}_{\mathrm{COG}}$	$\mu^{k-k}_{\mathrm{eff,COG}}$
	[D]	[D]	[D]	[D]
HOAc	2.4	3.9	2.4	3.9
OAc^-	4.7	4.7	8.4	5.4
Im_1	5.4	5.6	5.4	5.5
Im_1H^+	2.0	1.9	2.7	2.3
HTFA	3.0	-	3.0	-
TFA^-	5.7	7.2	5.2	4.8

Eq. 5.4 as they are composed of the same species. The summation for the collective rotational dipole moment $\vec{M}_{\mathrm{D}}$ according to Eq. 3.15 is here restricted to the molecular dipole moments of the species k. However, we consider both, $\vec{\mu}_{\mathrm{i}}$ based on the center of mass (Eq. 3.12), and the center of geometry (Eq. 3.14). The obtained values of μ^{k-k}_{eff} are listed in Table 5.2, together with the calculated dipole moments from quantum chemical calculations using a polarizable continuum model and CHELPG charges, analogously utilizing the center of mass ($\mu^{\mathrm{PCM}}_{\mathrm{COM}}$) or the center of geometry ($\mu^{\mathrm{PCM}}_{\mathrm{COG}}$) as a reference point for charged molecules. The values of μ^{k-k}_{eff} were found to be rather independent of composition. Thus, we only listed averaged values (see also Tables 5.7 and 5.8 in the SI).

The choice of the reference point in particular impacts the dipole moments for OAc^- and TFA^-, as for these molecular ions, the centers of mass and the centers of geometries are markedly displaced: While $\mu_{\mathrm{OAc^-}} < \mu_{\mathrm{TFA^-}}$ when using the center of mass, it is reversed using the center of geometry, where $\mu_{\mathrm{OAc^-}} > \mu_{\mathrm{TFA^-}}$. As will be discussed later, the differences in dipole moments, depending on the chosen reference point, will impact the attribution of the observed dynamics to rotational ($\hat{\varepsilon}(\nu)$) or translational contributions $\vartheta_0(\nu)$ of the dielectric spectra.

In general, we find that – irrespective of the reference point – the effective dipole moments obtained from the simulations agree well with the values obtained from the QM calculations for imidazolium-based molecular species Im_1 and Im_1H^+. Conversely, for HOAc, OAc^-, and TFA^-, the effective dipole moments from the simulations differ from the single molecule dipole moments obtained from the QM calculations. These discrepancies in absolute values can be attributed to the fact that the QM calculations uses only a single molecule and mimics the surrounding using the PCM model, while in the simulation, the molecules are surrounded by a multitude of other molecules. Consequently, molecules of the same species k may have various mutual orientations that significantly affect the sum dipole vector $\vec{M}^k_{\mathrm{D}}$ of that species. As such, the discrepancies in both values for HOAc, OAc^-, and TFA^- point to marked correlations

in their relative orientation for the ensemble of molecules in the ionic liquid.
Despite exhibiting linearity with respect to χ_{TFA^-}, the observed dielectric decrement in Fig. 5.2 presents a counter-intuitive phenomenon as one would expect a constant trend: The DFT-derived dipole moments $\mu^{\mathrm{PCM}}_{\mathrm{COM}}$ for both center of mass and center of geometry of the substituted species Im_1 and HOAc are very similar to the added species $\mathrm{Im}_1\mathrm{H}^+$ and TFA^-:

$$\mu^{\mathrm{PCM}}(\mathrm{Im}_1) \approx \mu^{\mathrm{PCM}}(\mathrm{TFA}-) \tag{5.5}$$
$$\mu^{\mathrm{PCM}}(\mathrm{HOAc}) \approx \mu^{\mathrm{PCM}}(\mathrm{Im}_1\mathrm{H}^+) \tag{5.6}$$

The concentration of species with similar dipole moment is rather insensitive to χ_{TFA^-} as visible from Table 5.1. Thus, the detected decrease in the static dielectric constant $\Sigma_0'(0)$ (as shown in Fig. 5.2) upon increasing χ_{TFA^-} cannot be simply explained by an increased number density and/or magnitude of dipoles and further decomposition of the dielectric spectra is required to understand this behavior.

5.4.2 Computational Decomposition of the Dielectric Spectra

Contrary to experimental results, the simulated frequency-dependent generalized dielectric constant $\Sigma_0'(\nu)$ may be dissected into its constituent rotational and translational contributions, as depicted in Fig.5.4. The rotational relaxation of dipoles is monitored by the permittivity $\hat{\varepsilon}(\nu)$ (Fig. 5.4b)) as a function of χ_{TFA^-}. A discernible shift toward lower frequencies in the broad $\hat{\varepsilon}$ peak indicates an enhancement in the system's viscosity, concomitant with increasing ionicity. This phenomenon may partially originate from the augmented volume of TFA^- compared to OAc^-. The translational contributions of the charged species are incorporated into the dielectric conductivity $\vartheta_0(\nu)$ (Fig. 5.4c)), yet, the translation of neutral molecules does not contribute to $\vartheta_0(\nu)$. Interestingly, the peak of the dielectric conductivity $\vartheta_0(\nu)$ experiences a slight shift to higher frequencies with increasing χ_{TFA^-} but also a significant decrease in amplitude. As a result of the complex interplay of translational and rotational contributions to the total spectrum of the generalized dielectric constant (Fig. 5.4a)), its direct interpretation can be complicated.
To further explore the peculiar decrease in the magnitude of the $\vartheta_0(\nu)$ spectrum with increasing χ_{TFA^-}, we investigate the effect of the choice of the reference point on these dynamics: As discussed above, the choice of the reference point, COG or COM, affects the calculated dipole moments and, in turn, the rotational and translational contributions to the computed spectra. As QM calculations (Table 5.2) indicate that the choice of the reference point is in particular critical for the acetate anion, the marked translational contributions to the spectra at low χ_{TFA^-} may thus stem from the choice of the reference point. However, our results suggest that the permittivity

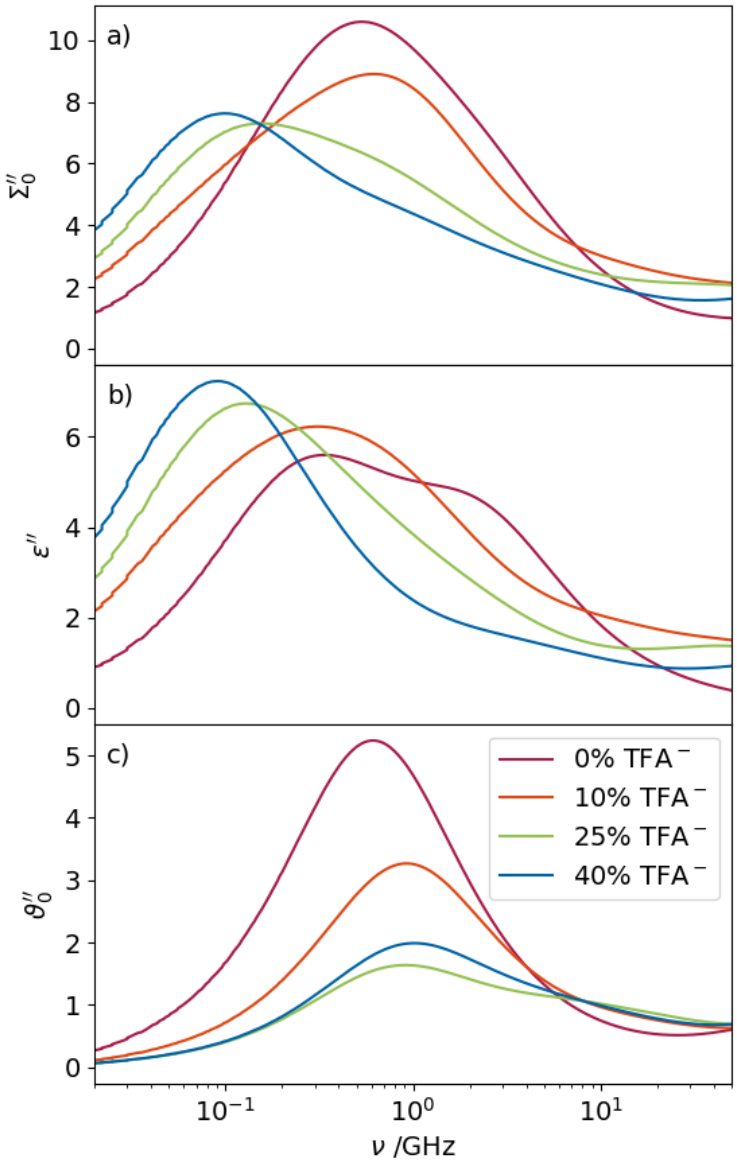

FIGURE 5.4: Imaginary parts of the computational dielectric spectra as a function of the TFA^- content. The top panel shows the total generalized dielectric function, the middle panel shows the rotational contributions, and the bottom panel shows the translational contributions based on the center of mass. *Reproduced from* [78].

spectra $\hat{\varepsilon}$ with the molecular dipole moments $\vec{\mu}_{\mathrm{i,COG}}$ with respect to the center of geometry (dashed lines in Fig. 5.5a) instead of $\vec{\mu}_{\mathrm{i,COM}}$ with respect to the center of mass (solid lines in Fig. 5.5a), are very similar (Fig. 5.5a). Yet, a significant difference can be detected for the contributions of OAc^- and TFA^- to the total spectrum, which is calculated by correlating the total dipole moment of species $k \in \{OAc^-, TFA^-\}$ with the total dipole moment: $< M_{\mathrm{D}}^{k}(0) M_{\mathrm{D}}^{\mathrm{tot}}(t) >$. The spectral amplitudes of OAc^- increase when using the center of geometry instead of the center of mass (Fig. 5.5b)), which is in agreement with the dipole values in Tab. 5.2. Conversely, the spectral amplitudes of TFA^- decrease (Fig. 5.5c)), in line with the calculated dipole moments (Tab. 5.2). Nevertheless, with respect to the overall rotational relaxation contributions,

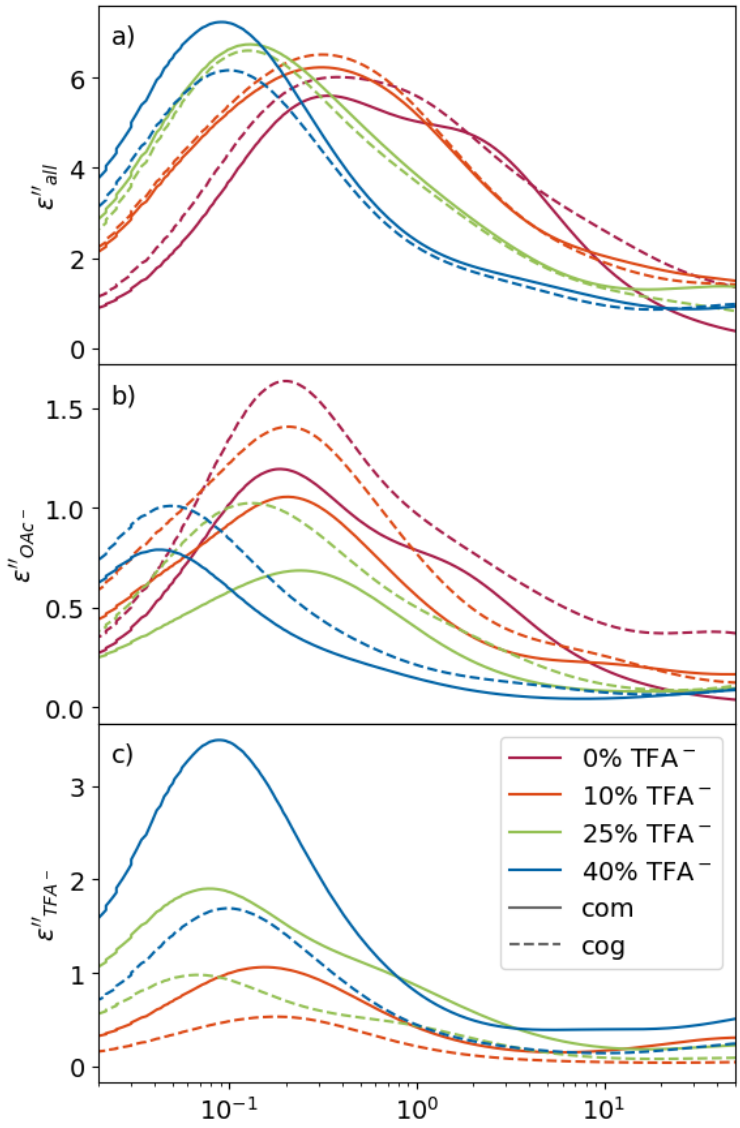

FIGURE 5.5: Total rotational contribution (a), contributions of OAc^- (b), and of TFA^- (c) to the imaginary part of the rotational dielectric function as a function of the TFA^- content. The solid line represents the usual method using the center of mass as a reference point, while the dashed lines use the center of geometry as a reference. *Reproduced from* [78].

the changes in the dielectric permittivity between OAc^- and TFA^- balance each other out. As such, the effect of the environment (cage) on the pivot of the rotational motion cannot explain the marked translational contributions to the $\vartheta_0(\nu)$ spectra.

Our DFT calculations for individual $[Im_1H]OAc$ and $[Im_1H]TFA$ ion pairs, employing a polarizable continuum model with a dielectric constant $\varepsilon = 8.8$, show that the binding energy of 115 kJ mol^{-1} for $[Im_1H]OAc$ is much stronger compared to that of $[Im_1H]TFA$ (80 kJ mol^{-1}), which suggests that cages incorporating acetate exhibit an enhanced strength leading to more pronounced hindered motions within these cages. Conversely, cages comprising also TFA^- exhibit a comparatively softer structure, resulting in less restrictive confinement of the central ion's motion, consequently diminishing its

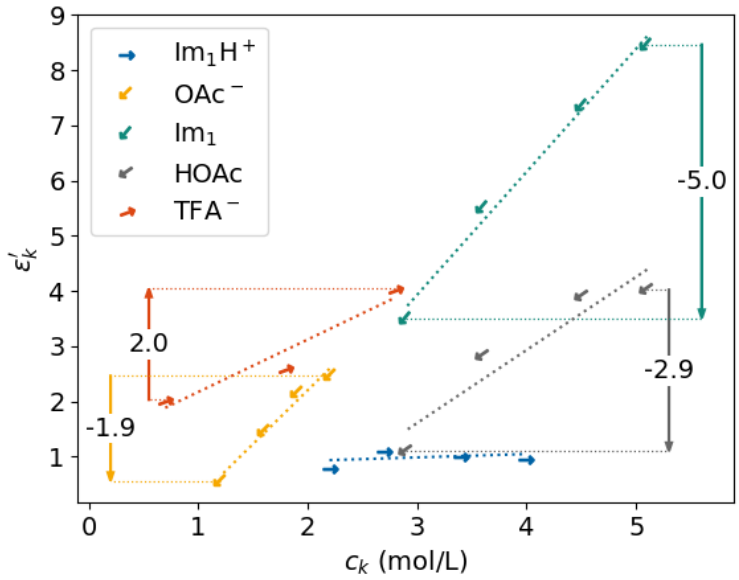

FIGURE 5.6: Concentration dependence of the permittivity ε'_k for the individual species k. The arrows depict the data points from Table 5.3 and their directions points towards increasing χ_{TFA^-} (0 %,10 %,25 %,40 %). *Reproduced from* [78].

rattling within the cage and promoting free ionic transport.

We further explore the contributions of the individual molecular species to the dielectric spectra. However, due to the largely varying spectral shapes of the $\Sigma''_0(\nu)$-peaks as a function of χ_{TFA^-}, it is challenging to directly relate the amplitudes at the maximum to the overall dielectric decrement of Fig. 5.2. However, the contributions of the individual molecular species to the static value, $\Sigma''_0(0)$ can be extracted (Table 5.3). As visible from Table 5.3, the permittivity contributions from the neutral 1-methylimidazole and acetic acid decrease with increasing TFA^- content as expected due to the increased ionicity of the systems.

However, although the concentration of Im_1 increases with increasing χ_{TFA^-}, its contribution to the spectrum remains rather constant and small. Except for the system

TABLE 5.3: Decomposition of the computational static generalized dielectric constant according to Eq. (5.3). The sum of all static permittivity contributions and the dielectric conductivity ϑ_0 yields the generalized dielectric constant Σ'_0. Except for ϵ_∞ all properties are extrapolations to $\nu = 0\,\mathrm{GHz}$. Values are given as the average ± standard deviation for the three replica. The standard deviation for ϵ_∞ is below 10^{-1}.

χ_{TFA}	Σ'_0	$\epsilon'_{\mathrm{Im}_1}$	$\varepsilon'_{\mathrm{HOAc}}$	$\varepsilon'_{\mathrm{Im}_1\mathrm{H}^+}$	$\varepsilon'_{\mathrm{OAc}^-}$	$\varepsilon'_{\mathrm{TFA}^-}$	ϑ_0	ϵ_∞
0.00	28.6 ± 1.0	8.5 ± 0.3	4.0 ± 0.6	0.8 ± 0.1	2.5 ± 0.4	-	10.5 ± 1.0	2.3
0.10	27.4 ± 0.6	7.4 ± 0.5	3.9 ± 1.2	1.1 ± 0.3	2.2 ± 0.3	2.0 ± 0.2	8.5 ± 1.6	2.3
0.25	22.0 ± 1.0	5.5 ± 0.5	2.8 ± 0.6	1.0 ± 0.1	1.5 ± 0.2	2.6 ± 0.2	6.3 ± 0.7	2.3
0.40	19.5 ± 1.0	3.5 ± 0.5	1.1 ± 0.4	1.0 ± 0.1	0.6 ± 0.1	4.0 ± 0.1	7.0 ± 0.9	2.3

with no TFA^-, the sum of the contributions of the anions acetate and trifluoroacetate is also almost constant with roughly $\varepsilon'_{OAc^-}(0) + \varepsilon'_{TFA^-}(0) \simeq 4.3$.
Fig. 5.6 visualizes the data of Table 5.3. The position of the arrows represents the corresponding values. The direction of the arrows points towards the highest TFA^- concentration. For uncorrelated rotational motion of dipoles, one would expect the slopes of these plots to correlate with the square of the effective dipole moment of the species.[114] However, the ranking $Im_1 \simeq OAc^- > TFA^- \simeq HOAc > Im_1H^+$ of the slopes does not coincide with the ranking of the DFT dipole moments in Table 5.2 illustrating that the mutual dynamic orientation of the dipoles plays a significant role in our systems, which we study in more detail in the following section.

5.4.3 Mutual Orientation of the Dipole Moments

The effective dipole moment is related to the molecular dipole moment via:[248, 249]

$$\mu_{\text{eff}}^2 = g_K \cdot \mu^2 \tag{5.7}$$

$$g_K = 1 + \rho \int 4\pi r^2 g^{110}(r)\, dr \tag{5.8}$$

using the Kirkwood factor g_K for the characterization of the mutual alignment of the dipoles, which can be evaluated from the orientational radial distribution functions:[250, 251]

$$g^{110}(r) = \frac{\sum_j \cos(\vec{\mu}_i, \vec{\mu}_j) \cdot \delta(r - r_{ij})}{4\pi r^2 \rho} \tag{5.9}$$

The three upper indices describe the order of the angular momentum, here $\cos(\vec{\mu}_i, \vec{\mu}_j)$.[251] The first two indices refer to the molecular dipole moments of the molecule i and j, respectively. The third index is for the distance between the respective center of masses. Consequently, the indices $1, 1, 0$ characterize the mutual orientation of the dipole moments, whereas $1, 0, 1$ their mutual position via $\cos(\vec{\mu}_i, \vec{r}_i j)$.
Positive cosine values indicate that the dipole moments $\vec{\mu}_i$ and $\vec{\mu}_j$ (with respect to the center of mass) are more or less parallel, while negative values show a preference for antiparallel alignment.
For instance, $g^{110}(r)$ below 5 Å is negative for Im_1-Im_1 (Fig. 5.7a)), which means that the imidazole rings are stacked but with antiparallel directions. Above 5 Å $g^{110}(r)$ becomes positive. Due to the r^2-amplifier in Eq. (5.8), the second shell contribution becomes more important, and g_K exceeds unity reflecting an overall preferred parallel alignment. With increasing TFA^--content, the second positive peak shifts to shorter distances, thereby reducing g_K. This reduction is one of the reasons for the dielectric decrement of -4.2 observed for ϵ'_{Im_1} in Table 5.3 and Fig. 5.6 (turquoise arrow).

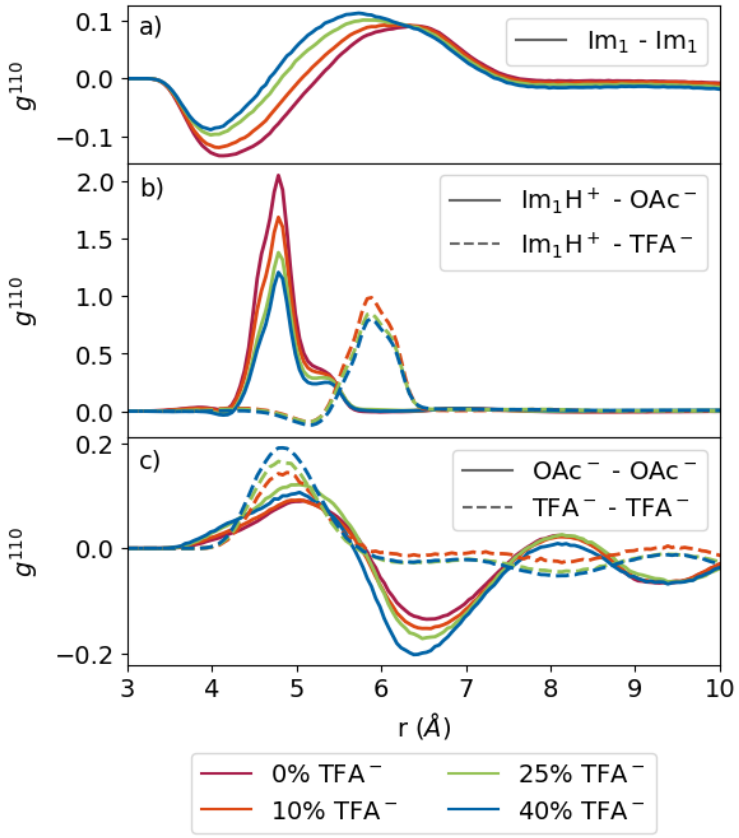

FIGURE 5.7: $g^{110}(r)$ functions of Im_1 with itself, Im_1H^+ with OAc^- and TFA^- as well as OAc^- and TFA^- with itself. *Reproduced from* [78].

The other predominant reason is the reduced concentration. The number of imidazoles declines from 350 at χ_{TFA}=0 to 215 at χ_{TFA}=0.40.

The parallel alignment of the imidazolium dipoles with those of the anions decreases with increasing χ_{TFA} (Fig. 5.7b). Due to the increasing concentration of imidazoliums with χ_{TFA} the total $\varepsilon'_{Im_1H^+}$ does not change as illustrated in Table 5.3 and Fig. 5.6. The shift of about 1 Å between the peaks of Im_1H^+-OAc^- and Im_1H^+-TFA^- can mainly be attributed to the differences in the center of masses, which is around 0.7 Å. In the case of acetate and trifluoroacetate, the alignment plays an important role, as shown in Fig. 5.7c. With increasing χ_{TFA}, the alignment of the trifluoroacetates becomes more parallel, resulting in an increasing ε'_{TFA}. This is also true for the first shell of acetates, but the second shell becomes more antiparallel, overruling the first shell's contribution.

For reference, we also calculated the radial distribution functions ($g^{000}(r)$) as seen in SI Fig. 5.10. Here, the three indices 0,0,0 indicate that we use the pure radial distribution function without cosine weighting like in Eq. (5.9).[251] An agreement between the peaks of the $g^{000}(r)$ and $g^{110}(r)$ curves is seen, indicating a significant density at the locations of the discussed signatures of the $g^{110}(r)$ functions.

Overall, this analysis demonstrates that the orientation of molecular dipoles in these systems is highly correlated, with the orientational constraints of cations relative to

the anions (together with the translational contribution) being a main source of the counter-intuitive static dielectric properties.

5.4.4 The Impact of Proton Transfers

As illustrated in Fig. 5.8, the conductivity $\sigma(0)$ for systems No. I (turquoise line) and No. II (yellow line) are significantly lower than the experimental values.

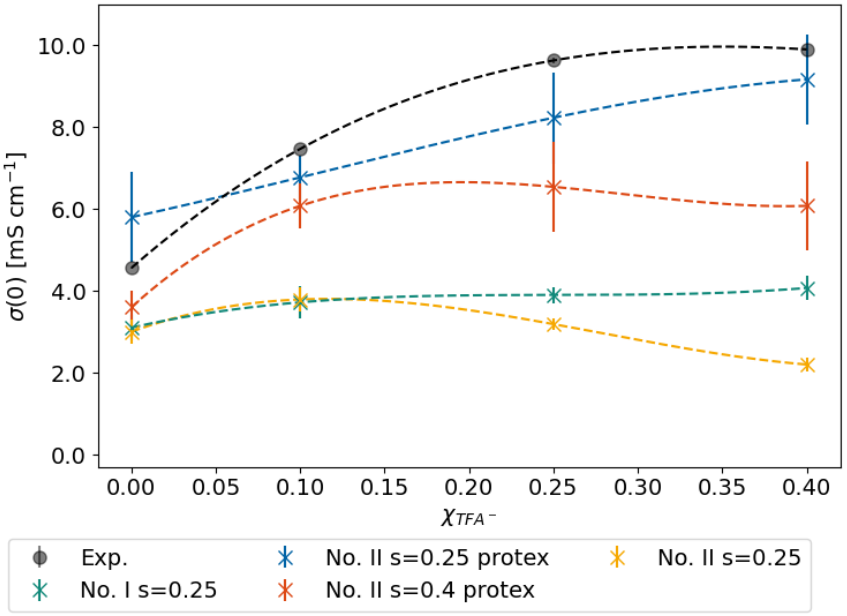

FIGURE 5.8: Conductivity of the different systems. *Reproduced from* [78].

One obvious explanation for this discrepancy is the lack of proton transfer in the simulated protic ILs. This finding aligns with our previous work on the pure 1-methylimidazolium acetate system,[243] where we enabled proton transfers using our in-house developed program PROTEX.[243] As a result, a substantial increase in conductivity was achieved (blue and orange curves in Fig. 5.8). However, employing a Lennard-Jones scaling factor $s = 0.25$ (see Eq. 5.10), consistent with the other polarizable simulations in the previously mentioned study (Ref. [243]), led to a more or less linear increase of the total conductivity with increasing TFA content. In contrast, the experimental conductivity appears to level off beyond 25 % TFA^-, a behavior that could only be captured by adopting s=0.4, albeit at the expense of a reduced overall conductivity $\sigma(0)$ (orange curve).

With increasing χ_{TFA}, the proton transfer seems to become even more relevant to cover the experimental rise in conductivity, in line with NMR diffusivities.[104] The difference between the yellow curve (no proton transfer) to the orange and especially blue curve (including proton transfer) of Fig. 5.8 increases with χ_{TFA}, indicating an important contribution of proton transport to the TFA^--rich systems. In this context,

it is important to note that within the PROTEX simulations, TFA^- cannot actively participate in proton transport (in line with its high acidity), nevertheless increasing TFA^- content facilitates an increased contribution of proton transport to the overall conductivity. This observation implies that the enhanced proton contribution must originate from the TFA^--induced increase in the concentration of Im_1H^+: Im_1H^+, Im_1, OAc^-, and HOAc actively take part in proton transfer in the simulations and an increased degree of protonation of Im_1 apparently enhanced proton transport. As such, our results imply that proton transport in this PIL is sensitive to the protonation equilibrium Im_1/Im_1H^+, which may offer routes towards enhancing proton and charge transport in PILs.

5.5 Conclusions

The protic ionic liquid 1-methylimdazolium acetate and mixtures with trifluoroacetate were investigated using a combined approach of experiment and theory. A reasonable agreement between the measured and computed dielectric spectra could be obtained using polarizable molecular dynamics simulations, allowing us to further break down the spectra into the different molecular contributions and gain deeper molecular-level insight into these liquids. Adding different amounts of [Im_1H]TFA (0 %, 10 %, 25 %, 40 %) to [Im_1H]OAc resulted in a linear decrease of the amplitude in the dielectric spectra, which might be counter-intuitive on first sight since a more polar species (TFA^-) is added. Looking at the decomposition of the spectra, this decrease can be attributed to a decrease in the dielectric conductivity, which could be attributed to a decrease of cage rattling with increasing TFA^- content and a reduced contribution of the neutral species (Im_1, HOAc) to the overall polarization dynamics.
Increasing concentration of TFA^- not only affects concentrations of dipolar species but also alters the mutual orientation of the dipole moments (dipolar correlations). The decrease in the contribution of Im_1, for example, stems not only from a reduced concentration but also a shift of the g^{110} function to shorter distances. On the other hand, the alignment of TFA^--TFA^- becomes more parallel, explaining the increase in permittivity for TFA^-, while the opposite trend for the second coordination shell of OAc^- is observed. Analyzing the alignment of Im_1H^+ with either OAc^- or TFA^- a strong parallel alignment is found, which decreases as TFA^- content increases. Overall, the contribution of Im_1H^+ to the dielectric permittivity does not change with TFA^- content since the decrease is outweighed by the increase of Im_1H^+ molecules. Moreover, the marked orientation of 1-methylimidazolium with the anions is a main contributor to the relatively high polarization in the IL, and this orientation seems intimately connected to the structure of the IL.
The conductivity increases with TFA^- content in the systems and levels off at 40 % TFA^-. The competition between a Grotthuss-like charge transport and vehicle transport is present. With more TFA^- molecules, the whole system becomes more ionic,

resulting in a pronounced enhancement of the conductivity of the IL. Allowing for explicit proton transfer, a remarkable increase in conductivity and a good agreement with experimental values are found. The increasing contribution of proton transport to the overall conductivity with increasing TFA^- content suggests that varying the degree of Im_1 protonation allows for engineering proton transport in the PIL.
Concluding, strong cage effects, in the case of OAc^-, induce a remarkably high polarization of the ionic liquid through the anions motion within the cage. The substitution with TFA^- results in the disruption of these cages, and the strong intermolecular interactions are manifested solely in a pronounced orientational correlation. These findings suggest that both the disruption of cages and the augmentation of Im_1H^+ cations in the systems containing TFA^- contribute favorably to proton transport.

5.6 Supplementary Information

Figures in this section have been reproduced from the SI of [78].

Physico-Chemical Properties

Density

TABLE 5.4: Density in g/cm^3. The accuracy of the experimental equipment is $\pm 5 \cdot 10^{-4}$ g/cm^3. For computational densities, the standard deviation is below 10^{-2} for all values.

% TFA$^-$	Exp.	No. I	No. II	No. II protex (s=0.25)	No. II protex (s=0.4)
0	1.07	1.03	1.03	1.04	1.05
10	1.11	1.05	1.06	1.06	1.07
25	1.16	1.07	1.10	1.10	1.11
40	1.21	1.10	1.13	1.13	1.15

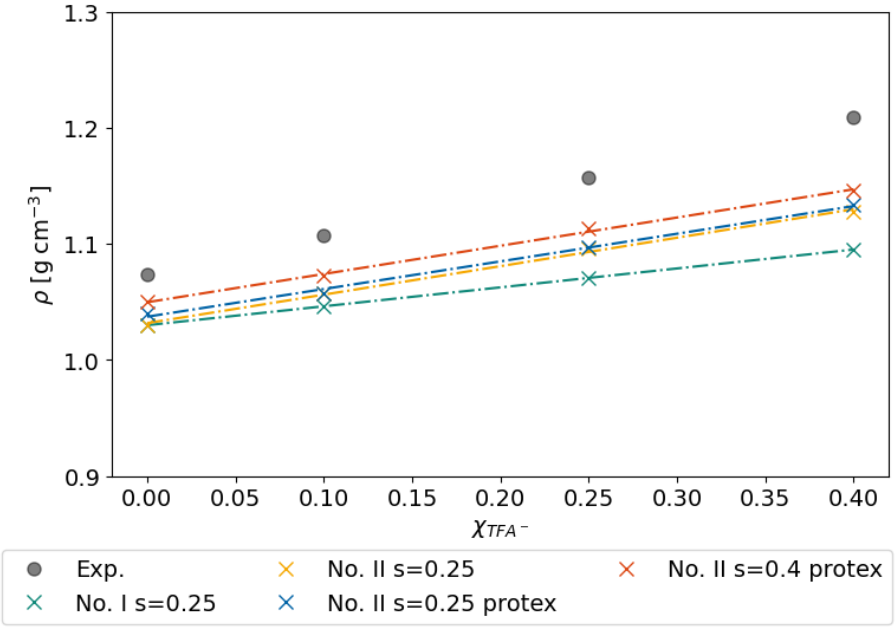

FIGURE 5.9: Density of the different systems.

The s-values denote the Lennard-Jones scaling factors according to:

$$\epsilon_\beta^{\mathrm{LJ}} = \epsilon_\beta^{\mathrm{LJ,unscaled}} \frac{\Big(\max(\alpha_\beta) - \alpha_\beta\Big) + s \cdot \max(\alpha_\beta)}{\max(\alpha_\beta) + s \cdot \Big(\max(\alpha_\beta) - \alpha_\beta\Big)} \tag{5.10}$$

Here, α_β is the polarizability of the atom β.

Conductivity

TABLE 5.5: Conductivity in mS/cm. Experimental uncertainties correspond to the standard deviation within 8 independent experiments.

% TFA^-	Exp.	No. I	No. II	No. II protex (s=0.25)	No. II protex (s=0.4)
0	4.56 ± 0.01	3.0 ± 0.3	3.0 ± 0.3	5.8 ± 1.1	3.6 ± 0.4
10	7.47 ± 0.01	3.8 ± 0.4	3.8 ± 0.3	6.8 ± 0.5	6.1 ± 0.5
25	9.63 ± 0.08	3.9 ± 0.2	3.2 ± 0.1	8.2 ± 1.1	6.5 ± 1.1
40	9.90 ± 0.03	4.1 ± 0.3	2.2 ± 0.2	9.2 ± 1.1	6.1 ± 1.1

Dipole Moments

Comparison of Different Functionals and Basis Sets

TABLE 5.6: Dipole moments, $\mu_{\mathrm{COM}}^{\mathrm{PCM}}$, of the molecular species based on DFT calculations using different functionals (B3LYP, B3LYP-D3, CAMB3LYP-D3, M06-D30, wB97X-D3) and basis sets (def2TZVP, def2QZVPP, def2TZVPP) and a polarizable continuum model. The calculations were performed using the Orca software package (see Methods).

Functional	B3LYP	B3LYP-D3	B3LYP-D3	CAMB3LYP-D3	M06-D30	wB97X-D3
Basis set	TZVP	QZVPP	TZVPP	TZVPP	TZVPP	TZVPP
	$\mu_{\mathrm{COM}}^{\mathrm{PCM}}$ [D]	$\mu_{\mathrm{COM}}^{\mathrm{PCM}}$ [D]	$\mu_{\mathrm{COM}}^{\mathrm{PCM}}$ [D]	$\mu_{\mathrm{COM}}^{\mathrm{PCM}}$ [D]	$\mu_{\mathrm{COM}}^{\mathrm{PCM}}$ [D]	$\mu_{\mathrm{COM}}^{\mathrm{PCM}}$ [D]
HOAc	2.3	2.3	2.3	2.3	2.3	2.3
OAc^-	4.7	4.7	4.5	4.7	4.5	4.7
Im_1	5.5	5.5	5.5	5.5	5.3	5.5
Im_1H^+	1.9	1.9	1.9	2.0	2.0	2.0
HTFA	3.0	2.9	2.9	2.9	2.9	2.9
TFA^-	5.8	5.8	5.7	5.8	5.8	5.9

Deviations between the different functionals and basis sets is below 0.2 D. These small deviations are probably due to the application of the polarizable continuum model diminishing potential discrepancies between the various combinations of the functionals and basis sets. There is also no systematic trend in the dipole when increasing the accuracy of the functional or basis set.

Effective Dipole Moment as a Function of the Concentration

TABLE 5.7: $\mu_{\mathrm{eff,COM}}^{k-k}$ for all species k for different concentrations of TFA^-.

% TFA^-	0	10	25	40
HOAc	3.79 ± 0.15	4.07 ± 0.33	3.97 ± 0.07	3.83 ± 0.17
OAc^-	4.65 ± 0.19	4.78 ± 0.34	4.71 ± 0.44	4.78 ± 0.27
Im_1	5.50 ± 0.07	5.47 ± 0.11	5.60 ± 0.10	5.63 ± 0.15
Im_1H^+	1.90 ± 0.01	1.88 ± 0.01	1.90 ± 0.05	1.81 ± 0.17
TFA^-	-	7.41 ± 0.54	6.95 ± 0.66	7.07 ± 0.55

TABLE 5.8: $\mu_{\mathrm{eff,COG}}^{k-k}$ for all species k for different concentrations of TFA^-.

% TFA^-	0	10	25	40
HOAc	3.76 ± 0.12	4.06 ± 0.31	3.97 ± 0.10	3.84 ± 0.11
OAc^-	5.36 ± 0.26	5.46 ± 0.36	5.36 ± 0.48	5.48 ± 0.34
Im_1	5.57 ± 0.05	5.41 ± 0.18	5.54 ± 0.06	5.56 ± 0.11
Im_1H^+	2.36 ± 0.08	2.36 ± 0.08	2.40 ± 0.10	2.24 ± 0.18
TFA^-	-	5.02 ± 0.38	4.63 ± 0.49	4.76 ± 0.33

Dielectric Spectrum

Amplitudes of the Dielectric Spectrum

Experimental values for the total dielectric strength $\Sigma_0'(0) - \epsilon_\infty$ of Fig. 5.2 of the main text. The total dielectric strength has been obtained from fitting the relaxation model (Eq. 5.12) to the data.

$$\Sigma_0'(0) - \epsilon_\infty = S_1 + S_2 + S_3. \tag{5.11}$$

The computed values can be found in Table 5.3 of the main article.

TABLE 5.9: Amplitudes of the real part of the dielectric spectrum. Uncertainties correspond to the standard deviation within 8 independent experiments.

% TFA^-	Exp.
0	27.53 ± 0.08
10	22.96 ± 0.07
25	17.31 ± 0.16
40	14.15 ± 0.09

Relaxation Model for Experimental Dielectric Spectra

To quantify contributions to the experimental dielectric spectra we use a relaxation model based on three Debye-type relaxation modes:[104]

$$\Sigma(\nu) = \frac{S_1}{1 + (2\pi \mathrm{i}\nu\tau_1)} + \frac{S_2}{1 + (2\pi \mathrm{i}\nu\tau_2)} + \frac{S_3}{1 + (2\pi \mathrm{i}\nu\tau_3)} + \varepsilon_\infty + \frac{\sigma(0)}{2\pi \mathrm{i}\nu\varepsilon_0} \tag{5.12}$$

with S_j and τ_j being the relaxation amplitudes and relaxation times, respectively. The infinite-frequency permittivity, ε_∞, comprises the polarization dynamics at frequencies, which are not covered by the accessible frequency range in our experiments. The last term of the equation describes contributions due to conductivity, for which we assume the conductivity to be real and independent of frequency (dc conductivity $\sigma(0)$). The static permittivity, $\Sigma'_0(0)$, equals the sum of the relaxation amplitudes and ε_∞ according to Eq. (5.11).

TABLE 5.10: Relaxation amplitudes S_j, relaxation times τ_j and ε_∞ obtained from fitting the experimental dielectric spectra of $[Im_1H]OAc/[Im_1H]TFA$ mixtures at 298 K according to Equation 5.12. Uncertainties correspond to the standard deviation within 8 independent experiments.

% TFA^-	S_1	S_2	S_3	τ_1 / ps	τ_2 / ps	τ_3 / ps
0	19.47±0.04	5.34±0.02	2.72±0.02	317±1	42.6±0.4	6.4±0.1
10	14.93±0.02	5.05±0.02	2.98±0.03	352±2	44.8±0.7	6.6±0.1
25	9.44±0.10	4.83±0.04	3.04±0.02	391±2	46.3±0.4	6.5±0.1
40	6.27±0.05	4.71±0.02	3.17±0.02	428±8	50.1±0.6	6.7±0.1

Radial Distribution Functions

$g^{000}(r)$

Fig. 5.10 shows the g^{000} functions of the different species in the system. All functions are listed below for reference.

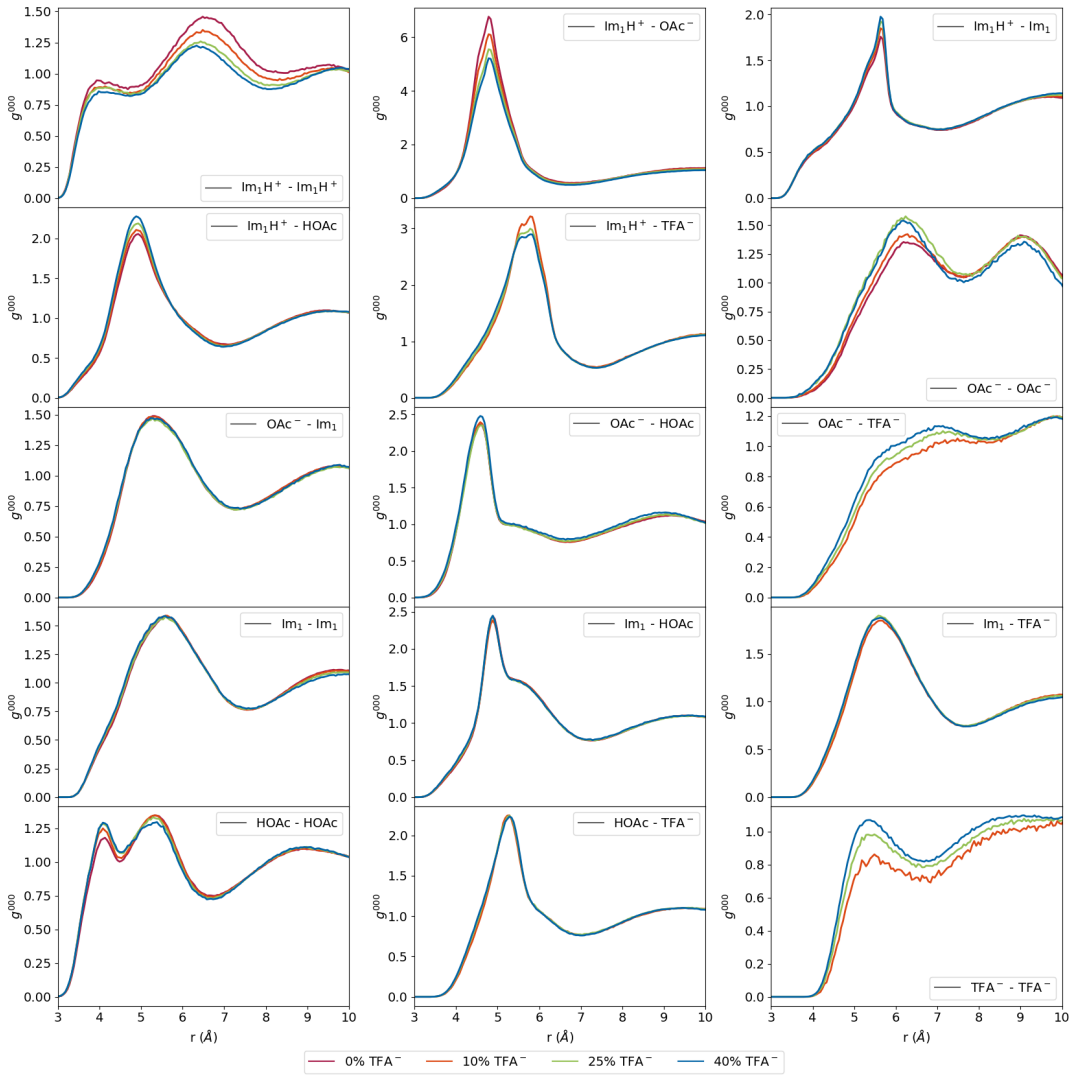

FIGURE 5.10: g^{000} functions for the different species.

$g^{110}(r)$

Fig. 5.11 shows the g^{110} functions of the different species in the system. All functions are listed below for reference. Please refer to the main article for the discussion.

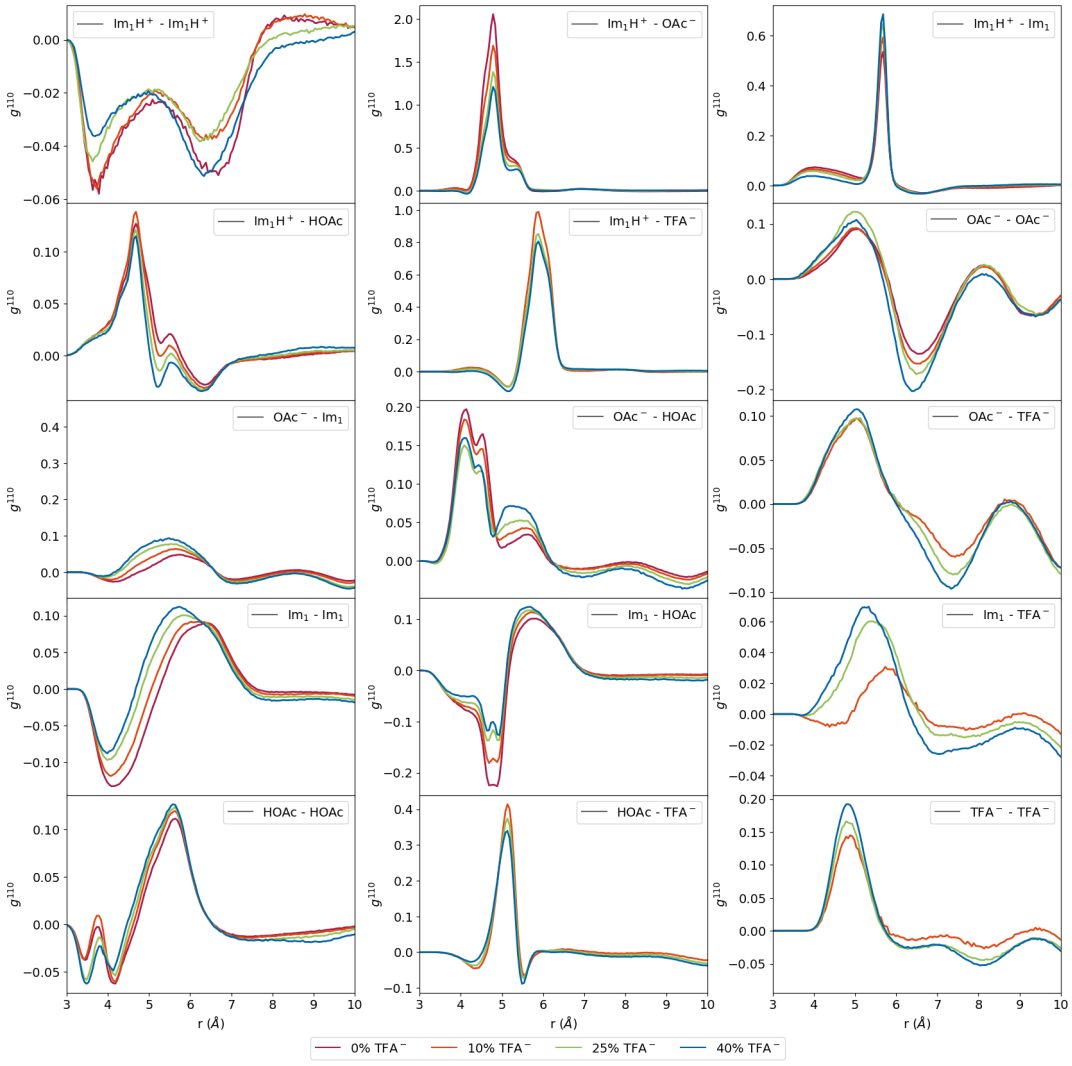

FIGURE 5.11: g^{110} functions for the different species.

Chapter 6

On the Effect of Temperature on the Ion Dynamics in 1-Methylimidazolium-Based Protic Ionic Liquids

6.1 Abstract

Protic ionic liquids (PILs), in principle, allow to overcome limitations of reduced charge mobility in ILs due to slow mass transport by decoupling charge and mass transport. However, for 1-methylimidazolium-based PILs, it appears that both vehicular-type transport of ionic species and Grotthuss-type proton transport contribute significantly to the overall charge transport, depending on the acidity of the anion. In 1-methylimidazolium-based PILs, a large fraction of ions is hindered in their mobility by rigid solvation cages. The hindered motion of ions in their cages is reflected in their dielectric response.

Here, we explore how thermal fluctuations affect these ion dynamics in 1-methylimidazolium-based PILs. By combining experimental dielectric spectra and computational spectra from polarizable molecular dynamics (MD) simulations of 1-methylimidazolium aetate/1-methylimidazolium trifluoroacetate mixtures at temperatures ranging from 15 °C and 65 °C, we confirm that the hindered translations of ions contribute to the dielectric response at low frequencies for acetate-rich PILs: The marked contributions of the motion of the ions in their solvation cages is experimentally evidenced by the lower-frequency relaxation being inconsistent with purely dipolar reorientational dynamics. The coincidence of the activation energies for the low-frequency relaxation with those of the macroscopic (dc) conductivity suggests a correlation between the fluctuations of ions within their cages and the transport of ions that have escaped these cages. MD simulations show that the fluctuations of the ions in their cages are enhanced with increasing temperature. Yet, the maximum dc conductivity shifts to compositions with higher trifluoroacetate contents with increasing temperature. At these compositions, translations of ions are only weakly impeded by solvation cages. Hence, our results imply that enhanced ionic mobility at elevated temperatures dominates the temperature dependence of the conductivity. Thermally-induced changes to the caging of the ions appear to have only moderate effects on the conductance, suggesting that in the studied temperature range, the thermal energy is insufficient to break up these cages. Our results highlight the impact of the temperature-dependent hydrogen-bonded structure of the PILs on the subtle balance between solvation cage formation, hindered translation of ions in these cages, and the diffusion of ions, which is pivotal for a complete understanding of the performance of PILs as electrolytes.

6.2 Introduction

Protic ionic liquids (PILs) – mixtures with high ionicity prepared via mixing of Brønsted acids with Brønsted bases – have the potential to decouple charge from mass transport via their ability to form extended H-bonded networks that allow for transport of protons.[1, 57, 202–204]

A prominent example of an PIL with unexpectedly high conductivity is the PIL 1-methylimidazolium acetate [Mim][AcOH].[57, 61, 71] Previous studies have indicated that the predominant molecular species in [Mim][AcOH] are neutral 1-methylimidazole [Mim] and acetic acid [AcOH],[61, 65, 104] consistent with the relatively low acidity of AcOH ($pK_a \approx 4.75$). Indeed, experimental observables are best reproduced by molecular dynamics simulations using only 30 % ionic species in the system.[66] As such, despite some conflicting findings from NMR experiments[67, 68], the bulk of experimental and theoretical studies[61, 63, 65, 66, 71–73, 78, 104] shows that the majority of acid and base molecules exist in an electro-neutral form in this PIL.

In a previous study[104], we have demonstrated that it is possible to effectively tune the equilibrium between charged and electro-neutral species within the PIL via the acidity of the Brønsted acid (exchange of AcOH for trifluoroacetate), which also alters the macroscopic conductivity. However, increasing ionicity does not necessarily go along with enhanced charge transport: The overall charge carrier dynamics depend on a complex interplay of coupled processes such as protonation equilibria, long-ranged translation of ions, hindered (confined) translation of ions in cages imposed by the PIL's molecular-level structure, and proton transfer.[71, 78, 104]

Yet, despite extensive studies of [Mim][AcOH], the subtle details of this complex interplay are still not entirely understood.[61–64] Inspired by MD simulations that have suggested that these different dynamics of ionic liquids are encoded in the dielectric response of the ionic liquids,[79] we have compared the experimental to computational dielectric spectra. This comparison indicated that not all ions are mobile. Rather, a fraction of ions are confined within ion cages.[78] The associated hindered translational motion of ions in these cages results in pronounced translational contributions to the dielectric spectra (i.e., a strong dispersion of the conductivity in the MHz/GHz range).[78] Reducing the confinement of ions via exchange of the Brønsted acid can go along with increased conductivity, likely also enhancing the contribution of proton hopping to the overall conductivity.[78] In addition to the molecular composition of the PIL, temperature may also affect the different molecular-level dynamics: Watanabe *et al.* have demonstrated that the activation energies associated with transport processes, such as Grotthuss-like proton transfer, rotational, and translational dynamics, differ.[72] As such, variation of temperature may be an efficient approach to tune the overall conductivity.

In the present study we explore how varying temperature can modulate the subtle balance between these different transport dynamics. We use [Mim][AcOH]/[MimH][TFA] mixtures to gain a deeper understanding of the interplay between different molecular

contributions: Can thermal energy break solvation cages that hinder the transport of ions?

To disentangle the different molecular-level dynamics, we use dielectric relaxation spectroscopy (DRS). DRS provides information about the dynamics of dipolar species as well as the translational motion of ionic species (e.g., conductivity) via the polarization dynamics.[74–77] To guide the interpretation of the experimental spectra, we use computational spectra based on polarizable molecular dynamics (MD) simulations, which can disentangle rotational and translational contributions to the dielectric response at the molecular level.[66, 78, 177]

Our data show that both, PIL composition and temperature affect the contribution of hindered translations to the dielectric response. Our data suggest that hindered ionic translations are thermally enhanced, yet increasing temperature shifts the maximum of the conductivity – reflecting mobile ions – to PIL compositions with less hindered translations and higher ionicity. Our results thus offer routes to optimizing of the performance of PILs as electrolytes.

6.3 Results and Discussion

6.3.1 Temperature-Dependent Dielectric Spectra

In this study, we explore the dynamics of molecules and ions in PIL mixtures with [Mim] as the Brønsted base. We systematically vary the protonation equilibrium within the PILs by gradually substituting [AcOH] for [TFA] as the corresponding Brønsted base. To assess the PIL dynamics at different time- (and length-)scales, we recorded the dielectric spectra at frequencies ranging from 0.1 GHz to 125 GHz, in line with our earlier work.[78, 104] To better discriminate between frequency-dependent translational and rotational contributions to the dielectric response and to explore the impact of thermal motions on the ion dynamics, we perform temperature-dependent studies from 15 °C to 65 °C.

With the dielectric spectra, we probe the macroscopic polarization dynamics of the samples as a function of an externally applied oscillating electric field of frequency ν. For dipolar liquids the measured polarization is typically expressed as the complex permittivity $\hat{\varepsilon}(\nu)$:[98]

$$\hat{\varepsilon}(\nu) = \varepsilon'(\nu) - \mathrm{i}\varepsilon''(\nu) \tag{6.1}$$

where the real part $\varepsilon'(\nu)$ is the dielectric permittivity and the imaginary part $\varepsilon''(\nu)$ is the dielectric loss. Considering liquids that consist of molecules with a permanent dipole moment μ_i, the polarization induced by an external electric field (in the case of dielectric relaxation spectroscopy in the microwave regime) mostly stems from the reorientation of these dipolar species. At low external field frequencies, the dipolar molecules align according to the external field, giving rise to a macroscopic polarization. As the field frequency increases, the dipolar molecules are no longer able to follow the external field, leading to a phase shift of the polarization that results in an absorption peak in the imaginary part $\varepsilon''(\nu)$ and a dispersion step in the real part $\varepsilon'(\nu)$. For charged molecules, the frequency-dependent translational motion of ions – the conductivity $\sigma(\nu)$ – contributes together with $\hat{\varepsilon}(\nu)$ to the generalized dielectric spectrum $\Sigma(\nu)$. Typically, the contribution of freely translating ions (represented by the dc conductivity) σ_0 is subtracted from both the experimental and the computational generalized dielectric spectrum yielding $\Sigma_0(\nu)$.

$$\Sigma_0(\nu) = \hat{\varepsilon}(\nu) + \frac{\sigma(\nu) - \sigma_0}{\nu} 2\mathrm{i} + \varepsilon_\infty = \hat{\varepsilon}(\nu) + \vartheta_0(\nu) + \varepsilon_\infty \tag{6.2}$$

Thus, Σ_0 includes rotational contributions to the frequency-dependent polarization dynamics, but also frequency-dependent translational contributions (e.g., hindered conduction), $\vartheta_0(\nu)$. These rotational and frequency-dependent translational contributions to the generalized dielectric spectrum are intrinsically entangled in the experiment and unambiguous separation is only possible in combination with MD simulations. While these translational contributions (cage rattling dynamics) for ionic liquids are often

observed to predominantly contribute at high frequencies[208], MD simulations have indicated that such translational dynamics contribute significantly (up to nearly 50 %) to the generalized dielectric spectrum at low frequencies for the [AcOH]-PIL and are reduced upon substitution of [AcOH] by [TFA].[66, 78]

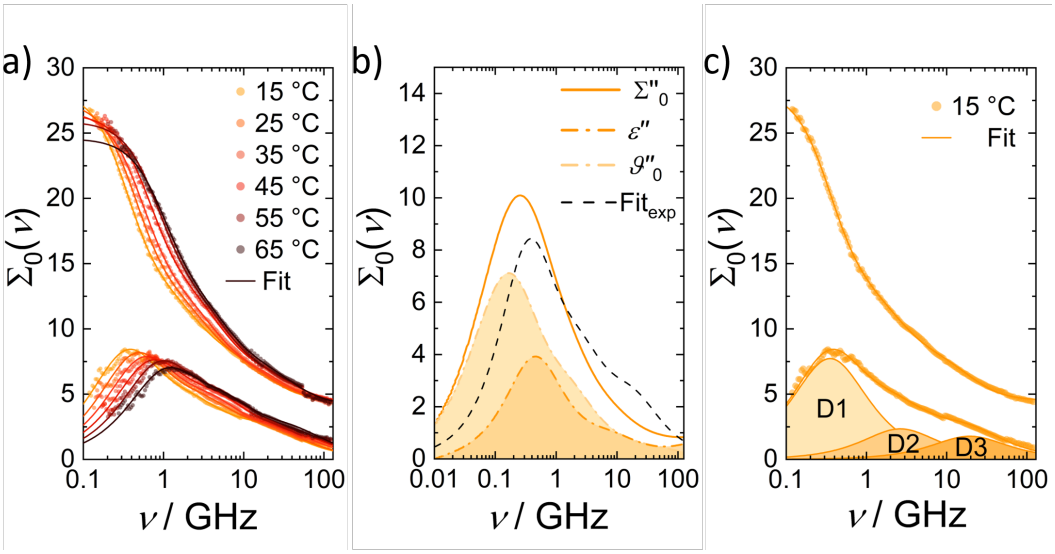

FIGURE 6.1: a) Generalized dielectric spectra, $\Sigma_0'(\nu)$ and $\Sigma_0''(\nu)$, for a [Mim][AcOH]/[MimH][TFA] mixture with $\chi(\mathrm{Ac}) = 0.9$ at temperatures ranging from 15 to 65 °C. Symbols show experimental data and solid lines the fit with the relaxation model (Eq. 6.3). b) Computational $\Sigma_0''(\nu)$ spectrum (imaginary part of the generalized dielectric spectrum) of a [Mim][AcOH]/[MimH][TFA] mixture with $\chi(\mathrm{Ac}) = 0.9$ at 15 °C. Colored dashed lines represent rotational (ε'') and translational (ϑ_0'') contributions to $\Sigma_0''(\nu)$. Dashed black line represents the fitted experimental data shown in panel a). c) Decomposition of the experimental $\Sigma_0''(\nu)$ spectrum of the [Mim][AcOH]/[MimH][TFA] mixture with $\chi(\mathrm{Ac}) = 0.9$ at 15 °C. Symbols represent experimental data and solid lines the fit according to Equation 6.3. Shaded areas indicate the contribution of the three Debye type relaxations (D1, D2 and D3) to the spectrum.

Figure 6.1a) shows the experimental spectra at a composition $\chi(\mathrm{Ac}) = 0.9$ as a function of temperature. As common to ionic liquids, the spectra are rather broad and featureless.[77, 212] Nevertheless, there is a dominant contribution to the dielectric loss of the spectra peaking at ~0.4 GHz at 15 °C. This asymmetrically broadened peak shifts to higher frequencies with increasing temperature, indicating an acceleration of the underlying molecular dynamics. In addition, the amplitude of the loss peak somewhat decreases with increasing temperature. Contributions at frequencies >10 GHz appear to be rather insensitive to varying temperature. The trends at other PIL compositions that were liquid over the studied temperature range resemble those observed for the PIL with $\chi(\mathrm{Ac}) = 0.9$ (see Figure 6.6a)–c)).

The total computed $\Sigma_0''(\nu)$ spectrum in Figure 6.1b) of the PIL mixture $\chi(\mathrm{Ac}) = 0.9$ at 15 °C and the experimental spectra (black dashed line in Figure 6.1b)) agree well, with

only a moderate shift of the computational results to lower frequencies as compared to the experimental data. In addition, there is a slight difference in amplitude for both the dominant contributions at low frequencies and the contribution at ~20 GHz. Decomposition of the computational spectrum into rotational and translational contributions shows that the rotational contribution, $\varepsilon''(\nu)$, dominates $\Sigma_0''(\nu)$ mainly at low frequencies, with a maximum at ~0.2 GHz. Additionally, there is a significant translational contribution, $\vartheta_0''(\nu)$, to $\Sigma_0''(\nu)$, with a maximum at around ~0.4 GHz. As such, the MD simulations show that at 15 °C for χ(Ac)=0.9, the rotational and translational contributions at the prevailing dielectric loss peak (at ~0.4 GHz) are comparable in magnitude: The MD simulations demonstrate marked contributions due to hindered translations to the predominant loss peak at <1 GHz.
To quantify the contributions at different frequencies to the experimental spectra, we fit a relaxation model consisting of three Debye-type relaxation modes to the experimental spectra:[104]

$$\hat{\varepsilon}(\nu) = \frac{S_1}{1 + (2\pi \mathrm{i}\nu\tau_1)} + \frac{S_2}{1 + (2\pi \mathrm{i}\nu\tau_2)} + \frac{S_3}{1 + (2\pi \mathrm{i}\nu\tau_3)} + \varepsilon_\infty + \frac{\sigma_0}{2\pi \mathrm{i}\nu\varepsilon_0} \tag{6.3}$$

where S_j and τ_j are the relaxation amplitudes and times, respectively. The high-frequency limit of the permittivity ε_∞ includes all polarization dynamics that are not accessible in the frequency range covered here. The fit parameters are listed in Tables 6.2-6.8 in the supplementary information. In Figure 6.1c) we exemplary show the contribution of the three Debye-type relaxation modes to the dielectric loss for $\chi(\mathrm{Ac}) = 0.9$ at 15 °C (D1 at ~0.4 GHz, D2 at ~3 GHz, D3 at ~20 GHz). We note, that due to the partial proton transfer in [Mim][AcOH],[66, 104] in our mixed systems of [Mim][AcOH] and [MimH][TFA] a variety of ionic and neutral molecular species exist (e.g., Mim, AcOH, $\mathrm{MimH^+}$, $\mathrm{AcO^-}$, $\mathrm{TFA^-}$).[104] Due to this molecular complexity and in light of the overlapping translational and rotational dynamics inferred from the computational results, the fit should merely be considered as a formal description of the experimental data. The relaxation modes represent various dynamics of different molecular-level origins. Nevertheless, the fit parameters allow quantifying trends in the polarization dynamics in different frequency ranges as a function of composition and temperature, which we analyze in more detail in the subsequent section.

6.3.2 Analysis of the Effective Dipole Moments

Although the experimental data do not allow for an unambigious decomposition into rotational and translational contributions, analysis of the fit parameters can provide further insights into these contributions: Assuming that only the rotation of dipolar species contributes to $\Sigma_0''(\nu)$, the thermal motion should counteract the orientational motion of the dipoles in the external field. Therefore, the decrease in the experimental amplitude S_j with increasing temperature T should be described by equation Eq.

6.4.[114] To test this hypothesis, we calculate the effective dipole moment $\mu_{\mathrm{eff},j}$ from the experimentally obtained data.

$$\frac{2\varepsilon_\mathrm{s}+1}{\varepsilon_\mathrm{s}} S_j = \frac{N_\mathrm{A} c_j}{k_\mathrm{B} T \varepsilon_0} \mu_{\mathrm{eff},j}^2 \tag{6.4}$$

with the static permittivity $\varepsilon_s = \varepsilon_\infty + \sum S_j$, the Avogadro constant N_A, the concentration of the relaxing species c_j, the Boltzmann constant k_B and the temperature T.

Since we do not distinguish between different molecular species, we assume that the concentration c_j is the total concentration (e.g., $c_j = c_\mathrm{acid} + c_\mathrm{base} = c_\mathrm{Mim} + c_\mathrm{AcOH} + c_\mathrm{TFA}$). The total concentration was estimated from the measured densities at 298 K and the respective sample composition.

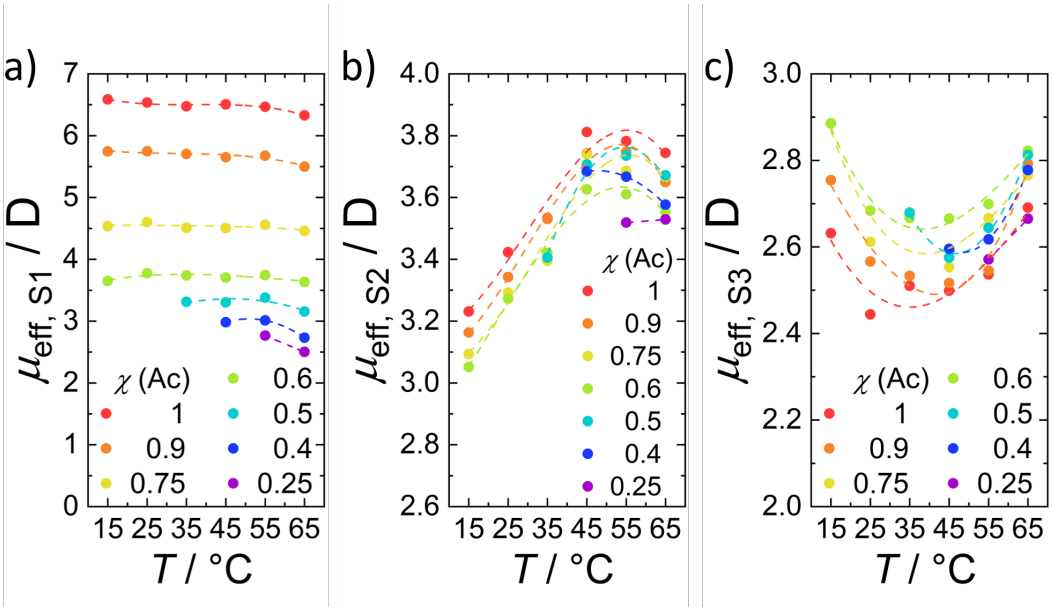

FIGURE 6.2: a) Effective dipole moment $\mu_{\mathrm{eff},1}$ calculated from the amplitude of the low-frequency Debye-type relaxation D1 as a function of temperature for all PIL compositions. b) Effective dipole moment $\mu_{\mathrm{eff},2}$ calculated from the amplitude of the intermediate Debye-type relaxation D2 as a function of temperature for all PIL compositions. c) Effective dipole moment $\mu_{\mathrm{eff},3}$ calculated from the amplitude of the high frequency Debye-type relaxation D3 as a function of temperature for all PIL compositions. Dotted lines are a guide to the eye.

Figure 6.2 shows the effective dipole moments $\mu_{\mathrm{eff},j}$ calculated from the respective relaxation amplitude S_j of the Debye-type relaxation modes (D1, D2, and D3) as a function of temperature for all PIL compositions. As can be seen from Figure 6.2a) $\mu_{\mathrm{eff},1}$ moderately changes with temperature. However, the composition of the PIL has a strong influence on $\mu_{\mathrm{eff},1}$. As χ(TFA) increases, the effective dipole moment decreases significantly. Thus, the rotational motion of an individual dipolar species cannot explain the decreasing amplitude S_1 of the D1 mode with decreasing χ(Ac), and also, the values of the dipole moments are inconsistent with the potentially contributing

species.[104] As such, this analysis is the experimental confirmation of the marked translations contributions to the spectra at this frequency range. In light of marked contributions due to hindered translational dynamics shown in Figure 6.1b), a decrease of the amplitude (i.e., effective dipole moment) with decreasing χ(Ac) suggests a decrease of the length over which ions can diffuse (or a decrease of their charge).
In contrast, as shown in Figure 6.2b) & c), $\mu_{\mathrm{eff},2}$ and $\mu_{\mathrm{eff},3}$ show only moderate changes upon varying PIL composition and temperature, consistent with a dominant mechanism of the underlying dynamics being insensitive to temperature. Also, the absolute values of the dipole moments, ranging from 2 to 4 D, are closer to the DFT-based dipole moments of individual molecular species than to those of ion pairs (upper boundary $\mu_{\mathrm{Mim}}^{\mathrm{DFT}} \approx 5.5\,\mathrm{D}$, lower boundary $\mu_{\mathrm{AcOH}}^{\mathrm{DFT}} \approx 2.5\,\mathrm{D}$).[104] We note, that assuming not all species contributing to the higher frequency relaxations (i.e., $c_j = c_{\mathrm{acid}} = c_{\mathrm{base}}$ in Eq. 6.4) would results in elevated ranges for the experimentally observed dipoles ($\mu_{\mathrm{eff,S1}}$ would range between ~9 D and ~3.5 D and $\mu_{\mathrm{eff,S2}}$ and $\mu_{\mathrm{eff,S3}}$ would fall between ~5 D and ~3.7 D). Consistent with a predominantly rotational contribution, the calculated effective dipole moments of the higher frequency relaxations hardly vary with temperature: The experimental relaxation amplitudes of D2 and D3 can be well described via the Boltzmann distribution of dipolar species in an external electric field with the field-dipole energy as Boltzmann factor.

6.3.3 Comparison of the Activation Energies

To gain further insight into the temperature dependence of the observed dynamics, we analyze the temperature dependence of the relaxation times τ_j of the respective relaxation modes, as well as the conductivity σ_0 via the Arrhenius equation:[252]

$$\ln \tau_j = \ln \tau_0 + \frac{E_{\mathrm{A}}}{RT} \tag{6.5}$$

with the pre-exponential factor τ_0 (ordinate intercept in the plot $\ln \tau$ vs T^{-1}), the activation energy E_{A} and the universal gas constant R.

Figure 6.3a)-c) shows the $\ln \tau_j$ vs. T^{-1} plot for the [Mim][AcOH]/[MimH][TFA] mixtures with the composition $\chi(\mathrm{Ac}) = 1$, $\chi(\mathrm{Ac}) = 0.9$, $\chi(\mathrm{Ac}) = 0.75$ and $\chi(\mathrm{Ac}) = 0.6$. Figure 6.3d) shows the Arrhenius plot for the conductivity of the above-mentioned PIL compositions. From the slopes of the respective linear fits, we calculated the activation energies, which are listed in Table 6.1.
Based on Table 6.1, the calculated values for E_{A} (τ_3) seem to be rather independent of the composition and are in the range of 14 to 15 kJ mol^{-1}. Similarly, E_{A} (τ_2) ranges from 12.9 to 15.3 kJ mol^{-1}. The activation energy, E_{A} (τ_1), is higher ranging from 16 to 18 kJ mol^{-1}. The similarity of the activation energies for τ_2 and τ_3 may point to a similar molecular origin. Assuming dipolar rotations dominate these dynamics, their similar activation behavior likely reflects the temperature-dependent hydrodynamic properties of the PILs. E_{A} (τ_1) is higher than E_{A} (τ_2). Within the margin of error, E_{A} (τ_1)

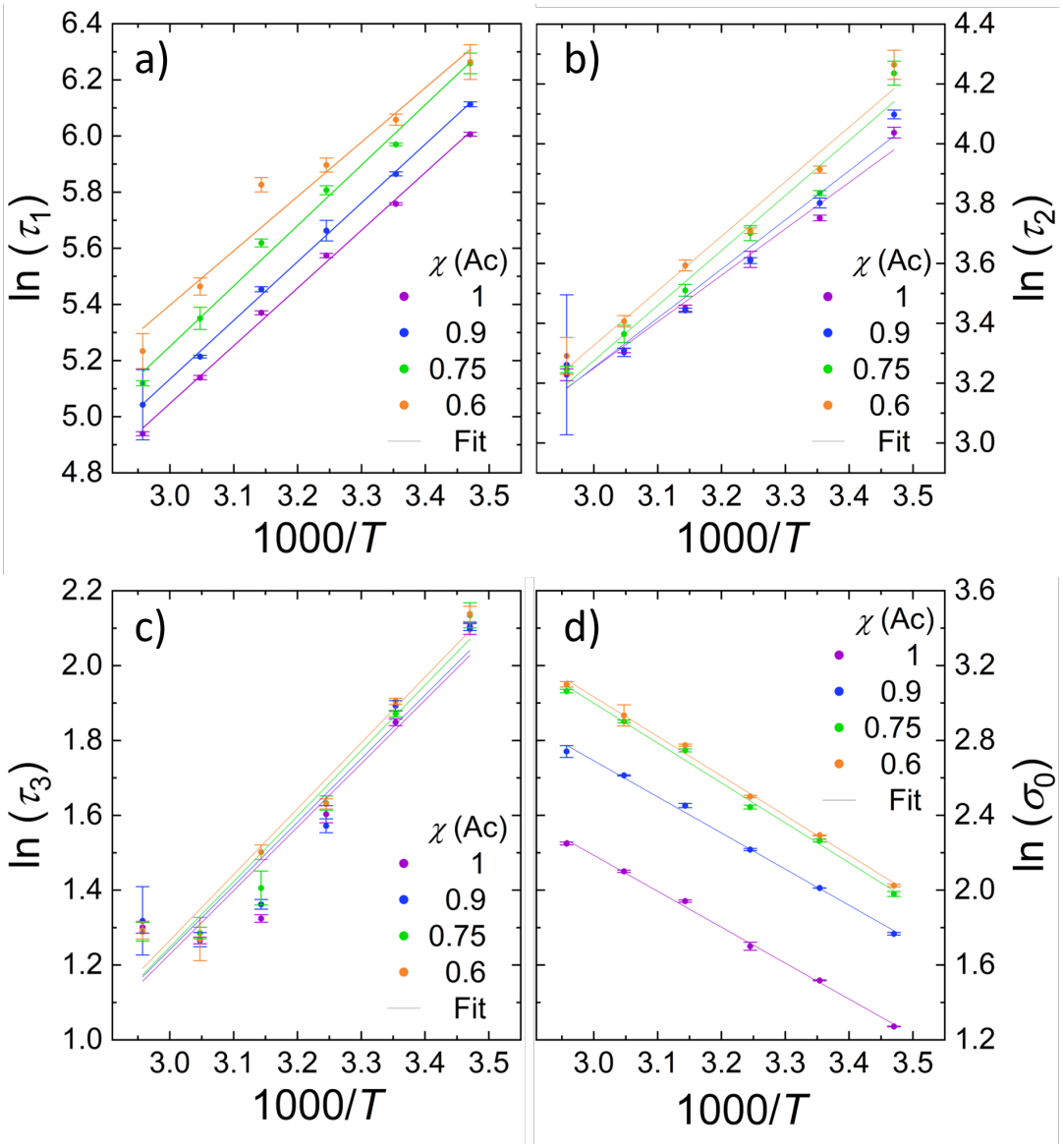

FIGURE 6.3: a)-c) Arrhenius plot ($\ln(\tau_j)$ vs. T^{-1}) for the experimental relaxation times τ_j of the respective relaxation mode (e.g., D1, D2 and D3) according to Equation 6.3 for the PIL compositions $\chi(\mathrm{Ac})= 1-0.6$. Symbols represent experimental data, solid lines the linear fit. d) Arrhenius plot for the experimental conductivity σ_0 for the PIL compositions $\chi(\mathrm{Ac})= 1-0.6$. Symbols represent experimental data, solid lines the linear fit.

exceeds $E_\mathrm{A}(\tau_3)$, although not as markedly as compared to $E_\mathrm{A}(\tau_2)$. Nonetheless, the elevated activation energy for the D1 relaxation mode compared to the other relaxation modes highlights the different origin of its dynamics. Although the activation of the D1 relaxation may in part reflect a temperature-induced change in the relative contribution of rotational and transnational contributions, its marked translational contributions suggest that the activation energy reflects the motion of the ions in the cages together with the thermally induced changes to the cages. In this context, it is interesting to note that the values of $E_\mathrm{A}(\tau_1)$ coincide with $E_\mathrm{A}(\sigma_0)$. As such, fluctuations of ions in their cages and transport of ions that have escaped the cage are correlated, similar to

TABLE 6.1: Calculated activation energies E_A for each relaxation time τ_j of the respective relaxation mode and of the conductivity σ_0.

χ(Ac)	$E_A(\tau_1)$ [kJ mol^{-1}]	$E_A(\tau_2)$ [kJ mol^{-1}]	$E_A(\tau_3)$ [kJ mol^{-1}]	$E_A(\sigma_0)$ [kJ mol^{-1}]
1	17.1 ± 0.4	12.9 ± 0.9	14.1 ± 2.2	16.2 ± 0.3
0.9	17.4 ± 0.3	13.7 ± 1.3	14.1 ± 2.3	16.7 ± 0.5
0.75	17.9 ± 0.9	15.3 ± 1.4	14.5 ± 1.7	18.1 ± 0.5
0.6	16.1 ± 1.8	15.2 ± 1.2	14.6 ± 1.5	18.6 ± 0.6

what has been suggested for aqueous electrolytes.[253]

6.3.4 Relative Translational Contribution

To assess the thermally induced changes to the relative contributions to the dielectric response, which also influence the thermal activation discussed above, we determined the temperature-dependent computational spectra for the PIL composition χ(Ac)=0.9. In Figure 6.4, we show the relative frequency-dependent translational contribution $(\vartheta_0''(\nu)/\Sigma_0''(\nu))$ as extracted from the simulated dielectric spectra.

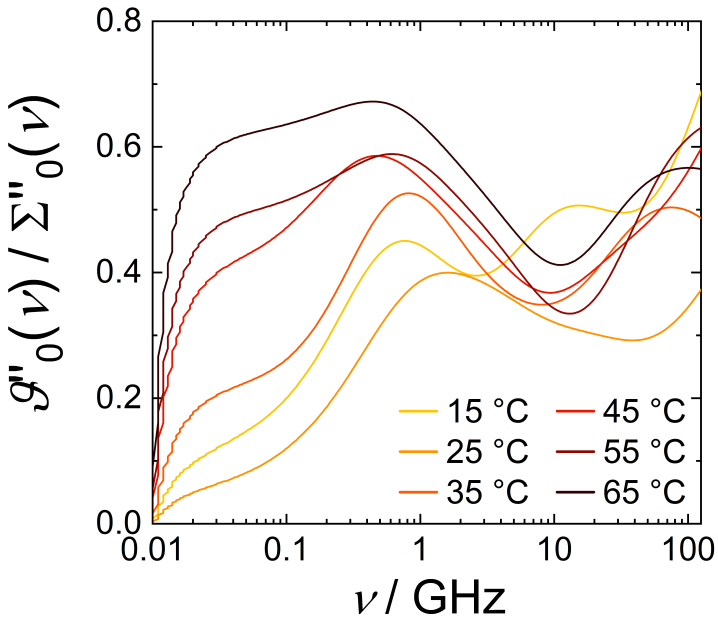

FIGURE 6.4: Relative translational contribution of $\vartheta_0(\nu)$ to $\Sigma_0''(\nu)$ for the PIL composition χ(Ac)=0.9 and χ(TFA)=0.1 at different temperatures obtained from MD simulations.

We find that the temperature-dependent changes of the contribution of $\vartheta_0''(\nu)$ in the frequency range above ~0.5 GHz are rather small (consistent with the experimentally found temperature insensitivity of D2 and D3). For low frequencies at ~$0.01 - 0.1$ GHz,

we find a significant increase in the relative translational contribution to $\Sigma_0''(\nu)$. Thus, the rise in temperature results in enhanced amplitudes of the hindered translation, while the contribution of reorientational alignment is counteracted at elevated T.[79] Yet, also dipolar correlations, which are present in these PILs[78] may contribute to the observed changes. The data in Figure 6.4 suggest that the relative contribution of translational dynamics does not seem to shift in frequency; rather, the magnitude of the contribution at lower frequencies is altered with temperature. This suggests that the activation energies of the relaxation times discussed above hardly reflect changes in the underlying dynamics of the observed relaxations – whether translational or rotational.

6.3.5 Analysis of the Experimental Conductivity

Our results collectively show that both composition (χ(TFA)) and temperature alter the hindered translations of ions in the PIL. The question arises as to how these parameters and the change in the caging of the ions affect the macroscopic conductivity, i.e., the free translation of ions as reflected in the conductivity σ_0. In Figure 6.5, we show the conductivity σ_0 as a function of PIL composition in the temperature range of $15-65\,^{\circ}\mathrm{C}$.

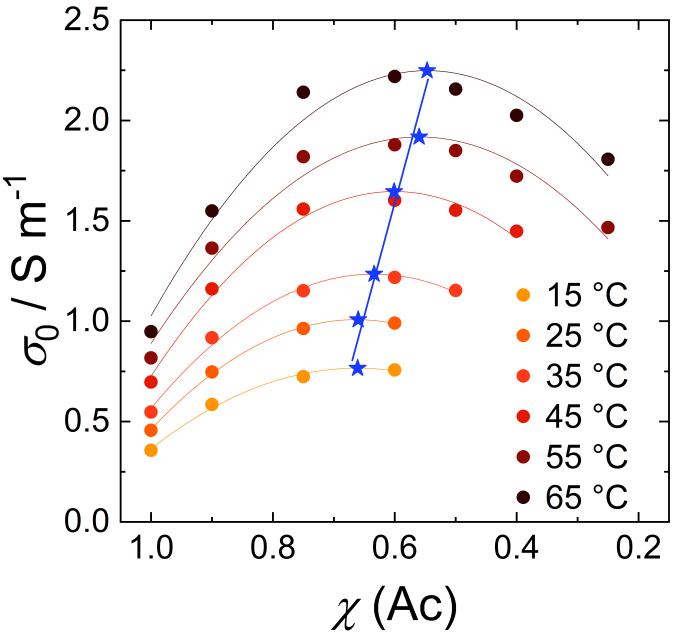

FIGURE 6.5: Experimental conductivity, σ_0, as a function of the PIL mixture's composition in the temperature range from $15\,^{\circ}\mathrm{C}-65\,^{\circ}\mathrm{C}$. Experimental data were fitted with a parabola (solid lines). Maxima of the conductivity, $\sigma_0^{\max}$, were extracted from the fit (blue symbols). The temperature-dependent shift of $\sigma_0^{\max}$ is indicated by the solid blue line.

The conductivity increases with increasing χ(TFA) due to an increasing number of ionic species.[104] However, at high χ(TFA) σ_0 decreases with increasing χ(TFA). This behaviour is attributed to the increasing viscosity due to the substitution of Ac by TFA. As expected, σ_0 increases with increasing temperature as thermal energy increases molecular mobility. Interestingly, the maximum of the conductivity, $\sigma_0^{\max}$, shifts towards higher χ(TFA) with increasing temperature. To visualise the latter, we fitted a parabola to the conductivity vs composition for each temperature to determine $\sigma_0^{\max}$, marked by the stars in Figure 6.5. This fit functions resembles the "conductivity dome" reported for many ionic liquids.[254, 255] Indeed, the blue line indicates the shift of $\sigma_0^{\max}$ with T. In other words, at high χ(Ac) increasing temperature results in a less pronounced increase in conductivity, as compared to intermediate χ(Ac). This implies that at high χ(Ac) enhanced thermal fluctuations go along with a less pronounced increase in ionic mobility as compared to intermediate compositions. Keeping in mind that hindered translations prevail at high χ(Ac), this shift in maximum implies that increasing temperature seems to be insufficient to break up the solvation cages that hinder the ions' translational motion to a significant extent, so that the fraction of free (mobile) ions increases at the expense of ions that are hindered in their cages. Rather, increasing temperature enhances the spatial magnitude of the hindered translations as demonstrated in Figure 6.4. Nevertheless, thermal changes to the balance between hindered and mobile ions are rather subtle and only moderately affect the thermally induced changes to the conductivity, σ_0, of these PILs. The predominant variation of conductance is governed by the marked increase of conductance with increasing temperature at all compositions.

6.4 Conclusion

In this study, we explore the temperature-dependent dynamics of 1-methylimidazolium-based PILs using a combination of experimental and computational DRS. We find a slight decrease in amplitude and a shift of the dominant relaxation in the experimental dielectric spectra to higher frequencies with increasing temperature, indicating an acceleration of the overall dynamics. We formally describe the experimental spectra with three Debye-type relaxations. The effective dipole moments derived from the relaxation amplitudes of the higher frequency relaxations are rather insensitive to temperature changes and to the PIL composition, consistent with significant rotational contributions. The similar activation energies of the D2 and D3 relaxation modes suggest that the underlying dynamics are little affected by temperature.
In contrast, the lower frequency relaxation has marked temperature-dependent contributions due to hindered translations of ions in their solvation cages, as demonstrated by computational spectra. These translational contributions result in large variations of the effective dipole moments, which are extracted assuming purely rotational contributions. Also, the thermal activation energy of this relaxation coincides with the activation energy of the conductivity, rather than the higher frequency relaxation modes. The magnitude of these hindered translations increases with increasing temperature, as demonstrated by the decomposition of the computational spectra. Remarkably, the temperature dependence of the maximum of the macroscopic conductivity as a function of composition shifts to higher TFA contents, where caging of ions is overall weaker. The thermally induced increase of the conductivity at low TFA contents, where marked caging of ions occurs, is less pronounced. These results collectively suggest that increasing temperature results in enhanced fluctuations of ions in their solvation cages, yet thermal energy is insufficient to markedly break up these cages. Understanding these rather subtle effects of temperature on the PIL dynamics at the molecular level may help understand the performance of PILs as electrolytes and support a task-specific design of PILs.

6.5 Supplementary Information

Dielectric Relaxation Spectroscopy

Dielectric Spectra

The dielectric spectra for the PIL compositions that were liquid over the whole temperature range (χ(Ac)=1, χ(Ac)=0.75 and χ(Ac)=0.6; see previous part for χ(Ac)=0.9) are shown in Figure 6.6 a)-c). Equation 6.3 was used to fit all complex permittivity spectra. The trends discussed in the main text are valid for all PIL compositions: the main contribution (~0.4 GHz) shifts towards higher frequencies with increasing temperature, and the amplitude of the contribution decreases slightly. However, contributions at frequencies above 10 GHz seem to be rather insensitive to temperature changes.

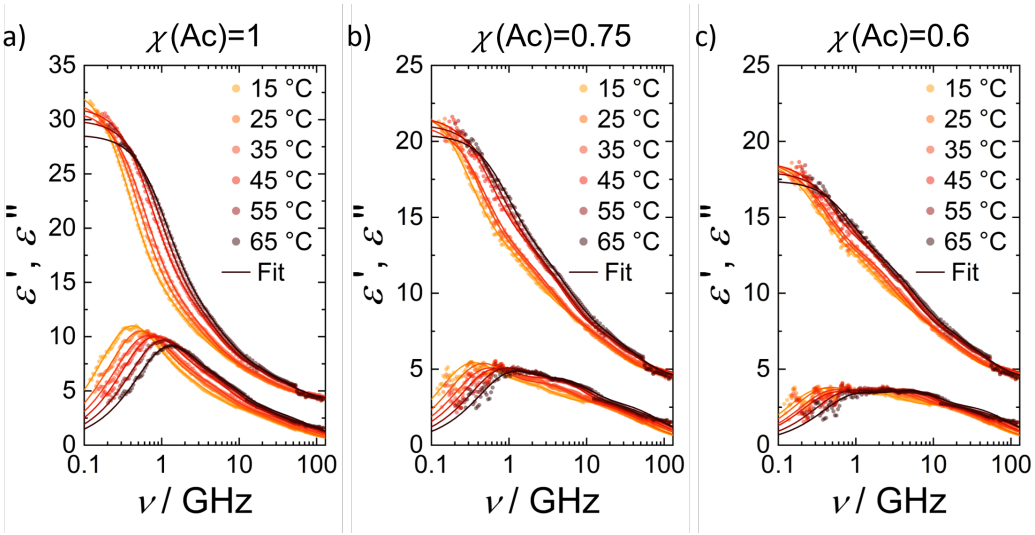

FIGURE 6.6: Complex permittivity spectra as a function of temperature (in the range of 15 - 65 °C). a) Spectra for PIL composition of χ(Ac)=1 and χ(TFA)=0, respectively. b) Spectra for PIL composition of χ(Ac)=0.75 and χ(TFA)=0.25. c) Spectra for PIL composition of χ(Ac)=0.6 and χ(TFA)=0.4.

Fit Parameters

The dielectric spectra in the main text and those shown in Figure 6.6 were modelled using three Debye-type relaxation modes (see eq. 6.3). Tables 6.2−6.8 show the temperature-dependent parameters obtained from the fit, i.e., permittivity ε_j, amplitude S_j and relaxation time τ_j of the respective relaxation mode for the different PIL compositions. ε_∞ is the limiting permittivity at very high frequencies (including polarization dynamics not covered by the experimental frequency range) and σ_0 the conductivity (translational contribution of charged species).

Table 6.2: Temperature dependent fit parameters for χ(Ac)=1 and χ(TFA)=0 according to eq. 6.3 of the main text.

T / °C	ε_1	ε_2	ε_3	ε_∞	S_1	S_2	S_3	τ_1 / ps	τ_2 / ps	τ_3 / ps	σ_0 / S m^{-1}
15	33.1	12.6	7.7	4.4	20.5	4.9	3.3	406	57	8	0.36
25	31.9	12.4	7.0	4.3	19.5	5.3	2.7	317	43	6	0.46
35	30.9	12.4	6.9	4.1	18.5	5.5	2.8	263	37	5	0.55
45	31.1	13.0	6.8	4.2	18.1	6.2	2.7	215	32	4	0.70
55	29.9	12.6	6.7	4.1	17.3	5.9	2.7	171	27	4	0.82
65	28.6	12.6	7.0	4.1	16.1	5.6	2.9	140	25	4	0.95

Table 6.3: Temperature dependent fit parameters for χ(Ac)=0.9 and χ(TFA)=0.1 according to eq. 6.3 of the main text.

T / °C	ε_1	ε_2	ε_3	ε_∞	S_1	S_2	S_3	τ_1 / ps	τ_2 / ps	τ_3 / ps	σ_0 / S m^{-1}
15	28.2	12.8	8.1	4.5	15.4	4.7	3.5	452	60	8	0.59
25	27.4	12.5	7.5	4.5	14.9	5.0	3.0	352	45	7	0.75
35	26.7	12.5	7.0	4.2	14.2	5.4	2.8	288	37	5	0.92
45	26.5	13.0	7.0	4.4	13.5	5.9	2.7	234	31	4	1.16
55	25.9	12.7	6.9	4.2	13.2	5.8	2.7	184	27	4	1.36
65	24.6	12.6	7.3	4.2	12.0	5.3	3.1	155	26	4	1.55

Table 6.4: Temperature dependent fit parameters for χ(Ac)=0.75 and χ(TFA)=0.25 according to eq. 6.3 of the main text.

T / °C	ε_1	ε_2	ε_3	ε_∞	S_1	S_2	S_3	τ_1 / ps	τ_2 / ps	τ_3 / ps	σ_0 / S m^{-1}
15	22.4	12.9	8.5	4.6	9.5	4.4	3.8	523	69	8	0.72
25	21.9	12.4	7.6	4.6	9.4	4.8	3.0	391	46	6	0.96
35	21.1	12.3	7.4	4.3	8.8	5.0	3.1	333	40	5	1.15
45	21.6	13.1	7.3	4.6	8.5	5.8	2.7	276	33	4	1.56
55	21.1	12.7	7.2	4.3	8.4	5.5	2.9	211	29	4	1.82
65	20.4	12.6	7.3	4.3	7.8	5.3	3.0	167	26	4	2.14

Table 6.5: Temperature dependent fit parameters for χ(Ac)=0.6 and χ(TFA)=0.4 according to eq. 6.3 of the main text.

T / °C	ε_1	ε_2	ε_3	ε_∞	S_1	S_2	S_3	τ_1 / ps	τ_2 / ps	τ_3 / ps	σ_0 / S m^{-1}
15	18.8	12.7	8.5	4.7	6.1	4.2	3.8	525	71	8	0.76
25	18.7	12.5	7.7	4.6	6.3	4.7	3.2	428	50	7	0.99
35	18.3	12.4	7.4	4.4	6.0	5.0	3.0	364	41	5	1.22
45	18.6	13.0	7.5	4.6	5.7	5.4	2.9	339	36	4	1.60
55	18.0	12.4	7.2	4.3	5.6	5.2	2.9	236	30	4	1.88
65	17.4	12.3	7.4	4.3	5.1	4.9	3.1	187	27	4	2.22

Table 6.6: Temperature dependent fit parameters for χ(Ac)=0.5 and χ(TFA)=0.5 according to eq. 6.3 of the main text.

T / °C	ε_1	ε_2	ε_3	ε_∞	S_1	S_2	S_3	τ_1 / ps	τ_2 / ps	τ_3 / ps	σ_0 / S m^{-1}
35	16.8	12.2	7.4	4.4	4.6	4.9	3.0	385	43	5	1.15
45	17.3	12.8	7.3	4.6	4.4	5.6	2.7	376	37	4	1.55
55	17.1	12.6	7.1	4.3	4.5	5.5	2.8	272	32	4	1.85
65	16.3	12.5	7.4	4.4	3.8	5.2	3.0	250	32	4	2.16

Table 6.7: Temperature dependent fit parameters for χ(Ac)=0.4 and χ(TFA)=0.6 according to eq. 6.3 of the main text.

T / °C	ε_1	ε_2	ε_3	ε_∞	S_1	S_2	S_3	τ_1 / ps	τ_2 / ps	τ_3 / ps	σ_0 / S m^{-1}
45	16.3	12.7	7.2	4.4	3.6	5.5	2.7	411	38	4	1.45
55	15.9	12.3	7.0	4.3	3.6	5.3	2.7	277	34	4	1.72
65	14.8	12.0	7.1	4.2	2.8	4.9	2.9	214	31	4	2.03

Table 6.8: Temperature dependent fit parameters for χ(Ac)=0.25 and χ(TFA)=0.75 according to eq. 6.3 of the main text.

T / °C	ε_1	ε_2	ε_3	ε_∞	S_1	S_2	S_3	τ_1 / ps	τ_2 / ps	τ_3 / ps	σ_0 / S m^{-1}
55	14.5	11.6	6.7	4.2	3.0	4.8	2.6	216	32	4	1.47
65	14.0	11.7	7.0	4.3	2.4	4.7	2.7	181	30	4	1.81

Chapter 7

Insights into Proton Transfer Intermediates and Dynamics in Solution of the Protic Ionic Liquid 1-Methylimidazolium Acetate from Transient Spectroscopy

7.1 Abstract

While protic ionic liquids (PILs) have the potential to address the issue of slow diffusive charge transport by facilitating proton transfer – thereby separating charge movement from the physical movement of ions – the specific contribution of proton transport to overall conductivity and the underlying mechanism are not yet fully understood. Using femtosecond visible pump–infrared probe spectroscopy, we study the proton transfer from the photoacid 8-hydroxypyrene-1,3,6-trisulfonic acid (HPTS) to proton acceptors in 1-methylimidazolium acetate [Mim][OAc] in MeOH to specifically isolate the proton contribution to the overall charge carrier dynamics. The release of an excess proton is triggered by photoexcitation of the HPTS with a 400 nm pump pulse. A second laser pulse, centered on the carbonyl stretching vibration frequency, is used to monitor the protonation of acetic acid species in real time after transport through the sample. Transient spectra revealed two spectral features at frequencies common to carbonyl (C=O) stretching vibrations, an induced absorption and a bleach, associated with the protonation of acetate and acetic acid, respectively. These results indicate that both the $AcO^- \rightleftharpoons AcOH$ and the $AcOH \rightleftharpoons AcOH_2^+$ equilibria are of fundamental importance to the proton transfer dynamics in [Mim][OAc]. Moreover, our results give experimental proof that the protonated acetic acid species, $AcOH_2^+$, is the active molecular species enabling Grotthuss-like transport in [Mim][OAc]. Varying the PIL concentration allowed us to extract the transport times. The results show that the transport times scale with the average distance between proton donor and acceptor. A comparison of the proton diffusion coefficients observed by NMR measurements in the neat PIL scenario versus those estimated from the concentration-dependent transient spectra of [Mim][OAc]/MeOH mixtures revealed that the latter exhibit higher values. This suggests that MeOH enhances proton transport through its ability to form extended H-bonded networks. The proton diffusion coefficients of the PIL/MeOH mixtures, determined from concentration-dependent transport times, exhibit higher values compared to those of neat MeOH reported in the literature. This indicates that Mim may act as a proton acceptor, contributing to proton transport and, consequently, leading to an overestimation of the calculated proton diffusion coefficient. In general, our results suggest that proton transfer plays a significant role in the charge carrier dynamics in [Mim][OAc]. However, in the investigated system, proton transfer is rather complex and seems to involve many ionic and electro-neutral molecular species and depends on the respective protonation equilibria.

7.2 Introduction

Proton transfer reactions are fundamental chemical processes, that play a pivotal role in a wide range of biological and chemical systems.[138, 256–258] Such reactions include the transfer of a proton from a donor to an acceptor and can, in principle, be simply described via the following reaction equation: $HA + B^- \rightleftharpoons A^- + HB$.[80] In such a scenario, the number and efficiency of proton transfer events is typically governed by the acidity and basicity of the donating Brønsted acid (HA) and the accepting Brønsted base (B^-).[258]

However, not only the properties of the proton donors and acceptors but also the properties of the solvent environment are important for an adequate description of proton transfer reactions.[259, 260] In aqueous media, an extended H-bonded network between water molecules is formed, allowing for a Grotthuss-type proton transfer leads to high H^+ mobilities.[261, 262] Thus, to facilitate Grotthuss-like proton transport, molecular species acting simultaneously as proton donor and acceptor are necessary.[71] High charge carrier mobilities are especially desirable for electrolytes in energy storage technologies.[71]

Protic ionic liquids (PILs), formed by reversible proton transfer between Brønsted acids and bases, are promising candidates for applications in next-generation batteries.[57, 192, 197, 201, 203] PILs are known to form extensive H-bonded networks and are, in principle, able to facilitate Grotthuss-type proton transport, allowing for high conductivities.[56, 57, 203] Especially for PILs, Grotthuss-like charge transport is desirable since the alternative vehicular-type mechanism is limited by the high viscosities of PILs.[55, 71]

An intensively studied PIL is 1-methylimidazolium acetate [Mim][OAc].[65, 72, 73] Although several experimental and computational studies have indicated, that [Mim][OAc] is dominated by neutral species[65, 66, 78, 104], the compound shows an unexpectedly high conductivity, that cannot be explained by simply considering the ratio of charged to electro-neutral species.[57, 61, 71].

Ab initio molecular dynamics (MD) simulations have indicated that Grotthuss-type conduction plays a significant role, primarily dominated by proton transfer between oxygen atoms within acetic acid/acetate molecules.[71] In addition, these simulations proposed that specifically chain-like structures of acetic acid allow for a Grotthuss-like transport mechanism with acetate molecules as terminating partner.[71] Furthermore, polarizable MD simulations studies required the explicit incorporation of proton transport via a Grotthuss-like mechanism, as opposed to solely relying on vehicular-type transport, to reproduce the experimental conductivity of [Mim][OAc].[66, 78]

In support of these findings by MD simulations, experimental studies have indicated, by comparison of the activation energies for translational and rotational diffusion, that such proton hopping contributes.[72] It has further been proposed that the transition of the conduction mechanism from vehicular to Grotthuss-type can be modulated by altering the acidity of the Brønsted acid in the PIL.[73] Consistent with Grotthuss-like

transport, Diffusion-Ordered Spectroscopy (DOSY) NMR experiments on [Mim][OAc] have indicated that proton mobility surpasses that of the corresponding acid and base molecules.[104] Despite such indirect evidence that the proton contributes to the overall charge carrier dynamics, direct experimental proof is still lacking.

The time-resolved study of the proton transfer reaction has become possible with the commercial availability of femtosecond lasers and the ability to observe ultrafast phenomena using spectroscopic techniques. Excitation of a photoacid with a short laser pulse enables a triggered release of a proton at a well-defined time. Nibbering *et al.* performed such ultrafast pump-probe spectroscopy using a photoacid to study the proton transfer in acid-base reactions in water.[262] Many other studies have extensively investigated proton transfer reactions in aqueous media using various spectroscopic techniques, including time-resolved absorption or fluorescence measurements.[261–264] A significant number of these studies are based on the photoacid 8-hydroxypyrene-1,3,6-trisulphonic acid (HPTS). Photoexcitation with a femtosecond laser pulse at 400 nm leads to a decrease in its pK_a value by about 6 units, and thus triggers the release of the hydroxylic proton. It has been shown that the proton transfer between HPTS and various carboxylates can be successfully studied by probing the vibrational response of the accepting base.[82, 261–264]

Here, we study the effect of the released proton on the acetic acid species in [Mim][OAc] by probing the vibrational response at ~1700 cm^{-1}, typical for the carbonyl stretching frequency of acetic acid, using femtosecond visible pump–infrared probe spectroscopy with HPTS. The transport time can be monitored in real time via a change in the vibrational response of acetate upon protonation.[80–82] To study the proton transport, we systematically vary the average transport distance between photoacid and acepting base by measuring different PIL concentrations in MeOH. To understand the spectral signatures of the PIL solution, we compare the PIL results with measured spectra of either sodium acetate (NaOAc) or AcOH in MeOH. In addition, measurements in AcO^-/AcOH mixtures will provide information about the protonation dynamics of AcOH relative to AcO^-. Our results show that protonation of both acetate and acetic acid occurs in the PIL mixture and in AcO^-/AcOH mixtures. The protonation of AcO^- gives rise to an induced absorption and the protonation of AcOH to a bleach. Our data provide experimental evidence, that $AcOH_2^+$ is the essential intermediate molecular species enabling Grotthuss-like proton transport in [Mim][OAc].

7.3 Results and Discussion

To elucidate the role of acetic acid species in proton transport within [Mim][OAc], we investigate solutions of the photoacid HPTS and the PIL in MeOH. Upon excitation of HPTS with 400 nm pump pulses, the hydroxylic (excess) proton is released into the PIL solution (see Figure 7.1 for a schematic representation). We monitor the dynamics of the excess proton via the vibrational response of the sample. For instance, protonation of the acetate anion results in a depletion of the absorption of the symmetric and asymmetric C−O stretching modes of the COO^- groups in the infrared spectra. Upon protonation these two modes decouple and the carbonyl stretching vibration (C=O) of the acetic acid emerges at ~1700 cm^{-1}. The emergence of such vibrational signatures are readily detected using a probe pulse centred at 1700 cm^{-1} via the transient spectra (i.e., difference spectrum, $\Delta\alpha$, between the pumped and unpumped sample). To unravel the proton dynamics, we follow the protonation of the acetate as a function of the delay time, t_w, between the pump and probe pulses, and the spectral response provides insights into the formed molecular species. Variation of the PIL concentration, and thus the acetate concentration, changes the average distance between photoacid and proton-accepting base. Assuming a homogeneous distribution of acetate molecules in the solution, the transport time as a function of distance can be tracked by performing concentration-dependent measurements.

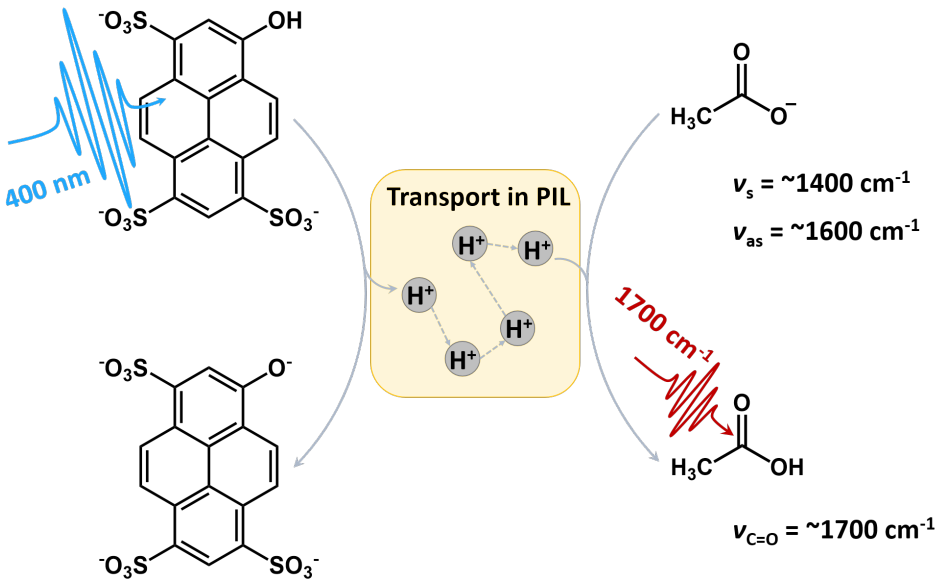

FIGURE 7.1: Schematic representation of the ultrafast visible pump–infrared probe experiment.

7.3.1 Transient Spectra of [Mim][OAc] in MeOH

Figure 7.2a) shows the transient signal, $\Delta\alpha$, as a function of frequency for different delay times, t_w, of 1 M [Mim][OAc] with 60 mM HPTS in MeOH. For early delay times, we observe a broad, featureless absorption covering the entire spectral detection range. At later delay times, two main spectral features emerge: a bleaching signal at ~1710 cm^{-1} and an induced absorption at ~1730 cm^{-1}.

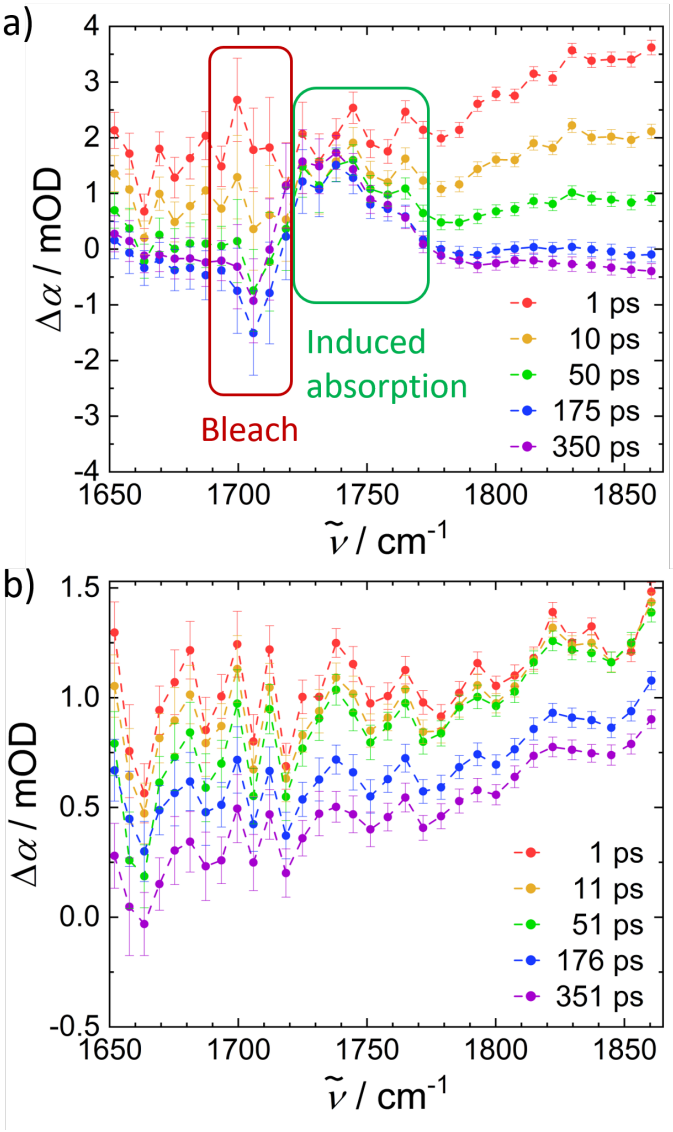

FIGURE 7.2: a) Transient spectra $\Delta\alpha$ of [Mim][OAc] (1 M) in MeOH with the photoacid HPTS (60 mM) as a function of frequency for different delay times between pump and probe pulse. b) Transient spectra $\Delta\alpha$ of the photoacid HPTS (50 mM) in MeOH as a function of frequency for different delay times. For early delay times, the broad absorption associated with solvated protons can be observed.

The observed spectral features partly resemble those documented in references[80, 82]: Solvated protons give rise to an induced absorption over a broad frequency range

at early times. Consistent with this notion, transient spectra for samples with only HPTS dissolved in MeOH (Figure 7.2b)) exhibit only this proton continuum and its amplitude decreases with increasing delay time.
Based on photoacid experiments in aqueous media[80, 82], the emergence of the carbonyl stretching band due to protonation of acetate is expected at ~1700 cm^{-1}. Our transient signals indeed show a broad absorption band at ~1730 cm^{-1} due to the protonation of acetate (e.g., formation of AcOH). The appearance of the induced absorption at late t_w indicates that the proton is first transferred via MeOH before reaching and protonating an acetate molecule. The slight shift of the acetate stretching vibration to higher wavenumbers in our PIL mixture in MeOH, as compared to the acetate stretching vibration in a NaOAc/D_2O mixtures[80], is likely due to the different solvation of acetic acid in water and MeOH, leading to different vibrational responses. Interestingly, we observe a bleaching signal at ~1710 cm^{-1} at late t_w – a frequency typically associated with the carbonyl stretching modes. No such bleach has been reported for acetate in D_2O in the literature.[80]
In general, this bleaching signal suggests that a molecular species with a vibrational mode at ~1710 cm^{-1} vanishes or the transition dipole moment of this vibrational mode decreases upon perturbation of the system with the pump pulse (i.e., in this case upon release of the excess proton). Since the absorption at 1710 cm^{-1} is characteristic of the C=O vibration, the bleach is presumably associated with AcOH (see FTIR spectra in the SI, Figures 7.8−7.10).
To elucidate the origins of the bleaching signal, it is crucial to note that [Mim][OAc] predominantly consists of electro-neutral molecular species – thus, acetic acid is also present in the PIL solution.[66, 104] Given the fact that the 1710 cm^{-1} absorption is typical for the C=O mode of AcOH, we hypothesize that the bleach is due to a transient reduction of AcOH species due to their protonation: $AcOH_2^+$ lacks a C=O absorption at 1710 cm^{-1}. This scenario is in fact supported by MD simulations, which demonstrate that such protonated acetic acid molecules ($AcOH_2^+$) are transiently formed in the PIL.[71] Furthermore, these simulations reveal that chains of the acetic acid, capable of simultaneously accepting and donating H^+, play an important role in Grothuss-like charge transport within [Mim][OAc].[71]

To explore if protonation of acetic acid species can explain the spectral signatures in Fig. 7.2a), we performed visible pump–IR probe experiments on i) sodium acetate (NaOAc)/MeOH mixtures with HPTS and ii) acetic acid/MeOH mixtures with HPTS. In scenario i), NaOAc should be almost completely deprotonated in solution, resulting in an induced absorption in the transient spectrum due to the protonation of the acetate. For scenario ii), only a bleach in the transient spectrum would be expected as a result of the protonation of the acetic acid.
Figure 7.3a) shows the transient spectra as a function of frequency of NaOAc in MeOH. Besides the moderate contribution of the broad proton continuum at early delay times, the transient signals are dominated by a broad induced absorption due to

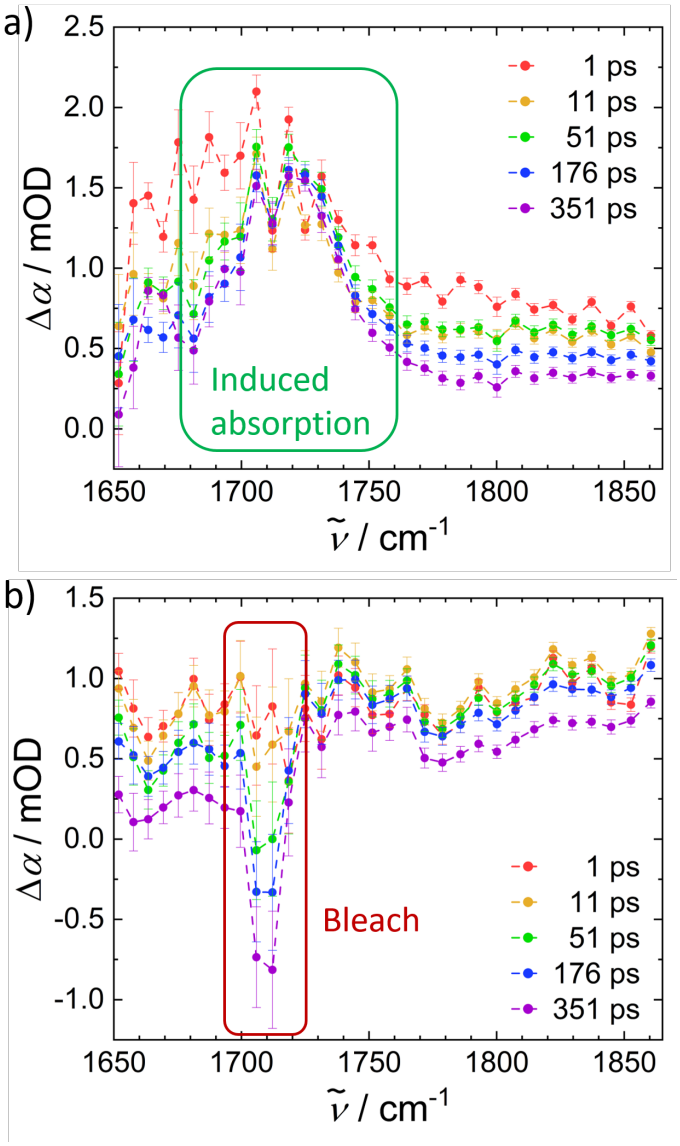

FIGURE 7.3: a) Transient spectra $\Delta\alpha$ of NaOAc (1 M) in MeOH with the photoacid HPTS (25 mM) as a function of frequency for different delay times between pump and probe pulse. b) Transient spectra $\Delta\alpha$ of AcOH (0.5 M) in MeOH with the photoacid HPTS (25 mM) as a function of frequency for different delay times between pump and probe pulse.

the protonation of the acetate molecules at ~1730 cm^{-1}. This observation is in line with experiments on aqueous solutions of NaOAc[80, 81, 138], and consistent with what one may expect for the proton-induced formation of acetic acid from acetate. Conversely, for solutions of acetic acid (Figure 7.3b)), we observe the broad proton continuum at early delay times, but at longer delay times, a narrow bleaching signal appears. As such, these experiments demonstrate that the narrow bleaching signal in the PIL solutions stems from protonation of acetic acid (e.g., formation of $AcOH_2^+$). The protonation of acetate would be expected to be favorable compared to the protonation of AcOH based on their pK_a values (p$K_a \approx 4.76$ for AcOH and p$K_a \approx -6.1$

for $AcOH_2^+$[265]). However, the transient absorption maxima and minima of the bleach and the induced absorption, observed for the PIL mixture in Fig. 7.2a), are approximately equal. The resulting ratio, $\frac{\Delta\alpha(\text{ind abs})}{\Delta\alpha(\text{bleach})}$, is expected to be proportional to the ratio of the acid association constants, $\frac{K_a(\text{ind abs})}{K_a(\text{bleach})}$, and consequently, by definition ($pK_a = -\log K_a$), to the pK_a values of AcOH and its protonated form $AcOH_2^+$. Note, that this relationship represents a simplified model, as for example, the total concentration of the respective molecular species also significantly affects the intensity ratio. In addition, the following pK_a values are, in the strict sense, only valid for aqueous conditions. In the case of AcOH ($pK_a \approx 4.76$) and $AcOH_2^+$ ($pK_a \approx -6.1$)[265] and a resulting difference of $\Delta pK_a \approx 11$, the acetate molecules should favorably undergo protonation. As a result, the ratio of the acid association constants, $\frac{K_a(\text{ind abs})}{K_a(\text{bleach})}$, should approach infinity. Observations from Fig. 7.2a) indicate that the ratio, $\frac{\Delta\alpha(\text{ind abs})}{\Delta\alpha(\text{bleach})}$, is approximately 1, suggesting that the pK_a values alone are not sufficient to elucidate the observed intensities in the transient spectra. Nonetheless, it is pertinent to note that the referenced pK_a values correspond to the aqueous case and, thus, may be different in the case of the neat PIL and its solution in MeOH. The latter implies that in the context of MeOH as the solvent, as in this study, ΔpK_a may be reduced compared to aqueous conditions.

It is important to note that the line width of the induced absorption in Figure 7.3a) is markedly broader than the line width of the beaching signal in (Figure 7.3b)). These differences in line widths demonstrate that acetic acid molecules that are generated by protonation of OAc^- give rise to a broader and somewhat red-shifted absorbance, as compared to the acetic acid molecules that are depleted upon protonation. Such differences for acetic acid can only be explained by their differing environment, such as interaction with MeOH or acetic acid. Apparently, only a subset of acetic acid molecules can be protonated by the photoacid.

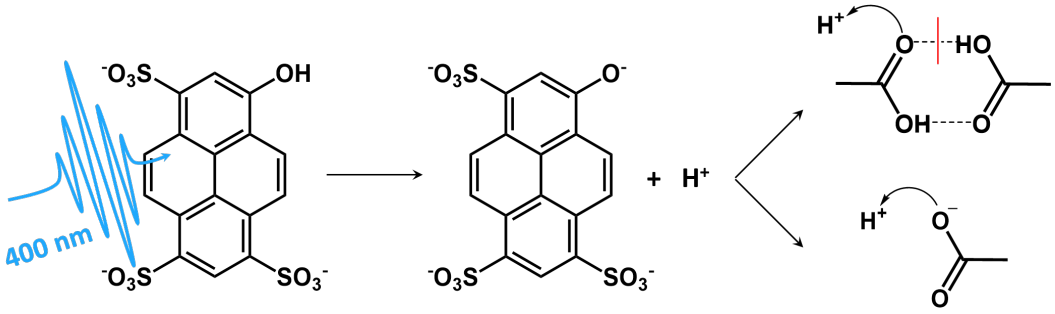

FIGURE 7.4: Schematic representation of the excitation of HPTS and resulting release of a proton, which either leads to the cleavage of a cyclic acetic acid dimer or the protonation of acetate.

Acetic acid is known to form a number of aggregates, both pure and in solution, such as cyclic dimers, chain-like structures, etc.[217] Some studies, by decomposition of IR spectra of AcOH in solution, proposed that the cyclic dimer C=O stretching vibration occurs at ~1710 cm^{-1}.[218] In light of these earlier findings that acetic acid

homodimers give rise to a vibrational band at ~1710 cm^{-1}[218], our findings suggest that protonation of acetic acid homodimers gives rise to the narrow beaching signal (see Figure 7.4 for a schematic representation). Conversely, other molecular species that contain acetic acid and contribute to the broad absorption band at ~1730 cm^{-1} are apparently not affected by the excess protons.
Together, the spectral signatures of the photoacid experiments evidence that in our PIL solution the induced absorption can be related to the protonation of acetate and the bleach to the protonation of acetic acid. In turn, our results imply that both acetate and acetic acid are proton acceptors in the PIL solutions (see Figure 7.4 for a schematic representation) and are therefore intermediates that contribute to proton transport in this PIL.

To elucidate the protonation ratios of AcOH relative to AcO^-, we performed pump-probe measurements of acetic acid/sodium acetate mixtures with HPTS in methanol. Figure 7.5 shows transient spectra for various delay times for mixtures with differing AcOH/AcO^- molar ratios. For early delay times, the proton continuum is present and, as discussed above, its intensity decreases with time.

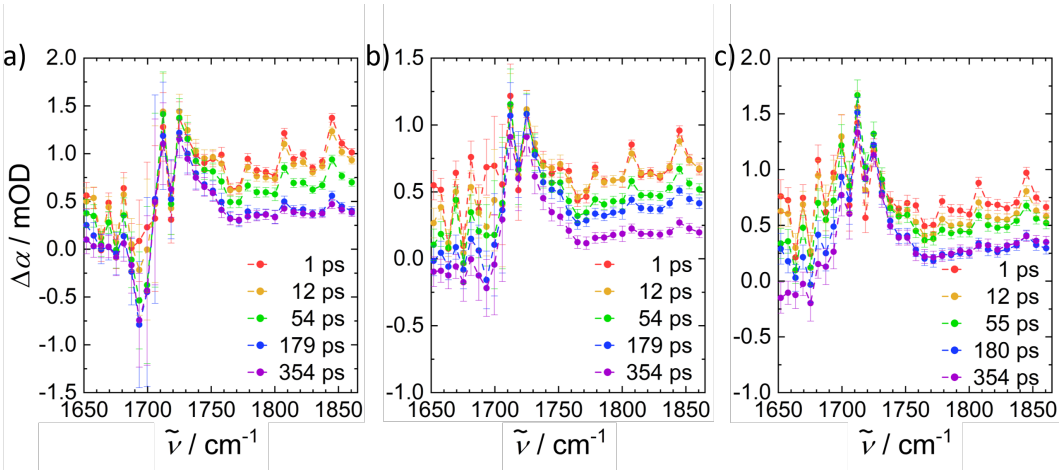

FIGURE 7.5: Transient spectra $\Delta\alpha$ of a) AcOH (0.75 M) and NaOAc (0.25 M) with 25 mM HPTS in MeOH, b) AcOH (0.5 M) and NaOAc (0.5 M) with 25 mM HPTS in MeOH and c) AcOH (0.25 M) and NaOAc (0.75 M) with 25 mM HPTS in MeOH.

For the mixture of 0.75 M AcOH and 0.25 M AcO^- (Figure 7.5a)), a pronounced bleach at ~1700 cm^{-1} and an induced absorption at ~1720 cm^{-1} can be observed, similar to the spectral characteristics found for the PIL in MeOH. The observed spectral features can be related to the protonation of acetate and acetic acid as explained in the previous section. Alterations in the AcOH/AcO^- ratio towards a higher acetate concentration minimally impact the intensity of the induced absorption. Conversely, a reduction in acetic acid concentration leads to the disappearance of the bleach. In the case of the 0.5 M AcOH/0.5 M AcO^- mixture (Figure 7.5b)) the bleach at ~1700 cm^{-1} is hardly discernible. For the 0.25 M AcOH and 0.75 M AcO^- mixture (Figure 7.5c)), no bleaching signal can be discerned. Assuming that the bleaching in

the transient spectra is due to the protonation of acetic acid dimers, its absence for the AcOH (0.25 M)/AcO^- (0.75 M) mixture suggests that dimers are nearly non-existent at these concentrations.

From these findings for varying molar ratios of AcO^- and AcOH, we can conclude that protonation of acetic acid occurs exclusively when there is a excess of AcOH, relative to acetate. In addition, this conclusion aligns with the transient spectra of the PIL, considering that [Mim][OAc] consists of ~70 % of electro-neutral species[66, 104] (e.g., excess of AcOH).

Thus, transient absorption experiments on acetic acid/acetate mixtures in MeOH consolidate our interpretation that in the spectra of the PIL solution, the induced absorption can be related to the protonation of acetate and the bleach to the protonation of acetic acid. Moreover, these results indicate that not only the $AcO^- \rightleftharpoons$AcOH protonation equilibrium but also the AcOH$\rightleftharpoons AcOH_2^+$ equilibrium plays a crucial role in the proton transfer dynamics.

7.3.2 Concentration-Dependent PIL Measurements

As mentioned previously, the strong absorption due to the carbonyl stretching vibration of acetic acid in [Mim][OAc] prevented us from measuring transient absorption experiments in a neat PIL sample. Nonetheless, by altering the [Mim][OAc] concentration in the PIL/MeOH mixtures, we can obtain the transport time as a function of distance (HPTS to acetate). The latter allows for extrapolation of the transport time of the neat PIL. Note that the concentration of the neat PIL is 7.55 M. Therefore, we measured the following PIL concentrations with a constant photoacid concentration (50 mM) in MeOH: 0.1 M, 0.25 M, 0.5 M, and 0.75 M. The photoacid concentration for the 1 M PIL sample is slightly higher (60 mM).

As can be seen from the transient spectra discussed earlier (Figure 7.2a), the spectral contrast between the transient signals of the proton continuum and the emerging acetic acid band at ~1730 cm^{-1} is rather weak. This indicates that the decay rate of solvated protons is comparable to the formation rate of acetic acid and, in addition, that the spectral intensities of both species are comparable at this frequency. Hence, the time-dependent decay of the proton continuum should contain equivalent information (e.g., the time taken for the proton to protonate an acetate molecule after being released from the photoacid). In literature, this is typically addressed by subtracting the proton continuum from the transient spectrum.[80, 81, 259] Here, we analyze the time-dependent decay of the proton continuum in the range 1800−1861 cm^{-1}. This, we achieve by determining the error weighted average of the transient signals at 1800−1861 cm^{-1}, and fitting a single exponential decay function to the experimentally obtained time traces:

$$N(t_w) = N_0 \exp(-t_w/\tau) \tag{7.1}$$

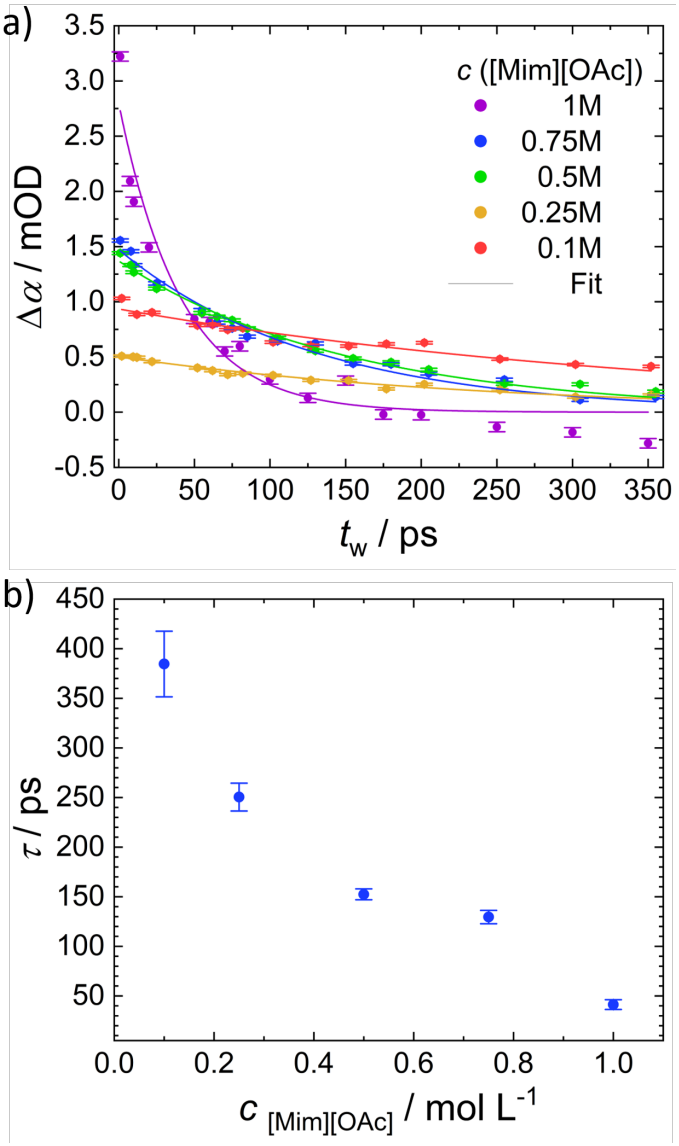

FIGURE 7.6: a) Transient signals averaged from 1800−1861 cm^{-1} of [Mim][OAc] with 50 mM HPTS in MeOH as a function of pump-probe delay time for different PIL concentrations. Symbols represent experimental data (with corresponding errors) and lines represent the respective fit according to Equation 7.1. b) transport time τ according to Equation 7.1 (with corresponding errors) as a function of PIL concentration.

Figure 7.6a) shows the concentration-dependent averaged time traces (transient absorption $\Delta\alpha$ as a function of the delay time between pump and probe pulse) with the fit according to Equation 7.1. As already apparent from the raw data, the signal of the proton continuum decreases more rapidly with increasing PIL concentration. This acceleration of proton dynamics is also reflected in the values of τ obtained from the fits, which excellently describe the experimental data (Figure 7.6a)). The thus obtained transport times displayed in Figure 7.6b) decrease from 385 ps for the 0.1 M PIL sample to 41 ps for the 1 M PIL sample. The transport time scales with the mean distance between the proton donor and the proton acceptor. This distance and, thus,

the transport time decreases with increasing concentration of [Mim][OAc].
To extrapolate the time taken for the proton to protonate an acetate molecule after being released from the photoacid for the case of neat [Mim][OAc] (e.g., $c = 7.55\,\mathrm{M}$), we plot the transport times τ as a function of the average distance between two accepting base molecules (e.g., $(N_\mathrm{A} \cdot c_{[\mathrm{Mim}][\mathrm{OAc}]})^{-1/3}$; see Figure 7.7). However, as apparent from the linear fit in Figure 7.7, extrapolation to the neat PIL case, indicated by the star-shaped symbol, yields a transport time $\tau < 0$. This observation may indicate that mainly faster transport via the H-bonded network of MeOH contributes to the overall proton transport in our system. Thus, extrapolating the transport time to the neat PIL case solely based on our experimental results is rather insufficient. Note that this extrapolation assumes the medium between the donor and acceptor to remain constant. However, as the PIL concentration increases, the medium transitions from being MeOH-rich to containing an increasing number of MeOH-PIL structures. Additional information, such as the separated molecular contributions obtained from MD simulations would be required to improve the extrapolation model.

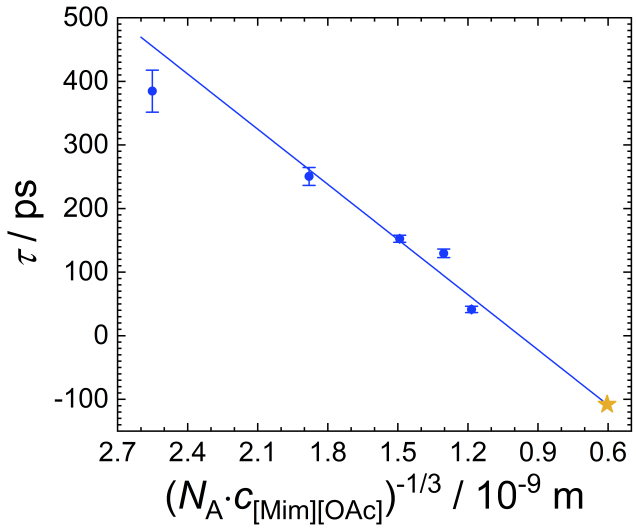

FIGURE 7.7: Transport times τ as a function of the average distance between two accepting base molecules, $(N_\mathrm{A} \cdot c_{[\mathrm{Mim}][\mathrm{OAc}]})^{-1/3}$. The average distance is $0.6 \cdot 10^{-9}\,\mathrm{m}$ for the case of the neat PIL ($c = 7.55\,\mathrm{M}$). The solid line represents the linear fit (fit eq.: $y = 2.9 \cdot 10^{10} x - 282.5$). The extrapolated neat PIL case is represented by the orange star-shaped symbol.

From the transport times and the respective concentrations, we calculated the average proton diffusion coefficient. We estimated the volume per accepting base molecules via the number of base molecules (from $c_{[\mathrm{Mim}][\mathrm{OAc}]}$) in a given volume. The average mean square displacement was estimated by the average distance between two base molecules (e.g., the radius of spherical volume per molecule), giving the diffusion coefficient by dividing by the transport time. Calculated diffusion coefficients are given in Table 7.1. This rough estimation of the diffusion coefficient for PIL concentrations ranging from 0.1 M to 0.75 M indicates a minimal dependency on PIL concentration. It is

TABLE 7.1: Estimated proton diffusion coefficients based on the transport times for different concentration of [Mim][OAc].

$c_{[\mathrm{Mim}][\mathrm{OAc}]}$ / $\frac{\mathrm{mol}}{\mathrm{L}}$	D / 10^{-9} $\frac{\mathrm{m}^2}{\mathrm{s}}$
0.1	6.51
0.25	5.43
0.5	5.62
0.75	5.05
1	13.07

interesting to note that the calculated diffusion coefficient for the 1 M PIL solution, $D = 13.07 \cdot 10^{-9}\ \frac{\mathrm{m}^2}{\mathrm{s}}$, is larger by a factor of 2 than the calculated values of D for the lower concentrations of [Mim][OAc]. This significant increase of D for the 1 M PIL solution in MeOH may suggest that considering a diluted PIL solution in MeOH is not appropriate at higher $c_{[\mathrm{Mim}][\mathrm{OAc}]}$ (e.g., formation of PIL structures at higher c_{PIL}, which in turn enhances D).

Compared to the proton diffusion coefficient for neat [Mim][OAc] of $D_{\mathrm{neat}}^{\mathrm{NMR}} \approx 0.25 \cdot 10^{-9}\ \frac{\mathrm{m}^2}{\mathrm{s}}$ found by DOSY NMR experiments[104], the calculated average value of D is larger by a factor of 20. Given the fact that the measured sample solutions contain [Mim][OAc] in concentrations of $c_{[\mathrm{Mim}][\mathrm{OAc}]} = 0.1 - 1\ \frac{\mathrm{mol}}{\mathrm{L}}$, methanol contributes significantly to the proton transport and, thus, may facilitate the latter, leading to the discrepancy between D and $D_{\mathrm{neat}}^{\mathrm{NMR}}$.

The proton diffusion coefficient in neat methanol is reported to be $D_{\mathrm{MeOH}} \approx 2.5 \cdot 10^{-9}\ \frac{\mathrm{m}^2}{\mathrm{s}}$[266], which is a factor of 2 lower than our calculated value for D.

In addition, the diffusion coefficient, $D_{\pm}$, can be estimated from the equivalent ionic conductivity, $\lambda_{\pm}$, via the Nernst-Einstein relation:[83]

$$\lambda_{\pm} = \frac{z_i^2 F^2}{RT} D_{\pm} \tag{7.2}$$

Therefore, we used the ionic conductivity of protons in MeOH, $\lambda_+ = 138.4\ \mathrm{S\,cm^2\,g\text{-}eq^{-1}}$[267] and $T = 298\,\mathrm{K}$, to calculate the proton diffusion coefficient in MeOH via Eq. 7.2, resulting in $D_+ \approx 3.7 \cdot 10^{-9}\ \frac{\mathrm{m}^2}{\mathrm{s}}$. The obtained value of D_+ exceeds the literature value, D_{MeOH}, yet remains below the experimentally derived value, D. In this context, it is important to note that the simplicity of the applied calculation model may contribute to the deviation of D from the reported values D_{MeOH} and D_+.

In addition, our experimental approach is not sensitive to the protonation of 1-methylimidazole. If Mim also acts as a proton acceptor (e.g., the proton continuum signal decreases due to the formation of [$\mathrm{MimH^+}$]), the mean distance between proton donor and acceptor would be overestimated and, consequently, D would be as well. Thus, the higher calculated values for D of the PIL/MeOH solution compared to

literature values for neat MeOH may suggest that [$MimH^+$] contributes to the proton transport in [Mim][OAc].

7.4 Conclusion

In the present study, we specifically investigate the proton contribution to the charge carrier dynamics in [Mim][OAc] in MeOH using femtosecond visible pump–IR probe spectroscopy. In accordance with previous studies about proton transport, we found a broad absorption in the transient spectra at early delay times, typical for solvated protons. At later delay times, transient spectra of the PIL solution showed two distinct spectral features, namely an induced absorption and a bleach at ~1730 cm^{-1} and ~1710 cm^{-1}, respectively. The induced absorption is associated with the protonation of acetate, whereas the bleach is associated with the protonation of acetic acid. This interpretation was confirmed by experiments in neat AcOH and NaOAc solutions in MeOH.

The narrower line width of the bleach compared to the induced absorption indicates that only a sub-ensemble of AcOH molecules is protonated in solution. Since AcOH is prone to form aggregates in solution, the observed narrower linewidth may indicate the H^+-induced disruption of such hydrogen-bonded acetic acid structures.

Measurements of AcOH/AcO^- mixtures suggest that AcOH is exclusively protonated in the presence of an excess of acetic acid, relative to acetate.

In line with the prevalence of electro-neutral AcOH in [Mim][OAc], the intensity ratio of the induced absorption and the bleach observed in the transient spectra of the PIL/MeOH mixture support this notion. Proton transport times, extracted by varying PIL concentrations, correlate with proton donor-acceptor distances. Proton diffusion coefficients, estimated from experimental proton transport times in [Mim][OAc]/MeOH solutions, exceed those obtained from DOSY NMR experiments of the neat PIL, but are comparable in magnitude to proton diffusion coefficients in neat MeOH. This suggests that MeOH enhances proton transport via its ability to form extensive hydrogen-bonded networks.

According to MD simulations studies[71], proton-accepting molecular species, such as Mim or AcO^-, may participate as terminating partners but are limited to supporting only vehicular-type conduction. In our experimental approach, however, we are only able to detect the protonation of AcO^-/AcOH. To further elucidate the role of Mim in the proton transfer dynamics, additional experiments or MD simulations would be required.

MD studies have shown, that $AcOH_2^+$ is the only molecular species in [Mim][OAc] capable of facilitating Grothuss-like proton tranport via the ability to simultaneously accept and donate protons.[71, 244] Our findings experimentally demonstrate the existence of $AcOH_2^+$ in [Mim][OAc] and its crucial role in enabling Grotthuss-like proton transport in the PIL. Thus, our results highlight the multifaceted role of molecular species and equilibria in governing proton transport dynamics within ionic liquids and deepen the understanding of how to specifically tune proton transfer for application-based PILs.

7.5 Supplementary Information

Fourier Transform Infrared Spectroscopy

To identify the relevant vibrational bands that exhibit alterations in the transient spectra, FTIR specta were measured of the respective species. Consequently, measurements of 1M solutions of acetic acid (AcOH), sodium acetate (NaOAc), and 1-methylimidazolium acetate ([Mim][OAc]) in methanol (MeOH) were conducted.

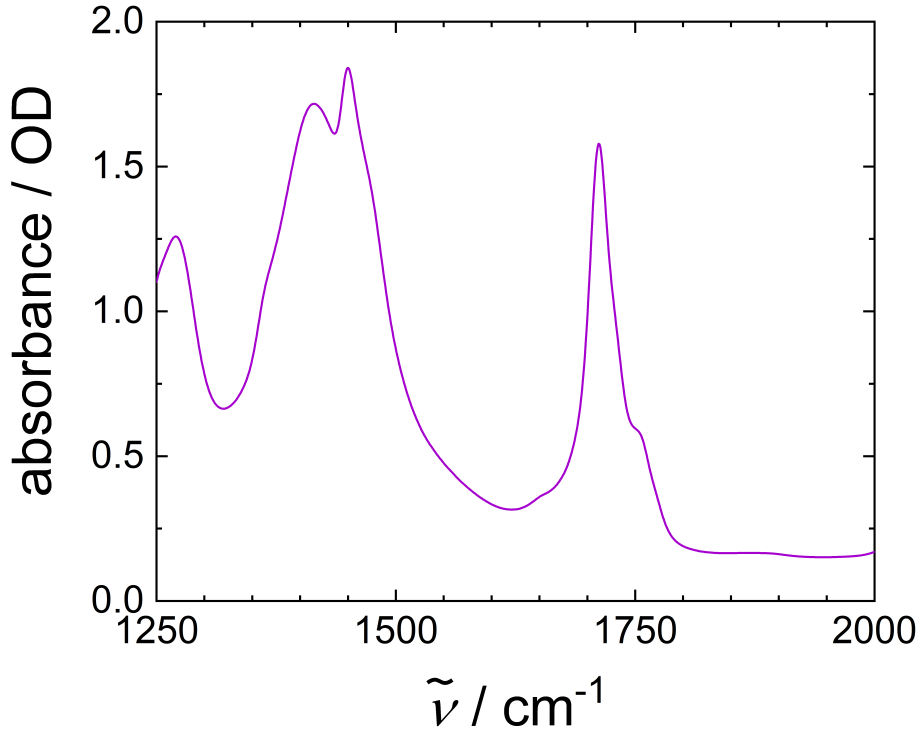

FIGURE 7.8: FTIR spectrum of 1 M AcOH in MeOH in the relevant frequency range. C=O stretching vibration is located at ~1710 cm^{-1}.

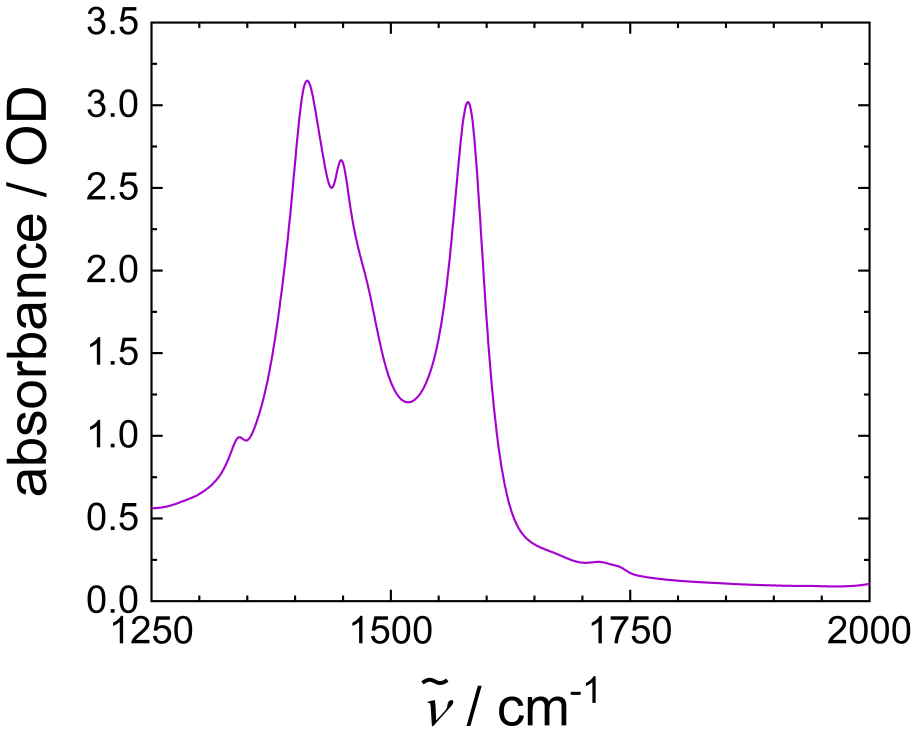

FIGURE 7.9: FTIR spectrum of 1 M NaOAc in MeOH in the relevant frequency range. The asymmetric COO^- stretching vibration is located at ~1600 cm^{-1}. The symmetric COO^- stretching vibration is located at ~1400 cm^{-1} but covered from MeOH's -CO stretching vibration.

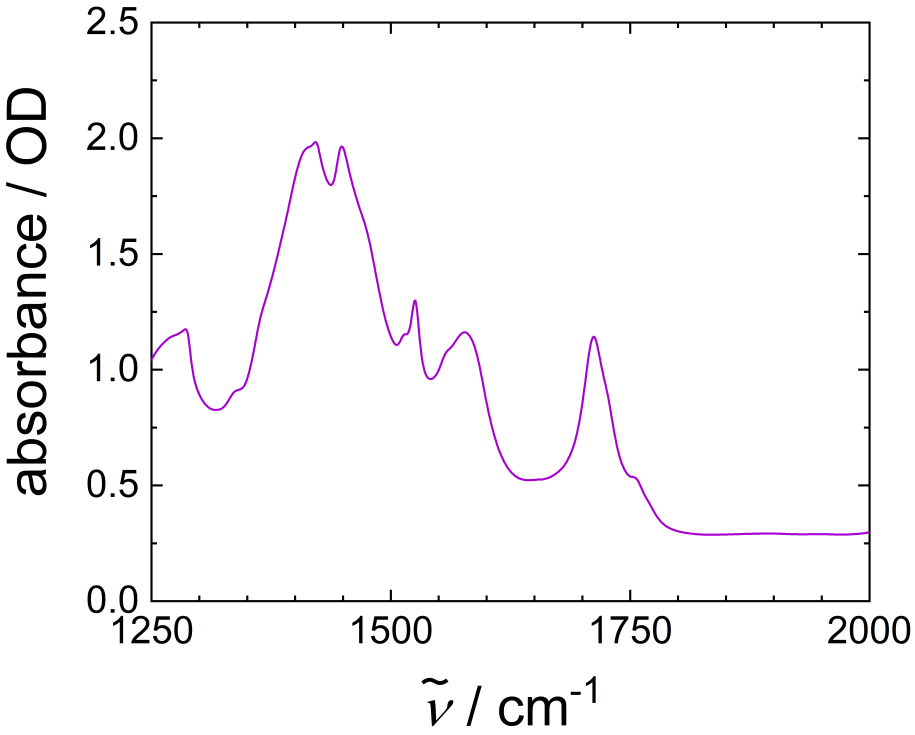

FIGURE 7.10: FTIR spectrum of 1 M [Mim][OAc] in MeOH in the relevant frequency range. C=O stretching vibration due to electroneutral AcOH molecules in [Mim][OAc] is located at ~1710 cm^{-1}.

Chapter 8

Conclusion and Outlook

The study presented in this thesis delves into the complex intermolecular interactions and charge transport dynamics in 1-methylimidazolium-based protic ionic liquids, in particular examining the effects of systematic anion substitution from acetate to trifluoroacetate. Via the combination of various experimental and computational techniques, such as dielectric relaxation spectroscopy, nuclear magnetic resonance spectroscopy, polarizable molecular dynamics simulations, and visible pump-infrared probe spectroscopy, my results elucidate the molecular-level properties and dynamics, e.g., proton distributions, macroscopic conductivity, translational and rotational dynamics, proton transport dynamics, and the influence of temperature and solvent environment on charge transport in these systems.

Key findings include the observation that substituting acetate with trifluoroacetate enhances the ionic nature of the system while reducing its dielectric constant. The high dielectric constant for [MimH][AcO] indicates the presence of dynamic dipolar correlations, typical for hydrogen-bonded liquids but also hindered translation of ions. Substitution of acetate with trifluoroacetate increases the overall conductivity of the PIL, despite increasing viscosity. The mobilities of molecular species obtained by DOSY experiments suggest that charge transport in [MimH][AcO] is dominated by a vehicular-type mechanism. Substitution with trifluoroacetate enhances proton mobility significantly, indicating a Grotthuss-type transport contributing to the charge carrier dynamics in the PIL. This substitution also leads to a significant increase in conductivity at high trifluoroacetate concentrations, attributed to enhanced proton transport and a shift from hindered to free ionic motion, as suggested by MD simulations. Temperature-dependent studies further reveal that thermal energy is not sufficient to break the cages that hinder ion translation. However, increased temperature accelerates the dynamics of the system and increases the dynamic nature of the cage structures. Additionally, the results highlight the critical role of the chemical environment in modulating protonation equilibria and dynamics, with polar solvents significantly impacting the mobility of ionic species and the overall conductivity of PIL solutions. In particular, aprotic DMF leads to the formation of electro-neutral molecular species and low conductivity, whereas MeOH facilitates high charge carrier mobility and efficiently solvates ionic species, likely through its ability to form an extended hydrogen-bonded network. Transient absorption experiments revealed two key spectral features indicative of the

protonation of acetate and acetic acid, highlighting the importance of $AcO^- \rightleftharpoons AcOH$ and $AcOH \rightleftharpoons AcOH_2^+$ equilibria in proton transfer dynamics. Specifically, the transient absorption experiments provide experimental evidence for the formation of $AcOH_2^+$ and its decisive role in enabling Grotthuss-like proton transport in [MimH][AcO]. However, protonation of AcOH only occurs for an excess of AcOH relative to acetate. The comparison of the linewidths of induced absorption and bleach indicates that only a sub-ensemble of AcOH in solution contributes to proton transport, suggesting the H^+-induced disruption of hydrogen-bonded acetic acid structures.
The nuanced understanding of these molecular dynamics, as garnered from the present thesis, underscores the potential for tailoring PILs with optimized charge transport properties for task-specific applications. By manipulating the chemical structure and environment, such as by altering proton acceptors and donors or the hydrogen-bonded structure that enables charge transport, it is possible to engineer PIL systems that exhibit high conductivity and favorable charge transport pathways. This work not only advances our knowledge of the fundamental properties and dynamics of PILs but also opens pathways for the development of highly efficient and customizable ionic liquids for a wide range of technological applications.

While the findings presented in this work contribute substantially to our understanding of charge carrier dynamics in PILs, they also open up avenues for further investigations worth addressing.
In particular, the study highlights the critical importance of protonation equilibria in optimizing the properties of PILs. Thus, variation of the donor/acceptor ratio via investigation of non-stoichiometric PIL systems might be of interest. Specifically, introducing an excess of Brønsted acid relative to Brønsted base may increase the number of additional protons in the PIL and might therefore have a significant impact on the charge carrier dynamics, potentially enhancing the Grotthuss-type contribution to the overall conductivity. Conversely, exploring the opposite ratio adjustment by introducing an excess of Brønsted base may provide valuable insights, as MD simulations proposed that both 1-methylimidazole and its protonated form participate in the Grotthuss-like transport.[71] Protonated acetic acid ($AcOH_2^+$) appears to act as an intermediate in the Grotthuss-type conduction process. Therefore, an excess of base molecules could promote such intermediates on the cationic side of PILs, resulting in an enhanced conductivity. Additionally, increasing the number of proton acceptor sites via substitution of 1-methylimidazole by imidazole may lead to a similar effect as an excess of base molecules and is worth investigating.
Moreover, the findings showed that the acidity of the Brønsted acid significantly affects the ionicity of the PIL and plays a crucial role in modulating the transport dynamics. To further elucidate the impact of acidity on property-function relationships in PIL systems, one could adjust the acidity – and consequently, the degree of protonation – by gradually altering the fluorination of the Brønsted acid in [MimH][AcO], ranging from acetate to trifluoroacetate (e.g. including H_2FC-COOH and HF_2C-COOH).

Experiments on such partially fluorinated PILs may provide additional insights into how acidity affects proton transfer. This thesis has revealed that the charge transport dynamics in PILs are intricate, and altering a single parameter can impact various facets of charge transport. Hence, predictions about the effects of acidity or non-stoichiometry of PILs on transport dynamics are challenging and a combined experimental and computational study is required to elucidate such effects in detail.

To advance the understanding of proton transport in protic ionic liquids, direct tracking via pump-probe measurements in the neat PIL is crucial. As discussed in the last chapter, the strong absorption of the carbonyl stretching vibration due to acetic acid in [MimH][AcO] prevented measurements in the neat PIL. Consequently, one approach could involve persisting with the model system while attempting to measure an alternative molecular vibration that undergoes significant changes upon protonation. Potential vibrations include those of N-H, C-N, or C-C (adjacent to N-H). Such experiments would have the potential to elucidate the contribution of the imidazolium ions to proton transport, which remained elusive based on the present findings.

In the context of potential applications in energy storage technologies, the understanding of charge transport in PILs at interfaces is pivotal for the tailored and efficient design of PILs. Several studies have indicated that ILs are highly ordered at interfaces.[268–270] The formation of electrical double layers can have a significant effect on diffusivities[270] and, consequently, on vehicular-type transport. The characteristics and behavior of these double layers are closely linked to the chemical structure and properties of the respective ILs.[270] Given the distinct differences in behavior between bulk and interfacial ILs, it can be anticipated that transport dynamics at interfaces differ from the bulk. Therefore, investigating charge transport at interfaces could provide valuable knowledge for applications where PILs serve as electrolytes. Such experimental studies might be particularly relevant for PILs such as [MimH][AcO] with incomplete deprotonation of the Brønsted acid, where charge transport and Grotthuss-like conduction depend on a subtle balance between charged and electro-neutral species, alongside the formation of a hydrogen-bonded network.

Bibliography

(1) Wojnarowska, Z.; Paluch, M. *J. Phys. Condens. Matter* **2015**, *27*, 073202.

(2) Yoshizawa, M.; Xu, W.; Angell, C. A. *J. Am. Chem. Soc.* **2003**, *125*, 15411–15419.

(3) Cottrell, T. L.; Gill, J. E. *J. Chem. Soc.* **1951**, 1798–1800.

(4) Gabriel S.; Weiner, J. *Ber. Dtsch. Chem. Ges.* **1888**, *21*, 2669–2679.

(5) Walden, P. *Bull. Acad. Imper. Sci. St. Petersburg* **1914**, *8*, 405–422.

(6) Wilkes, J. S.; Levisky, J. A.; Wilson, R. A.; Hussey, C. L. *Inorg. Chem.* **1982**, *21*, 1263–1264.

(7) Pena-Pereira, F.; Namieśnik, J. *ChemSusChem* **2014**, *7*, 1784–1800.

(8) Wilkes, J. S.; Zaworotko, M. J. *J. Chem. Soc., Chem. Commun.* **1992**, 965–967.

(9) Wang, B.; Qin, L.; Mu, T.; Xue, Z.; Gao, G. *Chem. Rev.* **2017**, *117*, 7113–7131.

(10) Maton, C.; De Vos, N.; Stevens, C. V. *Chem. Soc. Rev.* **2013**, *42*, 5963–5977.

(11) Freemantle, M. *Chem. Eng. News* **1998**, *76*, 32—37.

(12) Plechkova, N. V.; Seddon, K. R. *Chem. Soc. Rev.* **2008**, *37*, 123–150.

(13) Earle, M. J.; Seddon, K. R. *Pure Appl. Chem.* **2000**, *72*, 1391–1398.

(14) Yang, J. Z.; Wang, B.; Zhang, Q. G.; Tong, J. *Fluid Ph. Equilib.* **2007**, *251*, 68–70.

(15) Hapiot, P.; Lagrost, C. *Chem. Rev.* **2008**, *108*, 2238–2264.

(16) Wang, H.; Gurau, G.; Rogers, R. D. *Chem. Soc. Rev.* **2012**, *41*, 1519–1537.

(17) Zeng, S.; Zhang, X.; Bai, L.; Zhang, X.; Wang, H.; Wang, J.; Bao, D.; Li, M.; Liu, X.; Zhang, S. *Chem. Rev.* **2017**, *117*, 9625–9673.

(18) Zhang, Z.; Song, J.; Han, B. *Chem. Rev.* **2017**, *117*, 6834–6880.

(19) Hallett, J. P.; Welton, T. *Chem. Rev.* **2011**, *111*, 3508–3576.

(20) Freudenmann, D.; Wolf, S.; Wolff, M.; Feldmann, C. *Angew. Chem. Int. Ed.* **2011**, *50*, 11050–11060.

(21) Torimoto, T.; Tsuda, T.; Okazaki, K. I.; Kuwabata, S. *Adv. Mater.* **2010**, *22*, 1196–1221.

(22) Pârvulescu, V. I.; Hardacre, C. *Chem. Rev.* **2007**, *107*, 2615–2665.

(23) Zhang, Q.; Zhang, S.; Deng, Y. *Green Chem.* **2011**, *13*, 2619–2637.

(24) Riisager, A.; Eriksen, K. M.; Wasserscheid, P.; Fehrmann, R. *Catal. Lett.* **2003**, *90*, 149–153.

(25) Scholten, J. D.; Leal, B. C.; Dupont, J. *ACS Catal.* **2012**, *2*, 184–200.

(26) Liu, W.; Ye, C.; Gong, Q.; Wang, H.; Wang, P. *Tribol. Lett.* **2002**, *13*, 81–85.

(27) Phillips, B. S.; Zabinski, J. S. *Tribol. Lett.* **2004**, *17*, 533–541.

(28) Jork, C.; Seiler, M.; Beste, Y. A.; Arlt, W. *J. Chem. Eng. Data* **2004**, *49*, 852–857.

(29) Ventura, S. P.; E Silva, F. A.; Quental, M. V.; Mondal, D.; Freire, M. G.; Coutinho, J. A. *Chem. Rev.* **2017**, *117*, 6984–7052.

(30) Sun, X.; Luo, H.; Dai, S. *Chem. Rev.* **2012**, *112*, 2100–2128.

(31) Hassanzadeganroudsari, M.; Soltani, M.; Heydarinasab, A.; Nakhjiri, A. T.; Hossain, M. D.; Khiyavi, A. A. *J. Mol. Liq.* **2020**, *310*, 113254.

(32) Banerjee, A.; Ibsen, K.; Brown, T.; Chen, R.; Agatemor, C.; Mitragotri, S. *Proc. Natl. Acad. Sci. U.S.A.* **2018**, *115*, 7296–7301.

(33) Uddin, M.; Basak, D.; Hopefl, R.; Minofar, B. *J. Pharm. Pharm. Sci.* **2020**, *23*, 158–176.

(34) Qi, Q. M.; Mitragotri, S. *J. Control. Release* **2019**, *311*, 162–169.

(35) Davis, J. H.; Forrester, K. J.; Merrigan, T. *Tetrahedron Lett.* **1998**, *39*, 8955–8958.

(36) Shamshina, J. L.; Kelley, S. P; Gurau, G.; Rogers, R. D. *Nature* **2015**, *528*, 188–189.

(37) Jadhav, N. R.; Bhosale, S. P.; Bhosale, S. S.; Mali, S. D.; Toraskar, P. B.; Kadam, T. S. *J. Drug Deliv. Sci. Technol.* **2021**, *65*, 102694.

(38) Chowdhury, M. R.; Moshikur, R. M.; Wakabayashi, R.; Tahara, Y.; Kamiya, N.; Moniruzzaman, M.; Goto, M. *Mol. Pharm.* **2018**, *15*, 2484–2488.

(39) Marrucho, I. M.; Branco, L. C.; Rebelo, L. P. *Annu. Rev. Chem. Biomol. Eng.* **2014**, *5*, 527–546.

(40) Seddon, K. R. *J. Am. Chem. Soc.* **2003**, *2*, 948–959.

(41) Watanabe, M.; Thomas, M. L.; Zhang, S.; Ueno, K.; Yasuda, T.; Dokko, K. *Chem. Rev.* **2017**, *117*, 7190–7239.

(42) Macfarlane, D. R.; Tachikawa, N.; Forsyth, M.; Pringle, J. M.; Howlett, P. C.; Elliott, G. D.; Davis, J. H.; Watanabe, M.; Simon, P.; Angell, C. A. *Energy Environ. Sci.* **2014**, *7*, 232–250.

(43) Reynolds, G. F.; Dymek, C. J. *J. Power Sources* **1985**, *15*, 109–118.

(44) Zakeeruddin, S. M.; Grätzel, M. *Adv. Funct. Mater.* **2009**, *19*, 2187–2202.

(45) Kawano, R.; Matsui, H.; Matsuyama, C.; Sato, A.; Susan, M. A. B. H.; Tanabe, N.; Watanabe, M. *J. Photochem. Photobiol. A* **2004**, *164*, 87–92.

(46) Eftekhari, A. *Energy Storage Mater.* **2017**, *9*, 47–69.

(47) Ray, A.; Saruhan, B. *Materials* **2021**, *14*, 2942.

(48) Díaz, M.; Ortiz, A.; Ortiz, I. *J. Membr. Sci.* **2014**, *469*, 379–396.

(49) Lee, S. Y.; Ogawa, A.; Kanno, M.; Nakamoto, H.; Yasuda, T.; Watanabe, M. *J. Am. Chem. Soc.* **2010**, *132*, 9764–9773.

(50) Zhou, Y.; Qu, J. *ACS Appl. Mater. Interfaces* **2017**, *9*, 3209–3222.

(51) Wooster, T. J.; Johanson, K. M.; Fraser, K. J.; MacFarlane, D. R.; Scott, J. L. *Green Chem.* **2006**, *8*, 691–69.

(52) Earle, M. J.; Esperança, J. M.; Gilea, M. A.; Lopes, J. N.; Rebelo, L. P.; Magee, J. W.; Seddon, K. R.; Widegren, J. A. *Nature* **2006**, *439*, 831–834.

(53) Zhao, D.; Liao, Y.; Zhang, Z. D. *Clean - Soil, Air, Water* **2007**, *35*, 42–48.

(54) Pinkert, A.; Marsh, K. N.; Pang, S.; Staiger, M. P. *Chem. Rev.* **2009**, *109*, 6712–6728.

(55) Béguin, F.; Presser, V.; Balducci, A.; Frackowiak, E. *Adv. Mater.* **2014**, *26*, 2219–2251.

(56) Menne, S.; Pires, J.; Anouti, M.; Balducci, A. *Electrochem. Commun.* **2013**, *31*, 39–41.

(57) Greaves, T. L.; Drummond, C. J. *Chem. Rev.* **2008**, *108*, 206–237.

(58) Fumino, K.; Wulf, A.; Ludwig, R. *Angew. Chem. Int. Ed.* **2009**, *48*, 3184–3186.

(59) Fumino, K.; Reichert, E.; Wittler, K.; Hempelmann, R.; Ludwig, R. *Angew. Chem.* **2012**, *124*, 6340–6344.

(60) Hayes, R.; Imberti, S.; Warr, G. G.; Atkin, R. *Angew. Chem.* **2013**, *125*, 4721–4725.

(61) Doi, H.; Song, X.; Minofar, B.; Kanzaki, R.; Takamuku, T.; Umebayashi, Y. *Chem. Eur. J.* **2013**, *19*, 11522–11526.

(62) Shen, M.; Zhang, Y.; Chen, K.; Che, S.; Yao, J.; Li, H. *J. Phys. Chem. B* **2017**, *121*, 1372–1376.

(63) Greaves, T. L.; Drummond, C. J. *Chem. Rev.* **2015**, *115*, 11379–11448.

(64) Hollóczki, O.; Malberg, F.; Welton, T.; Kirchner, B. *Phys. Chem. Chem. Phys.* **2014**, *16*, 16880–16890.

(65) Kanzaki, R.; Doi, H.; Song, X.; Hara, S.; Ishiguro, S. I.; Umebayashi, Y. *J. Phys. Chem. B* **2012**, *116*, 14146–14152.

(66) Joerg, F.; Schröder, C. *Phys. Chem. Chem. Phys.* **2022**, *24*, 15245–15254.

(67) Chen, K.; Wang, Y.; Yao, J.; Li, H. *J. Phys. Chem. B* **2018**, *122*, 309–315.

(68) Zhang, J.; Yao, J.; Li, H. *J. Phys. Chem. B* **2022**, *126*, 2279–2284.

(69) Tolstoy, P. M.; Guo, J.; Koeppe, B.; Golubev, N. S.; Denisov, G. S.; Smirnov, S. N.; Limbach, H. H. *J. Phys. Chem. A* **2010**, *114*, 10775–10782.

(70) Schuster, I. I.; Dyllick-Brenzinger, C.; Roberts, J. D. *J. Org. Chem.* **1979**, *44*, 1765–1768.

(71) Ingenmey, J.; Gehrke, S.; Kirchner, B. *ChemSusChem* **2018**, *11*, 1900–1910.

(72) Watanabe, H.; Umecky, T.; Arai, N.; Nazet, A.; Takamuku, T.; Harris, K. R.; Kameda, Y.; Buchner, R.; Umebayashi, Y. *J. Phys. Chem. B* **2019**, *123*, 6244–6252.

(73) Watanabe, H.; Arai, N.; Kameda, Y.; Buchner, R.; Umebayashi, Y. *J. Phys. Chem. B* **2020**, *124*, 11157–11164.

(74) Stoppa, A.; Hunger, J.; Buchner, R.; Hefter, G.; Thoman, A.; Helm, H. *J. Phys. Chem. B* **2008**, *112*, 4854–4858.

(75) Marcus, Y.; Hefter, G. *Chem. Rev.* **2006**, *106*, 4585–4621.

(76) Stoppa, A.; Buchner, R.; Hefter, G. *J. Mol. Liq.* **2010**, *153*, 46–51.

(77) Hunger, J.; Stoppa, A.; Schrödle, S.; Hefter, G.; Buchner, R. *ChemPhysChem* **2009**, *10*, 723–733.

(78) Joerg, F.; Sutter, J.; van Dam, L.; Kanellopoulos, K.; Hunger, J.; Schröder, C. *J. Mol. Liq.* **2024**, *396*, 123834.

(79) Shim, Y.; Kim, H. J. *J. Phys. Chem. B* **2008**, *112*, 11028–11038.

(80) Siwick, B. J.; Bakker, H. J. *J. Am. Chem. Soc.* **2007**, *129*, 13412–13420.

(81) Siwick, B. J.; Cox, M. J.; Bakker, H. J. *J. Phys. Chem. B* **2008**, *112*, 378–389.

(82) Timmer, R. L.; Cox, M. J.; Bakker, H. J. *J. Phys. Chem. A* **2010**, *114*, 2091–2101.

(83) Wedler, G., *Lehrbuch der physikalischen Chemie*, 5. Auflage; Wiley-VCH: Weinheim, 2004.

(84) Poplavko, Y., *Dielectric Spectroscopy of Electronic Materials*; Woodhead Publishing: 2021.

(85) Böttcher, C. F. J.; Bordewijk, P., *Theory of electric polarization, Vol. I and II*, 2nd edition; Elsevier: Amsterdam, 1978.

(86) Chalmers, J. M.; Griffith, P. R., *Handbook of Vibrational Spectroscopy*; Wiley-VCH: Weinheim, 2001.

(87) Maxwell, J. C., *A treatise on electricity and magnetism: Pt. III. Magnetism. pt. IV. Electromagnetism*; Clarendon Press: 1881.

(88) Greschner, G. S., *Maxwellgleichungen: das elektromagnetische Feld in Physik und Chemie*; Hüthig & Wepf: 1981.

(89) Kremer, F.; Schönhals, A., *Broadband Dielectric Spectroscopy*; Springer-Verlag: Berlin Heidelberg, 2013.

(90) Atkins, P. W.; de Paula, J., *Physikalische Chemie*, Fünfte Auflage; Wiley-VCH: Weinheim, 2013.

(91) Barthel, J.; Bachhuber, K.; Buchner, R., *Kinetic Processes in Electrolyte Solutions in High Frequency Electric Fields*; Moreau, M., Turq, P., Eds.; Springer US: Boston, MA, 1988, pp 55–71.

(92) Barthel, J.; Bachhuber, K.; Buchner, R.; Hetzenauer, H.; Kleebauer, M. *Ber. Bunsenges. Phys. Chem.* **1991**, *95*, 853–859.

(93) Barthel, J. M. G.; Buchner, R. *Pure Appl. Chem.* **1991**, *63*, 1473–1482.

(94) Falkenhagen, H.; Hertz, H. G.; Ebeling, W., *Theorie der Elektrolyte*; Hirzel: Leipzig, 1971.

(95) Debye, P.; Falkenhagen, H. *Phys. Z.* **1928**, *29*, 401–426.

(96) Barthel, J; Buchner, R. *Chem. Soc. Rev.* **1992**, *21*, 263–270.

(97) Barthel, J.; Buchner, R.; Eberspächer, P. N.; Münsterer, M.; Stauber, J.; Wurm, B. *J. Mol. Liq.* **1998**, *78*, 83–109.

(98) Buchner, R.; Hefter, G. *Phys. Chem. Chem. Phys.* **2009**, *11*, 8984–8999.

(99) Barthel, J. M. G.; Buchner, R.; Bachhuber, K.; Hetzenauer, H.; Kleebauer, M.; Ortmaier, H. *Pure Appl. Chem.* **1990**, *62*, 2287–2296.

(100) Barthel, J.; Buchner, R.; Steger, H *Wissenschaftliche Zeitschrift der Technischen Hochschule Carl Schorlemmer Leuna-Merseburg* **1989**, *31*, 409–423.

(101) Buchner, R.; Barthel, J. *J. Mol. Liq.* **1995**, *63*, 55–75.

(102) Hunger, J.; Stoppa, A.; Buchner, R.; Hefter, G. *J. Phys. Chem. B* **2008**, *112*, 12913–12919.

(103) Hunger, J.; Stoppa, A.; Buchner, R.; Hefter, G. *J. Phys. Chem. B* **2009**, *113*, 9527–9537.

(104) Sutter, J.; Haese, C.; Graf, R.; Hunger, J. *J. Mol. Liq.* **2023**, *390*, 122975.

(105) Schröder, C. *J. Chem. Phys.* **2011**, *135*, 024502.

(106) Giraud, G.; Gordon, C. M.; Dunkin, I. R.; Wynne, K. *J. Chem. Phys.* **2003**, *119*, 464–477.

(107) Turton, D. A.; Hunger, J.; Stoppa, A.; Hefter, G.; Thoman, A.; Walther, M.; Buchner, R.; Wynne, K. *J. Am. Chem. Soc.* **2009**, *131*, 11140–11146.

(108) Debye, P., *Polar Molecules*; Dover Publications: 1929.

(109) Cole, K. S.; Cole, R. H. *J. Chem. Phys.* **1941**, *9*, 341–351.

(110) Cole, K. S.; Cole, R. H. *J. Chem. Phys.* **1942**, *10*, 98–105.

(111) Davidson, D.; Cole, R. H. *J. Chem. Phys.* **1950**, *18*, 1417–1417.

(112) Davidson, D. W.; Cole, R. H. *J. Chem. Phys.* **1951**, *19*, 1484–1490.

(113) Havriliak, S.; Negami, S. *J. Polym. Sci., Part C: Polym. Symp.* **1966**, *14*, 99–117.

(114) Cavell, E. A. S.; Knight, P. C.; A., S. M. *Trans. Faraday Soc.* **1971**, *67*, 2225–2233.

(115) Barthel, J.; Hetzenauer, H; Buchner, R. *Ber. Bunsenges. Phys. Chem.* **1992**, *96*, 1424–1432.

(116) Scholte, T. G. *Physica* **1949**, *15*, 437–449.

(117) Dote, J. L.; Kivelson, D.; Schwartz, R. N. *J. Phys. Chem.* **1981**, *85*, 2169–2180.

(118) Glarum, S. H. *J. Chem. Phys.* **1960**, *33*, 639–643.

(119) Powles, J. *J. Chem. Phys.* **1953**, *21*, 633–637.

(120) Madden, P.; Kivelson, D., *A consistent molecular treatment of dielectric phenomena*; Wiley Online Library: 1984, pp 467–566.

(121) Vogel, H. *Phys. Z.* **1921**, *22*, 645.

(122) Fulcher, G. S. *J. Am. Ceram. Soc.* **1925**, *8*, 339–355.

(123) Angell, C. *J. Non-Cryst. Solids* **1991**, *131*, 13–31.

(124) Hamm, P.; Zanni, M., *Concepts and Methods of 2D Infrared Spectroscopy*; Cambridge University Press: 2011.

(125) Demtröder, W., *Laserspektroskopie 1 Grundlagen*, 6. Auflage; Springer-Verlag: Berlin Heidelberg, 2007.

(126) Juozapavicius, M.; Kaucikas, M.; van Thor, J. J.; O'Regan, B. C. *J. Phys. Chem. C* **2013**, *117*, 116–123.

(127) Yagi, I.; Mikami, K.; Ebina, K.; Okamura, M.; Uosaki, K. *J. Phys. Chem. B* **2006**, *110*, 14192–14197.

(128) Pawlowicz, N.; Groot, M.-L.; van Stokkum, I.; Breton, J.; van Grondelle, R. *Biophys. J.* **2007**, *93*, 2732–2742.

(129) Van Wilderen, L. J. G. W.; Neumann, C.; Rodrigues-Correia, A.; Kern-Michler, D.; Mielke, N.; Reinfelds, M.; Heckel, A.; Bredenbeck, J. *Phys. Chem. Chem. Phys.* **2017**, *19*, 6487–6496.

(130) Wynne, K.; Hochstrasser, R. *Chem. Phys.* **1995**, *193*, 211–236.

(131) Rubtsov, I. V.; Redmore, N. P.; Hochstrasser, R. M.; Therien, M. J. *J. Am. Chem. Soc.* **2004**, *126*, 2684–2685.

(132) Yang, Y.; Jones, D.; von Haimberger, T.; Linke, M.; Wagnert, L.; Berg, A.; Levanon, H.; Zacarias, A.; Mahammed, A.; Gross, Z.; Heyne, K. *J. Phys. Chem. A* **2012**, *116*, 1023–1029.

(133) Ghosh, R.; Mora, A. K.; Nath, S.; Palit, D. K. *J. Phys. Chem. B* **2017**, *121*, 1068–1080.

(134) Hamm, P. *J. Biol. Phys.* **2009**, *35*, 17–30.

(135) Nibbering, E. T.; Elsaesser, T. *Chem. Rev.* **2004**, *104*, 1887–1914.

(136) Mazur, K.; Bonn, M.; Hunger, J. *J. Phys. Chem. B* **2015**, *119*, 1558–1566.

(137) Cox, M. J.; Siwick, B. J.; Bakker, H. J. *ChemPhysChem* **2009**, *10*, 236–244.

(138) Cox, M. J.; Timmer, R. L. A.; Bakker, H. J.; Park, S.; Agmon, N. *J. Phys. Chem. A* **2009**, *113*, 6599–6606.

(139) Finkler, B.; Spies, C.; Vester, M.; Walte, F.; Omlor, K.; Riemann, I.; Zimmer, M.; Stracke, F.; Gerhards, M.; Jung, G. *Photochem. Photobiol. Sci.* **2014**, *13*, 548–562.

(140) Chae, Y.; Min, S.; Park, E.; Lim, C.; Cheon, C.-H.; Jeong, K.; Kwak, K.; Cho, M. *Anal. Chem.* **2021**, *93*, 2106–2113.

(141) Alshamleh, I.; Krause, N.; Richter, C.; Kurrle, N.; Serve, H.; Günther, U. L.; Schwalbe, H. *Angew. Chem.* **2020**, *132*, 2324–2328.

(142) Deborde, C.; Moing, A.; Roch, L.; Jacob, D.; Rolin, D.; Giraudeau, P. *Prog. Nucl. Magn. Reson. Spectrosc.* **2017**, *102-103*, 61–97.

(143) Friebolin, H., *Ein- und zweidimensionale NMR-Spektroskopie Eine Einführung*, Zweite Auflage; VCH Verlagsgesellschaft: Weinheim, 1992.

(144) Hesse, M.; Meier, H.; Zeeh, B., *Spektroskopische Methoden in der organischen Chemie*; Georg Thieme Verlag: 2005.

(145) Frydman, L.; Lupulescu, A.; Scherf, T. *J. Am. Chem. Soc.* **2003**, *125*, 9204–9217.

(146) Kriwacki, R. W.; Pitner, T. P. *Pharm. Res.* **1989**, *6*, 531–554.

(147) Nyberg, N. T.; Duus, J. Ø.; Sørensen, O. W. *J. Am. Chem. Soc.* **2005**, *127*, 6154–6155.

(148) Köck, M.; Reif, B.; Fenical, W.; Griesinger, C. *Tetrahedron Lett.* **1996**, *37*, 363–366.

(149) Balayssac, S.; Gilard, V.; Delsuc, M.-A.; Malet-Martino, M. *Spectrosc. Eur.* **2009**, *21*, 10–14.

(150) Johnson, C. *Prog. Nucl. Magn. Reson. Spectrosc.* **1999**, *34*, 203–256.

(151) Tanner, J. E.; Stejskal, E. O. *J. Chem. Phys.* **1968**, *49*, 1768–1777.

(152) Leviti, M. H.; Freeman, R. *J. Magn. Reson.* **1979**, *33*, 473–476.

(153) Seddon, K. R.; Stark, A.; Torres, M.-J. *Pure Appl. Chem.* **2000**, *72*, 2275–2287.

(154) Andanson, J. M.; Meng, X.; Traïkia, M.; Husson, P. *J. Chem. Thermodyn.* **2016**, *94*, 169–176.

(155) Doblinger, S.; Donati, T. J.; Silvester, D. S. *J. Phys. Chem. C* **2020**, *124*, 20309–20319.

(156) Dabiri, M.; Baghbanzadeh, M.; Arzroomchilar, E. *Catal. Commun.* **2008**, *9*, 939–942.

(157) Zhao, G.; Jiang, T.; Gao, H.; Han, B.; Huang, J.; Sun, D. *Green Chem.* **2004**, *6*, 75–77.

(158) Shoaib, N., *Vector network analyzer (VNA) measurements and uncertainty assessment*; Springer: 2017; Vol. 1.

(159) Ensing, W.; Hunger, J.; Ottosson, N.; Bakker, H. J. *J. Phys. Chem. C* **2013**, *117*, 12930–12935.

(160) Blackham, D. V.; Pollard, R. D. *IEEE Trans. Instrum. Meas.* **1997**, *46*, 1093–1099.

(161) Balos, V.; Kim, H.; Bonn, M.; Hunger, J. *Angew. Chem. Int. Ed.* **2016**, *55*, 8125–8128.

(162) Barthel, J.; Buchner, R.; Wurm, B. *J. Mol. Liq.* **2002**, *98*, 51–69.

(163) Shirke, R. M.; Chaudhari, A.; More, N. M.; Patil, P. B. *J. Mol. Liq.* **2001**, *94*, 27–36.

(164) Gottlieb, H. E.; Kotlyar, V.; Nudelman, A *J. Org. Chem.* **1997**, *3263*, 7512–7515.

(165) Neese, F.; Wennmohs, F.; Becker, U.; Riplinger, C. *J. Chem. Phys.* **2020**, *152*, 224108.

(166) Becke, A. D. *J. Chem. Phys.* **1993**, *98*, 5648–5652.

(167) Lee, C.; Yang, W.; Parr, R. G. *Phys. Rev. B* **1988**, *37*, 785–789.

(168) Weigend, F.; Ahlrichs, R. *Phys. Chem. Chem. Phys.* **2005**, *7*, 3297–3305.

(169) Dote, J. L.; Kivelson, D. *J. Phys. Chem.* **1983**, *87*, 3889–3893.

(170) Lu, T.; Chen, F. *J. Comput. Chem.* **2012**, *33*, 580–592.

(171) Zhang, J.; Lu, T. *Phys. Chem. Chem. Phys.* **2021**, *23*, 20323–20328.

(172) Hait, D.; Head-Gordon, M. *J. Chem. Theory Comput.* **2018**, *14*, 1969–1981.

(173) Zapata, J. C.; McKemmish, L. K. *J. Phys. Chem. A* **2020**, *124*, 7538–7548.

(174) Grimme, S.; Ehrlich, S.; Goerigk, L. *J. Comput. Chem.* **2011**, *32*, 1456–1465.

(175) Schröder, C.; Steinhauser, O. *J. Chem. Phys.* **2010**, *132*, 244109.

(176) Schröder, C. *Phys. Chem. Chem. Phys.* **2012**, *14*, 3089–3102.

(177) Bedrov, D.; Piquemal, J.-P.; Borodin, O.; MacKerell, Jr., A. D.; Roux, B.; Schröder, C. *Chem. Rev.* **2019**, *119*, 7940–7995.

(178) https://cgenff.umaryland.edu/.

(179) Vanommeslaeghe, K.; Hatcher, E.; Acharya, C.; Kundu, S.; Zhong, S.; Shim, J.; Darian, E.; Guvench, O.; Lopes, P.; Vorobyov, I.; Mackerell Jr., A. D. *J. Comput. Chem.* **2010**, *31*, 671–690.

(180) Kumar, A.; Yoluk, O.; MacKerell Jr., A. D. *J. Comput. Chem.* **2020**, *41*, 958–970.

(181) Chatterjee, P.; Heid, E.; Schröder, C.; MacKerell, A. *Biophys. J.* **2019**, *116*, 142a.

(182) Becker, T. M.; Dubbeldam, D.; Lin, L.-C.; Vlugt, T. J. *J. Comput. Sci.* **2016**, *15*, 86–94.

(183) Martínez, L.; Andrade, R.; Birgin, E. G.; Martínez, J. M. *J. Comput. Chem.* **2009**, *30*, 2157–2164.

(184) Brooks, B. R. et al. *J. Comput. Chem.* **2009**, *30*, 1545–1614.

(185) Eastman, P.; Swails, J.; Chodera, J. D.; McGibbon, R. T.; Zhao, Y.; Beauchamp, K. A.; Wang, L.-P.; Simmonett, A. C.; Harrigan, M. P.; Stern, C. D.; Wiewiora, R. P.; Brooks, B. R.; Pande, V. S. *PLoS Comput. Biol.* **2017**, *13*, e1005659.

(186) Son, C. Y.; McDaniel, J. G.; Cui, Q.; Yethiraj, A. *J. Phys. Chem. Lett.* **2019**, *10*, 7523–7530.

(187) Gong, Z.; Padua, A. A. H. *J. Chem. Phys.* **2021**, *154*, 084504.

(188) Michaud-Agrawal, N.; Denning, E. J.; Woolf, T. B.; Beckstein, O. *J. Comput. Chem.* **2011**, *32*, 2319–2327.

(189) Richard J. Gowers; Max Linke; Jonathan Barnoud; Tyler J. E. Reddy; Manuel N. Melo; Sean L. Seyler; Jan Domański; David L. Dotson; Sébastien Buchoux; Ian M. Kenney; Oliver Beckstein In *Proceedings of the 15th Python in Science Conference*, ed. by Sebastian Benthall; Scott Rostrup, 2016, pp 98 –105.

(190) Austen Angell, C.; Ansari, Y.; Zhao, Z. *Faraday Discuss.* **2012**, *154*, 9–27.

(191) Rogers, R. D.; Seddon, K. R. *Science* **2003**, *302*, 792–793.

(192) Niedermeyer, H.; Hallett, J. P.; Villar-Garcia, I. J.; Hunt, P. A.; Welton, T. *Chem. Soc. Rev.* **2012**, *41*, 7780–7802.

(193) Endres, F.; Zein El Abedin, S. *Phys. Chem. Chem. Phys.* **2006**, *8*, 2101–2116.

(194) Stoimenovski, J.; Dean, P. M.; Izgorodina, E. I.; MacFarlane, D. R. *Faraday Discuss.* **2012**, *154*, 335–352.

(195) Chieng, N.; Rades, T.; Saville, D. *Eur. J. Pharm. Biopharm.* **2008**, *68*, 771–780.

(196) Wojnarowska, Z.; Grzybowska, K.; Hawelek, L.; Swiety-Pospiech, A.; Masiewicz, E.; Paluch, M.; Sawicki, W.; Chmielewska, A.; Bujak, P.; Markowski, J. *Mol. Pharm.* **2012**, *9*, 1250–1261.

(197) Xu, W.; Angell, C. A. *Science* **2003**, *302*, 422–425.

(198) Lewandowski, A.; Świderska-Mocek, A. *J. Power Sources* **2009**, *194*, 601–609.

(199) Frömling, T.; Kunze, M.; Schönhoff, M.; Sundermeyer, J.; Roling, B. *J. Phys. Chem. B* **2008**, *112*, 12985–12990.

(200) Belieres, J. P.; Gervasio, D.; Angell, C. A. *Chem. Commun.* **2006**, *111*, 4799–4801.

(201) Menne, S.; Kühnel, R. S.; Balducci, A. *Electrochim. Acta* **2013**, *90*, 641–648.

(202) Weingärtner, H.; Knocks, A.; Schrader, W.; Kaatze, U. *J. Phys. Chem. A* **2001**, *105*, 8646–8650.

(203) Fumino, K.; Wulf, A.; Ludwig, R. *Phys. Chem. Chem. Phys.* **2009**, *11*, 8790–8794.

(204) Fumino, K.; Fossog, V.; Stange, P.; Paschek, D.; Hempelmann, R.; Ludwig, R. *Angew. Chem. Int. Ed.* **2015**, *54*, 2792–2795.

(205) Zahn, S.; Thar, J.; Kirchner, B. *J. Chem. Phys.* **2010**, *132*, 124506.

(206) Stoimenovski, J.; Izgorodina, E. I.; MacFarlane, D. R. *Phys. Chem. Chem. Phys.* **2010**, *12*, 10341–10347.

(207) Stoyanov, E. S.; Stoyanova, I. V.; Reed, C. A. *Chem. Eur. J.* **2008**, *14*, 3596–3604.

(208) Schröder, C.; Haberler, M.; Steinhauser, O. *J. Chem. Phys.* **2008**, *128*, 134501.

(209) Alei, M.; Wageman, W. E.; Whaley, T. W.; Morgan, L. O. *J. Am. Chem. Soc.* **1980**, *102*, 2881–2887.

(210) Zanatta, M.; Antunes, V. U.; Tormena, C. F.; Dupont, J.; Dos Santos, F. P. *Phys. Chem. Chem. Phys.* **2019**, *21*, 2567–2571.

(211) Szabadi, A.; Honegger, P.; Schöfbeck, F.; Sappl, M.; Heid, E.; Steinhauser, O.; Schröder, C. *Phys. Chem. Chem. Phys.* **2022**, *24*, 15776–15790.

(212) Weingärtner, H. *Angew. Chem. Int. Ed.* **2008**, *47*, 654–670.

(213) Hunger, J.; Stoppa, A.; Thoman, A.; Walther, M.; Buchner, R. *Chem. Phys. Lett.* **2009**, *471*, 85–91.

(214) Fries, P. H.; Richardi, J.; Krienke, H. *Mol. Phys.* **1997**, *90*, 841–854.

(215) Balos, V.; Bonn, M.; Hunger, J. *Phys. Chem. Chem. Phys.* **2017**, *19*, 9724–9728.

(216) Balos, V.; Marekha, B.; Malm, C.; Wagner, M.; Nagata, Y.; Bonn, M.; Hunger, J. *Angew. Chem. Int. Ed.* **2019**, *58*, 332–337.

(217) Fujii, Y.; Yamada, H.; Mizuta, M. *J. Phys. Chem.* **1988**, *92*, 6768–6772.

(218) Lim, M.; Hochstrasser, R. M. *J. Chem. Phys.* **2001**, *115*, 7629–7643.

(219) Heyne, K.; Huse, N.; Dreyer, J.; Nibbering, E. T.; Elsaesser, T.; Mukamel, S. *J. Chem. Phys.* **2004**, *121*, 902–913.

(220) Malm, C.; Kim, H.; Wagner, M.; Hunger, J. *Chem. Eur. J.* **2017**, *23*, 10853–10860.

(221) Barthel, J.; Bachhuber, K.; Buchner, R.; Hetzenauer, H. *Chem. Phys. Lett.* **1990**, *165*, 369–373.

(222) Buchner, R.; Hölzl, C.; Stauber, J.; Barthel, J. *Phys. Chem. Chem. Phys.* **2002**, *4*, 2169–2179.

(223) Petong, P.; Pottel, R.; Kaatze, U. *J. Phys. Chem. A* **1999**, *103*, 6114–6121.

(224) Rinne, K. F.; Gekle, S.; Netz, R. R. *J. Phys. Chem. A* **2014**, *118*, 11667–11677.

(225) Alei, M.; Wageman, W. E.; Alamos, L. *Tetrahedron Lett.* **1979**, *20*, 667–670.

(226) Duereh, A.; Smith, R. L. *J. Supercrit. Fluids* **2018**, *141*, 182–197.

(227) Besghini, D.; Mauri, M.; Simonutti, R. *Appl. Sci.* **2019**, *9*, 1801.

(228) Mazan, V.; Boltoeva, M. *J. Mol. Liq.* **2017**, *240*, 74–79.

(229) Chen, A.; Johnson, J.; Lin, M.; Shapiro, M. J. *J. Am. Chem. Soc.* **1998**, *120*, 9094–9095.

(230) Lengvinaite, D.; Aidas, K.; Kimtys, L. *Phys. Chem. Chem. Phys.* **2019**, *21*, 14811–14820.

(231) Lin, J.; Korte, C. *RSC Adv.* **2020**, *10*, 42596–42604.

(232) Nikam, P. S.; Kharat, S. J. *J. Chem. Eng. Data* **2005**, *50*, 455–459.

(233) Qian, W.; Xu, Y.; Zhu, H.; Yu, C. *J. Chem. Thermodyn.* **2012**, *49*, 87–94.

(234) Hubbard, J.; Onsager, L; Van Beek, W.; Mandel, M *Proc. Natl. Acad. Sci. U.S.A.* **1977**, *74*, 401–404.

(235) Dong, Q.; Muzny, C. D.; Kazakov, A.; Diky, V.; Magee, J. W.; Widegren, J. A.; Chirico, R. D.; Marsh, K. N.; Frenkel, M. *J. Chem. Eng. Data* **2007**, *52*, 1151–1159.

(236) Hunt, P. A. *Mol. Simulat.* **2006**, *32*, 1–10.

(237) Shukla, S. K.; Khupse, N. D.; Kumar, A. *Phys. Chem. Chem. Phys.* **2012**, *14*, 2754–2761.

(238) Miran, M. S.; Hoque, M.; Yasuda, T.; Tsuzuki, S.; Ueno, K.; Watanabe, M. *Phys. Chem. Chem. Phys.* **2019**, *21*, 418–426.

(239) Wojnarowska, Z.; Wang, Y.; Pionteck, J.; Grzybowska, K.; Sokolov, A. P.; Paluch, M. *Phys. Rev. Lett.* **2013**, *111*, 225703.

(240) Shmukler, L. E.; Fedorova, I. V.; Fadeeva, Y. A.; Safonova, L. P. *J. Mol. Liq.* **2021**, *321*, 114350.

(241) Angell, C. A.; Byrne, N.; Belieres, J. P. *Acc. Chem. Res.* **2007**, *40*, 1228–1236.

(242) Verma, P. L.; Gejji, S. P. *J. Phys. Chem. A* **2018**, *122*, 6225–6235.

(243) Joerg, F.; Wieder, M.; Schröder, C. *Front. Chem.* **2023**, *11*, 1140896.

(244) Jacobi, R.; Joerg, F.; Schröder, C. *Phys. Chem. Chem. Phys.* **2022**, *24*, 9277–9285.

(245) Schröder, C.; Hunger, J.; Stoppa, A.; Buchner, R.; Steinhauser, O. *J. Chem. Phys.* **2008**, *129*, 184501.

(246) Volmari, A.; Weingärtner, H. *J. Mol. Liq.* **2002**, *98*, 293–301.

(247) Kirchner, B.; Malberg, F.; Firaha, D. S.; Hollóczki, O. *J. Phys. Condens. Matter* **2015**, *27*, 463002.

(248) Kirkwood, J. G. *J. Chem. Phys.* **1939**, *7*, 911–919.

(249) Honegger, P.; Steinhauser, O.; Schröder, C. *J. Phys. Chem. Lett.* **2023**, *14*, 609–618.

(250) Schröder, C.; Rudas, T.; Steinhauser, O. *J. Chem. Phys.* **2006**, *125*, 244506.

(251) Schröder, C.; Rudas, T.; Neumayr, G.; Gansterer, W.; Steinhauser, O. *J. Chem. Phys.* **2007**, *127*, 044505.

(252) Schrödle, S.; Annat, G.; MacFarlane, D. R.; Forsyth, M.; Buchner, R.; Hefter, G. *Chem. Commun.* **2006**, *16*, 1748–1750.

(253) Balos, V.; Imoto, S.; Netz, R. R.; Bonn, M.; Bonthuis, D. J.; Nagata, Y.; Hunger, J. *Nat. Commun.* **2020**, *11*, 1611.

(254) Varela, L. M.; Carrete, J.; García, M.; Gallego, L. J.; Turmine, M.; Rilo, E.; Cabeza, O. *Fluid Ph. Equilib.* **2010**, *298*, 280–286.

(255) Rilo, E.; Vila, J.; García-Garabal, S.; Varela, L. M.; Cabeza, O. *J. Phys. Chem. B* **2013**, *117*, 1411–1418.

(256) Douhal, A.; Lahmani, F.; Zewail, A. H. *Chem. Phys.* **1996**, *207*, 477–498.

(257) Hammes-Schiffer, S.; Stuchebrukhov, A. A. *Chem. Rev.* **2010**, *110*, 6939–6960.

(258) Mohammed, O. F.; Pines, D.; Pines, E.; Nibbering, E. T. *Chem. Phys.* **2007**, *341*, 240–257.

(259) Cox, M. J.; Bakker, H. J. *J. Chem. Phys.* **2008**, *128*, 174501.

(260) Denisov, G; Mikheev, V; Sokornova, T; Shraiber, V *Sov. J. Chem. Phys.* **1986**, *3*, 1739–1747.

(261) Rini, M.; Magnes, B.-Z.; Pines, E.; Nibbering, E. T. J. *Science* **2003**, *301*, 349–352.

(262) Mohammed, O. F.; Pines, D.; Dreyer, J.; Pines, E.; Nibbering, E. T. J. *Science* **2005**, *310*, 83–86.

(263) Rini, M.; Pines, D.; Magnes, B.-Z.; Pines, E.; Nibbering, E. T. J. *J. Chem. Phys.* **2004**, *121*, 9593–9610.

(264) Mohammed, O. F.; Pines, D.; Nibbering, E. T. J.; Pines, E. *Angew. Chem. Int. Ed.* **2007**, *46*, 1458–1461.

(265) Bruice, P. Y., *Essential organic chemistry*; Pearson Education Upper Saddle River, NJ, USA: 2006.

(266) Solntsev, K. M.; Huppert, D.; Agmon, N.; Tolbert, L. M. *J. Phys. Chem. A* **2000**, *104*, 4658–4669.

(267) Fraenkel, D. *Chem. Phys.* **2023**, *564*, 111626.

(268) Fedorov, M. V.; Kornyshev, A. A. *Chem. Rev.* **2014**, *114*, 2978–3036.

(269) Atkin, R.; Borisenko, N.; Drüschler, M.; Endres, F.; Hayes, R.; Huber, B.; Roling, B. *J. Mol. Liq.* **2014**, *192*, 44–54.

(270) Gil, P. S.; Jorgenson, S. J.; Riet, A. R.; Lacks, D. J. *J. Phys. Chem. C* **2018**, *122*, 27462–27468.

Acknowledgements